Thermophoresis of Polymers in Electrolyte Solutions

Manuel Wolff

Dissertation

München, Januar 2016

Thermophoresis of Polymers in Electrolyte Solutions

Manuel Wolff

Dissertation
zur Erlangung des Grades
Doktor der Naturwissenschaft (Dr. rer. nat.)

an der Fakultät für Physik
der Ludwig-Maximilians-Universität
München

vorgelegt von
Manuel Wolff
aus Fürstenfeldbruck

München, den 26. Januar 2016

Contents

Zusammenfassung

Thermophorese bezeichnet die gerichtete Bewegung von Molekülen in einem Temperaturgradienten und wird seit mehr als 150 Jahren untersucht. Neben der Grundlagenforschung erfreut sich vor allem die Thermophorese von Polymeren regem Forschungsinteresse durch die Möglichkeit, Bindungsaffinitäten von Biomolekülen mithilfe des Effekts zu bestimmen.

In dieser Arbeit wurde ein neues theoretisches Modell für die Thermophorese von Polymeren in Elektrolytlösungen entwickelt, welches die aktuellen Beiträge aus Nichtgleichgewichts- und Gleichgewichtsansätzen vereint, wie zum Beispiel Diffusiophorese. Des Weiteren wurden die elektrostatischen und elektrokinetischen Effekte erneut aufgegriffen und verfeinert um eine umfassendere theoretische Beschreibung zu erhalten.

Die resultierenden thermophoretischen Unterschiede von geladenen und ungeladenen Polymeren in Abhängigkeit von Ionenstärke und Temperatur wurden experimentell untersucht. Es konnte festgestellt werden, dass der häufig beobachtete charakteristische Anstieg der Thermophorese mit der Temperatur nicht auf nichtionischen Ursachen beruht, wie bisher angenommen, sondern durch die Wechselwirkung geladener Polymere mit der Ionenhülle über Diffusiophorese hervorgerufen wird. Ein weiteren Beleg dafür wurde mit einem PNA Polymer erbracht, der sein Thermophoreseverhalten komplett verändert, wenn seine Ladung mithilfe des pH-Werts modifiziert wird. Quantitativ ist der nichtionische Effekt klein gegenüber den ionischen Beiträgen.

Das Verständnis der Thermophorese birgt die Möglichkeit, Veränderungen des Soret-koeffizienten in Untersuchungen zur Bindungsaffinität vorherzusagen, welche wiederum zur Entwicklung von neuen Medikamenten unter Zurhilfenahme von Hochdurchsatzverfahren dienen. Das entwickelte theoretische Modell wurde erfolgreich an α-synuklein Proteinen in monomerer, oligomerer und fibrillarer Form bei verschiedenen Salzkonzentrationen angewandt.

Des Weiteren wurde eine innovative biotechnologische Anwendung von Thermophorese eingeführt und untersucht: Die Temperatur, an welcher der Phasenübergang von einem verzweigten Copolymer stattfindet, wurde in Übereinstimmung mit der herkömmlichen Messmethode über Absorptionsspektrophotometrie für verschiedene Ionenstärken mit Thermophorese bestimmt. Diese neue Messmethode verbindet die Vorteile bei niedrigen Konzentrationen und Volumen zu messen mit der Kompatibilität zu nativen biologischen Umgebungen.

Abstract

Thermophoresis, the directed movement of molecules in a temperature gradient, has been investigated for more than 150 years and is still object of intense research. Apart from fundamental research, the thermophoretic movement of polymers in electrolyte solution recently gained interest because of its application in sensing binding interactions of biomolecules.

First, this work expands the theoretical model of thermophoresis by joining the state of the art microscopic mechanisms stemming from local equilibrium and non-equilibrium effects, as e.g. diffusiophoresis. Additionally, the electrostatic and electrokinetic effects were revisited and refined to a more accurate theoretical description.

Second, the differences between charged and uncharged polymers with respect to ionic strength and temperature were studied experimentally. It could be concluded that the characteristic increase of thermophoresis with base temperature for charged polymers, which was so far attributed to nonionic effects, is based on charge interactions of the polymer with surrounding salt ions via diffusiophoresis. Further evidence is presented by the study of a PNA polymer that changes thermophoretic behavior by tuning the charge with pH. Quantitatively, the nonionic effects are found to be negligible compared to ionic contributions.

The understanding of thermophoresis of polymers provides the opportunity to predict changes of the Soret coefficient in binding affinity assays, which in turn lead to the development of novel pharmaceutics and allow high throughput sensing. The developed model has been successfully applied to disease related monomeric, oligomeric and fibrillar α-synuclein proteins at various salt concentrations.

Additionally, an innovative biotechnological application of thermophoresis was introduced and examined: The phase transition temperature of a smart branched copolymer was determined at variable ionic strength in accordance to absorption spectrophotometry. This novel method has the advantage of low concentration and low volume requirements, coupled with the compatibility to measure in native biological environments.

1   Introduction

Thermophoresis is the effect, which drives molecules in thermal gradients. It was first reported by John Tyndall [1] who observed aerosols repel from a hot source. Later on the effect of temperature gradients on salt mixtures in water has been investigated in greater detail by Ludwig [2] and Soret [3] independently 150 years ago. The concentrations of the solute at two different temperatures (T_1 and T_2) in this gradient can be related by [4]: $c(T_2)/c(T_1) = \exp(-S_T(T_2 - T_1))$

The Soret coefficient (S_T) herein quantifies the feedback of the molecules on the temperature and can be expressed in terms of two transport coefficients: thermal diffusion coefficient (D_T) and diffusion coefficient (D): $S_T = D_T/D$

Currently, the main focus of the field, apart from the study of binary [5] and ternary [6] liquid mixtures is on the behavior of colloids and complex polymer molecules [7, 8]. In organic solvents it has been found that the thermal diffusion coefficient D_T of polymers tends to reach a constant value after a few Kuhn segments [9]. For large molecules it has been recognized that mainly the outer Kuhn segments of a polymer coil dominate thermophoresis of an uncharged polymer [10], which can be pictured as a nondraining coil [11].

However, the most interesting solvent molecule - water - shows an even more complex behavior and the various contributions which influence the polymer to move to the hot or the cold are still under study. It is often difficult to separate these effects experimentally, since most contributions onto a polymer are affected by the same properties: charge, radius of hydration, the ionic shielding, or solvent properties as permittivity, viscosity, and density.

For nonionic polymers in water a similar behavior to the one in organic solvents has been found. Here, D_T reaches a constant value for large molecular weight polymers [12, 13]. However, no clear trend of increasing or decreasing S_T with molecular weight in the low-size range could be found for the different molecular species, such as polyethylene oxide [12] or oligosaccharides [14]. Since theories [15] also are not able to predict the behavior completely [13], further investigation of this contribution is necessary. Another interesting observation is the dependency of the Soret coefficient on base temperature. For a lot of polymers, a characteristic increase with base temperature can be observed [16–21]. We assume that it is connected to changes in the ionic layers, since for nonionic molecules the temperature dependency looks quite different, since S_T is rather constant.

In this work, a novel theoretical framework is tested which incorporates multiple effects and is able to explain most of the behavior of charged polymers in a temperature gradient.

Thermophoresis and its understanding can be exploited in novel bioanalytical techniques. It has been found that, in contrast to other techniques, thermophoresis allows the measurement of binding affinities at realistic conditions [22]. Furthermore, the temperature of coil to globule transition of polymers can be detected at low volume and low concentration [23]. Moreover, thermophoresis also enters as a second order effect in the field of bioengineering as e.g. for nanopores [24] or laser driven polymerase chain reaction (GNA biosolutions, Martinsried, Germany).

2 Theory

In this section the first part treats the theoretical framework for charges of polymers and how they interact with electric fields. In the second part the model for thermophoresis is discussed, where several separate effects are incorporated to build a new overall theory that is capable to predict thermal diffusion for charged of polymers.

2.1 Electrostatics and kinetics of polymers
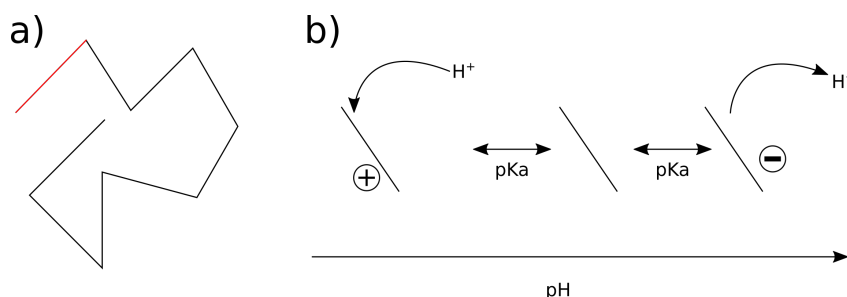
Figure 1: Polymers consist of monomers that can be charged upon pH: a) Polymers are molecules that are made up by the addition of multiple identical monomer segments (indicated red). b) The monomeric segments can either be protonated or deprotonated by *pH* depending on their chemical species. The logarithmic acid dissociation constant (*pK$_a$*) indicates the *pH* at which half of the species carries a charge. Note that for some monomers also multiple protonations or deprotonations might occur.

A polymer is a molecule that is made up by the addition of identical building blocks (monomers) as indicated in Fig. 1a. The diffusion of a polymer is described by its diffusion coefficient, which is related to its hydrodynamic radius *r* by Stokes Einstein with the viscosity η, Boltzmann constant k_B and temperature *T*:

$$D = \frac{k_B T}{6 \pi \eta r} \tag{1}$$

Polymers can be charged if the monomeric subunits are charged and thus interact via electrostatic and electrokinetic phenomena. In the following a theoretical framework will be presented that makes it able to calculate the charge *Q* of a polymer, the resulting zeta potential in aqueous solution ζ and the electrophoretic mobility μ which describes the polymers reaction to an electric field *E*.

2.1.1 Charge

The bare charge of a polymer depends on the *pH*, since some chemical subunits of a monomer can be protonated or deprotonated depending on their aqueous environment. Then they are positively or negatively charged. For a chemical residue the corresponding *pK$_a$* of protonation or deprotonation is a measure at which *pH* half of the population has changed its charge (see Fig. 1b). The bare charge of the

total polymer can be approximately determined by Henderson–Hasselbalch equation and the pK_a of the chemical residues of the monomers.

In the case of Deoxyribonucleic acid (DNA) and the potentially charged residues are the phosphate backbone and the nucleobases, namely Adenine (A), Cytosine (C), Guanine (G) and Thymine (T) [25]. For a DNA strand the corresponding Henderson–Hasselbalch equation reads:

$$Q = A \cdot \frac{1}{1 + 10^{ph-3.5}} + C \cdot \frac{1}{1 + 10^{ph-4.2}} - T \cdot \frac{10^{ph-9.9}}{1 + 10^{ph-9.9}} + G \cdot \left(\frac{1}{1 + 10^{ph-2.1}} - \frac{10^{ph-9.2}}{1 + 10^{ph-9.2}} \right)$$
$$- (A + T + G + C) \cdot \frac{10^{ph-2}}{1 + 10^{ph-2}} - \frac{10^{ph-13.5}}{1 + 10^{ph-13.5}} \quad (2)$$

Here A C G C are the number of corresponding nucleobases within a polymer. The last two terms correspond to the charge of the phosphate backbone and the hydroxyl group. The overall charge is largely changing at extreme pH. For peptides the backbone carries no charge, thus for Peptide Nucleic Acids (PNA)the last term vanishes.
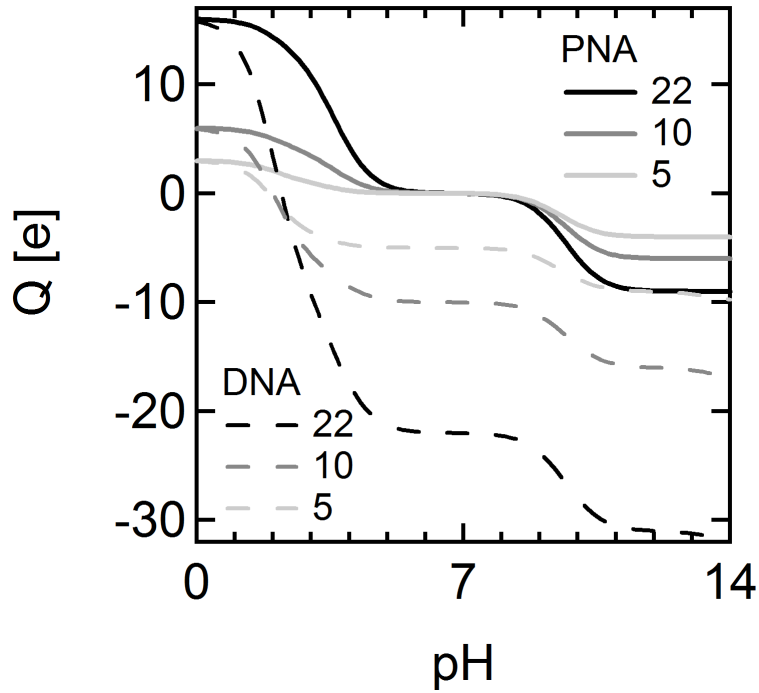
Figure 2: Predicted bare charge for DNA/PNA polymers by Henderson–Hasselbalch equation at various pH (eq. 2). The charges of the studied DNA and PNA molecules of 5, 10 and 22 bases length depend largely on pH due to the pK_a of the nucleobases and backbone (see chapter 3.1 and 3.5). The negatively charged backbone of DNA plays a major role at neutral pH.

For large polymers the effective charge in comparison to the charge determined by eq. 2 can differ, since the pK_a values of the monomeric subunits are also affected by the direct surrounding of the other monomers which are often polar. Nevertheless estimates for the net charge of proteins on the basis of the various pK_a values of the amino acids hold quite well [26, 27].

Still the effective charge, which is observable by e.g. electrophoresis can vary from the pure charge due to counter ion condensation to the backbone [28]. Most recently the decrease of effective charge for a polyelectrolyte with the degree of polymerization was mapped by multiple particle collision experiments [29, 30]. This data was taken into account for the further calculations of DNA, PNA molecules and the effective charges for thermophoresis are in close proximity to the predictions (see chapter 3.5).

2.1.2   Zeta potential

According to Maxwell's equations, charges result in an electric field which can be simplified to a scalar potential. Because of the charged polymer as well as the co- and counter ions a certain potential is build around polymer. For polymers in dilute solution the dissolved ions play an important role. The counterions tend to accumulate around the charged entity and the co-ions with the same charge repel.
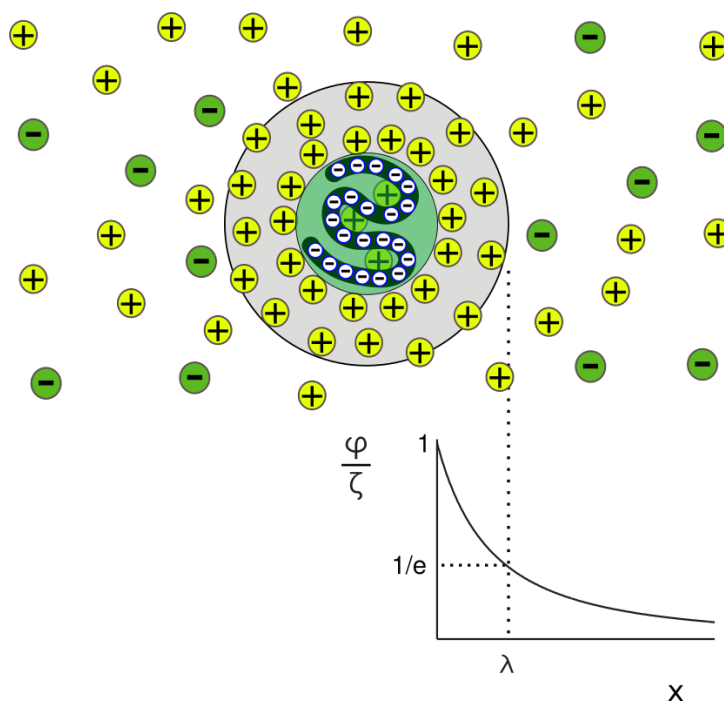
Figure 3: Zeta potential of a charged molecule. A charged polymer in an electrolyte depletes the concentration of identical charged co-ions and gathers oppositely charged counterions which form the so called Debye layer. The resulting potential on the basis of Debye-Hückel theory at the slipping plane is called zeta potential ζ and falls exponentially to $\frac{1}{e}\zeta$ at the Debye length λ (see eq. 5).

Historically Helmholtz [31] first introduced a theoretical model for the double layer with two parallel plane plates with opposite charge. Afterwards the idea of a diffuse double layer was independently evolved by Gouy and Chapman [32, 33]. Apart from the study of arbitrary geometries the most successful approximation for a spherical charged particle in an electrolyte was introduced by Debye and Hückel [34]. Their powerful key to solve the equations was the assumption to linearize the exponential Poisson-Boltzmann term [35].

The resulting potential ϕ around the sphere at radius r is characterized by the Debye length λ. At this characteristic length the potential decreased to a factor of 1/e. It can then be calculated by:

$$\phi = \frac{Q}{4\pi\varepsilon r} \cdot \frac{1}{1+r/\lambda} \tag{3}$$

The Debye length depends on Temperature T, permittivity ε, Boltzmann constant k_B and the concentration of an ionic species c_j in the solution with the corresponding charge q_j.

$$\lambda = \sqrt{\frac{\varepsilon k_B T}{\sum_{j=1}^{N} c_j q_j^2}} \tag{4}$$

For the diffuse layer around a polymers and colloids in solution a slipping plane at radius R is defined which separates the mobile and immobile fluid. In this study it was set equivalent to the stokes radius of hydration (eq. 1). The potential at this layer is called zeta potential(ζ). Here already the immobile ions have to be taken into account, which can alter the effective charge (Q_{eff})of the polymer.

$$\zeta = \frac{Q_{eff}}{4\pi\varepsilon R} \cdot \frac{1}{1+R/\lambda} \tag{5}$$

Since this model still oversimplifies the underlying differential equation and neglects ionic radius and local changes in permittivity a lot of improvements have been made by computational methods [36, 37]. Still the distribution of anions and cations around a polymer is studied: Also ionic species is found to have an impact on the constitution of the ion cloud [38, 39]. Nevertheless the Debye-Hückel framework has been proven to be a good assumption and serves as a basis for the theoretical model of thermophoresis in this work.

2.1.3 Electrophoretic mobility

Application of an electric field on a charged polymer in an electrolyte leads the molecule to move with a certain speed v in the direction of the electric field E. It is quantified by the electrophoretic mobility μ:

$$v = \mu \cdot E$$
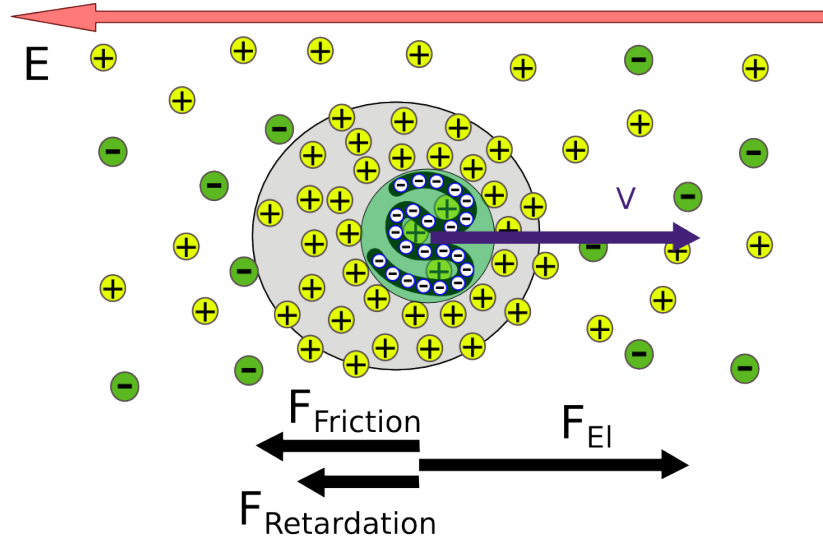
Figure 4: A charged polymer undergoes electrophoresis in the presence of an electric field E. At constant velocity, the electric drag force (F_{el}) is equal to the forces developed by friction ($F_{Friction}$) and retardation ($F_{Retardation}$). The latter one is caused by the attraction of the polymer to the oppositely charged ions, which move in the reverse direction. The velocity v at which the molecule moves is connected to the electric field E by the electrophoretic mobility μ via $v = \mu \cdot E$. The electrophoretic mobility can be calculated from the zeta potential by Henry equation (eq. 6).

Theoretical treatment of the electrophoretic mobility is rather complex since it involves the force exerted by the electric field, the frictional force of the polymer and the so called retardation force. The latter one is exerted by the Debye layer that is dragged in the opposite direction to the fluid.

$$F_{El} = F_{Friction} + F_{Retardation}$$

Early successful theories for a charged sphere in electrolyte were developed by Smoluchowski for thin [40] and Hückel for thick Debye layers.

Henry later on found that the discrepancy is based on an oversimplification of both treatments: Whereas Hückel neglects deformation of the electric field around the particle, Smoluchowski assumes it to be uniform and parallel [35, 41]. The complex part of this electrokinetic phenomena is hidden in the retardation force which is depending on the interplay of size of the particle r and the associated Debye layer λ. The gap between the two solutions can be bridged by a so called henry function $f(\kappa r)$ which connects electrophoretic mobility and zeta potential:

$$\mu_e = \frac{2\varepsilon_0\varepsilon_r\zeta f(\kappa r)}{3\eta} \tag{6}$$

It depends on Debye screening length ($\kappa = 1/\lambda$), viscosity , permittivity and radius R.

Nowadays computational methods refine analysis and yield very exact solutions to monitor the transi-

tion between thick and thin Debye layers [42–44]. In this work the electrophoretic mobility is connected to the zeta potential by a most recent Henry function which Ohshima developed for spherical particles [44]:

$$f(\kappa R) = 1 + 0.5 \frac{1}{(1 + \frac{2.5}{\kappa R(1 + 2e^{-\kappa R})})^3} \tag{7}$$

On the experimental side, electrophoretic mobility of proteins can be described in good accordance to Debye-Hückel theory [26]. Also DNA was studied in great detail with length, temperature and ionic strength [45, 46]. Manning condensation was confirmed to hold for electrophoresis [28, 45]. In this work this was taken into account by introducing effective charges for the molecules under study on the basis of multi-particle collision simulations [29, 30] (see chapter 2.1.1).

2.2 Theoretical model of thermophoresis

In general, thermophoresis, the movement of molecules in a temperature gradient ∇T, is defined by the thermophoretic diffusion coefficient D_T which is a measure for the exerted velocity onto a particle [4]: $v_T = -D_T \cdot \nabla T$

For a bulk concentration of molecules c, the connected thermal flux $j_T = c \cdot v_T = -c \cdot D_T \cdot \nabla T$ leads to a buildup of a concentration gradient. This in return is balanced by a counteracting flux, which quantified by the diffusion coefficient D: $j_D = -D \cdot \nabla c$.

The resulting overall flux then gives:

$$j = j_T + j_D = -c \cdot D_T \cdot \nabla T - D \cdot \nabla c \tag{8}$$

At steady state, $j = 0$, the equation can be solved and the relative concentrations at two different temperatures be calculated to:

$$\frac{c(T_2)}{c(T_1)} = \exp\left(-(D_T/D) \cdot (T_2 - T_1)\right) = \exp\left(-S_T \cdot (T_2 - T_1)\right) \tag{9}$$

The ratio of the transport coefficients is also simplified to the so called the Soret coefficient $S_T = D_T/D$.

However, up to this point no complete model for thermophoresis of polymers or colloids in aqueous solutions is yet given since there is the outstanding question whether thermophoresis is determined by the approach of local thermodynamic equilibrium [8, 47–51] or explicit hydrodynamic forces that act onto the molecule [7, 52, 53].

The theoretical model presented in this section is made up by a superposition of various state of the art effects which are found to play a role for thermophoresis [8, 9, 53, 54]. Only recently similar efforts have been proven to fit very successful to experimental data [21].

The Soret coefficient consists of six parts. Apart from the nonionic contribution $\left(S_T^{NI}\right)$, five of them are based on charge and electrolyte effects: One of them evolves, as discussed in the previous chapter, on behalf of electric fields exerted by the nonuniform thermophoresis of various ionic species result in a Seebeck term $\left(S_T^{EL}\right)$ analog to electrophoresis (chapter 2.1.3). Further explicit forces are exerted on the charged particle by the gradient of interfacial tension. This is caused by the gradient in temperature [55], permittivity [56] and also salt concentration [55] in the thermal field [53]. Since the first two are directly connected to the solvent, they are combined to $\left(S_T^{R+ES}\right)$. The last one is named $\left(S_T^{DP}\right)$.

Apart from the contributions arising from explicit forces, the approach of thermal local equilibrium yields two contributions towards the capacitor model identified by the change of free energy within the Debye layer $\left(S_T^{CM} + S_T^{DP-CM}\right)$.

Consequently the Soret coefficient according to the model is:

$$S_T = S_T^{NI} + S_T^{EL} + S_T^{R+ES} + S_T^{DP} + S_T^{DP-CM} + S_T^{CM} \tag{10}$$

Since parameters as ionic strength, radius or charge are shared by all the effects based on charge, they are experimentally hard to isolate. Nevertheless for the various contributions detailed predictions can be made for the dependency on temperature and Debye length. For a lot of small molecules capacitor effects dominate, as shown for example for a DNA 22-mer below (Fig. 5). The temperature response in this case is traced back to electrophoretic and diffusiophoretic effects connected to the thermal diffusion of the salt ions. The full set of equations can also be seen appendix 7.4. In the following the various contributions and their describing equations are presented.
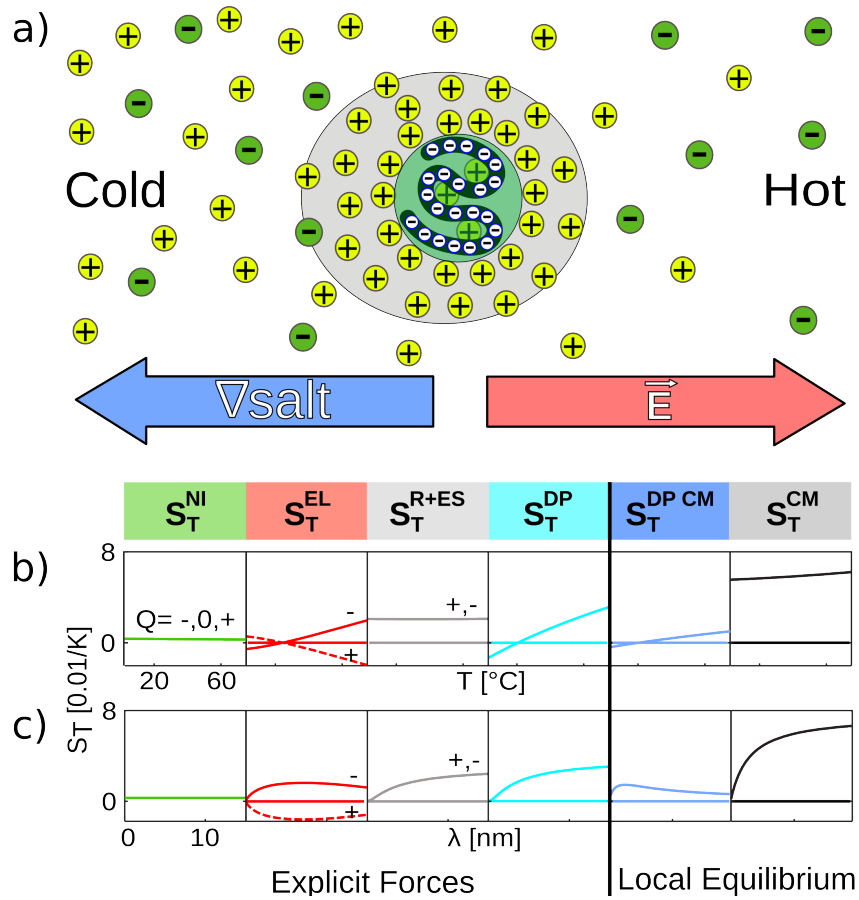
Figure 5: Thermophoresis, the movement of molecules in thermal gradients, is connected to various effects for a polyelectrolyte in water. (a) For charged molecules the response of the Debye layer to the thermal field plays a major role, since electric fields and salt gradients are created. Apart from the small empiric nonionic contribution (S_T^{NI}), the presented model for charged polymers is made up by the state of the art contributions stemming from explicit forces (S_T^{EL}, S_T^{R+ES}, and S_T^{DP}) and the local equilibrium approach (S_T^{CM} and S_T^{DP-CM}). Predictions of the individual contributions, which are discussed in this section, are shown for a DNA 22-mer on temperature at 1mM potassium chloride (b) and on Debye length at 65°C (c). Here the local equilibrium approach supports the largest contributions towards thermophoresis.

2.2.1 Nonionic contribution

The non-ionic contribution to the Soret coefficient of polymers is studied intensely in the last decades [10, 12]. However at present, no general framework exists that is able to describe these effects quantitatively [13, 15]. Newest findings on short molecules in water suggest the acceptor and donor sites, which form hydrogen bonds, influence the nonionic contribution in water to a large extent [57, 58]. Presumably water polarization in thermal gradients might also play a role here [59, 60] and is connected the entropy of the hydration shell [49].

Although D_T^{Ni} is found to increase [12] or decrease [14] with molecular weight for various polymers species and hard to predict, recently some empirical formulas have been found to describe the polymers behavior in dilute solution quite accurately [9, 17].

In this work the theoretical description is restricted to the ideal gas contribution 1/T and an empirical equation following the relation of Stadelmaier and Köhler [9], where the thermal diffusion is: $D_T = \frac{\Delta_T}{\eta} - \frac{a}{M^\alpha}$. The first part is characteristic for the polymer but not the solvent and the second part for length dependence in the solvent. Δ_T and a are empirical constants. The second part of the empirical relation was remodeled being dependent on one over the viscosity and radius (which implies $\alpha = 0.588$): $D_T^{Ni} = \frac{\Delta_T}{\eta} - \frac{a}{\eta r}$. As suggested by Wang and coauthors [13], these changes are joining the models of Würger [15] and Stadelmaier et al.

S_T^{NI} then reads:

$$S_T^{NI} = \frac{1}{T} + \frac{\Delta_T \cdot 6 \cdot \pi \cdot r}{k_B T} - \frac{a \cdot 6 \cdot \pi}{k_B T} \tag{11}$$

2.2.2 Seebeck effect

For charged molecules one important influence occurs on behalf of an electric field which is build up by the individual response of the ionic species upon a thermal gradient [61–63]. As a consequence of the macroscopic electric field a charged macromolecule will undergo electrophoresis (see chapter 2.1.3). In analogy to solid state physics the phenomena is names Seebeck effect S_T^{EL}. It was first discussed for 1:1 electrolytes by Guthrie [64], later on further developed by Würger [7] and successfully tested for Polystyrene beads [53], RNA and DNA molecules [8].

The thermophoretic contribution on a polymer with mobility μ and diffusion coefficient D reads [8]:

$$S_T^{EL} = -\frac{k_B T \mu}{eD} \frac{\sum_i z_i c_i S_{Ti}}{\sum z_i^2 c_i} \tag{12}$$

Here the valencies z_i, concentrations c_i and Soret coefficients S_{Ti} of the several ionic species i present play a role. The equation was also found to hold for multivalent ions or even the finite concentration of macromolecules present [8].
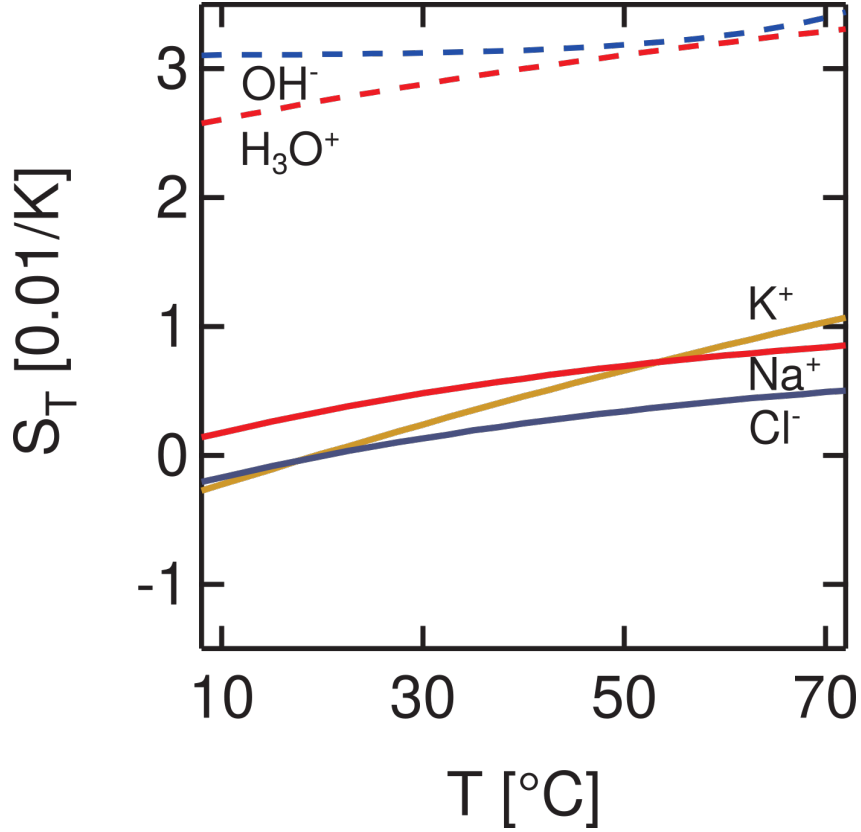
Figure 6: Single ion Soret coefficients of K$^+$, Na$^+$, Cl$^-$, H30$^+$ and OH$^-$. The finding that ions bear individual Soret coefficients [65] is the reason for the polymers to undergo electrophoresis according to the Seebeck effect [8, 64]. The single-ion Soret coefficients are set to reasonable values (see appendix 7.3) in the presented thermophoretic model and monitor the characteristic increase with temperature [66].

Unfortunately the single ion Soret coefficients of the cations $S_T^{M^+}$ and anions $S_T^{X^-}$ cannot be determined directly via potentiometric and conductometric methods, but only the Soret coefficient of the salt mixture S_T^{MX} [62, 67].

$$S_T^{MX} = \frac{1}{2}\left(S_T^{M^+} + S_T^{X^-}\right) \tag{13}$$

Historically it was first observed, that the exchange of one ionic species in an univalent salt mixture changes the Soret coefficient of salt mixture. Thus individual Soret coefficients for the different ionic species were then assigned on the agreement that $S_T^{Cl^-} = 0/K$ [61, 63] . They were later rescaled with the help of the thermal self diffusion of water and could be described by the reduction rule [62, 65, 68]. Nevertheless the data for the single ion Soret coefficients is sparse, since it is restricted to 0.01 M and 25°C base temperature.

The behavior of the single ion Soret coefficients over temperature and concentration is still not clear and the data is controversial (e.g. for sodium chloride [62, 66, 69–71]). Interestingly S_T^{MX} is found to

increase with temperature for potassium chloride (KCl) and sodium chloride (NaCl) in water at 500 mM concentration [66] and the slope of S_T^{MX} seems to be linear related to thermal expansion [70]. Contradicting data is found by Gaeta, were the Soret coefficient even decreases with temperature in a certain concentration range [69]. For KCl and NaCl salt mixtures at $25°C$ a dependence on concentration $\sqrt{c_{salt}}/(1+\sqrt{c_{salt}})$ is found [67].

In the following discourse reasonable values for the single Ion Soret coefficients of Na^+, K^+, Cl^-, H^+ and OH^- were set according to Fig. 6.

For detailed information see appendix 7.3.

2.2.3   Interfacial tension

The interfacial tension around the charged molecule is altered by the local temperature [55] and permittivity gradient [56] around the polyelectrolyte. The resulting explicit forces are depicted by S_T^{R+ES} and incorporate the latest developments of Würger [53], who progressed Ruckensteins theory of the temperature gradient.

$$S_T^{R+ES} = \frac{6\pi r}{12 k_B T^2} \varepsilon \, \zeta^2 \left(1 - \frac{T}{\varepsilon} \cdot \frac{\delta \varepsilon}{\delta T}\right) \tag{14}$$

2.2.4   Diffusiophoresis

An additional factor influencing the interfacial tension a charged polymers in solution arises from the osmotic pressure due to thermophoresis of salt ions (see chapter 2.2.2) and the connected overall salt gradient in the temperature field. The resulting effect on the polymer is called diffusiophoresis. The transport coefficient which is quantifying the logarithmic response of the polymers velocity v_{DP} to a salt gradient is called diffusiophoretic mobility D_{DP}.

$$v_{DP} = D_{DP} \cdot \nabla \ln c_{salt} \tag{15}$$

The theoretical description for diffusiophoretic mobility of a charged spherical particle in 1:1 electrolytes was derived by Prieve and Romain [72, 73], further developed by Anderson for strong adsorption [74] and even progressed to multiple multivalent ions [75]. Experimentally it was found to hold very accurate [76–78].

The diffusiophoretic effect caused by a thermal gradient onto a charged polymer can be derived by the balance of fluxes at steady state:

$$\sum j_i = -D\nabla c - D_T c \nabla T + c D_{DP} \nabla \ln c_{salt} = 0 \tag{16}$$

Analog to equation 9, thermophoresis of salts is measured by its Soret coefficient S_T^{MX} (see chapter 2.2.2) and the steady state of fluxes for the salt gives $\frac{\nabla c_{salt}}{c_{salt}} = \nabla \ln c_{salt} = -S_T^{MX} \cdot \nabla T$. This equation can be incorporated to eq. 16.

$$-\frac{\nabla c}{c} = \frac{D_T}{D} \cdot \nabla T + \frac{D_{DP}}{D} \cdot S_T^{MX} \cdot \nabla T = \left(S_T^{classic} + S_T^{DP} \right) \cdot \nabla T$$

The additional diffusiophoretic contribution towards thermophoresis is identified by S_T^{DP} and states:

$$S_T^{DP} = \frac{D_{DP}}{D} S_T^{MX} \tag{17}$$

The connected diffusiophoretic mobility D_{DP} for a spherical charged particle is [72]:

$$D_{DP} = -\frac{k_B T}{\eta} \frac{\log\left(1 - \gamma^2\right)}{2\pi\lambda_B} \tag{18}$$

Here γ=tanh($\zeta/4$), with the ζ as depicted in chapter 2.1.2 and the Bjerrum length according to $\lambda_B = \frac{e^2}{4\pi\varepsilon k_B T}$. Note that the additional electrophoretic part is omitted here because the model incorporates this contribution already by the Seebeck effect discussed above. The diffusiophoretic contribution is thus dependent on Q_{eff}^2 and linear to the Soret coefficient of the salt mixture:

$$S_T^{DP} = -\frac{k_B T}{\eta} \frac{\log\left(1 - \gamma^2\right)}{2\pi\lambda_B} \frac{S_T^{MX}}{D} \tag{19}$$

For S_T^{MX} (see eq. 13) the Soret coefficients of potassium, sodium and chloride were implemented but the Soret coefficients of hydron and hydroxide ions neglected if not differently depicted.

2.2.5 Diffusiophoresis - Capacitor Model

So far the contributions were derived on means of hydrodynamic forces onto the Debye layer, except for the empirical treatment of S_T^{Ni}.

Now we turn to the contributions which are caused by the approach of the assumption of local thermal equilibrium [8, 47–51]. As pointed out by Dhont and coauthors, the Soret coefficient is derived by the change of free energy $dW\left(T\right) = \frac{1}{2} \cdot Q \cdot d\varsigma\left(T\right)$ to build up the double layer [48] for an infinitesimal temperature step dT. Here the change of the free energy of the double layer is given by the charge of the polymer and the temperature dependent zeta potential $\varsigma\left(T\right)$ (see chapter 2.1.2). The zeta potential includes multiple parameters explicitly, which are temperature dependent: $\varsigma\left(T, \varepsilon\left(T\right), \rho\left(T\right), c_{salt}\left(T\right)\right)$. Other than temperature, permittivity and density [8], also the change of salt concentration $c_{salt}\left(T\right)$ due to thermophoresis of ions is taken into account for this study:

$$S_T = \frac{1}{k_B T} \frac{dW\left(T, \varepsilon\left(T\right), \rho\left(T\right), c_{salt}\left(T\right)\right)}{dT} = \frac{1}{k_B T} \frac{dW\left(T, \varepsilon\left(T\right), \rho\left(T\right)\right)}{dT} + \frac{1}{k_B T} \frac{dW\left(\lambda\right)}{d\lambda} \frac{d\lambda\left(c\right)}{dc} \frac{dc\left(T\right)}{dT}$$
$$= S_T^{CM} + S_T^{DP-CM} \tag{20}$$

The first part S_T^{CM} has already been derived [8, 48, 54] and is presented in the next chapter. The second part is connected to the thermal diffusion of salt ions and thus named S_T^{DP-CM}, because salt ions

are the driving force as in diffusiophoresis.

$$S_T^{DP-CM} = \frac{1}{k_BT} \frac{dW(\lambda)}{d\lambda} \frac{d\lambda(c)}{dc} \frac{dc(T)}{dT}$$

For a spherical capacitor it can be derived as:

$$S_T^{DP-CM} = \frac{Q_{eff}^2}{16\pi\varepsilon k_BT} \frac{1}{\lambda(1+r/\lambda)^2} \cdot S_T^{MX}$$

For a rod with radius r_{rod} and length L the deviation of the electric potential energy as stated in [54] yields :

$$S_T^{DP-CM(ROD)} = \left(\frac{Q_{eff}^2 \lambda}{8\,\varepsilon\,\pi\,k_B\,T} \right) \frac{\frac{2r_{rod}^2}{\lambda^2} + \frac{(L-2r_{rod})}{\left(\left(\ln\left(\frac{\lambda}{r_{rod}}+1\right)\right)^2 \cdot (\lambda+r_{rod})\right)}}{\left(2r_f\left(\frac{r_{rod}}{\lambda}+1\right) + \frac{L-2r_{rod}}{ln\left(\frac{\lambda}{r_{rod}}+1\right)}\right)^2} \cdot S_T^{MX} \tag{21}$$

S_T^{MX} was treated as in chapter 2.2.4.

2.2.6 Capacitor Model

Th classical capacitor effect S_T^{CM} which is related to the temperature dependent parameters density ρ, permittivity $\varepsilon=\varepsilon_0\varepsilon_r$ and temperature T was derived by Dhont [48]. It has been successfully tested for charged silica particles [79] and DNA oligonucleotides [8]. For spherical particles or molecules the capacitor model holds a major contribution to S_T [8]:

$$S_T^{CM} = \frac{Q_{eff}^2}{16\pi k_BT^2\varepsilon\lambda(1+R/\lambda)^2} \left(1 - \frac{\partial\log[\rho(T)]}{\partial\log[T]} - \frac{\partial\log[\varepsilon(T)]}{\partial\log[T]}\left(1-\frac{2\lambda}{R}\right)\right) \tag{22}$$

For long rod-like structures, the overall capacitance is described as a superposition of a spherical and a cylindrical capacitor (with length L and radius r_{rod}) [54].

$$S_T^{CM(ROD)} = \frac{Q_{eff}^2}{k_BT^24\pi\varepsilon[2r_{rod}(r_{rod}/\lambda+1)+(L-2r_{rod})/\log(\lambda/r_{rod}+1)]^2} \left(\frac{r_{rod}^2}{\lambda} + \frac{(L-2r_{rod})\lambda/r_{rod}}{2\log^2[\lambda/r_{rod}+1](\lambda/r_{rod}+1)} \right.$$
$$\left. + \frac{\partial\log\varepsilon}{\partial\log T}\left[\frac{(L-2r_{rod})\lambda/r_{rod}}{2\log^2(\lambda/r_{rod}+1)(\lambda/r_{rod}+1)} - \frac{r_{rod}^2}{\lambda} - 2r_{rod} - \frac{(L-2r_{rod})}{\log(\lambda/r_{rod}+1)} \right] \right) \tag{23}$$

3 Experimental section

Thermophoretic studies on different samples (chapter 3.1) were performed on a modified fluorescence microscope by the use of local heating with an infrared laser (chapter 3.2). In chapter 3.3 the measurement procedure is presented. In chapter 3.4 the evaluation of the temperature gradient with additional simulations to understand the behavior over base temperature are shown. The data evaluation based on the spatial approach is presented in chapter 3.5 altogether with an overview on the underlying data of charge and radius for the various molecular species.

3.1 Polymers studied

In this work different species of polymers were investigated, reaching from uncharged Polyethylene Glycol (PEG) to charged DNA polymers over PNA molecules, where the charge can be tuned by solvent condition. Additionally more complex molecules were studied, namely α-synuclein proteins and smart oligo(ethylene glycol) (OEG) methyl ether methacrylate copolymers.

polyethylene glycol (PEG)   peptide nucleic acid (PNA)   deoxyribonucleic acid (DNA)   protein polypeptide (a-synuclein)   pOEG copolymer
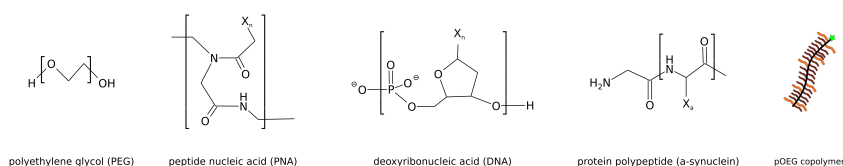
Figure 7: Structures of the polymers studied. They cover a large range of effective charge, ranging from uncharged PEG polymers to highly charged DNA molecules. PNA polymers were used to monitor the transition from charged to uncharged polymers, since their charge can be tuned on behalf of a neutral peptide backbone and nucleobases (X_n) with various pK_a values. Proteins with amino acids residues (X_a) can form large macromolecular assemblies, like the investigated α-synuclein. Moreover, branched pOEG copolymers are studied, which collapse at a certain temperature. Image of pOEG copolymer adapted with permission from [23]. Copyright 2014 American Chemical Society.

3.1.1 Polyethylene Glycol

For the experiments on the nonionic contribution, the Polyethylene Glycol polymers (CH30-PEG-NH2) of various molecular weight (750, 2000, 5000, 10000 and 20000 g/mol) were used (Rapp Polymere, Tübingen, Germany). They were labeled with a Bodipy-Fl succinimidyl ester (D2184 - 4,4-difluoro-5,7-dimethyl-4-bora-3a,4a-diaza-s-indacene-3-propionic acid, succinimidyl ester, Life Technologies, Darmstadt, Germany), which was chosen to minimize artifacts of the dye for thermophoresis, since it bears no net charge and is very small. Therefore each PEG polymer species was reacted at 2 mM in a 0.1 M Tetraboratbuffer at *pH* 8.5 to an 3x access amount of dye for 6 hours in a shaker. Afterwards the sample was put into dialysis membranes with suitable cut-off range for 12 hours and stirred in 5 l fresh milliQ water to get rid of the free dye. This step was repeated 3 times. Then the samples were stored. The concentration of labeled polymer was determined spectroscopically (nanodrop ND-1000, Thermo

fisher scientific, Wilmington, USA). Based on the assumption that there is no free dye present, labeling efficiency was high with ~63 % for PEG of Molecular weight of 20000.

The samples were stored in the fridge before use. For the thermophoresis measurements they were diluted in 1 mM Tris *pH* 7.6 buffer at variable concentration of PEG-polymers (labeled) and extrapolated to infinite dilution [80] (see chapter 4.2). For the measurement series on salt concentration, 6uM labeled polymers were brought into solution with potassium chloride of variable concentration (see ref. [81]).

For the exploratory measurements on extreme solvent conditions in chapter 4.2 there was used a universal buffer by the mixture of 0.2 M Na_2HPO_4 and 0.1 M with Citric acid [82] for the *pH* series. For the measurements in Methyl Ethyl Ketone and Ethanol the dye was attached synthesis of via a carboxyl group and dissolved to around ~30 µM. In water no significant change in S_T was observed for PEG20000 by the change of labeling chemistry between the addition of the dye by carboxyl and succinimidyl end group.

3.1.2 Deoxyribonucleic Acid

Deoxyribonucleic Acid oligonucleotides (DNA) of 5, 10, 22 bases were labeled with Hex-dye (6-carboxy-2',4,4',5',7,7'- hexachlorofluorescein) and purified by HPLC (Biomers, Ulm, Germany). For the measurements of S_T over base temperature they were diluted to 1 uM in 1 mM Tris *pH* 7.6 and 500 mM KCl. The following sequences of single stranded DNA of 5, 10 and 22 bases length were selected to avoid hairpins and dimers:

    DNA5 ($5' \rightarrow 3'$): HEX-TAG GT
    DNA10 ($5' \rightarrow 3'$): HEX-TAG GTC TAA T
    DNA22 ($5' \rightarrow 3'$): HEX-ATT GAG ATA CAC ATT AGA ACT A

To check the herein presented model on the dependency on Debye length, additional datasets of Herzog and Reichl [8, 20] for the same DNA strands were added. Those were measured and evaluated as depicted in Herzogs Thesis.

3.1.3 Peptide Nucleic Acid

Peptide nucleic acid (PNA) depicts a novel synthetic polymer species. They are made up by the four nucleobases as DNA, but connected by an uncharged amino backbone. They are found to have higher binding energies and also bind in independent direction. There is an ongoing discussion whether this molecule is a potential precursor of DNA in the context of the origin of life [83].

PNA single strands with identical sequences to the DNA molecules were studied. They were purified with HPLC (>90%) by Panagene (Panagene, Daejeon, Korea). For zero net charge at physiological *pH* the PNA was connected to Bodipy-Fl dye at the N-terminal. Higher solubility was achieved by an OO-linker.

    PNA5: BODIPY FL-OO-TAG GT

PNA10: BODIPY FL-OO-TAG GTC TAA T

PNA22: BODIPY FL-OO-ATT GAG ATA CAC ATT AGA ACT A

They were diluted to 100 μM with pure milliQ. Shortly before the experiment they were dried in a rotational vacuum concentrator (RVC 2-25, Martin Christ Gefriertrocknungsanlagen, Osterode am Harz, Germany). Then they were dissolved at 50 μM in the desired solvent. For the experiments onto charging of PNA the polymers were brought into acidic and basic conditions, concentrations of aqueous solutions of 100, 10, 1, 0.1 mM hydrogen chloride (HCl), 1 mM Tris *pH* 7.6, 20, 40, 60, 80, 100 mM potassium hydroxide (KOH) and 100 mM sodium hydroxide (NaOH) were used respectively. The *pH* of the solution was beforehand checked with *pH* electrode (Blueline, Si-Analytics, Mainz, Germany) and afterwards with *pH* stripe and found to be in reasonable proximity. For the measurements on Debye length the PNA was buffered in 1mM Potassium acetate *pH* 5. At acidic and basic conditions the charge is changed (Fig. 2). The *pH* was checked with an electrode before solvating PNA molecules and afterwards crosschecked with *pH*-stripes. The values were in reasonable agreement.

3.1.4 α-synuclein

Details on the preparation of monomeric, oligomeric and fibrillar α-synuclein and labeling can be found in the attached article [84].

3.1.5   Oligo(ethylene glycol) methyl ether methacrylate copolymer

The oligo(ethylene glycol) (OEG) methyl ether methacrylate (pOEG) copolymer was synthesized via RAFT polymerization. Details on the synthesis, purification and labeling with Bodipy-malemide can be found in [23].

3.2 Measurement setup
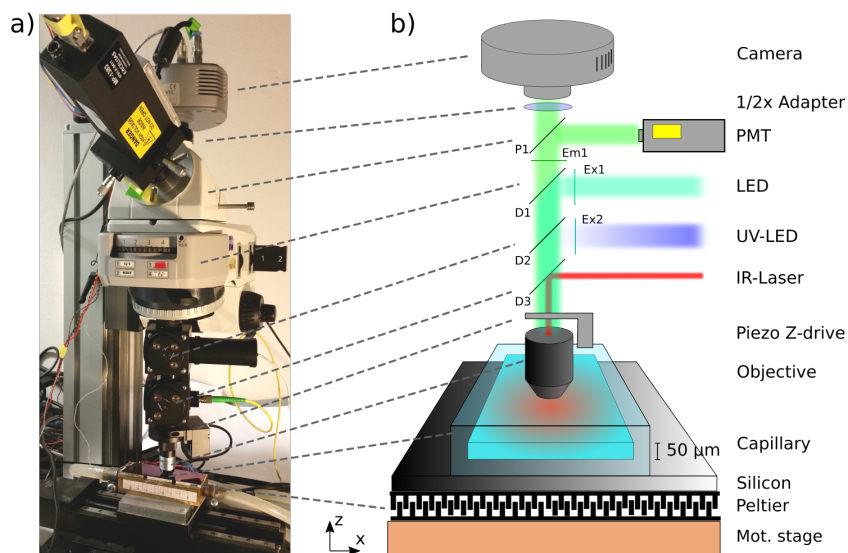
Figure 8: The experimental setup, a picture (a) and a schematic (b). The solutions under study are filled in rectangular capillaries (50 μm x 500 μm). These are placed on the silicon wafer and observed via a modified fluorescent microscope. For monitoring, either a CCD camera or a photomultiplier (PMT) can be selected by a sliding prism (P1). Illumination was performed by LED illumination and a fluorescent filter set. The light first has to pass an emission filter (Ex1), then gets reflected to the objective by a dichroic mirror (D1). The fluorescent molecules inside the capillaries are then excited and the emitted light of larger wavelength is gathered by the objective. The light passes the dichroic mirrors (D1-3) and emission filter (Em1) before it is focused by an 1/2x adapter onto the detector. For heating, an infrared laser is coupled into the path of light, by dichroic (D3). Base temperature of the sample is controlled by a silicon wafer that is regulated by Peltier elements on behalf of a PID loop. For automatized measurements, the stage is motorized in x-direction and a piezo element for focusing is inserted in the z-plane. Optional an UV-LED can be used for label free detection together with an excitation filter (Ex2) and an dichroic mirror (D2).

Thermophoresis measurements were performed at a modified fluorescence microscope of type Axioscope A1 (Zeiss, Jena, Germany) as illustrated in Fig. 8. For local heating an infrared laser at wavelength 1480nm was inserted into the path of light by a dichroic mirror (NT46-386, Edmund Optics, Barrington, USA). Due to the high absorption of water in the infrared, the aqueous sample, which was encapsulated inside rectangular borosilicate capillaries 50 μm x 500 μm (Vitrotube, Vitrocom, Mountain Lakes, USA), was exposed to a temperature gradient (see chapter 3.4). Imaging of the fluorescently labeled sample was performed with 40x Quartz objective with NA=0.8 (Partec, Lincolnshire, USA) in combination with a 0.5x adapter (Zeiss) for a larger field of view. Depending on the label the following combination of Light Emitting Diode (LED) and filter set were chosen:

BCECF and Bodipy-Fl: green LED at 505nm (Luxeon, Calgary, Canada), F76-522 (AHF Analysen-

technik, Tübingen, Germany)

6-Hex: blue LED at 530nm (Thorlabs, Dachau, Germany), F36-542 (AHF Analysentechnik)

Cy5: red LED at 627nm (Luxeon), F36-523 (AHF Analysentechnik)

The LED was powered selectively for low and high illumination by a LDC201 or LDC210 constant current power supply (Thorlabs). The emission light of the fluorescent molecules the sample could then be monitored by either a Luca DL-658M-TIL CCD camera (Andor, Belfast, United Kingdom) or optional a MP1383 photomultiplier (Excelitas, Waltham, USA).

The z-height was set with a P-725 piezo nanofocussing Z-drive (Physik Instrumente, Karlsruhe, Germany) which was driven by a E625 Piezo amplifier (Physik Instrumente). This feature compensates for inhomogeneities of the stage and automatically sharpens the sample at the place with maximum brightness (see [81]). In x-direction (Fig. 8) the stage was driven by an automatized stage (M404.6DG, Physik Instrumente).

For the control of the base temperature of the capillaries, they were thermally coupled with a thin film of paraffin oil (1ul) to a silicon wafer of 350 µm thickness. (see [81]). The silicon wafer was connected to a Peltier element (PC-128-10-05, Telemeter Electronic, Donauwörth, Germany) by thermal compound. The Peltier elements were brought in thermal contact to a copper block, which was in turn cooled by a CF40 water bath (Julabo, Seelbach, Germany). The temperature was read out with an temperature transmitter (GNTP-5015, Greisinger, Regenstauf, Germany) at the silicon wafer and the Peltier elements regulated by a power supply (EA-PS 3032-10B, Elektro Automatik, Viersen, Germany) via a PID loop.

For synchronized control of the various components, they were handled by a NI-PCI-6229 (National Instruments, Austin, USA) and a NI-PCI-6601 (National Instruments) via Labview (National Instruments). The Photomultiplier was governed by the Ni-PCI-6601 card with a BNC-2121 (National Instruments) interface. The camera trigger, LED current, laser power, temperature readout and control was managed by two BNC 2110 (National Instruments) interfaces with the NI-PCI-6229 card. Further details on the concept can be found in [8, 20, 85, 86]. Improvements were achieved the by implementation of a z-focus [81], the attachment of the laser fiber for a reproducible infrared source and the connection of the capillaries with a small oil film to the surface for smaller variation in the created temperature profile.

Settings for the individual measurements, as frame rate, Laser power, LED power and base temperature were saved in initialization file. Typical settings for a thermophoresis measurement on polymers were 4x4 binning, a frame rate of 2.5 Hz and minimal LED power to minimize artifacts caused by spatial bleaching, which has large influence on bulk measurements.

3.3 Measurements

For a measurement series, the silicon wafer of the stage was first cleaned with isopropyl alcohol and afterwards a thin film of paraffin oil (1ul) was spread onto it. After the preparation of samples according to chapter 3.1, the aqueous solutions were soaked into rectangular capillaries by surface tension. Care was taken to prevent the creation of air bubbles. Afterwards the capillaries were sealed by wax (sealing wax, Nanotemper Technologies, Munich, Germany) and the middle of the outer glass cleaned with iso-

propanol and precision wipes (Kimtech, Kimberly-clark, Canada). Then the sample solutions together with a capillary filled with BCECF for temperature calibration were placed onto the stage (chapter 3.4). When ambient humidity and temperatures were very high, a small steady flow of nitrogen was applied to the stage to prevent condensation of water onto the capillaries for the measurements at low base temperature.

The positions of the capillaries on the automatized stage were then determined with the photomultiplier. Afterwards a background picture was taken to correct for high background (~450 counts) and hot pixels of the CCD camera. Then the temperature gradient was ascertained by a BCECF measurement at 25°C base temperature with the camera as explained in chapter 3.4. Afterwards a measurement routine was set up. Typically the measurements were performed from high to low temperatures in decrements of 5°C from 65°C to 5°C.

Since spatial bleaching can cause large errors in data evaluation, the strategy was to go for long exposure times, typical frame rate~2.5 Hz, and low LED illumination. Binning was set to 4x4 to still preserve enough spatial information and minimize readout times. Afterwards a measurement procedure was created and the measurement protocol stored. Depending on the diffusion coefficient of the investigated molecule, thermophoresis and back diffusion were investigated for reasonable time scales to ensure equilibrium. As example for a 22-mer PNA, commonly 20 seconds bleaching, 120 seconds thermophoresis with IR laser on and 90 seconds back diffusion were taken.

3.4 Temperature gradient

3.4.1 Temperature calibration

The temperature calibration was performed by monitoring the fluorescence of 50 μM BCECF (2',7'-Bis-(2-Carboxyethyl)-5-(and-6)-Carboxyfluorescein, Invitrogen, Paisley, UK) in 10mM Tris buffer *pH* 7.6 . The excitation and emission properties of BCECF depend largely on *pH* [87]. Temperature can thus be observed indirectly by the change of *pH* onto temperature, because the pK_a of Tris buffer is temperature dependent [88].
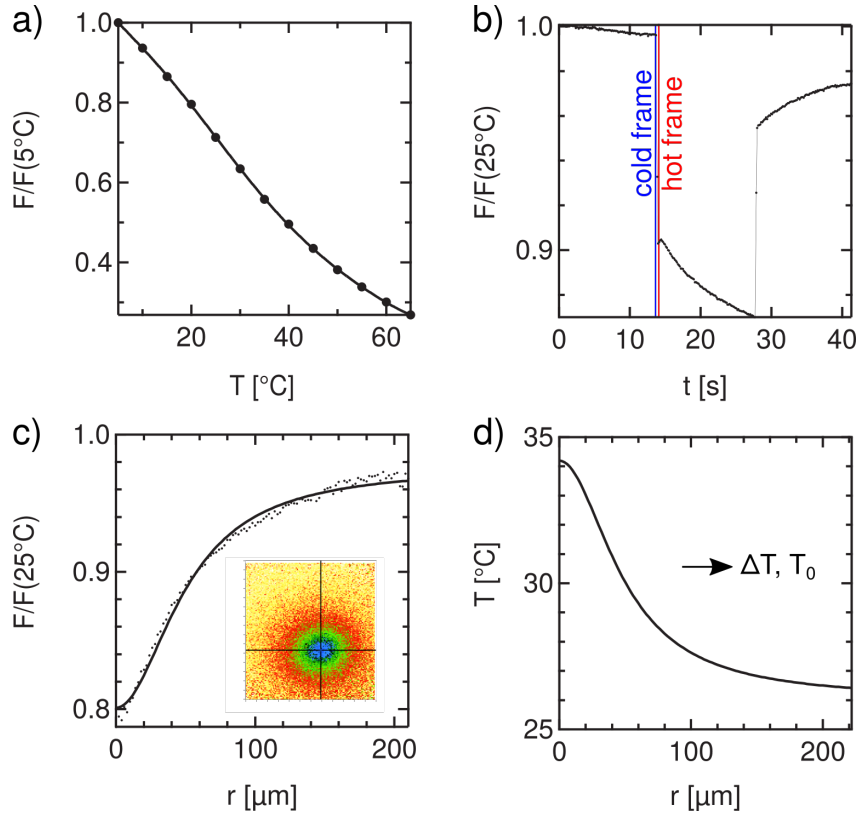
Figure 9: Evaluation of the temperature gradient inside a capillary by BCECF dye. a) The relative BCECF fluorescence over base temperature was calibrated by dependency of the fluorophore on base temperature. b) The sample was monitored at high frame rate to be able to separate the temperature jump from the ongoing thermal diffusion of BCECF. Here the normalized mean fluorescence of the acquired images is depicted over time. c) Division of hot by cold frame supplies the spatial temperature profile (inset). The radial distribution was matched by a Lorentzian function (eq.24). d) By the hand of the temperature calibration curve the spatial temperature profile was deduced and ΔT and T_0 extracted from the data. Here, a measurement with a Partec 40x Objective at a base temperature of 25 °C and 0.1 V laser control current is shown.

For the determination of the temperature profile a calibration curve of a BCECF sample inside a 50 μm x 500 μm capillary was taken at first. Therefore mean fluorescence was monitored with the CCD camera over base temperature, while care was taken to minimize spatial and temporal bleaching artifacts by low illumination and long exposure time. The resulting relative values in fluorescence were matched by an polynomial of seventh order (Fig. 9a).

To evaluate the temperature profile at a certain base temperature, a time trace was recorded at high camera frame rate (Fig. 9b). The laser was switched on after a period with only LED illumination. After the equilibration of temperature (~150-300 ms) thermophoresis led to a depletion of BCECF-dye molecules. When turning the laser off, fast thermal equilibration and back diffusion are visible.

To obtain the radial temperature distribution, the second picture after the temperature jump was

divided by the picture before the laser was turned on (Fig. 9b). The "hot" picture was taken shortly after the temperature jump to temporally separate it from the onset of thermophoresis. Since the first picture after temperature jump still incorporates the data of the capillary being heated up, it has to be rejected for evaluation.

The resulting fluorescence profile $I(r)$ (Fig. 9c) around the hot spot was then radially averaged and approximated by a Lorentzian function with width w, fluorescence offset I_0 and amplitude ΔI:

$$I(r) = I_0 + \Delta I \frac{1}{(1 + (r/w)^2)} \tag{24}$$

By the help of the calibration function (Fig. 9a) the radial temperature distribution could be calculated with the resulting base temperature T_0 and increase of ΔT at the peak temperature deduced (Fig. 9d). Further information can also be found in the Bachelor Theses of Haslauer [81] and Schendel [89].

3.4.2 Temperature gradient depends on base temperature

The local increase of temperature by the IR-laser was observed to depend largely on base temperature for various kind of objectives (Fig. 10a). Here measurements at IR-Laser control voltage of 0.1V and 0.2V are shown for three objectives: One Partec 40x, NA=0.8 and two Zeiss 40x EC Plan-NEOFLUOAR objectives, NA 0.9 (pol) of the identical series. The Zeiss objectives seem to absorb more IR power, since larger laser powers are needed to increase temperature to a comparable magnitude.

Relative fluorescence over radius for the Partec objective changes most at $T_0 = 25$ °C (Fig. 10b). Nevertheless due to the nonlinear temperature dependency of BCECF, ΔT is even larger for lower base temperature. The width of the Lorentzian profile is constant with a mean width of 50.73 μm (Fig. 10c).

To understand the decrease of ΔT with base temperature additional finite element simulations were performed with Comsol Multiphysics (COMSOL Inc., USA). Within the simulation a borosilicate capillary with dimensions of 50 μm x 500 μm capillary was heated by an Gaussian infrared beam (Fig. 10d). It was attached to a silicon wafer of 525 μm height. Simulations were implemented with heat transduction and laminar flow in radial symmetry. For heating a Gaussian laser profile with a beam waist of 30 μm was created, which was centered in the middle of the capillary. The infrared absorption was linearly extrapolated from experimental findings [90]. Standard material properties were used for borosilicate, silicon and water. As boundary conditions the top of the capillary was thermally insulated due to the small heat conduction of air, whereas the bottom of the silicon wafer with high heat conduction was set to a base temperature T. The base temperature was varied over a range of 5-65 °C by an increment of 5 °C. The determined heat profile in water was post-processed by linearizing temperature of water over capillary height (Fig. 10e). Subtraction the temperatures at the inner and outer boundary gave ΔT.
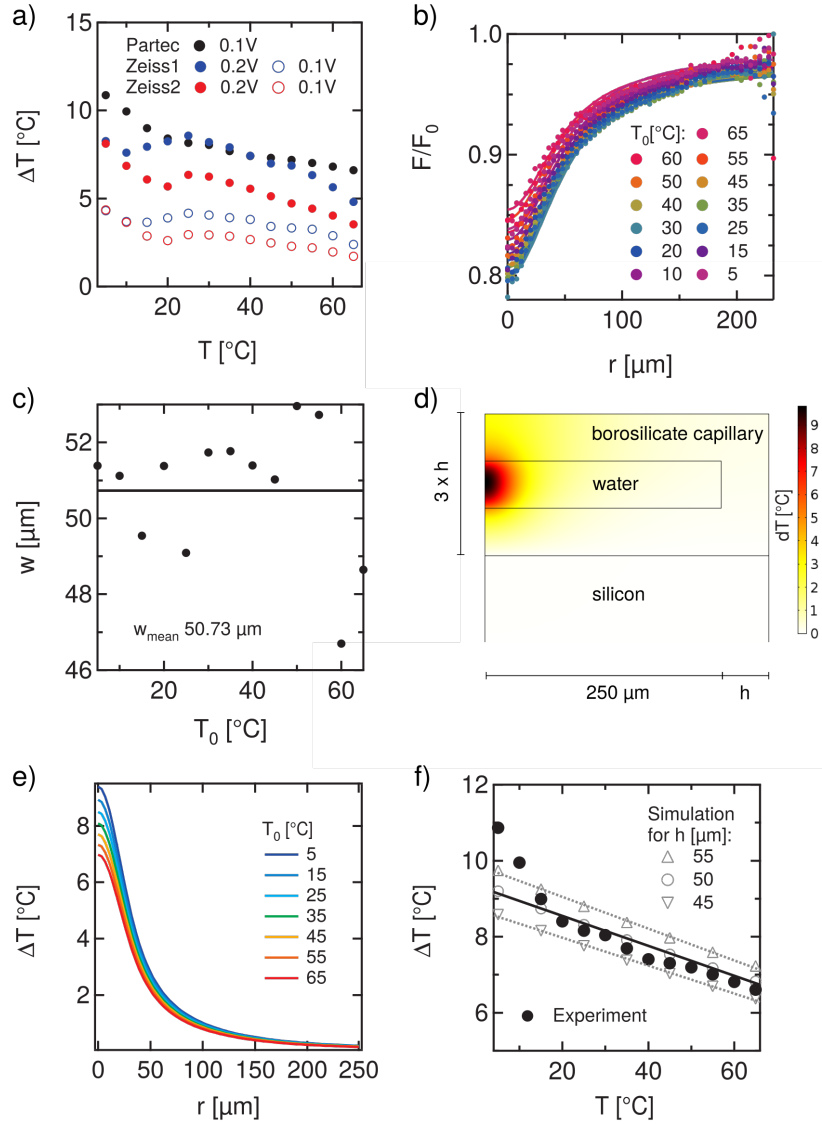
Figure 10: Evaluation of the temperature gradient with varying base temperatures. a) ΔT is decreasing with base temperature for various 40x objectives and different laser control currents. b) Relative fluorescence of the temperature jump changes most at 25 °C for the Partec 40x objective. c) The related Lorentzian width (eq. 24) was observed to be constant with ~51 μm. d) Finite element simulation for the temperature of the water inside a capillary which is heated by an IR-Laser (radial symmetry). Here the base temperature at the bottom of the silicon wafer is 25 °C and capillary height (h) is 50 μm. In this example the maximum local temperature increase is 9.8 °C. e) The extracted mean temperature along the radius of the capillary is calculated for different base temperatures. f) Evaluation of the temperature difference between center and outer boundary yields linear decrease with base temperature. The reason is found in the decreasing absorption of water at 1480 nm with temperature [90]. The values for ΔT are in good accordance to the experimental results. The numerical evaluation was extended by a variation of capillary thickness (h) to 45 and 55 μm as stated inaccuracy by the supplier (triangles). The result of a variation of height by $\pm 10\,\%$ results in a ΔT of $\pm 6.3\,\%$. The slope of ΔT over base temperature and the error are used for the experiments.

The extracted values for ΔT decrease with temperature and are in good agreements to the experimental findings on BCECF (Fig. 10f). The reason for this behavior is found in the temperature dependence of water absorption in the infrared region [90].

Additional parameter sweeps were incorporated on the variation of capillary thickness according to the error of production ($\pm 10\%$ as reported by the manufacturer). The scaling of capillary height results in a deviation of ΔT by $\pm 6.3\%$ (Fig. 10d). Larger height leads to more energy uptake and together with the heat transduction of the various materials to a higher temperature peak. This linear dependence of peak temperature was taken into account for the evaluation of S_T (chapter 3.5) after ΔT was determined with a BCECF capillary at 25°C as discussed before.

3.4.3 Correction of base temperature by finite temperature gradient

Another evidence has to be taken into account to determinate the associated corrected base temperature of a certain measurement. Apart from the slightly increased temperature T_0 inside the capillary with respect to the temperature set at the silicon wafer, which can be detected with BCECF (Fig. 9d), another effect arises since the temperature gradient ΔT is finite and not infinitely small. When the Soret coefficient changes with temperature, the concentration gradient that gets established within the thermal field is a result of nonuniform S_T over temperature.
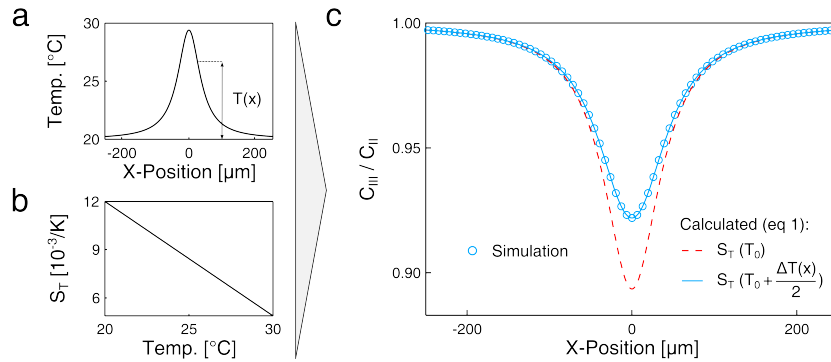
Figure 11: Correction of base temperature due to the finite steepness of the temperature gradient. The base temperature of the measured Soret coefficient has to be corrected to $T_0 + \frac{\Delta T}{2}$. This was found on the basis of a 1D finite element simulation. A Lorentzian temperature gradient (a) together with a linear dependency of the Soret coefficient on temperature (b) results in a concentration profile (c). This profile can be matched analytically by the prediction of the constant Soret coefficient at $T_0 + \frac{\Delta T}{2}$. Reprinted with permission from [23]. Copyright 2014 American Chemical Society.

A 1D finite element simulation (Femlab, Comsol) that incorporates a Lorentzian temperature gradient (Fig. 11a) together with a linear dependency of S_T on the temperature (Fig. 11b) was performed onto the interplay of diffusion and thermal diffusion (eq. 8): $-c \cdot D_T \cdot \nabla T - D \cdot \nabla c = 0$

The outcome of the simulation predicts that the established concentration gradient can be matched analytically by assuming a uniform S_T, which corresponds to the S_T at the temperature $T_0 + \frac{\Delta T}{2}$. For the

assumption of $S_T(T_0)$ being constant over the temperature range, the expected concentration gradient would be higher (Fig. 11c). This finding is in experimental coincidence to cloud point measurements [23].

This had to be taken into account for the presented data and was incorporated by associating the measured S_T with the temperature of $T_0 + \frac{\Delta T}{2}$.

3.5 Data evaluation

Soret coefficient

The Soret coefficients in this study were determined by spatial data analysis at steady state. Therefore the radial fluorescence distribution at steady state was divided by the one after the establishment of the temperature gradient with yet negligible thermophoretic effects (see Fig. 12 a). This method was found yield fast results and is in good agreement to spatial and temporal analysis (compare to [20]).
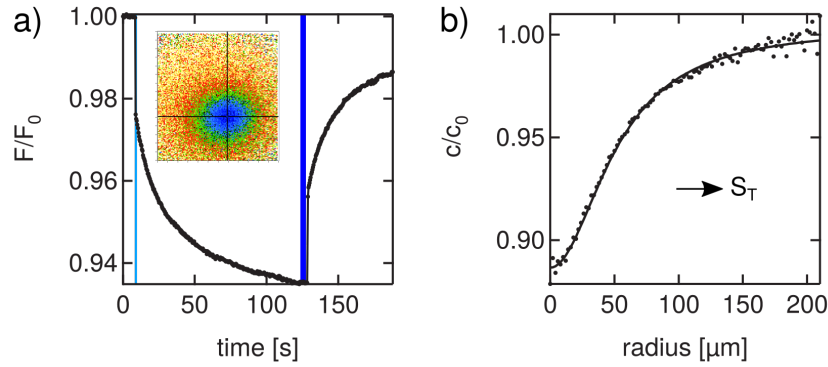
Figure 12: Determination of the Soret coefficient. a) For the radial data evaluation the fluorescence intensity at steady state after heating was averaged over 10 pictures (dark blue) and divided by the initial fluorescence (light blue) after temperature jump, as indicated by cursors in the mean fluorescence over time. b) By the assumption of a linear relationship between fluorescence and concentration, the radial concentration distribution was matched the Lorentzian temperature profile by $c(r)/c_0 = f_{bl} \cdot e^{-S_T \cdot \frac{\Delta T}{1+(r/w)^2}}$. Spatial homogeneous bleaching results in a constant prefactor f_{bl}. On the basis of temperature calibration S_T was extracted. Here a measurement on a single stranded DNA 22-mer in 500 mM KCl at 25 °C is shown.

To distinguish the onset of thermophoresis from the changing chromophore properties in the thermal gradient, the initial uniform concentration c_0 was assumed to be described by the second picture after the laser was triggered. The picture, which was recorded during the time when the thermal gradient in the capillary builds up, had to be omitted. Radial analysis has also the advantage of being insensitive to spatial homogeneous bleaching since it results in constant prefactor f_{bl} [81, 89]. By relating fluorescence I with a spatially constant bleaching prefactor f_{bl} with concentration c, the radial profile for constant S_T gives (see also [89]):

$$I\left(r\right)/I_0 = f_{bl} \cdot c\left(r\right)/c_0 = f_{bl} \cdot e^{-S_T \cdot \frac{\Delta T}{1+\left(r/w^2\right)}} \tag{25}$$

Here the Lorentzian temperature gradient (chapter 3.4) was set as driving force for thermophoresis (eq. 8) at a temperature independent S_T. To account for effects on the temperature dependency of the Soret coefficient, base temperature was corrected (see chapter 3.4.3). Note that the image was cut due to vignetting effects at the boarders of the picture to minimize errors on behalf of low illumination . Furthermore it was assumed that no thermophoresis was going on during the first picture after switching on the laser (~400ms), similar as established steady state at the last picture with laser on and linear detector sensitivity.

Another method, that incorporates all spatial and temporal data, is to compare the fluorescence intensity at each pixel over time with the predictions of a finite element simulation by the knowledge of the parameters S_T, $\Delta T\left(r\right)$, bleaching constant and diffusion constant. The most reasonable combination of parameters can be determined by the minimization of χ^2 between model and experiment [20]. Since this method takes a lot of calculation time, only single data sets (PNA 5,10, 22 mer at 55 °C, *pH* 1) were evaluated to elucidate r and S_T. Therefore a Labview program called the "binding evaluator" was used [20]. The temperature profile was set to the fluorescence profile of the PNA at steady state and the ΔT to 7.23K according to chapter 3.4. The obtained Soret coefficients are in good agreement to radial evaluation (table 1). Radial evaluation results in slightly smaller values for S_T with an error of <5% for the 3 data sets. One reason for this might stem from the loss of data during the first picture, where thermophoresis already sets in. Furthermore the obtained values for the radius of PNA are reasonable compared to detailed measurements and evaluation of DNA [8]. Slightly lower radius of the PNA molecules, as determined indirectly by the diffusion coefficient via Stokes law (eq. 1), might be the result of lower viscosity due to HCl and neglected spatial alternating viscosity due to temperature dependency. Also the slightly differing backbone and rigidity can be the reason.

	S_T^{Radial} [1/K]	S_T^{BE} [1/K]	r^{BE} [nm]	r_{DNA}^{BE} [nm] [8]
P5	0.0098	0.0093	1.16	1.35
P10	0.0075	0.0071	1.59	1.71
P22	0.0055	0.0053	1.91	2.02

Table 1: Radial steady state analysis is in good agreement to extensive space-time analysis by binding evaluator. The data of PNA 5, 10 and 22-mer were evaluated by radial steady state analysis and binding evaluator (see [20])**.** The base temperature was set to 55 °C and *pH* to 1. The obtained Soret coefficients are comparable in size. The radii obtained for PNA are similar to the ones obtained for DNA with the same sequence [8]. They were calculated via Stokes equation (eq. 1) at 55 °C with a viscosity of 0.504 mPas.

Further improvements can be obtained by incorporation of spatial bleaching on the basis of alternating light intensity and temperature: $f_{bl}(I_{xy}, T)$. Moreover data evaluation on finite elements can be improved by implementation of temperature dependency of viscosity, the connected diffusion and the

Soret coefficient, although the last argument might be hard to implement before the measurement.

The Soret coefficients of PEG, PNA, DNA and the various α-synuclein species over temperature were determined by radial evaluation. The same method was used for the measurements of PEG and PNA towards their dependency on Debye length and salt species. The Soret coefficients of DNA for the dependency on Debye length were taken from [8, 20]. For high sensitivity onto the measurements on bloc copolymers at low dye concentration, the S_T was solely determined by the mean fluorescence intensity over time, which was measured by a photomultiplier [23].

Radius

For the theoretical predictions of the thermophoretic models depicted in chapter 2.2, the values for radius r and effective charge Q_{eff} were set to reasonable values according to table 2 for the various molecules.
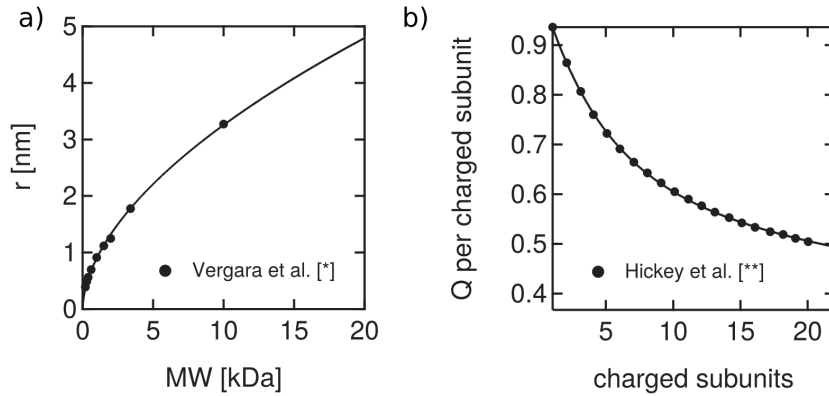
Figure 13: Additional information was incorporated for the estimation of PEG radii [91] and effective charge per charged subunit [29, 30] for the molecules. a) The radii of various PEG molecules were calculated by Stokes equation based on the measurements of Vergera et al [91]*. Exponential fit on the molecular weight results in a Flory exponent of 0.558 which is in good agreement for a polymer in good solvent with 0.588 [92]. b) The Effective charge per charged subunit for the theoretical determination of the charge was approximated by double exponential function based on data achieved by multiparticle collision dynamics by Hickey and coauthors **[29]****.

For DNA, the radii according to detailed data of Reichl and coauthors [8] were taken. For consistency, PNA radii were assumed to be the identical to the DNA radii, since they incorporate the identical sequences. The PEG, the radii were calculated on the basis of the measurements on the diffusion coefficient of PEG molecules of various length at infinite dilution determined by Vergera et coauthors [91, 93] (Fig. 13a). The herein presented diffusion coefficients were transformed into radii by stokes equation (eq. 1) and approximated by power law: $r\,[m] = 1.8989 \cdot 10^{-11} \cdot MW\,[Da]^{0.558}$. The exponent on dependence of radius onto molecular weight is in good agreement with Flory's predictions for polymers in a good solvent of 0.6 [94], and more detailed theoretical considerations 0.588 [92]. The radii of the α-synuclein monomers and oligomers were determined by fluorescence correlation spectroscopy (FCS),

whereas in the case of fibrils atomic force microscopy (AFM) was used [84]. All radii were assumed to be independent of temperature, what also seems to be a good approximation according to the data of Reichl and coauthors [8].

Effective charge

The effective charges Q_{eff} in comparison to the theoretical charges resulting from Henderson–Hasselbalch Q_H (eq. 2) and additional charge condensation Q_{Theory} are given in table 2. For DNA and PNA the underlying pK_a values of nucleobases were set as stated by Chun [26, 95]:

	$pK_a\,(X^+ \rightleftarrows X)$	$pK_a\,(X \rightleftarrows X^-)$
Adenosin	3.5	-
Guanin	2.1	9.2
Cytosin	4.2	-
Thymin	-	9.9
Phosphate	-	2

For DNA the pK_a of the hydroxyl group at the 3' end was approximated to 13.5. [96]. Moreover the HEX dye at the 5' end bears approximately two additional negative charges at neutral pH [8] since it is very similar to fluorescein [97]. For PNA the N-terminal is connected with the uncharged Bodipy-FL dye and an additional O linker where no change of charge should occur in the investigated range.

For the determination of the theoretical charge (Q_{Theory}), the charge according to Henderson–Hasselbalch (Q_H) was multiplied by the effective charge per charged subunit (Q_{pcs}) that was extrapolated from data of Multi Particle Collision simulations with explicit counter ion condensation performed by Hickey [29] (Fig. 13b). The underlying values for the charge per base are in good agreement to coarse grained molecular dynamics simulations and experimental data of capillary electrophoresis and NMR-electrophoresis [29, 30]. For the effective charge per base in dependency on total charge a double exponential function is in good agreement to the data of Hickey [29] (see Fig. 13b):

$$Q_{pcs} = 0.36589 + 0.27551 \cdot e^{-(Q_H - 1.0395)/4.3274} + 0.29362 \cdot e^{-(Q_H - 1.0395)/24.816}$$

.

For α-synuclein charges were determined independently with free flow electrophoresis [84].

	pH-(solvent condition)	$Q_H\,[e]$	$Q_{Theory}\,[e]$	$Q_{eff}\,[e]$	$r\,[nm]$
D5	Tris 7.8	-7.1	-4.71	-4.1	1.35*
D10	Tris 7.8	-12.1	-6.96	-6.5	1.71*
D22	Tris 7.8	-24.1	-11.64	-9.4	2.02*
P22	2 (HCl 10mM)	14.35	7.89	7.89	2.02*
P22	3 (HCl 1mM)	10.77	6.38	5.88	2.02*
P22	4 (HCl 0.1mM)	4.28	3.22	3.22	2.02*
P22	7 (Tris 1mM)	0	0	0	2.02*
P22	12.3 (KOH 20mM)	-8.97	-5.56	-1.7	2.02*
P22	12.6 (KOH 40mM)	-8.99	-5.60	-2.7	2.02*
P22	12.8 (KOH 60mM)	-8.99	-5.60	-3.4	2.02*
P22	12.9 (KOH 80mM)	-8.99	-5.60	-4.1	2.02*
P22	13 (KOH 100mM)	-8.99	-5.60	-5.61	2.02*
P22	13 (NaOH 100mM)	-8.99	-5.60	-5.61	2.02*
P5	1 (HCl 100mM)	2.85	2.34	3.9	1.35*
P10	1 (HCl 100mM)	5.84	4.01	6.9	1.71*
P22	1 (HCl 100mM)	15.74	8.46	8.7	2.02*
PEG750	Tris 7.8	0	0	0	0.77**
PEG2000	Tris 7.8	0	0	0	1.32**
PEG5000	Tris 7.8	0	0	0	2.21**
PEG10000	Tris 7.8	0	0	0	3.26**
PEG20000	Tris 7.8	0	0	0	4.79**
α-mono	Tris 7.4	-	-10.9***	-6.6	2.8 (FCS***)
α-oligo	Tris 7.4	-	-50.4***	-22.1	7.5 (FCS***)
α-fib	Tris 7.4	-	-(200-300)***	-78	l=200 r=4 (AFM***)

Table 2: Effective charge (Q_{eff}) and radius (r) of the investigated molecules for the fits of the theoretical model onto the experimental data. The effective charges Q_{eff} for the various molecules studied are close to the theoretical predicted charges Q_{Theory} , which are calculated by the pK_a of the nucleobases (Q_H) and further charge condensation on polyelectrolytes according to data of Hickey. * The radii of DNA were set according to [8]. For consistency radii of PNA were set respectively. ** Prediction of PEG radii based on extrapolation of measurements on the diffusion coefficients of PEG by Vergara and coauthors [91]. *** Radii of α-synuclein monomers, oligomers were determined by FCS and fibrils by AFM. The theoretical charges here represent the charges measured by free flow electrophoresis [84].

4 Results and Discussion

The measurements are presented in the following manner: First, the different behavior of S_T with respect to temperature and Debye length of charged and uncharged polymers is shown for the case of PEG, PNA and DNA polymers (chapter 4.1). Then, the nonionic contribution of thermophoresis is discussed in great detail, considering measurements of PEG and PNA (chapter 4.2). Following this, the transition between charged and uncharged polymer is presented for a PNA polymer that has a *pH* dependent charge (chapter 4.3). Then, the different thermophoretic contributions and their respective behavior upon ionic strength and base temperature is shown (chapter 4.4). Also, alternative theoretical scenarios are considered and discussed (chapter 4.5). Additionally, finite element simulations are presented that support the local equilibrium approach (chapter 4.6). Finally, the thermophoresis of complex macromolecules is shown in the context of the theoretical model with quantitative predictions for alpha-synuclein proteins. Interesting applications in sensing the transition upon collapse of macromolecules are presented (chapter 4.7).

4.1 Different thermophoretic behavior of charged and uncharged polymers
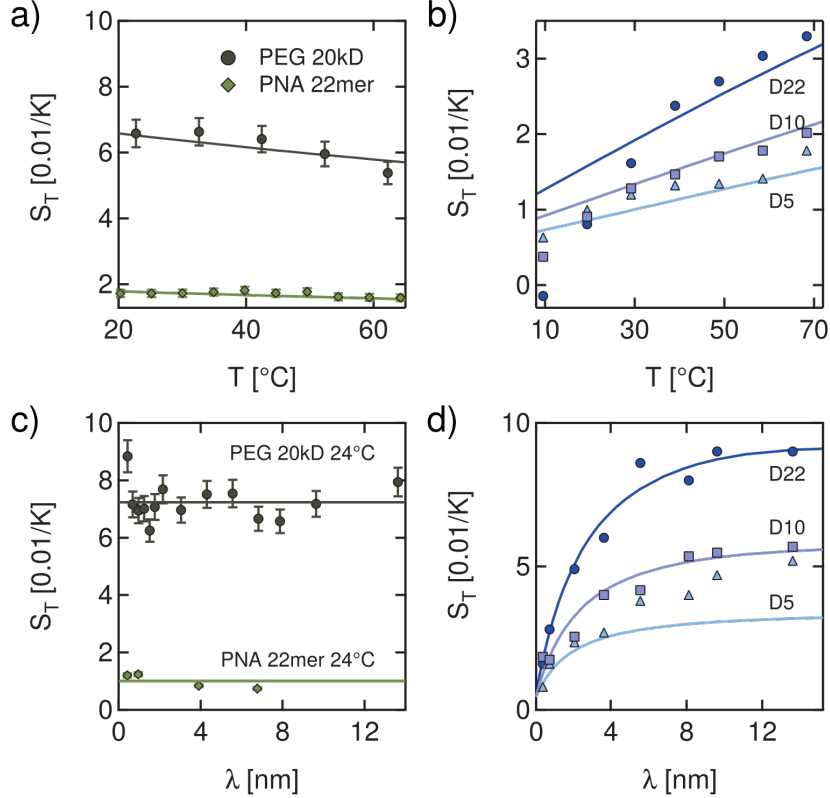
Figure 14: Charged and uncharged polymers behave strikingly different in terms of thermophoresis. a) The Soret coefficient of uncharged PNA 22-mer and PEG 20000 is decreasing with temperature. b) For charged DNA molecules (5-, 10- and 22-mer) instead S_T increases drastically. The main reason for the increasing S_T for charged molecules is traced back in the following chapters to diffusiophoresis. c) As expected ionic strength has no effect on PNA and PEG (lines to guide the eye). d) In contrast to that, the S_T of charged molecules is largely affected upon changes of the Debye length in accordance to the capacitor model. Data of S_T of DNA over Debye length according to [8, 20].

The Soret coefficient behaves completely different for charged and uncharged polymers.

For uncharged PEG and PNA, a slightly decreasing trend of S_T with temperature was found (Fig. 14a). For these uncharged, molecules S_T stays constant with changing salt concentration (Fig. 14c) and salt species (as shown in the following chapter) . This behavior is completely different to the one of DNA. For this charged molecule, S_T strongly changes with temperature (Fig. 14b), salt concentration (Fig. 14d) and salt species [8] .

The increase of S_T with temperature can be observed for a variety of molecules and was so far related to nonionic effects [16–20]. According to the presented theoretical model in this work, S_T^{Ni} is decreasing with temperature via eq. 11. Additionally, the increase of S_T with temperature for charged molecules as e.g. DNA (Fig. 14b), is traced back to the temperature dependent S_T of salt ions. Salt ions interact

via diffusiophoresis (chapter 2.2.4) and the Seebeck effect (chapter 2.2.2) with the charged polymers. Diffusiophoresis was found to play the larger role for DNA (chapter 4.4). The view that S_T increases with temperature is connected to a charge effect was recently supported by [21]. In the following this assumption is even more strengthened, when investigating a PNA polymer with pH dependent charge (chapter 4.3).

The change of S_T of DNA with the Debye length is mainly attributed to the capacitor model, which only plays a role for charged molecules. This is also found for other charged molecules, as Polystyrene [50] or ferrite particles [98].

Note that for DNA the nonionic parameters were assumed to be $\Delta_T = a = 0$ according to eq. 11, so only $\frac{1}{T}$ remains for S_T^{NI}. In the following chapter the uncharged PEG and PNA polymers are investigated in detail.

4.2   Nonionic contribution

The nonionic contribution to the Soret effect is still sparsely understood. Therefore a concentration series was arranged, which monitors the transition of S_T of uncharged PEG polymers towards the semidilute regime. Additionally, the changes of S_T upon base temperature, ion concentration and species were investigated. Finally, the data was matched to a theoretical model with two empirical parameters.

Concentration dependence of PEG
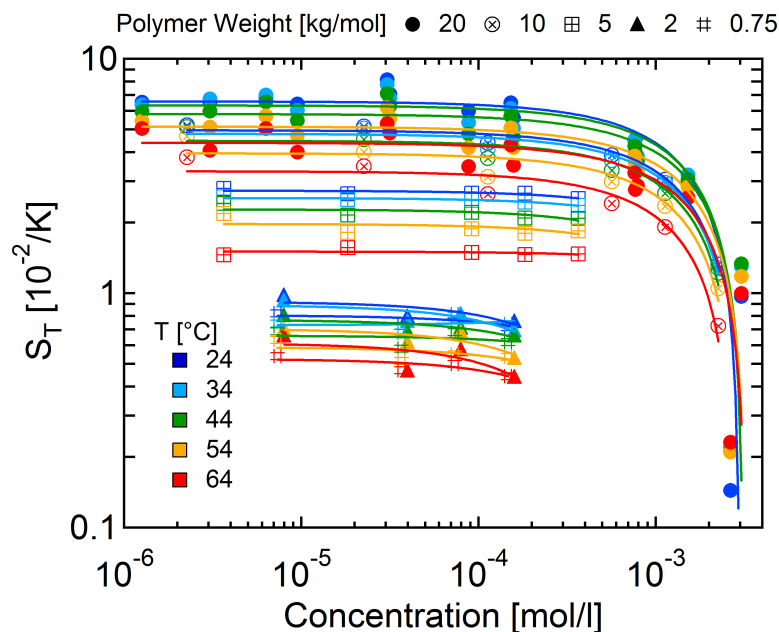
Figure 15: Soret coefficient of uncharged PEG polymers of variable molecular weight, at various concentration and at different temperatures. In the dilute micromolar range S_T is rather constant. At high concentrations (millimolar) a clear decrease of S_T can be observed for large PEG20000 and 10000. These concentrations are found to coincide with the transition to the semi-dilute regime. For polystyrene polymers organic solvents similar behavior could be observed and explained by enhanced diffusion due to collective motion [99]. The Soret coefficients of PEG were extrapolated to infinite dilution for further analysis [80].

For PEG, it was first tested whether the polymer concentration has effects on the Soret coefficient already at dilute conditions in the micromolar regime [8]. There, it has been traced back to a charge effect, which occurs due to the change of the Seebeck effect by the thermophoresis of the polymers.

It is observed that the S_T of uncharged PEG stays constant in the sub-millimolar regime for a certain polymer length and base temperature (Fig. 15). For PEG20000 and PEG10000, S_T decreases significantly at high micromolar concentrations. The overlap volume fraction, where the semi-dilute regime starts and the polymer coils begin to overlap, can be estimated as [94, 100]: $\rho* \cong \frac{1}{N_a \frac{4}{3}\pi r^3}$. For the different

PEG polymers it is obtained:

PEG [g/mol]	750	2000	5000	10000	20000
overlap concentration $\rho*$ [mMol/l]	868	172	37	11	3.6

It is most likely that the observed drop of S_T at high concentrations is caused by increasing polymer-polymer interactions (Fig. 15). For the polymers of lower molecular weight, the concentration was not high enough and would elaborate enormous dye consumption, if one does not want to go for a mixture of labeled and unlabeled polymers. A similar observation was already found in non-polar solvents as polystyrene in toluene [80, 99]. Here, the dependence of S_T onto concentration was traced back to increasing diffusion coefficient (D) based on collective motion and a constant thermal diffusion coefficient (D_T) in the semi-dilute regime. In the concentrated regime both, D_T and D, decrease. As expected,the polymers are also subjected to similar changes in water. Nevertheless, the detailed entropic or thermodynamic reasons for this behavior are not yet theoretically understood, although it has been found out that the solvent plays a minor role on D_T [101].

Noteworthy, this observation indirectly supports the findings on charged molecules onto the self-Seebeck effect. In contrast to DNA [8] and α-synuclein monomers (see Fig. 31), no effect on the S_T in the micromolar region can be observed for PEG molecules of comparable size.

For the following more detailed investigation of the dependency of S_T on temperature and radius, the measurements were extrapolated to an infinite dilution according to a first order virial expansion [80]:

$$S_T = S_T^0 \cdot \left(1 - k_s c + O\left(c^2\right)\right)$$

Qualitatively the obtained Soret coefficients are slightly lower compared to measurements in Thermal Diffusion Forced Rayleigh Scattering [13] and thermogravitational columns [12]. Reasons for this might stem from influences of the dye molecule, difference in concentrations of PEG molecules or sticking of PEG to the capillary wall.

Temperature

The S_T of PEG is slightly decreasing with temperature in the investigated temperature range (Fig. 16a). This was observed for different chain length. This finding is in accordance with the data on PEG at higher concentration by Wang and coauthors[13]. Rescaling of S_T to the Soret coefficient at 20 °C results in a unified picture (Fig. 16b).
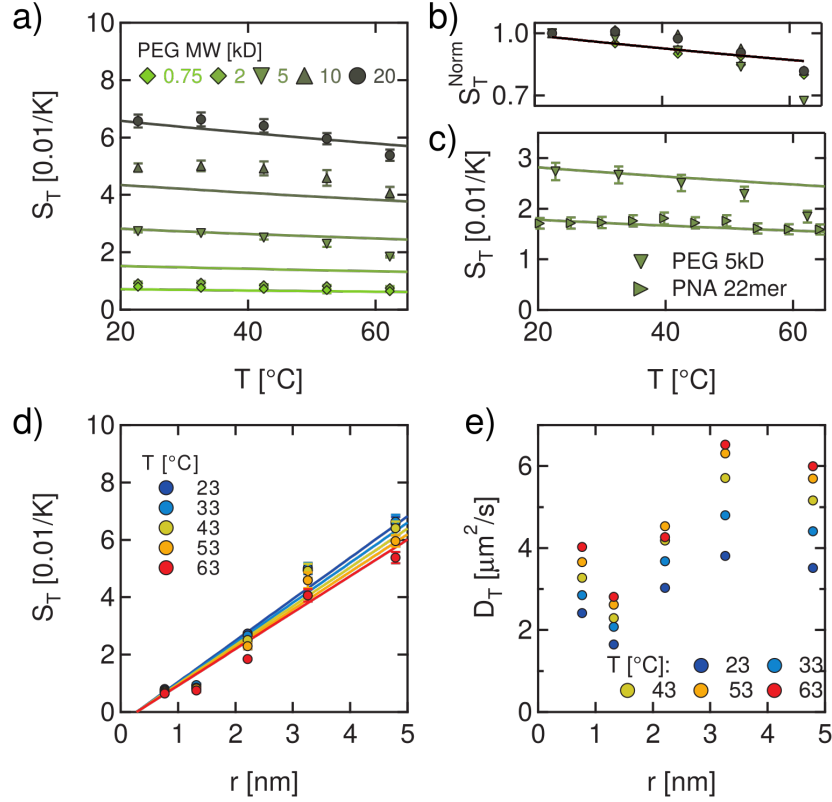
Figure 16: Nonionic thermophoresis decreases with base temperature and is proportional to the hydrodynamic radius. a) For uncharged PEG polymers of variable molecular weight, the Soret coefficient is decreasing with temperature . b) A normalization to the Soret coefficients at 20 °C shows a general behavior for PEG. c) Comparing S_T^{NI} of PEG and PNA molecules of similar size yields a slightly larger value for PEG. d) In contrast to charged molecules [49], the Soret coefficient of uncharged ones is found to increase linear with radius. e) Thermal diffusion coefficient, D_T, is rather constant with radius, similar to the behavior of PS in organic solvents [9]. Analog to the diffusion coefficient, the value increases with temperature.

According to eq. 11 the free parameters for PEG in water were determined to: $\Delta_T(PEG) = 31.3 \cdot 10^{-16} \frac{N}{K}$ and $a(PEG) = 1.6 \cdot 10^{-24} \frac{m^2 kg}{s^2 K}$. Here, the first parameter is corresponding to a polymer specific constant $D_T \cdot \eta$ in the high polymer length range, where S_T only varies with polymer size, because of changing diffusion coefficient $D(r)$. For polystyrene (PS) in organic solvents it was found to be in the same order of magnitude $\Delta_T^{PS} \approx 60 \cdot 10^{-16} \frac{N}{K}$ [9]. The second specific parameter cannot be directly compared to Köhler due to different α. Nevertheless, rough estimation for PEG20000 at 25 °C results for Köhler's original equation with $\alpha = 1$ yields: $a_{köhler} = \frac{a \cdot M^1}{2r\eta} \approx 7 \cdot 10^{-12} \frac{kg\,m^2}{s\,K\,mol}$. This is by an order of magnitude larger than what Köhler found for PS in organic solvents.

For an uncharged PNA 22-mer a similar dependence on temperature has been found (Fig. 16c). The S_T of PEG with comparable size (r (PEG5000)=2.21 nm and r(PNA22)=2.02 nm) is slightly higher by a factor of ~1.5.

The nonionic parameters of PNA were determined indirectly by the measurements on charged PNA at high HCl concentrations (Fig. 18c) to $\Delta_T \left(PNA \right) = -23.5 \cdot 10^{-16} \frac{N}{K}$ and $a \left(PNA \right) = -7.9 \cdot 10^{-24} \frac{m^2 \, kg}{s^2 \, K}$.

Radius

Although it has been found for charged molecules that S_T is proportional to r^2, the measurements on uncharged PEG indicate a linear increase of S_T^{Ni} (Fig. 16d). This is also suggested by Würger in his theoretical description of the thermal diffusion coefficient for uncharged molecules D_T^{Ni} based on entropy production [15].

For PEG, D_T^{Ni} shows a slight increase with the radius of PEG (Fig. 16e). The expected sharp change at the low molecular weight end could not be observed [12], since the smallest investigated polymer with 750 Dalton is yet larger than a Kuhn monomer [94]. This fits the predictions according to equation 11 and the measurements on PEG polymers in water [12, 13]. D_T increases with temperature similar to the diffusion coefficient, where viscosity is the important parameter. D_T was calculated by $D_T = S_T D$ and Stokes equation.

Debye length, Hofmeister

Charged polymers in electrolyte solution are largely influenced by ionic strength and ion species. It was tested whether thermophoresis of uncharged polymers is also influenced by ions, although they do not interact by electrostatics. As expected, it has been found for an uncharged PEG molecule of 20kD and a PNA 22-mer, that the ionic strength has no large effect and S_T^{NI} is independent of Debye length (Fig. 17a).
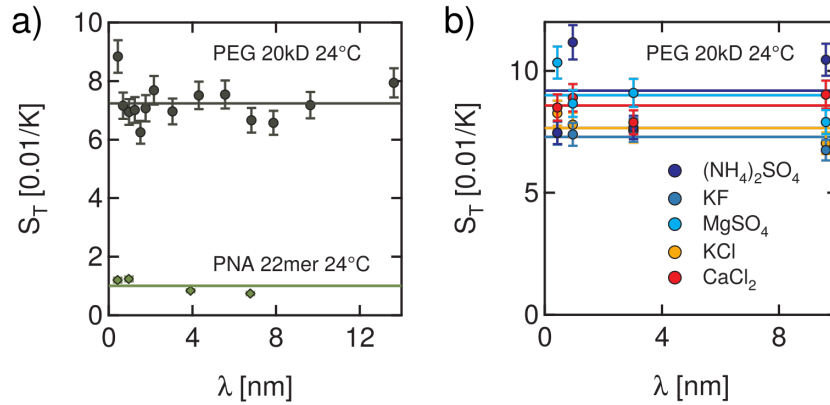
Figure 17: Dependence of the Soret coefficient of uncharged polymers on salt concentration and species. a) For PEG and PNA molecules, no dependence of S_T^{Ni} on Debye length in electrolyte solutions of potassium chloride (KCl) was found. Because the charged ions in solution are not expected to interact with the polymer to a large extend, this is in agreement to theory. b) Moreover no significant effect upon salt species was found for PEG according to the Hofmeister series. The lines represent the mean value to guide the eye.

Moreover, for the Soret coefficient of PEG no correlation has been found between the salt species and the Hofmeister series [102, 103] in the investigated range (Fig. 17b). In the presented data, the investigated salts range from kosmotropic to chaotropic in the following order:

$$(NH_4)_2\,SO_4 \rightarrow KF \rightarrow MgSO_4 \approx KCl \rightarrow CaCl_2$$

As the two most extreme salts with respect to the Hofmeister series show high S_T for PEG and the other salts species show slightly lower S_T, observed differences are attributed to measurement inaccuracy. Moreover, also for these various salt species no significant dependency on Debye length is observed.

More tests on PEG-Polymers in electrolyte solution can be found in the Bachelor Thesis of Michael Haslauer [81]. Here, additionally an attached Atto488 dye with one negative charge and detailed temperature dependency for PEG in various salt species is presented. As shown in [81], the dependence of the Soret coefficient on temperature in electrolyte solution is similar to Fig. 16a and S_T decreases with temperature.

In appendix 7.2 preliminary data on thermophoresis of PEG in various solvents is presented. The results are quite puzzling. For the nonionic contribution it can be concluded, that a fundamental model is still missing, which explains the S_T of an uncharged polymer in various solvents. First models based on interaction energies still leave a large gap between experiment and theory [13].

4.3 Charge transition of a polymer

In the following it is shown how the behavior of S_T completely changes with temperature T, when a PNA22 polymer undergoes the transition from uncharged to charged state. Note that the lines in the graph are predictions by the full theoretical model.
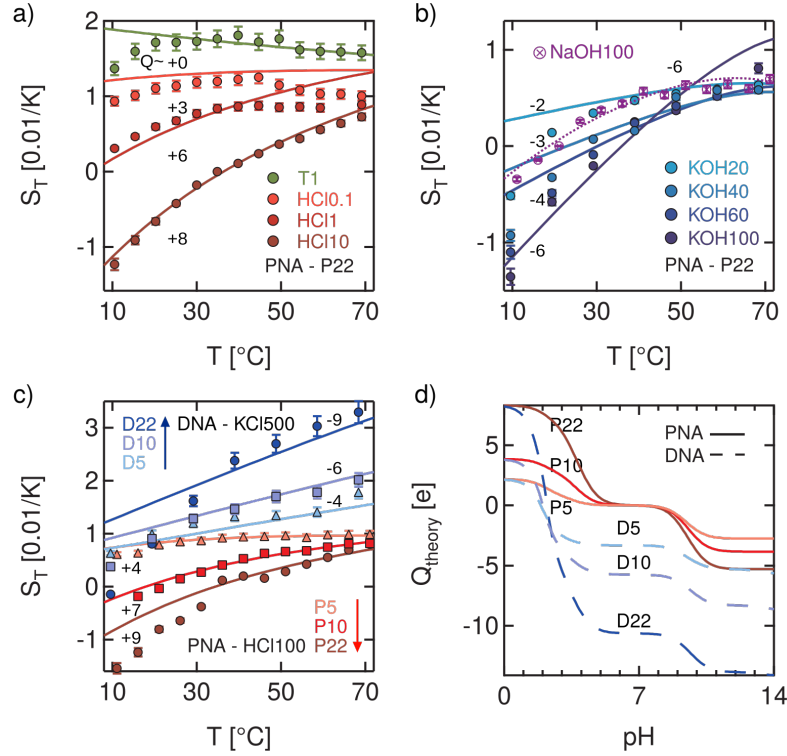
Figure 18: Transition of the Soret coefficient from uncharged to charged PNA. a) A PNA 22 mer completely changes behavior when the charge is increased (indicated in Graph) by different concentrations of HCl (in mM) compared to 1 mM Tris *pH* 7.6 (T1). The absolute value of S_T decreases mainly on behalf of the Seebeck effect. The transition of the slope of S_T over temperature from decreasing to increasing matches the predictions. b) In basic environment a similar trend is found. The slopes of S_T for NaOH and KOH (at 100 mM) are in good agreement to the predictions. Even the different thermophoretic behavior of sodium and potassium ions (see Fig. 6) is observed. c) At 100 mM HCl concentration PNA molecules of different length (5-, 10- and 22-mer) show a similar trend as DNA polymers in 1 mM Tris *pH* 7.6 at 500 mM KCl with comparable slope of S_T with temperature and charge. Data of DNA taken from [8, 20]. d) The effective charges for the underlying fits are in good agreement to the calculated charges according to Henderson–Hasselbalch and charge condensation.

When the HCl concentration is increased, the Soret coefficient of the PNA polymer gets smaller while the slopes of S_T over temperature get steeper (Fig. 18a). This is in correlation to the increasing *pH* and thus assumed increase in charge according to chapter 3.5 by the pK_a of the nucleobases (Fig. 18d). Since the 22-mer gets more positively charged, S_T overall decreases due to Seebeck effect, which

drags the polymer to the hot, because of the large Soret coefficient of the H^+ ion. Moreover the capacitor model also gives less pronounced contribution at higher concentration. The increasing slopes of S_T with temperature are connected to diffusiophoresis in this picture as shown in detail in the next chapter.

When PNA is brought in basic environment the trend is similar (Fig. 18b), although it is hard to access experimentally because the fluorescence of the Bodipy dye is observed to be unstable in that range. Nevertheless similar to in the acidic case, it can be observed, that the more hydroxide salts are added, the steeper the slopes of S_T with temperature get and the S_T is also decreasing. It cannot be distinguished whether this is on behalf of electrophoresis or diffusiophoresis just by this observation, since both, the charge of PNA and the electric field due to the high S_T of hydron and hydroxide [68], change sign (Fig. 18a compared to Fig. 18b).

The behavior of PNA in NaOH compared to KOH is also very intriguing. Since KCl and NaCl were found to have a slightly different temperature dependency (see [66]), S_T of potassium and sodium are also behaving differently (Fig. 6). This is also monitored in the case of PNA, where the slope of $S_T(T)$ of PNA is more flat in NaOH than in KOH electrolyte. The predictions for the charge of PNA in KOH are not exactly according to the Henderson–Hasselbalch equation. This might be attributed to the high solubility of carbon dioxide in water and correlating carbonic acid, that can alter the *pH* of the solution [104].

Next, the S_T of PNA of different length at very acidic conditions is tested (Fig. 18c). Interestingly, the slope of S_T is also increasing with size and charge. For a detailed investigation whether the steepness of $S_T(T)$ is related to Q or Q² (or r vs r²), very precise measurements of the charge and radius would be important in addition to the exact characterization of S_T of the salt ions. The result is very similar to DNA molecules in 500mM potassium chloride, where the steepness is influenced by length.

Unfortunately, due to a changing contribution by the Seebeck effect for charged PNA molecules, the screening with Debye length is more complex than described by the capacitor model alone. , Because of the fixed HCl amount, the ratio of the ionic species in solution is changing when screening with potassium chloride. Therefore, the ratio of potassium and hydron ions would largely change. In contrast, screening with HCl would result in a different charging of the molecule (Fig. 6d), which also makes the capacitor model not directly accessible.

The effective charges by calculation of Henderson–Hasselbalch and charge condensation after chapter 3.5 (Fig. 6d) are in good agreement with the charges for the underlying fits as indicated by the respective numbers in Figure 6a-c.

Altogether the transition of the PNA molecule from uncharged to charged state supports the theory that the increase with temperature is most likely attributed to a charge effect. In the following, a detailed picture on the influence of the various contributions will be presented.
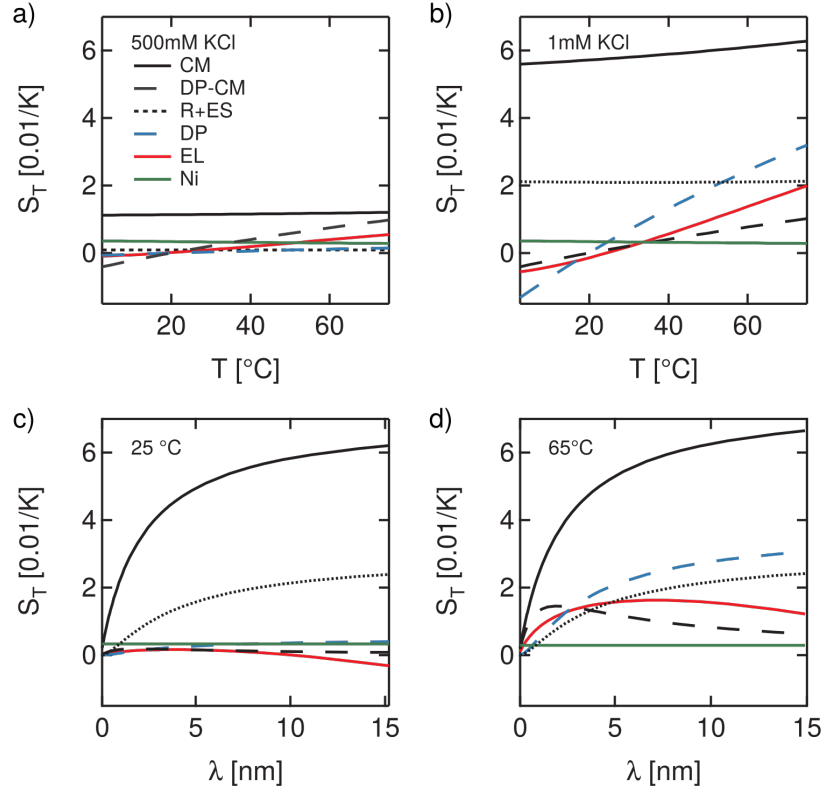
4.4 The different contributions to thermophoresis

The different contributions on the Soret effect all play together to form S_T according to our current model (chapter 2.2). Here it is shown how these different contributions effect the overall thermophoresis for a DNA 22-mer in detail (Fig. 19) at the variation of ionic strength and temperature.

Furthermore, the effects of explicit and local equilibrium forces are shown more generally for the studied DNA and PNA molecules (Fig. 20).

It can be observed that at high salt concentration all contributions are rather low for a DNA 22-mer. The temperature dependency mainly stems from the salt ions by S_T^{DP-CM} followed by S_T^{EL} and S_T^{DP}. A similar picture is found at low salt concentrations. Here the largest contribution onto temperature stems from S_T^{DP}, which is larger than S_T^{DP-CM}. Over Debye length it is observed at a base temperature of 25 °C, that due to the low S_T^{MX} of the salt ions at this temperature, S_T^{CM} dominates thermophoresis followed by a much smaller S_T^{R+ES}. For a high temperature of 65 °C it can now be seen that diffusiophoretic and electrophoretic effects are larger, with similar behavior as S_T^{R+ES}. According to chapter 3.5 the effective charge of DNA was set to -9.4 e and the radius to 2.02 nm.

Figure 19: Theoretical predictions for the different thermophoretic contributions of a DNA 22-mer on temperature and ionic strength. S_T over base temperature at high (a) and low salt concentration (b) is dominated by the capacitor model (CM), which predicts higher S_T at low ionic strength. Diffusiophoretic (DP and DP-CM) and Seebeck (EL) contributions are mainly responsible for the increase with temperature. S_T over Debye length is ruled by the capacitor model at 25 °C followed by the contribution relying on interfacial tension (R+ES) (c). At higher temperature (d) it still makes up the largest contribution, but the other contributions increase. Only the nonionic contribution (Ni) is small and almost constant for DNA.

If one now combines S_T^{R+ES}, S_T^{DP} and S_T^{EL} to $S_T^{Expl.}$, the following picture for PNA and DNA is presented (Fig. 20).

The nonionic contribution is observed to be much larger for PNA than for DNA. For DNA it was assumed, that $\Delta_T = a = 0$ according to eq. 11, that means only $\frac{1}{T}$ remains for S_T^{NI}. For PNA on the other side the S_T is in a similar order of magnitude as for PEG (see chapter 4.2).

$S_T^{Expl.}$ shows a slight change with temperature and Debye length. Nevertheless $S_T^{Expl.}$ is too small to explain the experimental data on DNA. For PNA the H$^+$ Ion results in a large splitting for the differently charged molecules because of the Seebeck effect. The temperature dependency here mainly stems from diffusiophoresis as presented in Fig. 19.

When turning to the contributions arising from the local equilibrium approach, one finds the temperature dependency further increased by the additional diffusiophoretic contributions on behalf of the

capacitor model (Fig. 20a,c,d). Finally the capacitor model with the largest contribution sets in and leads to the characteristic behavior for DNA in water over Debye length at 25°C (Fig. 20b).
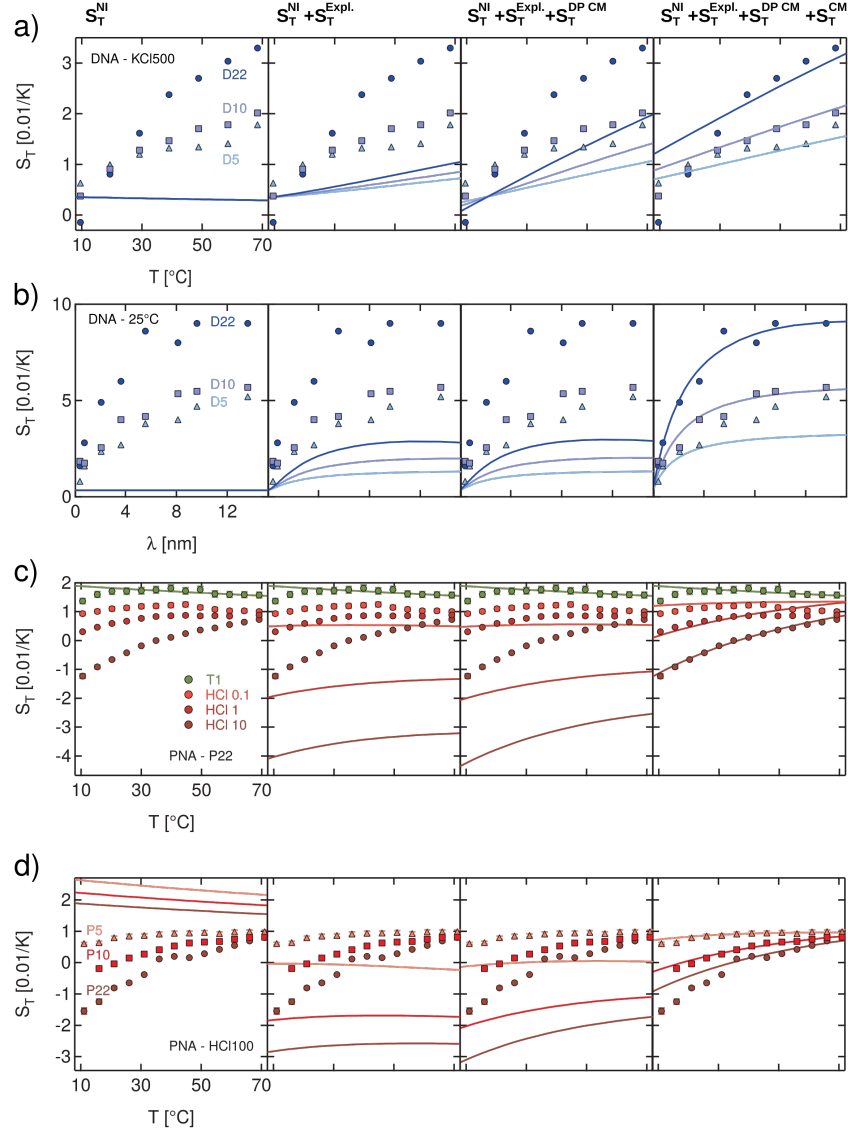

Figure 20: Quantitative predictions of the various contributions for the investigated DNA and PNA molecules. For DNA (a,b) and PNA (c,d) molecules it is shown how the S_T is affected by the different contributions: S_T^{Ni}, $S_T^{Expl.}$ and the two contributions from local equilibrium S_T^{DPCM} and S_T^{CM}. The typical behavior over Debye length (b) is to a large extent caused by the capacitor model, which builds the largest absolute contribution. For PNA (c,d) the explicit forces have a large impact on behalf of the Seebeck effect by the hydron ion. Temperature dependency enters mainly by the diffusiophoretic contributions which scale with temperature dependent S_T of salt ions. The salt concentration, KCl and HCl, is indicated in mM in the figures. Note: Data of S_T of DNA over Debye length according to [8, 20].

4.5 Consideration of alternative theoretical settings

In the following, alternative theoretical models are considered. First, it is tested whether electrophoresis can also be the cause for the temperature dependency of S_T. Next, it is shown if the explicit forces can result in the perceived S_T for DNA and PNA by settings of maximum charge without the contributions from local equilibrium. Then it is shown how the incorporation of hydron ions into the Debye layer would change the overall picture. Furthermore water polarization as additional effect is discussed as well as the effect of a temperature dependent charge of the macromolecule in spite of the capacitor model.

4.5.1 Electrophoresis as reason for temperature dependency of the Soret coefficient

In the following, it is discussed why the increase of S_T with temperature is not associated to a temperature dependent Seebeck effect, which is linear in charge ($\sim Q$), but stems from an effect which is proportional to Q^2, such as diffusiophoresis.
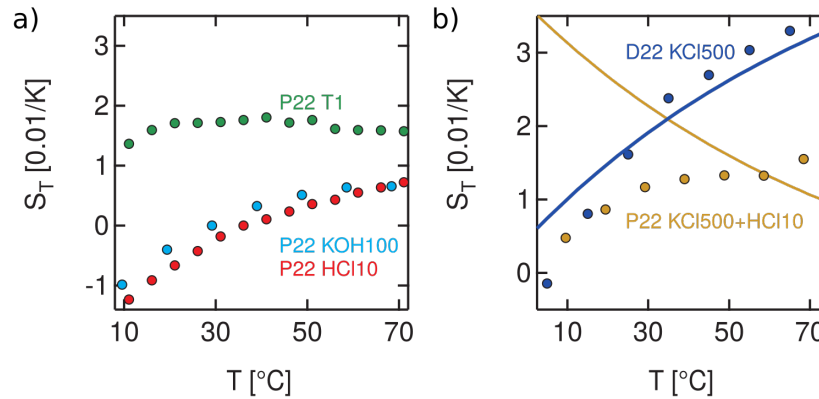
Figure 21: Temperature dependency of the Soret coefficient is not caused by Seebeck effect: a) The measurements of oppositely charged PNA in 10 mM HCl and 100 mM KOH both show an increased slope of S_T with temperature compared to PNA in 1 mM Tris. Since both, charge and electric field change, one cannot distinguish if the underlying effect is proportional to Q or Q². b) S_T of PNA polymers also shows an increase with temperature in 500 mM KCl with 10 mM HCl as well as negatively charged DNA molecules in 500 mM KCl. Since the Seebeck conditions are almost identical, the assumption of the Seebeck-term causing the temperature dependency for DNA would result in a completely different prediction of $S_T(T)$ for the oppositely charged PNA. The theoretical predictions of the Seebeck effect alone being responsible for the temperature dependency of the Soret coefficient are shown by the lines.

The measurements of PNA in KOH and HCl do not solve the question whether the temperature dependency is related to Seebeck effect (Fig. 21a). The temperature dependence of S_T is similar. However, although the charges are opposite in these cases, the reason for similar temperature dependency still can be due to a change in the temperature dependency of the electric field E(T), which is caused by different ions. Also S_T of negatively charged DNA in 500 mM KCl (1 mM Tris) increases with temperature. For

PNA in 1mM Tris there is a rather flat temperature dependence.

A measurement that directly supports the view of the temperature dependency of S_T not being linear to charge is found for a PNA 22-mer in 500 mM KCl and 10 mM HCl compared to a DNA 22-mer in 500 mM KCl (Fig. 21b). Here the charges are opposite and the electric field induced by the KCl electrolyte is almost identical, as there is 50x more KCl than HCl. Nevertheless they both show a similar trend of S_T with temperature. Assuming a model where the Seebeck-term is responsible for the temperature dependency of DNA, one would also expect a drastic decrease with temperature for positively charged PNA (Fig. 21b).

4.5.2   Soret coefficient made up solely by non-equilibrium contributions

Here, it is tested how the Soret coefficients would look like for the predictions of only explicit forces being active and neglecting the contributions from local equilibrium approach.
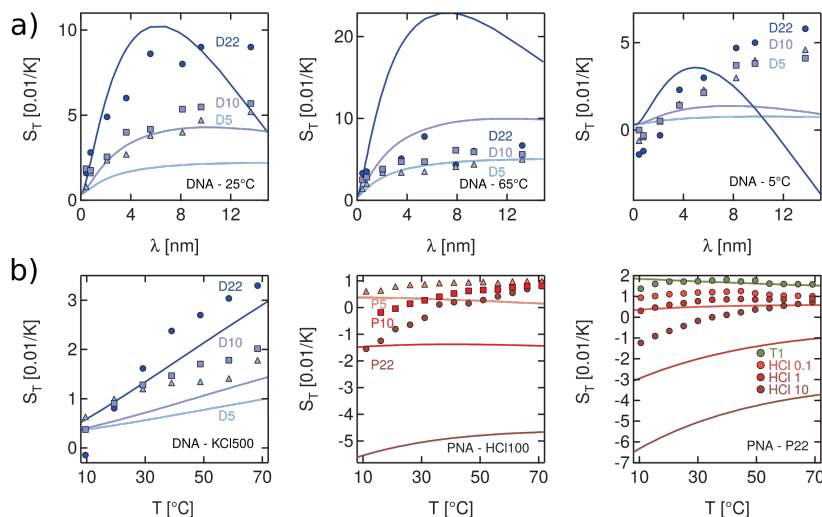
Figure 22: Explicit forces alone are unlikely to explain the thermophoretic behavior of DNA and PNA without the contributions stemming from local equilibrium approach. a) The Soret coefficients over Debye length are reasonably described at 25 °C by explicit forces, when the charges of DNA are increased to the maximum (22-mer carries a charge of -22e then). Nevertheless for high and low temperature the predictions are far off. b) The slope over temperature is matched very good for DNA. On the other side the predictions fail the experimental data of PNA (without even increasing the effective charge). Note: Data of S_T of DNA over Debye length according to [8, 20].

Therefore, the effective charges of DNA 22, 10 and 5mer were increased to the maximal bare charge (-22e, -10e, -5e). The dependency of S_T on Debye length is matched poorly at 25 °C, even if the maximum charges are applied (Fig. 22a). Moreover, for 65 °C and 25 °C the predictions of explicit forces are completely off over Debye length.

Over Temperature the slopes of S_T for DNA and PNA seem reasonable at high salt, but for PNA the

offsets are not in the right range (Fig. 22b). It therefore can be concluded that even at best conditions for the explicit forces, further contributions to thermophoresis are likely.

4.5.3 Hydron and hydroxide in Debye layer

The presented model shows a large discrepancy to the experimental data when the hydron or hydroxide ions are incorporated into the Debye layer. For the measurements at neutral *pH*, e.g. for DNA, these ions do not have a large impact on the model because $c(H^+) = c(OH^-) = \sim 10^{-7}$, but for high hydron or hydroxide concentration the situation changes completely.
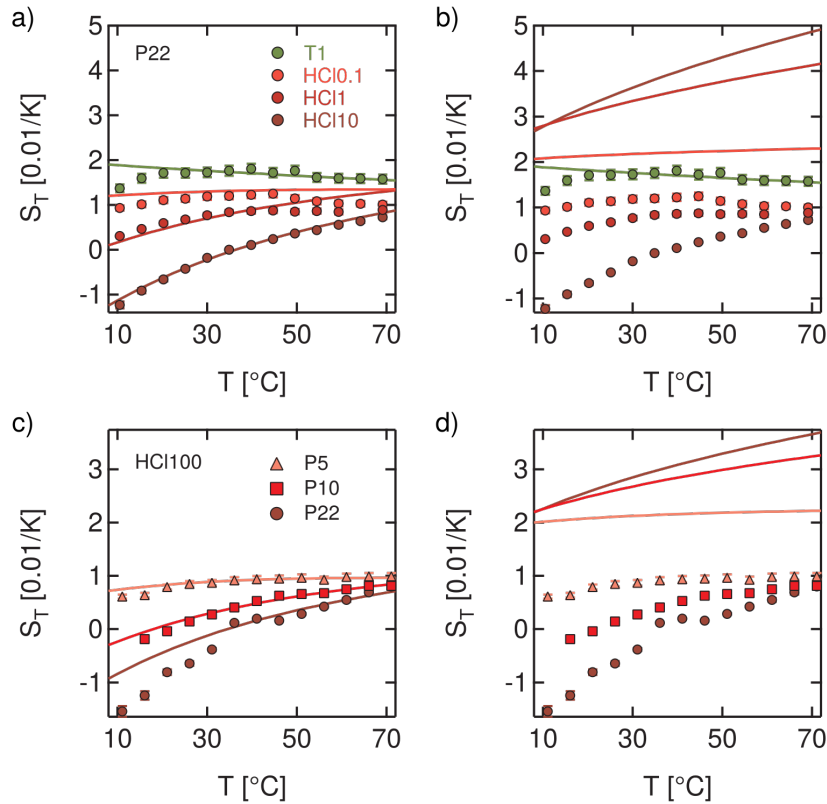
Figure 23: The incorporation of H⁺ and OH⁻ ions in the Debye layer would result in too high Soret coefficients. H⁺ and OH⁻ ions behave special in the presented theoretical model. For PNA molecules at high HCl concentration, theory matches the experiment well when the hydron is neither incorporated in the Debye layer, nor in diffusiophoretic contributions, but interacts solely by Seebeck effect (a,c). The insertion of the hydron into the Debye layer would result in a large discrepancy between experiment and theoretical model (b,d). This is mainly due to an enhanced diffusiophoresis.

In Figure 23 the effects of the incorporation of hydron into the Debye layer and diffusiophoresis is shown. It can be observed that the predictions for S_T are too high when incorporating H⁺. The increase is mainly caused by enhanced diffusiophoresis of PNA because of the hydron ions. This astonishing result has to be investigated in greater detail and tested. It was attributed to the special nature of H⁺ and OH⁻,

since they differ from ordinary ions by their self dissociation and their special diffusion mechanisms [105].

4.5.4   Water polarization

Another effect, which was taken into account, is the polarization of water. It was found in simulations that thermal gradients also result in a polarization of water [59, 60]. The resulting electric field to a thermal gradient is coupled by the ratio of phenomenological coefficients *Lpq* and *Lpp*.

$$E = (1 - \frac{1}{\varepsilon_r}) \cdot \frac{L_{pq}}{L_{pp}} \cdot \frac{\nabla T}{T}$$

Therefore the effect on the Soret coefficient can be calculated by a balance of fluxes:

$$0 = -D\nabla c + c\mu E = -D\nabla c + c\mu(1 - \frac{1}{\varepsilon_r}) \cdot \frac{L_{pq}}{L_{pp}} \cdot \frac{\nabla T}{T}$$

From this follows the contribution of water polarization (S_T^{Pol}) to the Soret coefficient :

$$S_T^{Pol} = -\frac{\mu}{D \cdot T}(1 - \frac{1}{\varepsilon_r})\frac{L_{pq}}{L_{pp}} \tag{26}$$

Until now the numerical simulations do not yet converge to a common theory or picture for water polarization. The size of the phenomenological coefficients varies largely for the temperature range under investigation [59, 106–108]. Further experimental tests still need to validate the simulation results.

In the following, the effect onto S_T^{Pol} is estimated for DNA using two extreme coupling constants $\frac{L_{pq}}{L_{pp}}$: -0.5 V [107] on the one and 10 V [108] on the other side (Fig. 24).

The predicted impact of water polarization would in both cases be very extreme. For DNA the S_T over Debye length is matched by $\frac{L_{pq}}{L_{pp}} > 0$ similar to the capacitor model, while the trend of S_T over temperature is matched by $\frac{L_{pq}}{L_{pp}} < 0$ for DNA (Fig. 24). This is slightly contradictory, although it might also be the case that the coefficients are not constant with temperature and salt concentration. Notably this effect also scales with charge and would be mirrored for positive compared to negative charge.

Therefore it is most likely that the value for $\frac{L_{pq}}{L_{pp}}$ is much smaller. It is not excluded that water polarization is responsible for the slight deviation of S_T in the low temperature range.
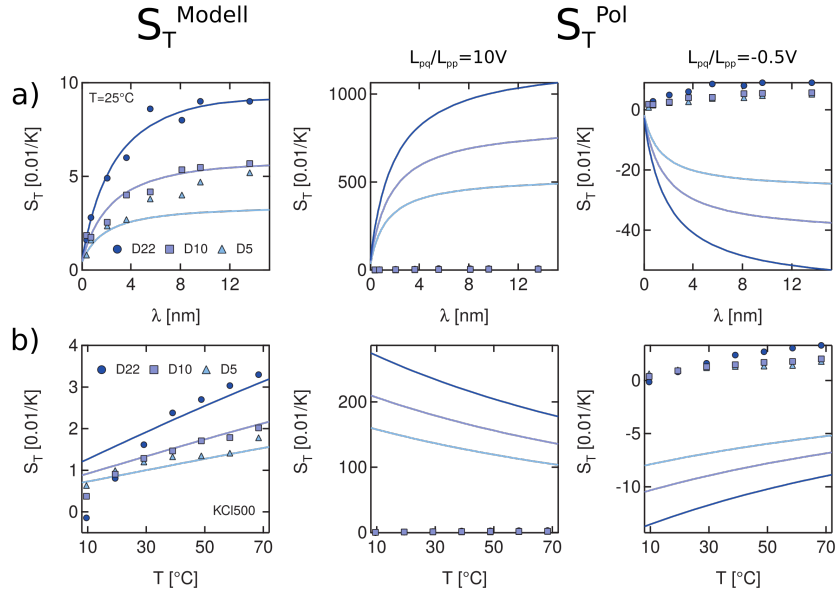
Figure 24: The effect of water polarization in a thermal gradient. The predictions for the $S_T(\lambda, T)$ of DNA (22-, 10- and 5-mer). a) Data calculated by the variation of Debye length λ at constant temperature (T = 25°). b) Temperature dependency of S_T at constant Debye length at 500 mM KCl. On the left, the experimental and theoretical values according to eq. 10. The contribution to the Soret coefficients which is caused by polarization of water according to eq. 26 are shown for a coupling constant of 10 V [108] in the middle and -0.5 V [107] on the right. Note: Measurements of S_T of DNA over Debye length according to [8, 20].

4.5.5   Temperature dependency of effective charge

So far the effect of a temperature dependence of charge was not considered, although this behavior was found for some molecules like e.g. ferrite nanoparticles [21]. For the measurements on DNA molecules no large shifts in charge are expected since pK_a and pH are very distant. Also for the measurements on PNA at high HCl concentration (e.g. 0.01 M), there should be only little deviations on pH, since the change of pK_W with temperature is mainly reflected in the concentration of hydroxide ($\sim 10^{-12}$ M). But changes in the pK_a of the nucleobases are not excluded.

To obtain a broader view onto these effects on thermophoresis, an estimation of the capacitor model (chapter 2.2.6) was performed on the basis of a linear temperature dependency of charge:

$$Q_{eff}(T) = Q_{eff0} + a(T - T_0) \cdot e \tag{27}$$

Here, a represents the slope of Q and T_0 the temperature, at which the second term vanishes. The additional part of the capacitor model, $S_T^{CM-Q(T)}$, which arises due to a change of the energy

$W = \frac{Q(T)^2}{8\pi\varepsilon R(\frac{R}{\lambda}+1)}$ stored inside inside the capacitor [48] is calculated by:

$$S_T^{CM-Q(T)} = \frac{1}{k_B T} \frac{\partial W(Q(T))}{\partial T} = \frac{1}{k_B T} \frac{2 \cdot a \cdot e\left(Q_{eff0} + a\left(T - T_0\right)\right)}{8\pi\varepsilon R(\frac{R}{\lambda}+1)} \tag{28}$$

As can be seen in Fig. 25, even a slight change of charge with temperature results in large effects on S_T. Here, the effect onto the S_T of a DNA 22-mer is shown with $a = \pm0.01$ and $T_0 = 5\,^\circ C$, which means $dQ = \pm0.6\,e$ over the depicted temperature range. S_T changes according to enhanced or increased charge slightly. For negatively charged DNA (Q=-9.4e) the Soret coefficient decreases for $a = 0.01$ and increases for $a = -0.01$. Remarkably, even this slight change in charge results in enormous effect by the additional capacitor model contribution $S_T^{CM-Q(T)}$(eq. 28).

Note that for positively charged PNA 22-mer the effect would be opposite, that means larger S_T for a=0.01 and lower S_T for a=-0.01.

For nonlinear charge dependency, the additional contribution can take arbitrary shapes and it is not excluded that this is responsible for the deviations of our model and the experimental values in the low temperature range.
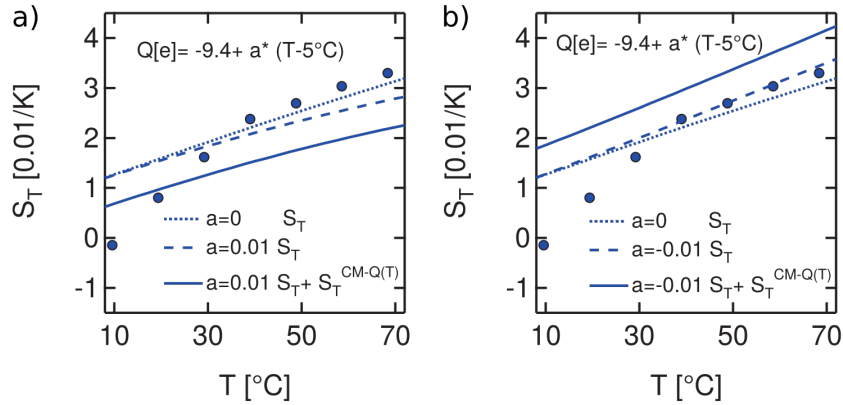
Figure 25: Effects of a temperature dependent charge shown for a DNA 22-mer. Even slight changes of charge result in large effects on S_T (eq. 28). Here, the charge only changes linearly about $|0.6e|$ over the temperature range, but S_T varies enormous. a) For the parameter $a = 0.01$, which is connected to the charge by eq. 27, S_T decreases since the absolute value of charge decreases. The changed S_T without the additional contribution from eq. 28 is also presented and deviates only slightly from the treatment with constant charge. b) For $a = -0.01$, the absolute charge for DNA increases and so does S_T. Nonlinear effects in charge could might explain the deviations of the theoretical model to the measured S_T in the low temperature range.

4.6   Finite element simulations on Capacitor Model

The capacitor model is based on a linearized Poisson-Boltzmann equation [48]. In the following, it was extended to a more realistic setting of the fluxes by electric field and concentration gradients directly interacting by a finite element simulation (Nernst-Planck equation). Therefore two simulations in COM-SOL Multiphysics 4.4 were performed, one which calculates S_T with Debye length on behalf of the changing energy stored inside a capacitor in a thermal gradient, the other one based on the assumption that the S_T can be calculated by the entropy of a system.

4.6.1   Capacitor model derived by electric potential

The following model was set up to test whether the capacitor model is also true for non-linearized Poisson-Boltzmann equation. Two fixed spheres were placed in the center of a cylinder at radial symmetry (Fig. 26a). The properties of the spheres were chosen according to a DNA 22-mer with diameter 4.02 nm and typical homogeneous effective surface charge of $\frac{-11e}{4\pi r^2}$ (Q = -11). To avoid an interference of the ion layers they were separated by 380 nm distance and the surrounding box was chosen to be 760 nm x 190 nm.

Furthermore, electrostatics were applied to the system together with diffusion of potassium and chloride ions at various concentrations from 1 mM to 500 mM. Moreover, a temperature gradient is applied in the z-direction of 0.01 K. Permittivity and viscosity are assumed to be temperature dependent. The base temperature was set to 25 °C.

Since the ions are now free to assemble as governed by electrostatic interaction, they build ionic layers around the charged particles. The resulting electrostatic potential decreases faster to 1/e than predicted by Poisson-Boltzmann (Fig. 26b). For 10 mM KCl this is the case after 1.3 nm instead of 3 nm as predicted by the Debye model. To some extend this may be caused by simplifications, such as neglected size of ions and their influence on static permittivity [109].

Now the Soret coefficient is calculated by the energy difference between the energy stored inside the two capacitors: $S_T = -\frac{1}{kT}\frac{dW}{dT}$. The electrostatic energy stored within the capacitor is calculated by $W = \frac{Q \cdot V|_{surface}}{2}$. The resulting S_T follows a similar trend as predicted by the analytical model with linearized Poisson-Boltzmann term (Fig. 26c). It is slightly lower than the predictions of the analytical model, even without the $1/T$-Term and constant density over temperature, which are both not incorporated into the simulation. Implementation of the finite size of the ions and $\varepsilon\left(c_{salt}\right)$ would be further optional improvements. Nevertheless, this more realistic simulation yields remarkably similar results to the analytical model.
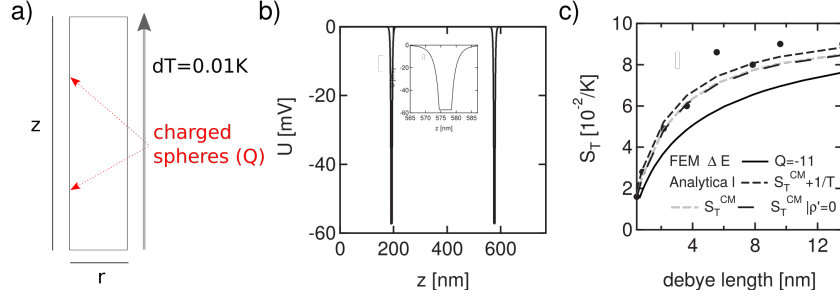
Figure 26: Explicit calculation of the capacitor model with non-linearized Poisson-Boltzmann term. a) Two spheres are placed inside a box with electrostatics present and salt ions of variable concentrations. A temperature gradient of 0.01 K is applied along the z-direction. b) The potential around the spheres decays very rapidly, even faster to 1/e than predicted by the Debye-Hückel model. Here simulation at 10 mM KCl along the z-axis is presented. In the inset, it can be seen that the potential decreased to 1/e after 1.3 nm instead of the expected 3 nm after Debye-Hückel model. c) The calculated S_T, which is evaluated by the difference in potential energy of the spheres, shows the typical increase with Debye length. The analytical solution for the capacitor model for a charge of $-11e$ is in good agreement with the simulation with no linearized Poisson Boltzmann term. Furthermore, it is shown that the 1/T term and the dependency of the density on temperature that are neglected in the numerical simulation bring the analytical solution closer to the numerical solution.

4.6.2   Soret coefficient derived by entropy of the electrolyte

The idea that the Soret coefficient can also be accessed by the entropy S of the solute in an electrolyte solution, was pioneered by Eastman [47, 52] and now could be written as: $S_T = -S/kT$

The entropy of the ions in the solution can be calculated by their densities [110] :

$$S = -k_B \cdot N_A \int dV \cdot \left(c_p \cdot log\left(\frac{c_p}{c_S} \right) + c_n \cdot log\left(\frac{c_n}{c_S} \right) \right)$$

For a univalent salt, c_p and c_n are the concentrations for the positively and negatively charged ions and c_s gives mean salt concentration. Thus, the Soret coefficient can be calculated by the entropy of the solvent shell around a molecule:

$$S_T = \int dV \cdot \left(c_p \cdot log\left(\frac{c_p}{c_S} \right) + c_n \cdot log\left(\frac{c_n}{c_S} \right) \right) \frac{N_A}{T} \tag{29}$$

This was tested in an almost identical setting as above by finite element simulation (Fig. 27a). For charge neutrality, two spheres of opposite charge were placed in an electrolyte solution with uniform temperature of 25 °C. That means no temperature gradient is present. The entropy of the ions in the solvent around a charged sphere was calculated according to eq. 29 by integrating over a volume of a cylinder built around the negatively charged sphere (radius and length are 50nm). It turned out that the result for a sphere with opposite charge would be identical as predicted by the capacitor model ($\sim Q^2$).

The concentration of ions that assemble around the charged spheres can be read out (Fig. 27b). It

can be seen that already at small distances, the concentration is in equilibrium again.

When calculating S_T from the entropy, it is found that the shape is close to the analytical model, but the magnitude of S_T is too low for Q = -11 e. Interestingly, the application of the bare charge of DNA (without condensation) Q = -22 e leads to a reasonable behavior. The slight decrease at very high Debye length has also been found for some DNA molecules [8]. The use of bare charge is logical, since also the adsorbed charges play a role in the picture of entropy around the molecule.

Nevertheless, the shape over Debye length is slightly deviating. Perhaps this is due to the simplified model, where the ions are infinitely small and the change of dielectric constant with respect to ion concentration is neglected [104, 109]. These effects might result in changes of the spatial distribution and by that of the entropy and S_T.
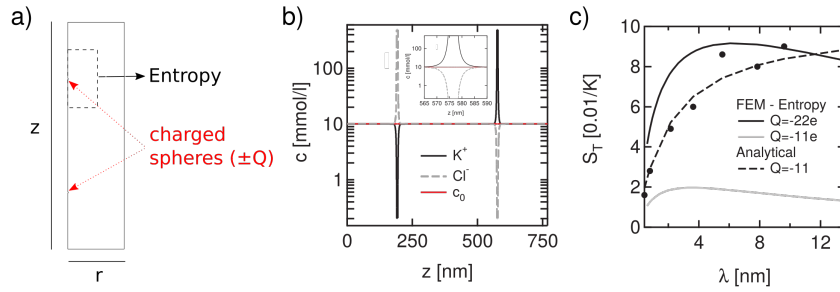
Figure 27: Soret coefficient calculated from the entropy around a charged particle. a) A finite element simulation of two spheres in a box was performed. They were charged oppositely for overall charge neutrality at constant temperature of 25 °C. From the concentration of ions around the charged molecule (indicated by the box) the entropy and the S_T can be calculated via eq. 29. b) The ion concentrations around the molecules of potassium and chloride show an increase or decrease in concentration around the spheres. In the inset, the simulation result for the concentration along the z-axis at 10 mM KCl is shown. c) The obtained S_T for this simplified DNA 22-mer is in good agreement with the analytical Debye theory (eq. 22), when a bare charge of -22 e instead of -11 e is applied. Since for the entropy also the adsorbed ions play a role, it is plausible that the simulation only works for the bare charge of the DNA molecule.

4.7   Thermophoresis of complex macromolecules

In this section, the thermophoresis of complex polymers is presented.

First, the phase transition of an uncharged copolymer is shown where thermophoresis allows the determination of cloud point at low volume format. The presented data also suggests, that nonionic S_T is very low and the hydrophobic backbone plays a major role. The connected publication can be found in the appendix [23].

Second, the thermophoretic properties of disease related α-synuclein proteins are investigated in its monomeric, oligomeric and fibrillar form. Here radius and charge were accessed independently by various other techniques, as FCS, AFM and free flow electrophoresis. The determined Soret coefficients over salt concentration and temperature are in good agreement to the theoretical model based on the charge effects. More related information can be found in the attached article [84].

### 4.7.1   Phase transition of uncharged branched copolymers

So far only thermophoresis of polymers at good solvent conditions was investigated. In the following, special polymers, that collapse at a certain temperature (theta temperature) are investigated with respect to thermophoresis. This feature is interesting for biotechnological applications, as for example drug delivery [111]. Here an OligoEthyleneGlycole methyl ether methacrylate (pOEG) copolymer of 100kDa was studied that carries no net charge. This polymer changes the transition temperature according to salt concentration.

It has been found, that the Soret coefficient decreases with the temperature for the coiled conformation at low temperature (Fig. 28). At the theta temperature, the S_T increases. At high temperatures, the collapsed polymers begin to agglomerate and the S_T decreases again with temperature. In accordance to the findings on the nonionic PEG-polymer, the decrease of S_T with temperature is plausible for the pOEG copolymers (chapter 4.2). The increase of S_T around the transition can be understood in a change of the radius according to eq. 11. Further agglomeration makes it hard to differ whether the S_T after transition is related to the typical nonionic property or ongoing agglomeration. Since these measurements were performed with the photomultiplier to gain insight into the transition temperature of pOEG copolymers at nanomolar dilute condition, some errors in S_T might also occur because of spatial bleaching and rather short detection time span.

The S_T of pOEG copolymer is an order of magnitude smaller than the one of PEG 20000 at comparable size. This is remarkable, since PEG of 20kD has around the same radius of hydration as the non-collapsed branched OEG copolymer. This indicates that the hydrophobic interaction of the backbone has a large impact on the thermophoresis of the pOEG polymer.

Another interesting observation can be drawn, when comparing the studied pOEG copolymer to PNIPAM polymers[112, 113]. There it was found that for the linear PNIPAM polymer, D_T undergoes a huge drop [112] and S_T increases linearly with temperature for the PNIPAM microgel [113]. Since these polymers presumably carry charges, whereas pOEG is purely uncharged, the large Soret coefficient and

different behavior compared to pOEG are attributed to complex changes in the ionic shell.
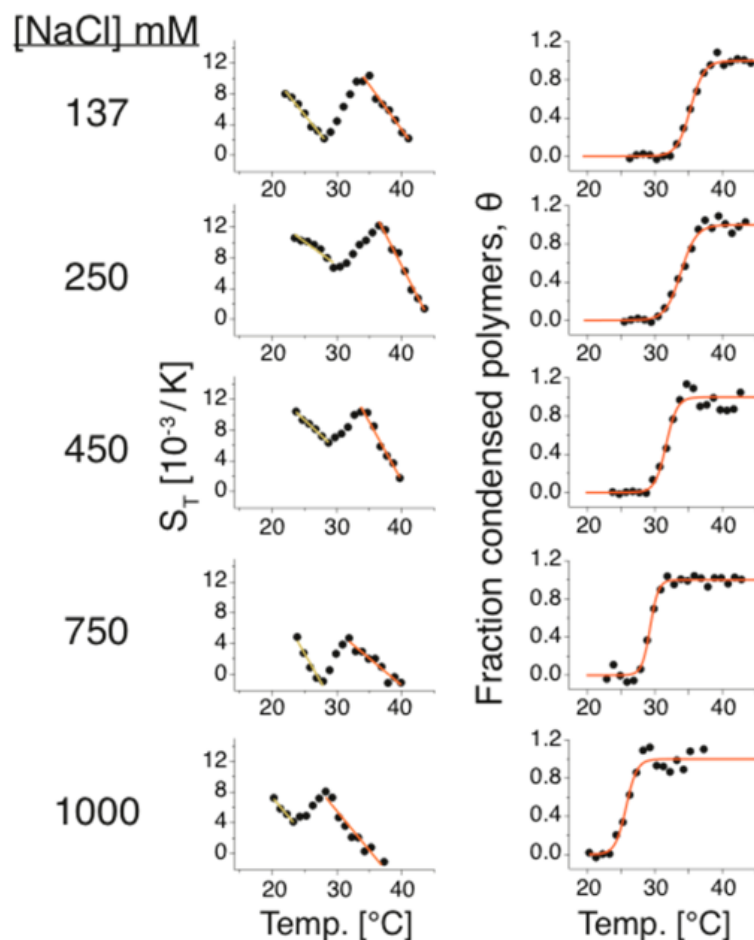
Figure 28: Thermophoresis of 100 kDa OligoEthyleneGlycole (OEG) methyl ether methacrylate copolymer was investigated at variable salt concentrations. The S_T of this uncharged branched copolymer (shown on the left) is very low compared to charged PNIPAM [113]. As found for nonionic PEG, S_T of uncharged coiled pOEG copolymer decreases with temperature at low base temperatures. When the polymer collapses, S_T increases in accordance to eq. 11. Afterwards the polymers begin to agglomerate with temperature and S_T decreases again with temperature. These Soret coefficients obtained at variable salt concentrations can be transformed to determine the fraction of condensed polymers and the transition temperature at which the polymers collapse (shown on the right). Reprinted with permission from [23]. Copyright 2014 American Chemical Society.

The measurements of OEG copolymer allow to determine the transition temperature after the correction of base temperature by $\Delta T/2$ according to chapter 3.4.3. The thermophoresis based assessment at low volume and diluted condition is in good agreement with the traditional cloud point extinction spectrophotometry (Table 29). Moreover, the determination of the transition temperature by the Soret coefficient needs much less polymer and is compatible with the native biological environment.

[NaCl] (mM)	θ midpoint (°C)	Abs. cloud point (°C)
137	35.3 ± 0.34	35.4 ± 0.3
250	33.8 ± 1.89	33.6 ± 0.3
450	31.6 ± 0.15	30.9 ± 0.3
750	29.3 ± 0.46	26.9 ± 0.3
1000	25.7 ± 1.34	25.7 ± 0.3

[a]The errors for θ indicate ± one standard deviation of the midpoint fit

Figure 29: Transition temperature determined with cloud point measurement is in good agreement to the thermophoresis measurements. Advantages of thermophoresis to the conventional method are the low volume and low concentration requirements joined with the compatibility to native biological environment. Reprinted with permission from [23]. Copyright 2014 American Chemical Society.

4.7.2 Quantitative predictions of the Soret coefficient of α-synuclein

Thermophoresis of proteins is interesting in terms of biological and disease related research [114]. But although microscale thermophoresis (MST) is a powerful tool to detect binding of proteins in native environment by change of thermophoretic depletion [114], the thermophoresis of protein polymers is not yet understood.

Here a study on thermophoresis of α-synuclein is presented. This class of proteins supports the interesting feature to study several sub-species which differ in size and charge. Since this protein is related to Parkinson's disease, the study of assembly and development of treatments is accompanied by huge scientific interest [115]. The development of drugs also requires high throughput screening techniques over a large set of binding partners. Here thermophoresis of proteins is investigated in spite of the current model (eq. 10). Also in view onto the nonionic contribution proteins are presumed to reveal novel findings on hydrophilic and hydrophobic effects.

It is shown, that the S_T can be predicted by the electrostatic properties of the proteins and that the change of the ionic environment can lead to a change of S_T according to the current model. The monomeric, oligomeric and fibrillar α-synuclein molecules differ in their size and also electrophoretic mobility as determined by FCS and free flow electrophoresis (see Table 2 and Reference[84]). The radii of monomers and oligomers are almost differing by a factor of 3 from 2.8nm to 7.5nm. Nevertheless charges in free flow electrophoresis only differ by a factor of 5 with -10.9 e and -50.4 e albeit a typical oligomer is made up by 30 monomers [116]. Fibrils are highly ordered protein structures which were determined to a radius of 4 nm and a length of 200 nm. Electrophoresis measurements suggest a charge of -(200-300) e [84]. These elongated objects also yield an interesting test of the changed capacitor for rod-like molecules (eq. 21 and 23). Here the S_T of Tris was assumed to be the same as sodium. This is a good approximation as $S_T (Tris)$ was determined to 0.0031/K based on a fit based on changing Seebeck effect by changing salt concentration [84].
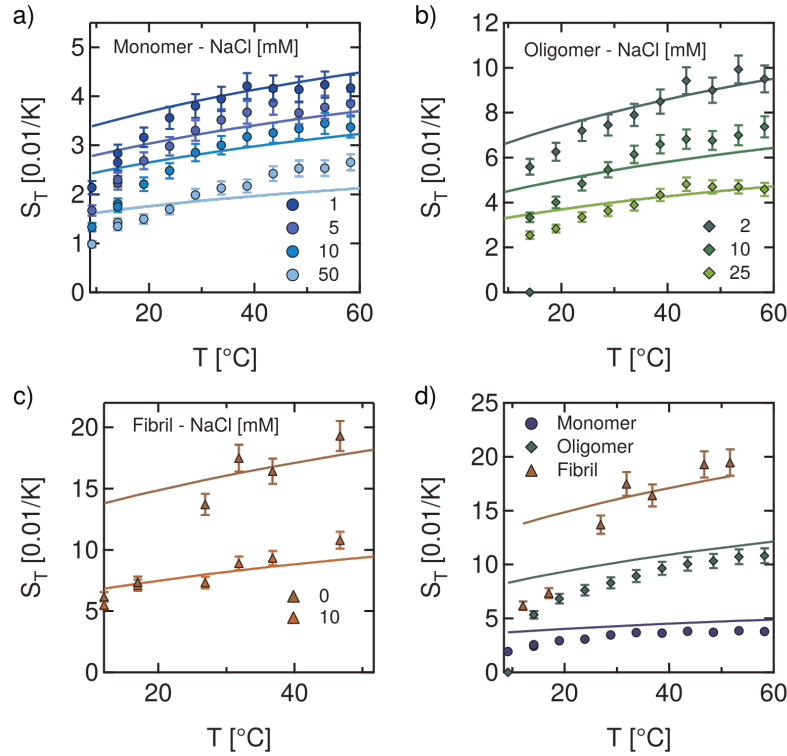
Figure 30: Thermophoresis of α-synuclein protein at various temperatures and ionic strengths.
a) The Soret coefficients of monomers b) oligomers and c) fibrils can be described by the full model of thermophoresis without other nonionic contributions else than 1/T. The decrease of S_T with ionic strength is mainly on behalf of the capacitor model contributions. The temperature dependency is described to a good extend by diffusiophoresis alone. Due to the underlying Soret coefficients of sodium and chloride in our model (Fig. 6), the electric field is constant with temperature and temperature dependency of the Seebeck effect plays a negligible role. d) The different α-synuclein species largely differ in Soret coefficient according to their size and charge in 1 mM Tris *pH* 7.4. In contrast to the attached article [84], thermophoresis of a α-synuclein is described by the full thermophoretic model (eq. 10) and no nonionic effect other than 1/T is needed ($\Delta_T = a = 0$ according to eq. 11). The predictions are in good agreement, although the charge determined by thermophoresis and electrophoresis differ by a factor of 1/2, which is open to discuss.

The Soret coefficient of monomers, oligomers and fibrils depends on the salt concentration according to the current model, dominated by the capacitor part (Fig. 30). Furthermore it is now possible to associate the increase of S_T with temperature directly to the temperature dependence of diffusiophoresis as shown in chapter 4.4. Note that electrophoresis in the case of Na and Cl gives a constant offset over temperature. In case of the fibrillar structures the S_T at 10 mM is compared to the case of 1mM Tris. The Soret coefficient of monomers, oligomers and fibrils also differs largely due to their different size and charge (Fig. 30d). Here no additional nonionic contribution else then 1/T was assumed, that means $\Delta_T = a = 0$ according to eq. 11.

The charges which were obtained by the best fit of the thermophoretic model are in a reasonable

range. For monomers minimal deviation is achieved by -6.6 e, for oligomers -22.1 e. For Fibrils the fit according to the elongated capacitor model gives -78 e (eq. 21 and eq. 23).

Still, the charges obtained by electrophoresis and thermophoresis differ by a factor of 2 and the temperature dependency is not yet fully matched (Fig. 30). If this is on behalf of the still simplified models, an additional unknown S_T^{Ni} or uncertainties in the S_T of salts is not yet clear. Nevertheless the predictions of the model are in good agreement to experiments without any empirical nonionic contribution other than 1/T.
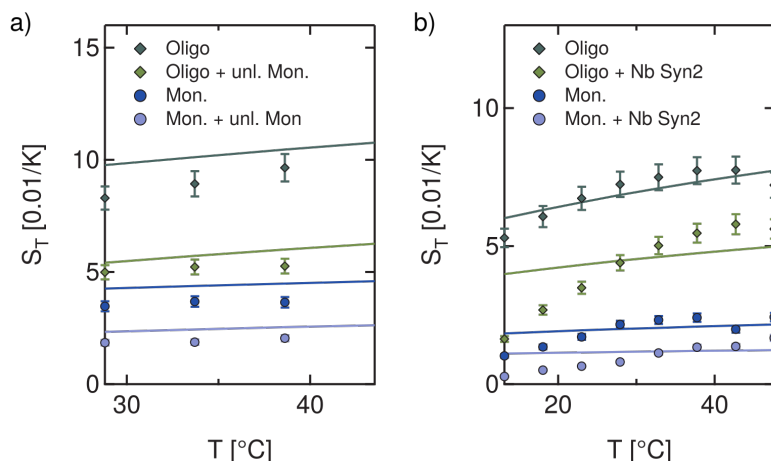
Figure 31: Electrostatic changes of the environment alter the S_T of α-synuclein. a) In accordance to the Seebeck effect, the addition of 70 μM unlabeled monomers leads to a decrease of the S_T of monomers and oligomers. b) The binding of the charged nanobody Nb-Syn2 [117] also results in lower S_T due to the reduced charge of the monomers and oligomers. The fit suggests binding of one nanobody to the monomer and three nanobodies to the oligomer.

Additionally the influence of changes in the electrostatic environment around α-synuclein was studied (Fig. 31). The effect of additional 70 μM unlabeled monomeric species with $S_T (unl. Monomer) = \frac{1}{T} + S_T^{CM} = 0.023/K$ according to the Seebeck effect results in a decrease of S_T (Fig. 31a). One reason for the experimentally lower S_T to the one predicted by the model might rely on the fact that $S_T^{Tris^+}$ here was set to $S_T^{Na^+}$, whereas it is presumably slightly lower [84].

Furthermore, the effects of binding of nanobody Nb-Syn2 [117] was studied over a large temperature range (Fig. 31b). The nanobody is assumed to inhere a charge of +1.5 e at this *pH* [84]. As reflected by the change of charge from -4.7 e to -3.1 e for the monomers and -20.2 e to -15.4 e oligomers, the thermophoresis curves suggest the binding of one nanobody to the monomer and three nanobodies to the oligomer. The change of S_T could also be used to obtain the kD to 124 nM for monomers and 234 nM for the oligomers by microscale thermophoresis (see attached article [84]). Interestingly also for binding of uncharged epigallocatechin gallate a change of the S_T can be found for oligomers and fibrils (see attached article [84]). Since these complexes are not thought to inhere a charge, possible explanations might be found in a change of size or hydrophobicity and the connected nonionic contribution.

These measurements show that the presented model explains the behavior of complex molecules over salt concentration and temperature qualitatively and quantitatively.

5   Conclusions

In this work, a novel theoretical model of thermophoresis has been developed, which combines contributions from non-equilibrium and equilibrium effects. It could be successfully applied to a wide collection of polymers and predicts the different thermophoretic behavior of charged and uncharged polymers with respect to Debye length and base temperature (chapter 4.1).

Uncharged PEG and PNA molecules are not affected by ionic strength (chapter 4.2), whereas charged DNA molecules show a characteristic increase with Debye length in agreement with the capacitor model (chapter 4.4).

The increase of the Soret coefficient with the base temperature, which was formerly attributed to nonionic effects [17], could now be traced back to a charge effect, namely diffusiophoresis (chapter 4.4). This effect scales linearly with the S_T of salt, which in turn increases with temperature (see appendix 7.3). On the other hand, only decreasing slopes of S_T with respect to temperature were observed for uncharged polymers (chapter 4.2). The transition between these two states was monitored by tuning the charge of PNA polymers with *pH* (chapter 4.3).

Moreover, alternative theoretical settings were discussed (chapter 4.5). It was shown that the temperature dependency of the S_T cannot be explained by electrophoresis, since oppositely charged polymers in similar electrolyte solutions both show increasing S_T (chapter 4.5.1). Furthermore, it was concluded that explicit forces alone are unable to explain thermophoresis of DNA (chapter 4.5.2). The incorporation of the hydron and hydroxide in the Debye layer would result in large discrepancy based on diffusiophoresis (chapter 4.5.3). Additional effects of water polarization (chapter 4.5.4) and temperature dependency of the charge (chapter 4.5.5) were analytically investigated and were found to be capable to result in significant contributions. It is not excluded that they are responsible for small discrepancies between the so far developed model and the experiments.

Furthermore, finite element simulations successfully confirmed that the capacitor model still holds if the Poisson-Boltzmann term is not linearized (chapter 4.6). The S_T was additionally accessed by the entropy of the ionic species around the charged molecules and proven to be in good agreement with the theory.

Thermophoresis was then applied to a set of more complex macromolecules (chapter 4.7). It was shown that the phase transition from coil to globule for smart pOEG copolymers can be detected by thermophoresis in low volume and dilute (nM) format (chapter 4.7.1).

Moreover, thermophoresis of α-synuclein proteins in monomeric, oligomeric and fibrillar forms was studied (chapter 4.7.2). Although they vary widely over size and charge, the dependencies of S_T on ionic strength and temperature matched the theoretical model without the application of an additional S_T^{NI} term other than 1/T. This leads to the conclusion that changes in the hydration shell play a minor role for the thermophoresis of charged polymers.

6   Outlook

Although the developed model predicts the thermophoresis of charged polymers to a large extend, further investigation would be desirable to explain deviations at low base temperature and the discrepancy of charge determined by thermophoresis and electrophoresis (see attached article [84]).

One important step for a more crucial understanding would be gained by more precise predictions of the Seebeck effect and diffusiophoresis. The reinvestigation of thermophoresis of the electrolyte would help to obtain the full picture of Soret coefficients of single salt ions with temperature and concentration. So far, the complete parameter space can only be approximated by single data sets. Techniques as Terahertz spectroscopy [118] or molecular dynamics simulations [66] might access the single ion Soret coefficient indirectly by entropy of the surrounding water molecules or directly by determination of the change in concentration.

Moreover, it would be highly interesting to investigate the special position of hydron and hydroxide for the thermophoresis of polymers, since they only seem to interact via the Seebeck effect, but not by the Debye layer.

Further refinement of the underlying model can be achieved by including the concentration dependency of permittivity, viscosity and density (~10% [104]).

Additional thermophoretic effects are still open to investigate as the direct experimental assessment of the polarization of water in thermal gradients or the expansion of the theory to diffusiophoresis with no net charge [119–121]. Also, thermophoresis of nonionic polymers yet lacks the full microscopic understanding, as e.g. how the solvent shell or hydrogen bridges are changed by temperature [57].

On the experimental side, very accurately characterized samples in terms of size and charge, as for example Gold nanoparticles [122, 123] , could help to settle the dispute over non-equilibrium and equilibrium contributions.

The full understanding of this effect can improve established [114] but also novel applications as e.g. in the fields of microfluidics [124] or laser driven PCR (GNA Biosolutions and see appendix 7.1.2). Novel applications of thermophoresis are imaginable in the field of polymer phase transitions, where polymers that do not agglomerate after coil to globule transition are invisible to classical photo spectrometry.

Another special case is presented by thermophoresis in 2D systems, like supported lipid bilayers. Apart from basic research, thermophoresis of lipids can result in interesting applications in binding assays (see appendix 7.1.1).

7 Appendix

7.1 Assorted Projects

7.1.1 Thermophoresis of lipids in a supported lipid bilayer

Introduction   Supported lipid bilayers (SLB) represent an interesting arrangement of molecules [125, 126]. Lipid molecules can form 2D films of fatty acids on a support by self assembly (Fig. 32a). Due to their high density, diffusion is rather low [127] compared to molecules of the same size in free solution. These 2D lipid landscapes and the molecules attached to it are easily accessible by various methods as AFM, surface acoustic waves [128], electric fields [129–131]. Due to this interesting applications as 2D-electrophoretic devices or flatland factories [128, 132, 133] may emerge. Lipid membranes are also interesting physical model systems for phase separation [134] and artificial minimal systems [135, 136]

So far thermophoresis has only been investigated for lipid vesicles but not on supported lipid bilayers. Yet first theoretical considerations evolved for lipid membranes in thermal gradients [137]. An experimental realization and first results for thermophoresis of lipids in Supported Lipid Bilayers will be presented in the following.

Materials and Methods   For the experiments small unilamellar vesicles (SUVs) of 1% NBD-DOPE (1,2-dioleoyl-sn-glycero-3-phosphoethanolamine-N-(7-nitro-2-1,3-benzoxadiazol-4-yl (ammonium salt)), Avanti Polar lipids, Alabaster, USA) and 99% DOPC (1,2-dioleoyl-sn-glycero-3-phosphocholine, Avanti Polar lipids) were prepared according to reference [132]. They were soaked into the capillary (50 µm x 500 µm capillary) by a microsyringe (ILS) connected with a PE-tube. Afterwards they were flushed with MilliQ for 5 times. The supported lipid bilayer that had formed could be observed on the upper and lower inner rim of the Capillary. Then the desired salt species (KCl, NaCl and KF) buffered in 0.5 mM Tris *pH* 7.6 was flushed in at concentrations of 1, 10, 100, 500 mM salt. Afterwards the buffer was cleaned by milliQ again and the next electrolyte solution was flushed in.

For the experiments laser heating was performed from the bottom through a silicon wafer with an infrared laser. The base temperature was set to 23 °C and the temperature gradient had a peak of 8.55 °C, determined by BCECF beforehand.
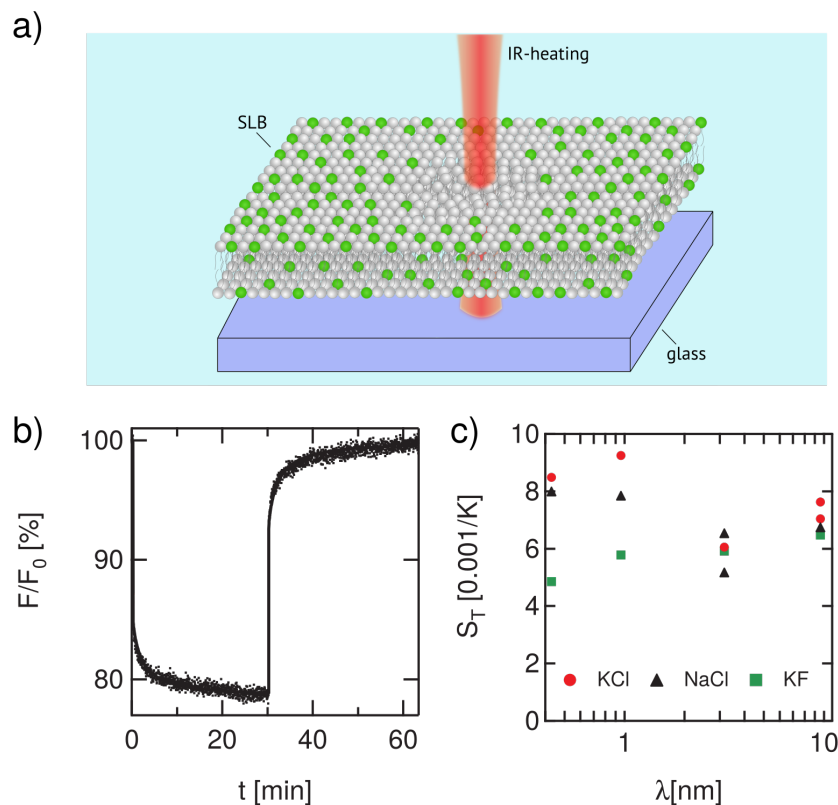
Figure 32: Thermophoresis of lipids. a) Cartoon of a lipid bilayer which is heated by an infrared laser. The membrane, which consists of binary mixture of labeled and unlabeled molecules, is demixing in the thermal gradient. b) Thermophoretic time trace of fluorescence of NBD-DOPE molecules in a supported bilayer of DOPC at 100mM NaCl. The extracted diffusion coefficient of $3.8 \frac{\mu m^2}{s}$ is in good agreement with literature [127]. The thermal diffusion coefficient of $\sim 0.03 \frac{\mu m^2}{s\,K}$ is low compared to PEG polymers with $\sim 5 \frac{\mu m^2}{s\,K}$ (see chapter 4.2). c) S_T of the examined lipid is rather insensitive towards salt concentration and species. Calculations suggest that the lipids demix in the hot zone.

Results and discussion The typical thermophoretic behavior (compare Fig. 12) is also found for SLB's, starting with temperature response of the dye, the slow onset of thermal diffusion and according behavior when the laser is set off. (Fig. 32b). The Soret coefficient is rather low with ~0.01/K for all salt species (Fig. 32c). It is observed to be slightly lower for KF. Moreover S_T stays constant for the various salt concentrations. since there is only single negative charge assumed, no major changes for the capacitor model are expected.

The obtained diffusion coefficient (see Binding evaluator chapter 3.5) of the NBD-DHPE molecules within the SLB at 100mM NaCl gives a typical diffusion coefficients of 3.8 µm²/s. For comparison FRAP measurements of NBD-DHPE in POPC membranes show diffusion coefficients of comparable size (3.7 µm²/s) at 20°C) [127]. Thermophoresis thus can additionally be used as a novel way to asses diffusion coefficient, which is conventionally measured by Fluorescence Recovery After Photobleaching

[138–140] or Fluorescence Correlation Spectroscopy [141].

The thermal diffusion coefficient is very low 0.027 μm²/s/K compared to PEG with ~5 μm²/s/K (see Fig. 16). If this can be traced back to the concentrated regime, the 2D thermal diffusion or the almost equal size of the lipids has still to be theoretically and experimentally investigated.

One can also argue whether the depletion of labeled NBD-lipids is caused by expansion of the membrane. The calculation suggests that the change in the area per head is smaller than the perceived signal. For a typical expansivity of 0.0029/K for a DOPC membrane[142] the fluorescence should decrease by 2.4%. In thermophoresis a depletion of ~5% and more measured in the center. That means on the other side that the ratio of unlabeled to labeled lipids changes in the hot zone and a demixing occurs.

Outlook: It has been shown that there is thermal diffusion ongoing in SLBs which is most likely resulting in a demixing and not just expansion of the whole bilayer system. This might also have high potential for binding affinities between small attached molecules and also is a more interesting natural environment for pharmaceutical conditions, since the a large proportion of medications developed targets membrane proteins.

It also would be interesting to test whether the binding of two proteins can also be monitored indirectly, quasi "label free", by monitoring a change of S_T of the lipids. There is also potential to combine this binding approach with microfluidic flatland factories binding assays.

7.1.2 Thermophoresis of gold nanoparticles coated with DNA

Gold nanoparticles have great features because of their plasmonic properties. They also have proven to be useful for rapid cycling (GNA biosolutions, Martinsried, Germany). Here the thermophoretic properties of gold nanoparticles of 60 μm diameter which were chemically modified with DNA linkers were studied (GNA biosolutions):

$S235ECLNPR5C + 2 ** A35 SP9 60 5'ThiolAAAAAAAAAAAAAAAAAAAAAAAAAAAAAAAAAAAA$
$/iSp9//iSp9/GGTTCAGGCACAGCACATCAA$

Here complementary DNA-sequences, labeled with 6-HEX, were annealed to the macromolecule at a ratio of 187:1 with a final concentration of 160 pM nanoparticles and 30 nM attached DNA of the sequence: 5'-Hex–TAGTGTGCTGTGCCTGAAC. A sketch is presented in Fig. 33a.

These particles were brought to the following Buffer conditions: a) 100 mM NaCl, 4 mM Phosphate buffer- 0.8 mM EDTA and 0.08% Tween b) 0.5 mM Tris *pH* 7.2 c) 0.5 mM Tris *pH* 7.2 and 20 mM KCl. Therefore the buffer was exchanged by centrifugation of the nanoparticles and following replacement of the excess solvent by buffer. This step was performed for 10 times. Due to the slow diffusion of these large objects, the thermophoresis was monitored at a frame rate of 0.1 Hz for 1940 s to minimize minimal bleaching. Furthermore temperature jump was neglected in analysis since 6-Hex is very insensitive towards temperature. Additionally to the thermophoretic measurements, the charge and radius of these complex molecules were determined by a Zetasizer Nano S (Malvern Instruments, Malvern, UK).

Results: The radius of the construct was determined at 0.5 mM Tris *pH* 7.2 and 20 mM KCl to 52 nm. The value is in a reasonable range for 30 nm Gold particle and 20 nm for DNA with spacers.

At 100 mM NaCl, 4 mM Phosphate buffer- 0.8 mM EDTA and 0.08 % Tween the Soret coefficient of the construct increases with temperature until the DNA detaches (Fig. 33a). There a peak of the S_T occurs, perhaps because of the change of charge after detachment at around 60 °C. Note that an overlay of bound and unbound DNA is monitored then. Afterwards the S_T of DNA decreases to a small value, presumably because the DNA is monitored instead of the cold nanoparticle constructs.

For a more detailed investigation the particles were investigated at 0.5 mM Tris *pH* 7.2 with or without the addition of 20 mM KCl. Interestingly the S_T at low salt is lower in contrary to the predictions of the capacitor model (Fig. 33b). The charges obtained by the thermophoretic model are -232 e for 0.5 mM Tris and -640 e for 0.5 mM Tris with 20 mM KCl and the Nonionic parameters: $\Delta_T = 0 \frac{N}{K}$ and $a = 8.3 \cdot 10^{-23} \frac{m^2 kg}{s^2 K}$.
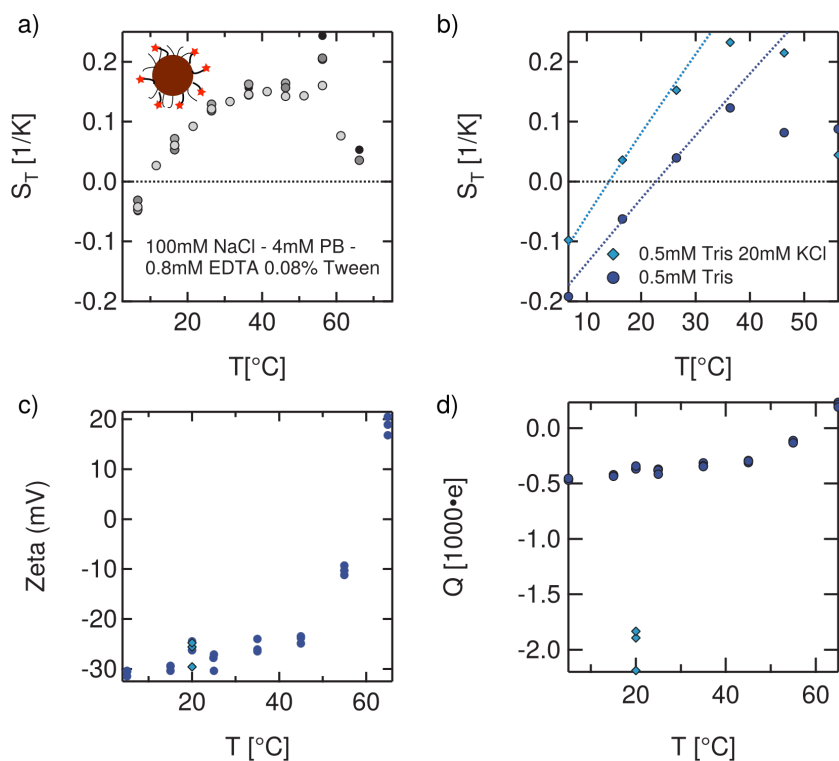
Figure 33: Thermophoresis of gold nanoparticles with conjugated, labeled DNA. a) The Soret coefficient increases with temperature for these macromolecules. For higher temperatures the DNA detaches and the S_T of the free, labeled DNA polymers is measured as a secondary effect. Multiple different measurements show the reproducibility. A cartoon of the macromolecule is shown in the inset. b) The measurements on salt concentration first seems to contradict the capacitor model, since the S_T at low salt is higher. The predictions of the model can only be brought into accordance by alternating charges. Here, they are set to -232 e in 0.5 mM Tris and -640 e in 0.5 mM Tris with 20mM KCl. c) The zeta potential for these two buffer conditions interestingly stays the same. d) This, consequently, would also suggest different charges for the different buffer conditions. This agrees with the finding for thermophoresis, although the charges differ by a factor of around two, similar to the case of α-synuclein (chapter 4.7.2).

Interestingly, the change of charge at different KCl concentrations is also found in the zetasizer. First of all the detachment of DNA can also be monitored over temperature, second the zeta potential stays the same for 20 mM KCl with 0.5 mM Tris (*pH* 7.2) and 0.5 mM Tris (*pH* 7.2) at 20 °C (Fig. 33c). This suggests that the charge is more negative at high salt concentration (Fig. 33d), perhaps because of more charge condensation of Cl^- onto the highly positively charged gold nanoparticles. This explains higher S_T at higher salt concentration, which seems contradictory. Nevertheless, there is a deviation between the charge computed by Soret effect to the charge from zeta sizer. Perhaps this is also due to the simplified treatment of these highly charged complex macromolecules.

7.2   Thermophoresis of PEG molecules in extreme solvents (preliminary)

Additional experiments on the S_T of PEG on extreme changes of the solvent were performed (Fig. 34). Since these measurements were experimentally challenging, large errors are connected to the S_T values. Nevertheless, they are shown for the sake of completeness, since at least some qualitative results can be drawn out of them.

In contrast to the theory the S_T of PEG 20000 is slightly changing with pH (Fig. 34a). It is also found that the measured S_T is lower compared to Fig. 16a. These findings are most likely caused by errors due to non-automatized focusing at the time of acquisition. Additional errors might stem from a wavy stage [81] or changes of refractive index with temperature and *pH*.

Since PEG is highly soluble in a variety of solvents, additional measurements in Ethanol (EtOH) and Methyl Ethyl Ketone (MEK) were performed (Fig. 34b). The solvent properties differ much for these liquids, starting with a high static permittivity of H_2O compared to MEK and EtOH. MEK as organic solvent has on the other side no hydroxyl group, thus it does not perform autoprotolysis, has a low dipole moment and no ability to perform hydrogen bonds. The viscosity of H_2O and EtOH is comparable, while MEK is less viscous [104].
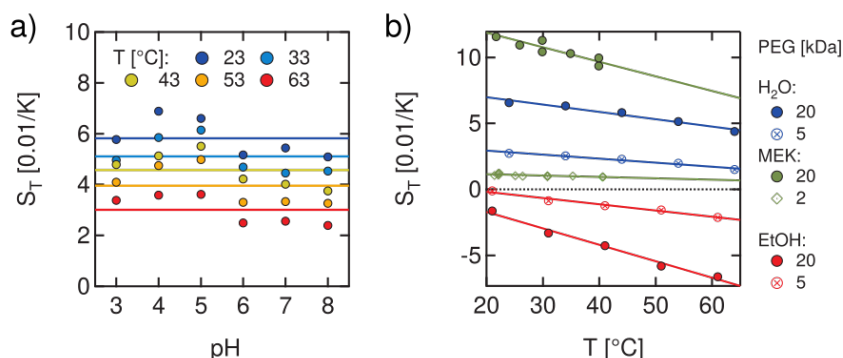
Figure 34: Effect of pH and solvent on the Soret coefficient of PEG (preliminary data). a) S_T of PEG 20000 does not significantly depend on *pH*. Lower S_T compared to the measurements in Fig. 16 are attributed to non-automatized z-focus. b) Preliminary data on the S_T of PEG of different molecular weight in MEK and EtOH compared to H_2O. In MEK the Soret coefficient of PEG is higher, whereas in EtOH even the sign of S_T switches compared to water. This behavior is counterintuitive, since in MEK no hydrogen bonds can be formed. Lines are drawn to guide the eye.

For the measurements of PEG in MEK, indirect heating was applied by a chrome layer (~200 nm) at the bottom of a capillary. The capillary was connected to a microsyringe (ILS, Stützerbach, Germany). For ethanol, the absorption in the infrared was used and a temperature calibration was performed with Cy5-dye in EtOH.

For those measurements, flows to either side of the capillary were observed. Therefore, the maximum depletion or accumulation over the course of time was taken to evaluate S_T, although the concentration distribution of PEG in the thermal gradient might not have been yet at the steady state. The drifts may

result from lower viscosity of these solvents, on the one hand, and leakiness of the capillaries, on the other hand. Also inhomogeneities of the chrome layer might play a role here.

Although $S_T^{MEK}(PEG\ 20000)$ is larger to the S_T in water, it is interesting that the behavior for PEG in MEK is so similar to the one in H_2O. Since these solvents differ drastically in their ability to establish hydrogen bonds. Like in water, S_T of PEG in MEK decreases with temperature. This implies that for the thermophoresis of PEG hydrogen bridges play a minor role in contrast to recent findings [57, 58].

Surprisingly, the behavior of S_T of PEG in EtOH is completely different to the one in water, although the solvent is closer to H_2O than MEK with respect to hydrogen bond formation and viscosity. S_T of PEG in EtOH is negative and also decreases with temperature. This behavior was also observed by Wang and coauthors [13] for small PEG of 2200 g/mol. The negative Soret coefficient for PEG in EtOH [143] is, moreover, expected by a lattice model based on interaction energies [144]. Nevertheless this decrease of S_T with temperature contrasts these predictions.

The effect of different solvents on PEG-molecules is quite puzzling and should be observed in greater detail, starting from precise measurements with no drift. In future investigations, one has to exclude that H_2O gets soaked into MEK by contact with the air, and might thus effect thermophoresis.

7.3 Single Ion Soret coefficients

Due to the lack of detailed data on $S_T^{MX}(c, T)$, the model was set to reasonable values as depicted in Fig. 6. For NaCl and KCl, the model is based on the temperature dependency of the latest measurements of Römer and coauthors [66]. Since the concentration is very high with 500mM [66], the Soret coefficient was scaled by a factor of two to be closer to predictions for the lower concentration range [67, 71] :

$$S_T^{NaCl}(T) = 0.01(1 - e^{-(T-283)/55}) K^{-1} \tag{30}$$

For the Soret coefficients of the sodium $S_T^{Na^+}$ and chloride ions $S_T^{Cl^-}$, the same steepness of S_T over temperature was assumed. Furthermore, the ratio of the Soret coefficients at 25 °C set is according to Takeyama [62] $S_T^{Na^+}(25°C)/S_T^{Cl^-}(25°C) = 6.5$.

By the relation for the sum of ions $S_T^{NaCl} = \frac{1}{2}\left(S_T^{Na^+} + S_T^{Cl^-}\right)$ the single ion Soret coefficients are obtained:

$$S_T^{Cl^-}(T) = S_T^{NaCl}(T) - 0.0017 K^{-1} = S_T^{NaCl}(T) = 0.01(1 - e^{-(T-283)/55}) K^{-1} - 0.0017 K^{-1} \tag{31}$$

$$S_T^{Na^+} = S_T^{NaCl}(T) + 0.0017 K^{-1} = 0.01(1 - e^{-(T-283)/55}) K^{-1} + 0.0017 K^{-1} \tag{32}$$

Following the presented procedure for NaCl, the Soret coefficient of KCl is:

$$S_T^{KCl}(T) = 0.0196(1 - e^{-(T-293)/102}) K^{-1} \tag{33}$$

According to eq. 13, the Soret coefficient of potassium is assigned to

$$S_T^{K^+}(T) = 2 \cdot S_T^{KCl}(T) - S_T^{Cl^-}(T) = 2 \cdot 0.0196(1 - e^{\frac{-(T-293)}{102}}) K^{-1} - 0.01(1 - e^{\frac{-(T-283)}{55}}) K^{-1} + 0.0017 K^{-1} \tag{34}$$

For the Soret coefficients of H^+ and OH^-, the best fits of the theoretical model to the PNA measurements resulted in:

$$S_T^{H^+}(T) = 0.01399 \cdot (1 - e^{\frac{(293-T)}{102}}) K^{-1} + 0.0274911 K^{-1}$$

$$S_T^{OH^-}(T) = -0.00431 \cdot (1 - e^{\frac{(349-T)}{-16}}) K^{-1} + 0.035311 K^{-1}$$

7.4   Equations for the analytical model

In the formulas below, all the values are in SI-units, r is the radius, Q [e] is the charge. They were implemented in a Labview code.

Solvent, constants and general relations:

Constants

$k = 1.3806504E - 23$, $e = 1.602176487E - 19$, $pii = 3.14159265359$, $Na = 6.02214129E + 23$

$Tk = T + 273.15$

Permittivity

$eps = (-6.7121 + 94.545 \cdot exp(-(0.0042005 \cdot T))) \cdot 8.854187817E - 12$

$depsdt = 94.545 \cdot (-0.0042005) \cdot exp(-(0.0042005 \cdot T)) \cdot 8.854187817E - 12$

Density

$rho = (0.99995 + 0.000020207 \cdot T - .0000059174 \cdot T \cdot T + 0.00000001569 \cdot T \cdot T \cdot T) \cdot 1E3$

$drhodt = (0.000020207 - 2 \cdot .0000059174 \cdot T + 3 \cdot 0.00000001569 \cdot T \cdot T) \cdot 1E3$

Viscosity

$eta = 0.00013752 + 0.0010386 \cdot exp(-0.019758 \cdot T) + 0.00061092 \cdot exp(-0.065462 \cdot T)$

Polymer, Ionic shielding

$Ionstrength = 1/2 \cdot rho/997.4 \cdot (0 \cdot cH + cCl + cNa + 0 \cdot cOH + cPNA \cdot Q \cdot Q + CMON \cdot QMON \cdot QMON) \cdot 1E + 3$ (0->H$^+$and OH$^-$ in Debye layer are excluded; last term for experiment on addition of unlabeled monomers)

$debye = sqrt(eps \cdot k \cdot Tk/2/Na/e/e/Ionstrength)$

$D = k \cdot Tk/(6 \cdot pii \cdot eta \cdot r)$

$henry = 1 + 0.5/(1 + 2.5 \cdot debye/r/(1 + 2 \cdot exp(-r/debye)))/(1 + 2.5 \cdot debye/r/(1 + 2 \cdot exp(-r/debye)))/(1 + 2.5 \cdot debye/r/(1 + 2 \cdot exp(-r/debye)))$

$zeta = Q \cdot e/(4 \cdot pii \cdot eps \cdot r \cdot (1 + r/debye))$

$mu = 2/3 \cdot henry \cdot eps/eta \cdot zeta$

special parameters for fibrils: $L = 171E - 9$, $rf = 4E - 9$

Salt ions

$STKCLTHEO = 0.0098 \cdot (1 - exp(-(Tk - 293)/102))$

$STNACLTHEO = 0.005 \cdot (1 - exp(-(Tk - 283)/55))$

$if(NAKselect == 1)STSALT = STNACLTHEO; elseSTSALT = STKCLTHEO$

$STCL = (0.00415 - 0.00599 \cdot exp(-0.018 \cdot T)) \cdot 2$

$STNA = (2 \cdot STSALT - (aa + bb \cdot exp(-dd \cdot T) + ee \cdot (T - cc))) \cdot 2$

$STH = 0.01399 \cdot (1 - exp((293 - T)/102))) + 0.0274911$

$STOH = -0.00431 \cdot (1 - exp((349 - T)/ - 16))) + 0.035311$

Thermophoretic contributions

Capacitor Model

$STCM = e \cdot e \cdot Q \cdot Q / (16 \cdot pii \cdot k \cdot Tk \cdot Tk \cdot eps \cdot debye \cdot (1 + r/(debye)) \cdot (1 + r/(debye))) \cdot (1 - (Tk/rho \cdot drhodt) - (Tk/eps \cdot depsdt) \cdot (1 + 2 \cdot debye/r))$

$STCMROD = (Q \cdot e) \cdot (Q \cdot e) / (k \cdot (Tk \cdot Tk) \cdot 4 \cdot pi \cdot eps \cdot (2 \cdot rf \cdot (rf/debye + 1) + (L - 2 \cdot rf)/ln(debye/rf + 1)) \cdot (2 \cdot rf \cdot (rf/debye + 1) + (L - 2 \cdot rf)/ln(debye/rf + 1))) \cdot (rf \cdot rf/debye + (L - 2 \cdot rf) \cdot debye/rf/(2 \cdot (ln(debye/rf + 1)) \cdot (ln(debye/rf + 1)) \cdot (debye/rf + 1)) + Tk/eps \cdot depsdt \cdot ((L - 2 \cdot rf) \cdot debye/rf/(2 \cdot (ln(debye/rf + 1)) \cdot (ln(debye/rf + 1)) \cdot (debye/rf + 1)) - rf \cdot rf/debye - 2 \cdot rf - (L - 2 \cdot rf)/ln(debye/rf + 1)))$

Seebeck effect

$STSEE = -(k \cdot Tk)/(e \cdot D) \cdot mu \cdot ((cH \cdot STH - cCl \cdot STCL - cOH \cdot STOH + cNa \cdot STNA) + cPNA \cdot Q \cdot STCM + CMON \cdot QMON \cdot STMON)/(cH + cCl + cNa + cOH + cPNA \cdot Q \cdot Q + CMON \cdot QMON \cdot QMON)$

Diffusiophoresis (DP)

$STSALTSUM = 1 \cdot (0 \cdot cH \cdot STH + cCl \cdot STCL + 0 \cdot cOH \cdot STOH + cNa \cdot STNA)/(0 \cdot cH + cCl + cNa + 0 \cdot cOH)$ ($0 \to H^+$ and OH^- in Debye layer are excluded)

$psi = 1 \cdot e \cdot zeta/k/Tk$; $gamma = tanh(psi/4)$

$lb = 1 \cdot e \cdot 1 \cdot e/(4 \cdot pii \cdot eps \cdot k \cdot Tk)$

$Ddp = k \cdot Tk/eta \cdot (-ln(1 - gamma \cdot gamma) + 0 \cdot 0.5 \cdot beta \cdot psi)/(2 \cdot pii \cdot lb)$

$STDP = (1 \cdot Ddp/D) \cdot STSALTSUM$

Diffusiophoresis capacitor model (DP CM)

$DiffuCM = Q \cdot e \cdot Q \cdot e/(16 \cdot pi \cdot eps \cdot k \cdot Tk)/debye/(1 + r/debye)/(1 + r/debye)$

$STDPCM = DiffuCM \cdot STSALTSUM$

$STDiffuCMROD = (Q \cdot e \cdot Q \cdot e \cdot ((2 \cdot rf \cdot rf)/(debye \cdot debye) + (L - 2 \cdot rf)/((ln(debye/rf + 1) \cdot ln(debye/rf + 1)) \cdot (debye/rf + 1) \cdot rf)))/(4 \cdot eps \cdot pii \cdot (2 \cdot rf \cdot (rf/debye + 1) + (L - 2 \cdot rf)/ln(debye/rf + 1)) \cdot (2 \cdot rf \cdot (rf/debye + 1) + (L - 2 \cdot rf)/ln(debye/rf + 1))) \cdot debye/2 \cdot STSALTSUM/k/Tk$

Electrostrictive

$STWUERGER = 6 \cdot pii \cdot r/k/Tk/Tk \cdot eps \cdot zeta \cdot zeta/12 \cdot (1 - Tk/eps \cdot depsdt)$

Nonionic

$STOFF = 1/Tk + koehlA \cdot 6 \cdot pii \cdot r/k/Tk - koehlB/pow(r, alphani) \cdot 6 \cdot pii \cdot r/k/Tk$

References

[1] Tyndall J (1870) *Scientific Addresses* (New Haven, Conn., C.C. Chatfield & Co.).

[2] Ludwig C (1856) Diffusion zwischen ungleich erwärmten Orten gleich zusammengesetzter Lösungen *Sitzungsbericht. Kaiser. Akad. Wiss. (Mathem.-Naturwiss. Cl.), Wien* 65:539.

[3] Soret C (1879) Sur l'état d'équilibre que prend, du point de vue de sa concentration, une dissolution saline primitivement homogène, dont deux parties sont portées à des températures différentes *Archives de Genève* 3e période, tome II,:48.

[4] Groot, S. R. de, Mazur P (1984) *Non-equilibrium thermodynamics* (Dover Publications, New York), Dover edition.

[5] Hartmann S, et al. (2012) Thermophobicity of Liquids: Heats of Transport in Mixtures as Pure Component Properties *Physical Review Letters* 109:065901.

[6] Gebhardt M, Köhler W (2015) Soret, thermodiffusion, and mean diffusion coefficients of the ternary mixture n-dodecane+isobutylbenzene+1,2,3,4-tetrahydronaphthalene *The Journal of Chemical Physics* 143:164511.

[7] Würger A (2008) Transport in Charged Colloids Driven by Thermoelectricity *Physical Review Letters* 101:108302.

[8] Reichl M, Herzog M, Götz A, Braun D (2014) Why Charged Molecules Move Across a Temperature Gradient: The Role of Electric Fields *Physical Review Letters* 112:198101.

[9] Stadelmaier D, Köhler W (2009) Thermal Diffusion of Dilute Polymer Solutions: The Role of Chain Flexibility and the Effective Segment Size *Macromolecules* 42:9147–9152.

[10] Schimpf ME, Giddings JC (1989) Characterization of thermal diffusion in polymer solutions by thermal field-flow fractionation: Dependence on polymer and solvent parameters *Journal of Polymer Science Part B: Polymer Physics* 27:1317–1332.

[11] Morozov KI, Köhler W (2014) Thermophoresis of polymers: nondraining vs draining coil *Langmuir : the ACS journal of surfaces and colloids* 30:6571–6576.

[12] Chan J, Popov JJ, Kolisnek-Kehl S, Leaist DG (2003) Soret Coefficients for Aqueous Polyethylene Glycol Solutions and Some Tests of the Segmental Model of Polymer Thermal Diffusion *Journal of Solution Chemistry* 32:197–214.

[13] Wang Z, Afanasenkau D, Dong M, Huang D, Wiegand S (2014) Molar mass and temperature dependence of the thermodiffusion of polyethylene oxide in water/ethanol mixtures *The Journal of Chemical Physics* 141:064904.

[14] Kishikawa Y, et al. (2012) Temperature dependence of thermal diffusion for aqueous solutions of monosaccharides, oligosaccharides, and polysaccharides *Physical chemistry chemical physics : PCCP* 14:10147–10153.

[15] Würger A (2009) Molecular-Weight Dependent Thermal Diffusion in Dilute Polymer Solutions *Physical Review Letters* 102:078302.

[16] Iacopini S, Rusconi R, Piazza R (2006) The "macromolecular tourist": Universal temperature dependence of thermal diffusion in aqueous colloidal suspensions *The European Physical Journal E* 19:59–67.

[17] Iacopini S, Piazza R (2003) Thermophoresis in protein solutions *Europhysics Letters (EPL)* 63:247–253.

[18] Braibanti M, Vigolo D, Piazza R (2008) Does Thermophoretic Mobility Depend on Particle Size? *Physical Review Letters* 100:108303.

[19] Vigolo D, Buzzaccaro S, Piazza R (2010) Thermophoresis and thermoelectricity in surfactant solutions *Langmuir* 26:7792–7801.

[20] Herzog M (2012) Ph.D. thesis (Ludwig-Maximilians-Universität, München).

[21] Sehnem AL, et al. (2015) Temperature dependence of the Soret coefficient of ionic colloids *Physical Review E* 92:042311.

[22] Lippok S, et al. (2012) Direct detection of antibody concentration and affinity in human serum using microscale thermophoresis *Analytical Chemistry* 84:3523–3530.

[23] Wolff M, Braun D, Nash MA (2014) Detection of Thermoresponsive Polymer Phase Transition in Dilute Low-Volume Format by Microscale Thermophoretic Depletion *Analytical Chemistry* 86:6797–6803.

[24] Nicoli F, Verschueren D, Klein M, Dekker C, Jonsson MP (2014) DNA translocations through solid-state plasmonic nanopores *Nano Letters* 14:6917–6925.

[25] Liu J (2012) Adsorption of DNA onto gold nanoparticles and graphene oxide: surface science and applications *Physical Chemistry Chemical Physics* 14:10485.

[26] Chun MS, Lee I (2008) Rigorous estimation of effective protein charge from experimental electrophoretic mobilities for proteomics analysis using microchip electrophoresis *Colloids and Surfaces A: Physicochemical and Engineering Aspects* 318:191–198.

[27] Gitlin I, Carbeck JD, Whitesides GM (2006) Why Are Proteins Charged? Networks of Charge–Charge Interactions in Proteins Measured by Charge Ladders and Capillary Electrophoresis *Angewandte Chemie International Edition* 45:3022–3060.

[28] Manning GS (1969) Limiting Laws and Counterion Condensation in Polyelectrolyte Solutions I. Colligative Properties *The Journal of Chemical Physics* 51:924.

[29] Hickey OA, Shendruk TN, Harden JL, Slater GW (2012) Simulations of Free-Solution Electrophoresis of Polyelectrolytes with a Finite Debye Length Using the Debye-Hückel Approximation *Physical Review Letters* 109:098302.

[30] Grass K, Böhme U, Scheler U, Cottet H, Holm C (2008) Importance of Hydrodynamic Shielding for the Dynamic Behavior of Short Polyelectrolyte Chains *Physical Review Letters* 100:096104.

[31] Helmholtz H (1853) Ueber einige Gesetze der Vertheilung elektrischer Ströme in körperlichen Leitern mit Anwendung auf die thierisch-elektrischen Versuche *Annalen der Physik und Chemie* 165:211–233.

[32] Gouy M (1910) Sur la constitution de la charge électrique à la surface d'un électrolyte *Journal de Physique Théorique et Appliquée* 9:457–468.

[33] Chapman DL (1913) LI. A contribution to the theory of electrocapillarity *Philosophical Magazine Series 6* 25:475–481.

[34] Debye P, Hückel E. (1923) Zur Theorie der Elektrolyte. I. Gefrierpunktserniedrigung und verwandte Erscheinungen *Physikalische Zeitschrift* 24:185–206.

[35] Hunter RJ (1981) *Zeta potential in colloid science: Principles and applications*, Colloid science (Academic Press), New paperback edition.

[36] Lipfert J, et al. (2014) Double-stranded RNA under force and torque: similarities to and striking differences from double-stranded DNA *Proceedings of the National Academy of Sciences of the United States of America* 111:15408–15413.

[37] Nicholls A, Honig B (1991) A rapid finite difference algorithm, utilizing successive over-relaxation to solve the Poisson-Boltzmann equation *Journal of Computational Chemistry* 12:435–445.

[38] Gebala M, et al. (2015) Cation-Anion Interactions within the Nucleic Acid Ion Atmosphere Revealed by Ion Counting *Journal of the American Chemical Society* 137:14705–14715.

[39] Ben-Yaakov D, Andelman D, Podgornik R (2011) Dielectric decrement as a source of ion-specific effects *The Journal of Chemical Physics* 134:074705.

[40] Smoluchowski Marian von (1903) Contribution à la théorie de l'endosmose électrique et de quelques phénomènes corrélatifs *Bull. Int. Acad. Sci. Cracovie*.

[41] Henry DC (1931) The Cataphoresis of Suspended Particles. Part I. The Equation of Cataphoresis *Proceedings of the Royal Society A: Mathematical, Physical and Engineering Sciences* 133:106–129.

[42] Wiersema P, Loeb A, Overbeek J (1966) Calculation of the electrophoretic mobility of a spherical colloid particle *Journal of Colloid and Interface Science* 22:78–99.

[43] O'Brien RW, White LR (1978) Electrophoretic mobility of a spherical colloidal particle *Journal of the Chemical Society, Faraday Transactions 2* 74:1607.

[44] Ohshima H (1994) A Simple Expression for Henry's Function for the Retardation Effect in Electrophoresis of Spherical Colloidal Particles *Journal of Colloid and Interface Science* 168:269–271.

[45] Stellwagen E, Stellwagen NC (2003) Probing the Electrostatic Shielding of DNA with Capillary Electrophoresis *Biophysical Journal* 84:1855–1866.

[46] Stellwagen NC, Gelfi C, Righetti PG (1997) The free solution mobility of DNA *Biopolymers* 42:687–703.

[47] Eastman ED (1926) Thermodynamics of non-isothermal systems *Journal of the American Chemical Society* 48:1482–1493.

[48] Dhont JKG, Wiegand S, Duhr S, Braun D (2007) Thermodiffusion of Charged Colloids: Single-Particle Diffusion *Langmuir* 23:1674–1683.

[49] Duhr S, Braun D (2006) Why molecules move along a temperature gradient *Proceedings of the National Academy of Sciences* 103:19678–19682.

[50] Duhr S, Braun D (2006) Thermophoretic Depletion Follows Boltzmann Distribution *Physical Review Letters* 96:168301.

[51] Astumian RD (2007) Coupled transport at the nanoscale: the unreasonable effectiveness of equilibrium theory *Proceedings of the National Academy of Sciences of the United States of America* 104:3–4.

[52] Würger A (2013) Is Soret equilibrium a non-equilibrium effect? *Comptes Rendus Mécanique* 341:438–448.

[53] Eslahian KA, Majee A, Maskos M, Würger A (2014) Specific salt effects on thermophoresis of charged colloids *Soft Matter* 10:1931.

[54] Reichl M, Herzog M, Greiss F, Wolff M, Braun D (2015) Understanding the similarity in thermophoresis between single- and double-stranded DNA or RNA *Physical Review E* 91:062709.

[55] Ruckenstein E (1981) Can phoretic motions be treated as interfacial tension gradient driven phenomena? *Journal of Colloid and Interface Science* 83:77–81.

[56] Huang KR, et al. (2008) Simulation on binding efficiency of immunoassay for a biosensor with applying electrothermal effect *Journal of Applied Physics* 104:064702.

[57] Maeda K, Shinyashiki N, Yagihara S, Wiegand S, Kita R (2015) Ludwig-Soret effect of aqueous solutions of ethylene glycol oligomers, crown ethers, and glycerol: Temperature, molecular weight, and hydrogen bond effect *The Journal of Chemical Physics* 143:124504.

[58] Maeda K, Shinyashiki N, Yagihara S, Wiegand S, Kita R (2014) How does thermodiffusion of aqueous solutions depend on concentration and hydrophobicity? *The European Physical Journal E* 37:94.

[59] Armstrong JA, Bresme F (2013) Water polarization induced by thermal gradients: The extended simple point charge model (SPC/E) *The Journal of Chemical Physics* 139:014504.

[60] Bresme F, Lervik A, Bedeaux D, Kjelstrup S (2008) Water Polarization under Thermal Gradients *Physical Review Letters* 101:020602.

[61] Snowdon PN, Turner, J. C. R. (1960) The Soret effect in some 0.01 normal aqueous electrolytes *Transactions of the Faraday Society* 56:1409.

[62] Takeyama N, Nakashima K (1988) Proportionality of intrinsic heat of transport to standard entropy of hydration for aqueous ions *Journal of Solution Chemistry* 17:305–325.

[63] Agar JN, Mou CY, Lin JL (1989) Single-ion heat of transport in electrolyte solutions: a hydrodynamic theory *The Journal of Physical Chemistry* 93:2079–2082.

[64] Guthrie G, Wilson JN, Schomaker V (1949) Theory of the Thermal Diffusion of Electrolytes in a Clusius Column *The Journal of Chemical Physics* 17:310.

[65] Takeyama N, Nakashima K (1983) Thermodynamics of Thermal Diffusion in Aqueous Ionic Solutions *Journal of the Physical Society of Japan* 52:2699–2705.

[66] Römer F, Wang Z, Wiegand S, Bresme F (2013) Alkali Halide Solutions under Thermal Gradients: Soret Coefficients and Heat Transfer Mechanisms *The Journal of Physical Chemistry B* 117:8209–8222.

[67] Delahay P, Tobias CW (1963) *Advances in Electrochemistry and Electrochemical Engineering: J.N. Agar - Thermogalvanic Cells* (Wiley).

[68] Takeyama N, Nakashima K (1983) A Reduction Rule in Heats of Transfer for Aqueous 1–1 Electrolytes *Journal of the Physical Society of Japan* 52:2692–2698.

[69] Gaeta FS, Perna G, Scala G, Bellucci F (1982) Nonisothermal matter transport in sodium chloride and potassium chloride aqueous solutions. 1. Homogeneous system (thermal diffusion) *The Journal of Physical Chemistry* 86:2967–2974.

[70] Caldwell DR (1973) Measurement of negative thermal diffusion coefficients by observing the onset of thermohaline convection *The Journal of Physical Chemistry* 77:2004–2008.

[71] Sanyal SK, Mukherjee AK (1988) Heat of transport and heat capacity of transport of some aqueous electrolytes *Canadian Journal of Chemistry* 66:435–438.

[72] Prieve DC, Roman R (1987) Diffusiophoresis of a rigid sphere through a viscous electrolyte solution *Journal of the Chemical Society, Faraday Transactions 2* 83:1287.

[73] Anderson JL (1989) Colloid Transport by Interfacial Forces *Annual Review of Fluid Mechanics* 21:61–99.

[74] Anderson JL, Prieve DC (1991) Diffusiophoresis caused by gradients of strongly adsorbing solutes *Langmuir* 7:403–406.

[75] Chiang TY, Velegol D (2014) Multi-ion diffusiophoresis *Journal of Colloid and Interface Science* 424:120–123.

[76] Abécassis B, Cottin-Bizonne C, Ybert C, Ajdari A, Bocquet L (2008) Boosting migration of large particles by solute contrasts *Nature Materials* 7:785–789.

[77] Abécassis B, Cottin-Bizonne C, Ybert C, Ajdari A, Bocquet L (2009) Osmotic manipulation of particles for microfluidic applications *New Journal of Physics* 11:075022.

[78] Palacci J, Abécassis B, Cottin-Bizonne C, Ybert C, Bocquet L (2010) Colloidal Motility and Pattern Formation under Rectified Diffusiophoresis *Physical Review Letters* 104:138302.

[79] Ning H, Dhont JKG, Wiegand S (2008) Thermal-Diffusive Behavior of a Dilute Solution of Charged Colloids *Langmuir* 24:2426–2432.

[80] Zhang KJ, Briggs ME, Gammon RW, Sengers JV, Douglas JF (1999) Thermal and mass diffusion in a semidilute good solvent-polymer solution *The Journal of Chemical Physics* 111:2270.

[81] Haslauer M (2013) Bachelor Thesis towards Thermophoresis of Polyethylene Glycol: Bachelor Thesis.

[82] McIlvaine TC (1921) A buffer solution for colorimetric comparison *Journal of Biological Chemistry* 49:183–186.

[83] Joyce GF (2002) The antiquity of RNA-based evolution *Nature* 418:214–221.

[84] Wolff M, et al. (2016) Quantitative thermophoretic study of disease-related protein aggregates *Scientific reports* 6:22829.

[85] Keil L (2011) A setup for RNA melting curves and label free thermophoresis: Bachelor Thesis.

[86] Wienken CJ, Baaske P, Duhr S, Braun D (2011) Thermophoretic melting curves quantify the conformation and stability of RNA and DNA *Nucleic Acids Research* 39:e52.

[87] Rink TJ, Tsien RY, Pozzan T (1982) Cytoplasmic pH and free Mg2+ in lymphocytes *The Journal of Cell Biology* 95:189–196.

[88] Goldberg RN (1999) Thermodynamic Quantities for the Ionization Reactions of Buffers *Journal of Physical and Chemical Reference Data* 31:231.

[89] Schendel LC (2014) Soret coefficients of molecules with regulable charges switched by adjusting different pH: Bachelor Thesis.

[90] Goldstein R, Penner S (1964) The near-infrared absorption of liquid water at temperatures between 27 and 209°C *Journal of Quantitative Spectroscopy and Radiative Transfer* 4:441–451.

[91] Vergara A, Paduano L, Vitagliano V, Sartorio R (1999) Mutual diffusion in aqueous solution of poly(ethyleneglycol) samples. Some comments on the effect of chain length and polydispersity *Physical Chemistry Chemical Physics* 1:5377–5383.

[92] Le Guillou, J. C., Zinn-Justin J (1977) Critical Exponents for the n -Vector Model in Three Dimensions from Field Theory *Physical Review Letters* 39:95–98.

[93] Paduano L, Sartorio R, D'Errico G, Vitagliano V (1998) Mutual diffusion in aqueous solution of ethylene glycol oligomers at 25 °C *Journal of the Chemical Society, Faraday Transactions* 94:2571–2576.

[94] Rubinstein M, Colby RH (2003) *Polymer physics* (Oxford University Press, Oxford and New York).

[95] Verdolino V, Cammi R, Munk BH, Schlegel HB (2008) Calculation of pKa values of nucleobases and the guanine oxidation products guanidinohydantoin and spiroiminodihydantoin using density functional theory and a polarizable continuum model *The journal of physical chemistry. B* 112:16860–16873.

[96] Velikyan I, Acharya S, Trifonova A, Földesi A, Chattopadhyaya J (2001) The pKa's of 2'-Hydroxyl Group in Nucleosides and Nucleotides *Journal of the American Chemical Society* 123:2893–2894.

[97] Sjöback R, Nygren J, Kubista M (1998) Characterization of fluorescein–oligonucleotide conjugates and measurement of local electrostatic potential *Biopolymers* 46:445–453.

[98] Sehnem AL, et al. (2014) Thermodiffusion in positively charged magnetic colloids: influence of the particle diameter *Physical Review E* 89:032308.

[99] Rauch J, Köhler W (2003) Collective and thermal diffusion in dilute, semidilute, and concentrated solutions of polystyrene in toluene *The Journal of Chemical Physics* 119:11977.

[100] Doi M, Edwards SF (1986) *The theory of polymer dynamics*, The International series of monographs on physics (Clarendon Press, Oxford) Vol. 73.

[101] Rauch J, Hartung M, Privalov AF, Köhler W (2007) Correlation between thermal diffusion and solvent self-diffusion in semidilute and concentrated polymer solutions *The Journal of Chemical Physics* 126:214901.

[102] Hofmeister F (1888) Zur Lehre von der Wirkung der Salze *Archiv für Experimentelle Pathologie und Pharmakologie* 24:247–260.

[103] Zhang Y, Cremer PS (2006) Interactions between macromolecules and ions: The Hofmeister series *Current opinion in chemical biology* 10:658–663.

[104] Lide DR (2001) *CRC handbook of chemistry and physics, 2001-2002* (CRC Press, Boca Raton), 82nd ed. edition.

[105] Lee SH, Rasaiah JC (2011) Proton transfer and the mobilities of the H+ and OH- ions from studies of a dissociating model for water *The Journal of Chemical Physics* 135:124505.

[106] Armstrong J, Lervik A, Bresme F (2013) Enhancement of the thermal polarization of water via heat flux and dipole moment dynamic correlations *The journal of physical chemistry. B* 117:14817–14826.

[107] Armstrong J, Daub CD, Bresme F (2015) Note: How does the treatment of electrostatic interactions influence the magnitude of thermal polarization of water? The SPC/E model *The Journal of Chemical Physics* 143:036101.

[108] Muscatello J, Römer F, Sala J, Bresme F (2011) Water under temperature gradients: polarization effects and microscopic mechanisms of heat transfer *Physical chemistry chemical physics : PCCP* 13:19970–19978.

[109] Hasted JB, Ritson DM, Collie CH (1948) Dielectric Properties of Aqueous Ionic Solutions. Parts I and II *The Journal of Chemical Physics* 16:1.

[110] Chaikin PM, Lubensky TC (1995) *Principles of condensed matter physics* (Cambridge University Press, Cambridge and New York, NY, USA).

[111] Schmaljohann D (2006) Thermo- and pH-responsive polymers in drug delivery *Advanced drug delivery reviews* 58:1655–1670.

[112] Kita R, Wiegand S (2005) Soret Coefficient of Poly(N -isopropylacrylamide)/Water in the Vicinity of Coil−Globule Transition Temperature *Macromolecules* 38:4554–4556.

[113] Wongsuwarn S, et al. (2012) Giant thermophoresis of poly(N-isopropylacrylamide) microgel particles *Soft Matter* 8:5857.

[114] Seidel, Susanne A I, et al. (2013) Microscale thermophoresis quantifies biomolecular interactions under previously challenging conditions *Methods* 59:301–315.

[115] Knowles, Tuomas P J, Vendruscolo M, Dobson CM (2014) The amyloid state and its association with protein misfolding diseases *Nature reviews. Molecular cell biology* 15:384–396.

[116] Lorenzen N, et al. (2014) The role of stable α-synuclein oligomers in the molecular events underlying amyloid formation *Journal of the American Chemical Society* 136:3859–3868.

[117] Guilliams T, et al. (2013) Nanobodies raised against monomeric α-synuclein distinguish between fibrils at different maturation stages *Journal of molecular biology* 425:2397–2411.

[118] Schmidt DA, et al. (2009) Rattling in the cage: ions as probes of sub-picosecond water network dynamics *Journal of the American Chemical Society* 131:18512–18517.

[119] Huang PY, Keh HJ (2012) Diffusiophoresis of a spherical soft particle in electrolyte gradients *The journal of physical chemistry. B* 116:7575–7589.

[120] Staffeld PO, Quinn JA (1989) Diffusion-induced banding of colloid particles via diffusiophoresis *Journal of Colloid and Interface Science* 130:88–100.

[121] Staffeld PO, Quinn JA (1989) Diffusion-induced banding of colloid particles via diffusiophoresis *Journal of Colloid and Interface Science* 130:69–87.

[122] Merk V, et al. (2014) In situ non-DLVO stabilization of surfactant-free, plasmonic gold nanoparticles: effect of Hofmeister's anions *Langmuir* 30:4213–4222.

[123] Koenen S, et al. (2015) Continuous Electrophoretic Deposition and Electrophoretic Mobility of Ligand-Free, Metal Nanoparticles in Liquid Flow *Journal of the Electrochemical Society* 162:D174–D179.

[124] Vigolo D, Rusconi R, Stone HA, Piazza R (2010) Thermophoresis: microfluidics characterization and separation *Soft Matter* 6:3489.

[125] Sackmann E (1996) Supported Membranes: Scientific and Practical Applications *Science* 271:43–48.

[126] Czolkos I, Jesorka A, Orwar O (2011) Molecular phospholipid films on solid supports *Soft Matter* 7:4562.

[127] Vaz, Winchil L. C., Clegg RM, Hallmann D (1985) Translational diffusion of lipids in liquid crystalline phase phosphatidylcholine multibilayers. A comparison of experiment with theory *Biochemistry* 24:781–786.

[128] Hennig M, Neumann J, Wixforth A, Rädler JO, Schneider MF (2009) Dynamic patterns in a supported lipid bilayer driven by standing surface acoustic waves *Lab on a Chip* 9:3050.

[129] Athmakuri K, Rohovie M, Padala C, Cole R, Kane RS (2010) Influence of Chain Length on the Diffusion and Electrophoresis of DNA Adsorbed on Heterogeneous Supported Lipid Bilayers *Langmuir* 26:13393–13398.

[130] Stelzle M, Miehlich R, Sackmann E (1992) Two-dimensional microelectrophoresis in supported lipid bilayers *Biophysical Journal* 63:1346–1354.

[131] Kahl V, Hennig M, Maier B, Rädler JO (2009) Conformational dynamics of DNA-electrophoresis on cationic membranes *Electrophoresis* 30:1276–1281.

[132] Hennig M, et al. (2011) DNA Concentration Modulation on Supported Lipid Bilayers Switched by Surface Acoustic Waves *Langmuir* 27:14721–14725.

[133] Monson CF, Pace HP, Liu C, Cremer PS (2011) Supported Bilayer Electrophoresis under Controlled Buffer Conditions *Analytical Chemistry* 83:2090–2096.

[134] Baumgart T, Hess ST, Webb WW (2003) Imaging coexisting fluid domains in biomembrane models coupling curvature and line tension *Nature* 425:821–824.

[135] Keber FC, et al. (2014) Topology and dynamics of active nematic vesicles *Science* 345:1135–1139.

[136] Heinemann F, Vogel SK, Schwille P (2013) Lateral membrane diffusion modulated by a minimal actin cortex *Biophysical Journal* 104:1465–1475.

[137] Atia L, Givli S (2014) A theoretical study of biological membrane response to temperature gradients at the single-cell level *Journal of The Royal Society Interface* 11:20131207.

[138] Soumpasis DM (1983) Theoretical analysis of fluorescence photobleaching recovery experiments *Biophysical Journal* 41:95–97.

[139] Axelrod D, Koppel DE, Schlessinger J, Elson E, Webb WW (1976) Mobility measurement by analysis of fluorescence photobleaching recovery kinetics *Biophysical Journal* 16:1055–1069.

[140] Endress E, Weigelt S, Reents G, Bayerl TM (2005) Derivation of a closed form analytical expression for fluorescence recovery after photo bleaching in the case of continuous bleaching during read out *The European Physical Journal E* 16:81–87.

[141] Macháň R, Hof M (2010) Lipid diffusion in planar membranes investigated by fluorescence correlation spectroscopy *Biochimica et Biophysica Acta (BBA) - Biomembranes* 1798:1377–1391.

[142] Pan J, Tristram-Nagle S, Kucerka N, Nagle JF (2008) Temperature dependence of structure, bending rigidity, and bilayer interactions of dioleoylphosphatidylcholine bilayers *Biophysical Journal* 94:117–124.

[143] Kita R, Wiegand S, Luettmer-Strathmann J (2004) Sign change of the Soret coefficient of poly(ethylene oxide) in water/ethanol mixtures observed by thermal diffusion forced Rayleigh scattering *The Journal of Chemical Physics* 121:3874.

[144] Luettmer-Strathmann J (2003) Two-chamber lattice model for thermodiffusion in polymer solutions *The Journal of Chemical Physics* 119:2892.

8 Danksagung

Ich möchte mich bei allen Menschen bedanken, die diese Doktorarbeit ermöglicht und begünstigt haben:

- Dieter Braun für Möglichkeit in seinem Labor zu arbeiten, sowie das Lehren einer Vielzahl von Methoden und Techniken. Vielen Dank auch für die großzügige Art, welche sich unter anderem in diversen Aktionen, wie zum Beispiel Paragliden und Schlittenfahren, wiedergespiegelt hat.

- Michael Nash und Alexander Büll für zahlreiche Diskussionen. Ihr habt mich nicht nur um einiges an Wissen bereichert und ich möchte euch für die super Zusammenarbeit danken!

- Besonders Joachim Rädler und Martin Hennig möchte ich neben dem ersten Kontakt mit dem Wissenschaftskosmos auch für das offene, positive Arbeitsumfeld und die viele Unterstützung auf dem Weg danken.

- Danke an dieser Stelle auch an alle Mitglieder des Gaub, Rädler, Liedl und Feldmann Lehrstuhls! Danke für die Möglichkeit auf so einen großen Pool an Maschinerie, Chemikalien und Expertise zurückzugreifen! Ebenfalls vielen Dank an CeNS für die großartige Organisation und Unterstützung bei diversen Projekten.

- An alle Studenten für die intensive und fruchtsame Zusammenarbeit: Besonders Leonhard Schendel, Michael Haslauer, Matthias Vollmer und Thore Klink.

- An Christof und Simon, ohne euch wäre jede Workstation und jedes Betriebssystem innerhalb von Wochen über den Jordan gegangen. P.S. Mein Laptop läuft wieder ohne externen Bildschirm!

- Vielen Dank für die wertvollen Kommentare zum Manuscript: Georg, Franzi, Ferdi, Friederike, Nadine, Matze und Zhenya! Julian, danke für deine geduldige Hilfe bezüglich formeller eMails.

- Danke an alle restlichen Braunies und Peter für das gute Arbeitsklima! Natürlich auch Danke an die ehemaligen Urgesteine für so manche gute Stunde: Mathias, Ilka, Silke, Christian, Svenja und David.

- Zu guter Letzt danke an meine Familie! Besonderer Dank geht an meine Eltern, Monika und Hansjörg, für jegliche Unterstützung in jeder Lebenslage!

9   Publications

1. M. Wolff, D. Braun, M. A. Nash
   "Detection of Thermoresponsive Polymer Phase Transition in Dilute Low-Volume Format by Microscale Thermophoretic Depletion"
   Analytical Chemistry, 2014, doi: 10.1021/ac5008283
   Table 1 and Figure 4 reprinted with permission. Full article reprinted with permission.
   © 2014 American Chemical Society.

2. M. Reichl, M. Herzog, F. Greiss, M. Wolff, and D. Braun:
   "Understanding the similarity in thermophoresis between single- and double-stranded DNA or RNA"
   Physical Review E, 2015, doi: 10.1103/PhysRevE.91.062709
   Full article reprinted with permission.
   © 2015 American Physical Society

3. M. Wolff, J.J. Mittag, T. W. Herling, E. De Genst, C. M. Dobson, T. P. J. Knowles, D. Braun & A. K. Buell:
   "Quantitative thermophoretic study of disease-related protein aggregates"
   Scientific Reports, 2016, doi: 10.1038/srep22829
   Full article reprinted with permission.
   © 2016 Macmillan Publishers Limited

---

1. M. Hennig, M. Wolff, J. Neumann, A. Wixforth, M. F. Schneider, and J. O. Rädler
   "DNA Concentration Modulation on Supported Lipid Bilayers Switched by Surface Acoustic Waves"
   Langmuir, 2011, doi: 10.1021/la203413b

Detection of Thermoresponsive Polymer Phase Transition in Dilute Low-Volume Format by Microscale Thermophoretic Depletion

Manuel Wolff,[†,‡] Dieter Braun,[†,‡] and Michael A. Nash*[‡,§]

[†]Systems Biophysics, Ludwig-Maximilians-Universität, D-80799 Munich, Germany
[‡]Center for Nanoscience, Ludwig-Maximilians-Universität, D-80799 Munich, Germany
[§]Chair for Applied Physics, Biophysics and Molecular Materials, Ludwig-Maximilians-Universität, D-80799 Munich, Germany

ABSTRACT: Environmentally responsive polymers are becoming increasingly important in the biomaterials field for use as diagnostic reagents, drug carriers, and tissue engineering scaffolds. Characterizing polymer phase transitions by cloud point curves typically requires large milliliter volumes of sample at high micromolar solution concentrations. Here we present a method based on quantification of thermophoretic Soret diffusion that allows determination of polymer phase transitions using only ~1 μL of liquid at dilute nanomolar concentrations, effectively reducing the amount of sample required by a factor of 10^6. We prepared an oligo(ethylene glycol) (OEG) methyl ether methacrylate copolymer via RAFT polymerization. End-group modification with fluorescent BODIPY-maleimide provided a dye-labeled pOEG-BODIPY conjugate with a lower critical solution temperature (LCST) in the range of ~25−35 °C. Thermophoresis measurements in dilute solution demonstrated a marked change in polymer thermodiffusion in the vicinity of the LCST. We measured the temperature dependence of thermodiffusion and transformed these data sets into sigmoidal curves characterizing the phase transition of the polymer. Finite element modeling suggested a correction to the measured values that brought the transition temperatures measured by thermophoresis into accord with the cloud point curves. Our results demonstrate that observation of polymer thermodiffusion in a low volume dilute format is a facile method for determining polymer phase transition temperatures.
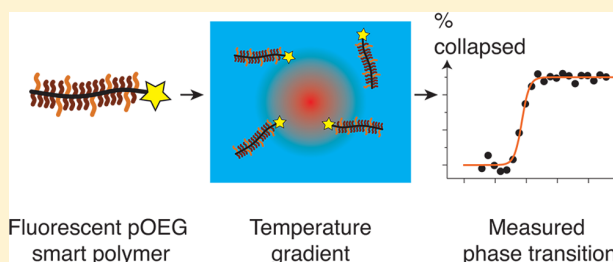
Environmentally responsive polymers represent a class of macromolecules with tunable properties that undergo dramatic conformational changes in response to slight changes in environmental conditions (e.g., temperature, pH, and light).[1−6] Such polymers have been developed for use in biological applications, including as drug delivery vehicles,[7,8] tissue engineering scaffolds,[9] and reagents for affinity separation of diagnostic targets.[10] Poly(*N*-isopropylacrylamide) (pNIPAm) is among the most widely studied thermoresponsive polymer systems, and attachment of this polymer to biological entities such as antibodies, enzymes, and nanoparticles has proven advantageous in biotechnology applications, including molecular diagnostics[11] and cell-surface interface engineering.[12] PNIPAm, however, also has associated limitations, including a significant hysteresis upon cooling. Due to intramolecular hydrogen bonding, it is generally difficult to completely rehydrate pNIPAm after hydrophobic collapse,[13] requiring cooling well below the LCST.

More recently, polymers made from oligo(ethylene glycol) (OEG) have proven versatile both in terms of synthetic flexibility and biochemical properties.[14] Poly−OEG (pOEG) consists of a hydrocarbon backbone with comblike OEG side chains of variable length. Poly(OEG) can be synthesized using a variety of living free radical polymerization methods, including ATRP and RAFT,[15,16] facilitating control over molecular weight, block architecture, and functional end-

group incorporation. Although they are more hydrophobic than standard poly(ethylene glycol), pOEGs are still biocompatible and water-soluble. Moreover, pOEGs possess a temperature-responsive LCST behavior and have smaller hysteresis than pNIPAm. The transition temperature of pOEG can be tuned from 0−100 °C, by varying the side-chain length of the OEG macromonomers.[17]

To measure the transition temperature of a polymer solution, light extinction is typically monitored as the temperature is slowly raised, resulting in a so-called "cloud point" curve describing the lower critical solution temperature (LCST). The cloud point process in fact involves two processes: the coil-to-globule transition of individual polymer chains and interchain aggregation that increases solution turbidity. Interactions with biomolecules can affect the LCST of biohybrid protein−polymer conjugates.[18] This makes determining the precise transition point of a conjugate in specific biological milieu challenging. Performance of environmentally responsive materials in vivo may not be optimized correctly based on bulk cloud point measurements alone, therefore an assay to detect the transition point using small sample volumes at biologically relevant nanomolar solution concentrations would
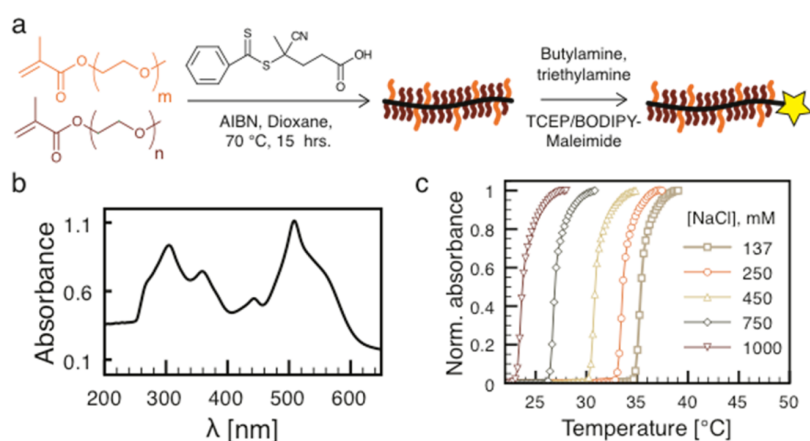
Figure 1. Preparation of an end-labeled thermoresponsive oligo(ethylene glycol) copolymer. (a) Copolymerization of oligo(ethylene glycol) methyl ether methacrylates ($n = 2$, $m = 8.5$) using a dithiobenzoate RAFT agent resulted in a thermoresponsive pOEG copolymer. Following purification and aminolysis of the RAFT agent, labeling of the resulting thiol groups with BODIPY-maleimide produced the final 100 kDa pOEG-BODIPY conjugate. (b) Absorbance spectrum of the polymer exhibited chromophore absorbance at 505 nm and peaks associated with the cleaved RAFT agent at 300 and 360 nm. (c) LCST behavior of the fluorescent copolymer in 10 mM phosphate buffered saline at pH 7.4 with variable NaCl showed a decrease in LCST with increasing NaCl. The LCST values were then compared with those determined from thermodiffusion measurements of the same samples.

be an advantage in conjugate optimization studies for biological applications.

Thermophoresis, or the Ludwig-Soret effect, describes the tendency of molecules to move along temperature gradients. Although the effect has been known for more than 150 years, the underlying theory is still fragmentary. Several predictions of the electrostatic and electrophoretic contributions to the Soret coefficient (S_T) have been supported by experimental data on DNA and charged beads,[19−26] but the contribution of nonionic interactions remains less clear.[27−29] Meanwhile, the importance of developing a solid theoretical framework is highlighted by several newly discovered applications of bioanalytics, bio-detection, and molecular trapping.[30,31] Differences in thermal diffusion of a labeled binding partner can be used to detect the presence of a second binding partner. This assay format requires minimal sample volume and has proven facile, rapid, and compatible with a wide range of samples.[32]

Hydration water and its associated entropy are also suspected to contribute to thermodiffusion. Since release of "caged" hydration water molecules is known to play a role in smart polymer phase transitions,[33] we postulated that a smart polymer system would be an informative sample for thermodiffusion measurements. We tested whether the thermodiffusion behavior of an environmentally responsive polymer would be indicative of its conformational changes near the LCST. A prior report on thermodiffusion of pNIPAm using a different measurement method (i.e., thermal diffusion forced Rayleigh scattering[34]) also suggested the phase transition could potentially be observed in changes of the Soret coefficient with temperature. We selected a synthetic route that included cleavage of the RAFT chain transfer agent and subsequent modification with an uncharged BODIPY-FL derivative. This allowed the thermophoretic depletion to be measured using LED-induced fluorescence detection and IR-laser heating inside a microcapillary. The thermodiffusion of the thermoresponsive fluorescent polymer could therefore be directly characterized using small volumes and dilute solutions. A computational steady-state model was further used to validate the

experimental results and predict a correction to the experimental data.

■ RESULTS AND DISCUSSION

The synthetic steps en route to an end-labeled thermoresponsive pOEG polymer are shown in Figure 1a. The pOEG-BODIPY was synthesized using thermally initiated RAFT polymerization. We used a dithiobenzoate chain transfer agent together with AIBN as the thermally activated initiator. A RAFT agent to initiator ratio of 4:1 was used. The target molecular weight of the polymerization was 100 kDa. Poly(ethylene glycol)$_{8.5}$ methyl ether methacrylate and di-(ethylene glycol)$_2$ methyl ether methacrylate were loaded into the polymerization feed at a molar ratio of 1:4 (i.e., 20 mol % OEG$_{8.5}$). Our previous work had indicated that this ratio would provide an LCST of ∼37 °C in standard PBS buffer containing 137 mM NaCl.[15] Since OEG$_{8.5}$ is more hydrophilic than OEG$_2$, inclusion of this monomer at higher loadings tended to decrease the transition temperature of resulting copolymers. Following purging with N$_2$ to remove inhibitory oxygen, the reaction proceeded for 15 h at 70 °C. The reaction mixture was then cooled and the product recovered by precipitation and dialysis. The molecular weight of the product was estimated by extinction spectrophotometry of the dithiobenzoate end group contained in the polymer prior to aminolysis (see Experimental Section). We determined the extinction coefficient of the chain transfer agent to be $\varepsilon_{\lambda=300\ nm} = 1.47 \times 10^4$ mol cm^{-1}, and the pOEG molecular weight to be $M_n = 92.3 \pm 6.5$ kDa. Following purification, the polymer was freeze-dried and transferred into dimethylformamide for aminolysis. A 10-fold excess of triethylamine and butylamine was used to cleave the trithiocarbonate group at the end of the RAFT agent, resulting in a thiol group that could be modified directly with BODIPY FL-maleimide, as previously described.[35] Shown in Figure 1b is the absorbance spectrum of the polymer following BODIPY labeling. The absorbance spectrum exhibited peaks at 300, 360, and 510 nm with a chromophore shoulder extending out to 560 nm, consistent with successful aminolysis and fluorescent labeling of the polymer. Following fluorescent labeling, the

polymer was purified using aqueous HPLC, and a narrow sample fraction under the monomodal elution peak was collected to further decrease sample polydispersity prior to thermophoresis measurements. Figure 1c shows normalized cloud point curves of the BODIPY-labeled pOEG obtained in water with variable amounts of NaCl. An increase in the amount of NaCl clearly depressed the LCST values due to the well-known Hofmeister effect.[36]

The experimental setup for measuring thermodiffusion is depicted in Figure 2a. An upright microscope was equipped
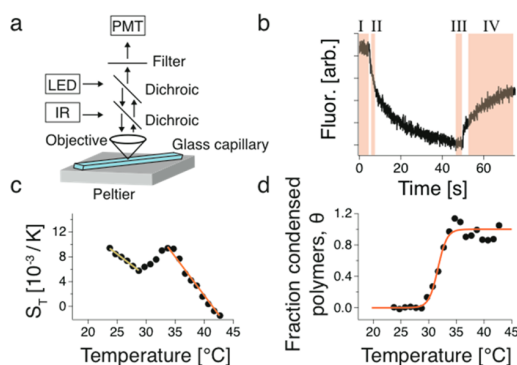
Figure 2. Measuring thermophoretic diffusion of thermoresponsive polymers. (a) Schematic of the setup. A photomultiplier tube (PMT) was inserted into the detection path of an epi-fluorescent microscope outfitted with a light emitting diode (LED) for fluorescence excitation, and an infrared (IR) laser for generating temperature gradients within the capillary. IR laser heating was used to induce Soret diffusion of the polymer sample. (b) Raw data trace showing a typical polymer thermodiffusion curve with regions as follows: region I, IR laser was off; region II, IR laser was on and fluorescence rapidly dropped due to temperature dependence of the dye; region III, near steady-state thermodiffusion of the sample occurred; region IV, IR laser was turned off and sample diffused back into the depletion zone. (c) The Soret coefficient (S_T) was calculated over a range of sample Peltier temperatures from time traces as in (b) using eq 1. (d) Thermal melting analysis (eq 3) was used to transform curves as in (c) into LCST curves that reported the transition temperature of the thermoresponsive polymer. The temperature axes show $T_0 + \Delta T/2$, as described in the finite element model (see below).

with a photomultiplier tube in the detection path, a cyan LED ($\lambda_{ex} = 505$ nm) for fluorophore excitation, and an IR laser that locally heated the sample liquid within a confocal volume inside the rectangular glass microcapillary. Rectangular capillaries were used to minimize fluid transport due to thermal convection, which can confound thermodiffusion measurements.[20] The PMT was used to measure fluorescence emission from the same region of the sample that was heated by the IR laser, providing a measure of heat-induced depletion of fluorescently labeled polymer when the IR laser was switched on. Fluorescent labeling of the sample is therefore a prerequisite for the measurement. Thermophoresis curves in aqueous buffers were obtained following previously described protocols for such a setup.[21,30,32,37] The fluorescence signal measured by the PMT was monitored over time within 4 distinct zones of the thermophoresis curve (Figure 2b). In zone I, the IR laser was off and the homogeneous fluorescence distribution within the capillary was nearly constant or decreasing slightly due to photobleaching. At $t = 5$ s, the IR laser was switched on and a temperature gradient was quickly established on a short time scale (~50 ms). This temperature rise resulted in a rapid drop

in fluorescence (Figure 2b, II) due to an inherent temperature dependence of dye emission. Approximately 0.5 s of data following the switching on of the IR laser were excluded from the calculation of the intensity in zone II to exclude the temperature dependence of dye emission. After this temperature jump, the IR laser remained on while thermodiffusion took place on a slower timescale, eventually approaching a steady state at t ≈ 50 s (Figure 2b, III). While the IR laser was on (t = 5−50 s), the fluorescence intensity decreased monotonically, indicating that the labeled pOEG molecules were depleted from the heated zone and migrated toward the cooler zone, exhibiting a positive Soret coefficient. After a steady-state had been reached, the IR laser was switched off at time $t = 50$ s, and the pOEG molecules diffused back into the now cool detection region for the remainder of the curve (Figure 2b, IV). The Soret coefficient, S_T, was calculated from such a curve, according to eq 1,

$$c_{III}/c_{II} = \exp(-S_T \Delta T) \approx 1 - S_T \Delta T \qquad (1)$$

where c_{III}/c_{II} is the average fluorescence in zone III divided by that of zone II and ΔT is the temperature difference between the hot and cold regions. Typically ΔT will depend on setup parameters such as IR laser power and capillary dimensions. We calibrated the setup using a pH/temperature sensitive dye 2′,7′-bis (2-carboxyethyl)-5-(and-6) carboxyfluorescein (BCECF) and found that with rectangular capillary dimensions of 0.1 × 1 mm², the temperature difference between hot and cold regions was $\Delta T = 9.4 \pm 0.8$ K. Thermophoresis curves such as that shown in Figure 2b were collected over a range of Peltier base temperatures (T_0). From this data set, we were able to monitor how S_T changed with temperature as the polymer underwent its phase transition. On the basis of the results of a steady-state computational model described in further detail below, we corrected the temperature axis by adding $\Delta T/2$ to the Peltier base temperature (T_0). The temperature axes in Figures 2 and 3 therefore represent $T_0 + \Delta T/2$. Due to the temperature dependence of S_T, thermodiffusion of sample molecules is not constant but rather changes depending on a molecule's position within the Lorentzian temperature distribution imposed by IR heating, and this effect was accounted for with the correction of $\Delta T/2$. Apparently thermodiffusion in an inhomogeneous temperature field strictly averages to half of the peak thermal field as shown by simulations and calculations below.

As shown in Figure 2c, the Soret coefficient of pOEG in 450 mM NaCl exhibited three distinct zones with differing slopes. From 23−28 °C, a negative slope of −7.1 × 10⁻⁴ K⁻¹ °C⁻¹ was obtained. In the intermediate range from 28−34 °C, a positive slope of 7.7 × 10⁻⁴ K⁻¹ °C⁻¹ was observed, while in the upper range again a negative slope of −12.4 × 10⁻⁴ K⁻¹ °C⁻¹ was found. The two portions of the curve showing negative slope are fitted with solid lines. The absorbance cloud point curve (Figure 1c, 450 mM) for the same sample indicated the LCST of pOEG in 450 mM NaCl was ~31 °C. Since the S_T crossover point from negative to positive slope observed in Figure 2c occurred near the polymer LCST, we interpreted this zigzag pattern as an indication that the pOEG had two distinct thermodiffusion regimes above and below the cloud point. The positive slope portion of the curve near the LCST then represented the transition of pOEG from one regime to the other.

To assist in analysis and pinpoint the observed crossover point more precisely, we transformed the S_T versus temperature
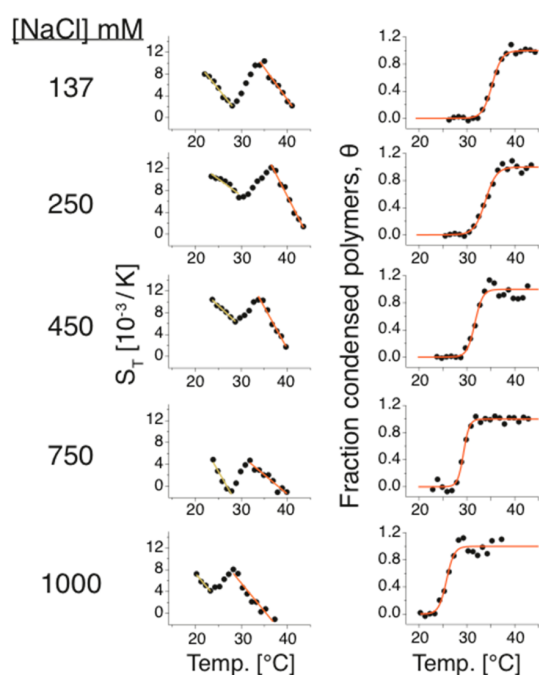
Figure 3. Characterization of Hofmeister effect on LCST using thermodiffusion measurements. Soret diffusion coefficients (S_T) and phase transition curves (θ) of the labeled pOEG copolymer at 1 nM (100 ng/mL) in PBS buffer with variable NaCl show that the transition temperature dropped steadily with increasing NaCl.

data into sigmoidal plots using an analysis method originally developed for thermal melting of DNA strands.[38] The results from such a transformation are shown in Figure 2d. We assumed the two thermodiffusion regimes fitted in Figure 2c with solid lines represented a two-state system. The fitted baseline from 23–28 °C we will call $S_{T, low}$. This equation of a line is a function of temperature and indicates the expected S_T values that would be measured if the whole system did not exhibit a phase transition. We call the fitted line from 35–43 °C, $S_{T, high}$, which indicates the expected S_T values for the system above the LCST, where the pOEG is collapsed and dehydrated. When the polymer underwent its transition, the S_T values we measured were in fact a superposition of S_T values from the fraction of molecules above transition (θ) together with the fraction of molecules below transition ($1 - \theta$). Since $S_{T, low}$ and $S_{T, high}$ are linear with respect to temperature, the measured signal can be expressed according to eq 2:

$$S_{T,measured} = \theta S_{T,high} + (1 - \theta)S_{T,low} \qquad (2)$$

Rearranging and solving for θ, we obtained the following expression for the fraction of condensed polymers, eq 3:

$$\theta = \frac{S_{T,measured} - S_{T,low}}{S_{T,high} - S_{T,low}} \qquad (3)$$

We note that $S_{T, low}$ and $S_{T, high}$ are both linear functions of temperature and are evaluated at the temperature at which $S_{T, measured}$ was determined. From these transformed data, we could then obtain a sigmoid fit using the Hill equation (Figure 2d, solid line) and determine the midpoint of the transition. The midpoint of the phase transition in this case was found to be 31.6 ± 0.15 °C, in agreement with the Abs$_{50\%}$ cloud point measurement of 30.9 ± 0.3 °C. It is important to note here that

correction of the base temperature T_0 by adding $\Delta T/2$ was required to achieve agreement between the cloud point and thermophoresis data. This correction was supported by the finite element model described below.

The key finding here is that differences in thermodiffusion behavior of the polymer molecules are indicative of its conformational change. The S_T curves were obtained in dilute solution (~1 nM or 100 ng/mL) on a timescale of 50 s. Since the polymer design ensured an uncharged molecule save only a single ionizable carboxyl group at the polymer's ω end, ionic contributions to Soret diffusion are kept to a minimum. The ionic contribution to Soret diffusion might otherwise overwhelm the signal and no transition behavior would be observed in S_T.

To further confirm that the changes in S_T that we measured were in fact indicative of the phase transition, we obtained thermophoresis curves for pOEG over a range of base temperatures (T_0) and salt concentrations from 137–1000 mM NaCl. We performed data analysis as described above by first fitting linear regions of the S_T versus temperature curve, and then transforming the data into a format that could be fitted with a sigmoidal function to estimate the transition temperature under each buffer condition. The results from such an experiment are shown in Figure 3. The midpoints of the fitted sigmoidal curves (Figure 3, right column) steadily shifted to lower temperatures as the amount of NaCl increased, consistent with the Hofmeister effect that was observed in the absorbance cloud point curves.

A comparison between the absorbance-based cloud points and the thermophoresis-based transition temperatures is presented in Table 1. On the basis of this comparison, it is

Table 1. Comparison of pOEG Transition Temperatures Determined Using Thermophoresis and Absorbance-Based Cloud Point Curves[a]

[NaCl] (mM)	θ midpoint (°C)	Abs. cloud point (°C)
137	35.3 ± 0.34	35.4 ± 0.3
250	33.8 ± 1.89	33.6 ± 0.3
450	31.6 ± 0.15	30.9 ± 0.3
750	29.3 ± 0.46	26.9 ± 0.3
1000	25.7 ± 1.34	25.7 ± 0.3

[a]The errors for θ indicate ± one standard deviation of the midpoint fit parameter of the Hill equation. The absorbance cloud point was defined as the temperature that reached 50% maximal absorbance. The 0.3 °C error for all cloud points represents the resolution of the temperature controller used in the extinction spectrophotometer.

clear that the thermophoresis result is consistent with the cloud point method and reproduces the transition points with high accuracy. The thermophoresis measurement, however, had several advantages, such as requiring 1000-fold less sample (~1 μL instead of 1 mL). Additionally more dilute samples could be used because the fluorescence measurement was much more sensitive than the absorbance-based measurement. Cloud point curves are typically obtained using a high concentration of the polymer (e.g., ~micromolar or milligram per milliliter range) in order to produce a sharp rise in signal at the characteristic temperature. Our thermophoresis-based measurement allowed us to measure the transition temperature using concentrations of only ~1 nM (100 ng/mL). This concentration range could be an advantage when studying interactions between thermoresponsive polymers and biological compo-
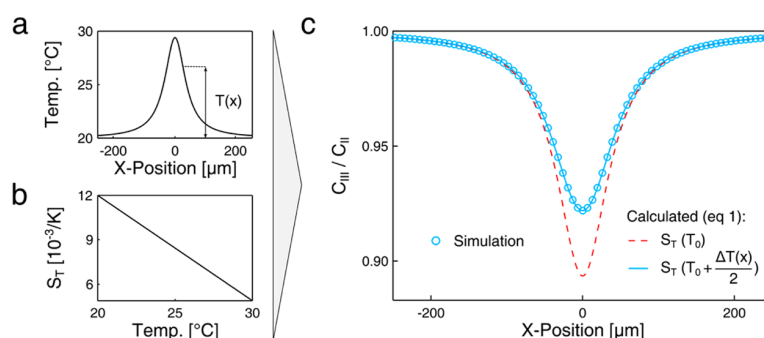
Figure 4. Finite element model of the system predicts a base temperature correction of $\Delta T/2$. (a) A Lorentzian temperature distribution was centered at the origin with a height of $T_0 + \Delta T = 20 + 9.4$ °C. (b) The temperature dependence of the Soret coefficient S_T was assumed linear over the range from 20−30 °C. (c) Simulation result (O) showing fluorescence depletion (C_{III}/C_{II}) calculated from a steady-state finite element model of transport eq 4. The C_{III}/C_{II} fluorescence depletion predicted by eq 1, assuming an S_T equal to 12×10^{-3} K^{-1} [i.e., S_T at the base temp, $S_T(T_0)$] overestimates thermophoretic depletion (red dashed line). Correcting S_T by an amount corresponding to $S_T(T_0 + \Delta T(x)/2)$ results in good agreement between eq 1 and the finite element simulation (blue solid line).

nents, which may themselves be present only in exceedingly low quantities (e.g., < nanomolar).

To understand the interplay between the base temperature and the observed thermodiffusion coefficients (S_T), we used a finite element method to model the system at steady state. An overview of the modeling results is shown in Figure 4. Two sets of given information went into the simulation. First, the temperature distribution was assumed to Lorentzian (Figure 4a) with base temperature $T_0 = 20$ °C, a ΔT at the peak of 9.4 °C, and a laser spot size of 40 μm according to the relation $T = 20$ °C + 9.4 °C $[1/(1 + (x/40\ \mu m)^2]$. Second, the temperature dependence of the Soret coefficient (Figure 4b) was considered to be linear with temperature and follow the relation: $S_T(T) = 2.6 \times 10^{-2}$ K$^{-1} - 7.1 \times 10^{-4}$ K^{-1} °C$^{-1} \times T$. We furthermore presumed a concentration of 1 at the boundaries. At steady state, we assumed the net flux of molecules at each position was zero according to eq 4,

$$j_D = -D\nabla C - S_T D C \nabla T = 0 \tag{4}$$

where j$_D$ is the molecular flux, D is the diffusion coefficient, C is the polymer concentration, S_T is the Soret coefficient, and T is the temperature. This transport equation accounts for diffusion of the sample in the first term and thermodiffusion in the second term. At steady state, j$_D$ = 0 and the diffusive flux is equal to the negative of the thermodiffusive flux. Since D appears in both fluxes, it cancels out for the steady state and the solution is independent of the diffusion coefficient. This steady state equation along with the two given sets of information were programmed into a finite element modeling program (FEM-LAB), and the normalized 1D concentration was determined at each point. The size of the bounding simulation box was kept very large (50000 μm) to minimize edge effects. The results from such a simulation are shown in Figure 4c (right plot, blue O). The simulation result confirmed that thermophoretic depletion of pOEG from the heated zone should occur in accordance with the positive Soret coefficients across this temperature range. It also estimated the magnitude of this depletion given the Lorentzian temperature profile, and the temperature-dependence of the thermodiffusion behavior.

In a second step, we calculated the expected C_{III}/C_{II} distribution based on eq 1. We determined how well eq 1 predicted the simulated C_{III}/C_{II} profile given a correction to the Soret coefficient. We calculated C_{III}/C_{II} at every point from eq 1 by plugging in a S_T at the base temperature $T_0 = 20$ °C and a

$\Delta T(x) = T(x) - T_0$ or the distance-dependent temperature difference from the base temperature. We found that with no correction, eq 1 overestimated the depletion in comparison with the finite element model (Figure 4, right plot, dotted red line). When we corrected the S_T values by assuming $S_T = S_T(T_0 + \Delta T(x)/2)$, eq 1 was found to be consistent with the steady-state simulation (Figure 4, right plots, solid blue line). This accordance between the steady-state solution and eq 1 with a corrected S_T value supported the interpretation that the finite steepness of the temperature gradient necessitated a correction to the measured S_T values or rather a shift in the temperature axis from T_0 to $T_0 + \Delta T/2$. Apparently molecules with Soret coefficients that are linearly dependent on temperature establish a concentration profile in a Lorentzian temperature field according to Soret coefficients evaluated at a temperature of $T_0 + \Delta T(x)/2$, following eq 5,

$$\ln[c(x)/c_0] = -S_T|_{T_0 + \Delta T(x)/2} \cdot \Delta T(x) \tag{5}$$

This correction holds for all kinds of microscale thermophoresis measurements and implies that the finite steepness of the temperature profile should, for example, also be taken into account in analysis of temperature-dependent binding curves or thermophoresis experiments on protein unfolding. However, it remains to be determined if the $\Delta T/2$ correction also holds for systems with a nonlinear temperature dependence of S_T or for non-Lorentzian temperature distributions.

Since the C_{III}/C_{II} fluorescence ratios that were measured experimentally were analyzed using eq 1 to obtain relevant Soret coefficients, the simulation results imply a temperature axis shift by $\Delta T/2$ is required. It is noted that the correction in this case was necessary to bring the transition temperatures determined by thermodiffusion into agreement with the LCST cloud points. This is also a further confirmation of the validity of the model, since the transition point of the polymer is expected to be independent of the method used to measure it.

In summary, we prepared a thermoresponsive pOEG polymer using RAFT polymerization and fluorescently tagged the polymer with an uncharged fluorophore using aminolysis in tandem with maleimide-BODIPY labeling. We characterized the LCST of the fluorescently labeled pOEG as a function of added NaCl using cloud point curves and further investigated pOEG thermodiffusion behavior over base temperatures (T_0) that ranged above and below the LCST. A correction to the temperature axis from T_0 to $T_0 + \Delta T/2$ that was predicted by a

finite element steady-state model brought the LCST values determined by thermodiffusion measurement into accord with those determined using conventional cloud point curves. By transforming the data using an analysis method originally developed for DNA melting curves, we found that the phase transition could be accurately determined based solely on thermodiffusion data. The measurement was performed at a polymer concentration of ~1 nM (100 ng/mL) using only ~1 μL of sample, making our approach compatible with determination of polymer LCST at low concentrations in biological milieu (e.g., small volume cell lysate). Since both thermophoresis and thermoresponsive polymers are compatible with measurement in biological liquids,[32,39] moving into biological liquids should be straightforward with this method and requires further experimental work. This approach should prove useful for determining phase transition behavior of biohybrid environmentally responsive polymer systems in a low-volume dilute format.

■ EXPERIMENTAL SECTION

Polymer Synthesis. Oligo(ethylene glycol)$_{8.5}$ methacrylate (M_n 475, 100 ppm MEHQ, 200 ppm BHT inhibitor, product number 447943) and di(ethylene glycol)$_2$ methyl ether methacrylate (M_n 188.22, 95% pure, product number 447927) were purchased from Sigma and purified through a neutral aluminum oxide column prior to use. The RAFT chain transfer agent 4-cyano-4-(phenylcarbonothioylthio)pentanoic acid (DTB, M_n 279.38, 97% pure, product number 722995) was purchased from Sigma and used as received. The initiator 2,2′-azobis(2-methylpropionitrile) (AIBN, M_n = 164.21) was purchased from Sigma and recrystallized from methanol. In a typical polymerization with a target molecular weight of 100 kDa, a reaction vial with Teflon stopper was loaded with 1.6 g of di(ethylene glycol) methyl ether methacrylate and 0.4 g of the oligo(ethylene glycol)$_{8.5}$ methacrylate. Next, 6.4 mg of the DTB chain transfer agent and 540 μg of the initiator dissolved in dioxane were added. Two grams of dioxane were then added such that the mass ratio of dioxane to monomers was 1:1. The flask was purged for 30 min with N$_2$. The reaction proceeded at 70 °C for 17 h and was then precipitated into hexane at 4 °C. The precipitate was next dissolved into tetrahydrofuran and precipitated two more times into chilled hexane. Finally, the product was collected by centrifugation, dried under vacuum, and recovered via dialysis and lyophilization.

Aminolysis and BODIPY Labeling. The lyophilized polymer was dissolved at 300 mg/mL in dimethylformamide (DMF). A 10-fold excess of butyl amine and triethylamine were added, and the reaction proceeded overnight at room temperature. The reaction progress was monitored by UV-spectrophotometry. The product was recovered via precipitation into an ice cold 1:1 hexane:ether mixture, followed by drying under vacuum. Next the polymer was dissolved in PBS buffer, pH 7, 4 °C, 2 mg/mL. Ten microliters TCEP disulfide reducing slurry (Pierce) per milliliter polymer solution was added. The TCEP slurry was mixed with polymer for 1−2 h at room temperature and removed via centrifugation. The BODIPY-maleimide dye was dissolved at 10 mM in DMF and added in a 10-fold molar excess to the polymer in PBS buffer. The reaction was allowed to proceed overnight at 4 °C. The product was recovered using gel filtration (GE Healthcare PD-10 column) and HPLC.

Polymer Analysis. To estimate the molecular weight of the polymer, the molar extinction coefficient of the DTB chain transfer agent was determined. Since DTB is not water-soluble, we first determined the molar extinction coefficient of DTB in methanol (see main text). Next, the polymer absorbance at known mass concentrations was determined in both water and methanol. The DTB molar extinction coefficient was then corrected by the ratio of polymer absorbance in water/methanol. This provided a measure of the molarity of DTB and therefore polymer chains in the aqueous polymer sample. On the basis of this mass/molarity ratio, we calculated the average molecular weight of the polymer to be M_n = 92.3 ± 6.5 kDa. To further decrease polydispersity prior to thermophoresis measurements, HPLC (GE Äkta, Superdex gel filtration media) was used to isolate a narrow fraction under the primary monomodal elution peak.

Absorption Spectrophotometry. Cloud point curves of the polymer dissolved at 1 mg/mL in water with variable NaCl were obtained using a UV−vis spectrometer (Jasco GmbH, Germany) equipped with a temperature controller (PAC-743) with control accuracy of ±0.3 °C. We acquired an absorbance spectrum of our sample at 15 °C and blanked the instrument. Next a heating ramp of 0.3 °C/min was applied, with measurements taken every 0.2 °C at a wavelength of 400 nm. We used a sample volume of 1 mL in poly(styrene) cuvettes with an optical path length of 1 cm. Data curves were normalized by the maximal absorbance above transition.

Thermophoresis Measurements. The thermophoresis measurement setup has been described previously.[20,31,32] We modified an AxioScope Vario fluorescence microscope (Carl Zeiss GmbH, Germany) with a 1480 nm IR laser (Fibotec Fiberoptics, Germany). A Partec Objective (40×, 0.80 mm working distance, 0.8 NA) was used to focus both LED excitation light and IR laser light. The pOEG polymer was dissolved at 1 nM (100 ng/mL) in phosphate-buffered saline/Roti-block (nonspecific blocker, Carl Roth) with variable amounts of NaCl. Polymer samples were loaded into rectangular borosilicate capillaries with dimensions of 0.1 × 1 mm^2 (Vitrocom, Mountain Lakes, NJ) by capillary action within a few seconds. Afterward, the open ends were sealed with wax (Tight Sealing Wax, NanoTemper, Munich, Germany) and the outer surface cleaned with isopropyl-alcohol and a piece of clean tissue. Then the capillaries were placed on a Peltier element and heated from below. The base temperature T_0 of the Peltier element was set using feedback control programmed in LabView. The C_{III}/C_{II} fluorescence ratios were determined by averaging the PMT signal over a time period of 2 s within the respective regions of the thermophoresis curves.

■ AUTHOR INFORMATION

Corresponding Author
*E-mail: michael.nash@lmu.de.

Notes
The authors declare no competing financial interest.

■ ACKNOWLEDGMENTS

■ REFERENCES

(1) Hoffman, A. S.; Stayton, P. S. *Prog. Polym. Sci.* **2007**, *32*, 922−932.

(2) Kumar, A.; Srivastava, A.; Galaev, I. Y.; Mattiasson, B. *Prog. Polym. Sci.* **2007**, *32*, 1205−1237.

(3) Nash, M. A.; Lai, J. J.; Hoffman, A. S.; Yager, P.; Stayton, P. S. *Nano Lett.* **2010**, *10*, 85−91.

(4) Smith, A. E.; Xu, X.; McCormick, C. L. *Prog. Polym. Sci.* **2010**, *35*, 45.

(5) Gil, E. S.; Hudson, S. M. *Prog. Polym. Sci.* **2004**, *29*, 1173−1222.

(6) Stuart, M. A. C.; Huck, W. T. S.; Genzer, J.; Müller, M.; Ober, C.; Stamm, M.; Sukhorukov, G. B.; Szleifer, I.; Tsukruk, V. V.; Urban, M.; Winnik, F.; Zauscher, S.; Luzinov, I.; Minko, S. *Nat. Mater.* **2010**, *9*, 101−113.

(7) Qiu, Y.; Park, K. *Adv. Drug Delivery Rev.* **2012**, *64*, 49−60.

(8) Schmaljohann, D. *Adv. Drug Delivery Rev.* **2006**, *58*, 1655−1670.

(9) Furth, M. E.; Atala, A.; Van Dyke, M. E. *Biomaterials* **2007**, *28*, 5068−5073.

(10) Nash, M. A.; Waitumbi, J. N.; Hoffman, A. S.; Yager, P.; Stayton, P. S. *ACS Nano* **2012**, *6*, 6776−6785.

(11) Nash, M. A.; Yager, P.; Hoffman, A. S.; Stayton, P. S. *Bioconjugate Chem.* **2010**, *21*, 2197−2204.

(12) Yang, J.; Yamato, M.; Shimizu, T.; Sekine, H.; Ohashi, K.; Kanzaki, M.; Ohki, T.; Nishida, K.; Okano, T. *Biomaterials* **2007**, *28*, 5033−5043.

(13) Lutz, J.-F.; Akdemir, Ö.; Hoth, A. *J. Am. Chem. Soc.* **2006**, *128*, 13046−13047.

(14) Gao, W.; Liu, W.; Christensen, T.; Zalutsky, M. R.; Chilkoti, A. *Proc. Natl. Acad. Sci. U.S.A.* **2010**, *107*, 16432−16437.

(15) Nash, M. A.; Gaub, H. E. *ACS Nano* **2012**, *6*, 10735−10742.

(16) Lutz, J.-F. *J. Polym. Sci. A, Polym. Chem.* **2008**, *46*, 3459−3470.

(17) Lutz, J.-F. *Adv. Mater.* **2011**, *23*, 2237−2243.

(18) Buller, J.; Laschewsky, A.; Lutz, J.-F.; Wischerhoff, E. *Polym. Chem.* **2011**, *2*, 1486.

(19) Reineck, P.; Wienken, C. J.; Braun, D. *Electrophoresis* **2010**, *31*, 279−286.

(20) Jerabek-Willemsen, M.; Wienken, C. J.; Braun, D.; Baaske, P.; Duhr, S. *ASSAY and Drug Development Technologies* **2011**, *9*, 342−353.

(21) Wienken, C. J.; Baaske, P.; Duhr, S.; Braun, D. *Nucleic Acids Res.* **2011**, *39*, e52−e52.

(22) Mast, C. B.; Braun, D. *Phys. Rev. Lett.* **2010**, *104*10.1103/PhysRevLett.104.188102.

(23) Schoen, I.; Krammer, H.; Braun, D. *Proc. Natl. Acad. Sci. U.S.A.* **2009**, *106*, 21649−21654.

(24) Duhr, S.; Braun, D. *Proc. Natl. Acad. Sci. U.S.A.* **2006**, *103*, 19678−19682.

(25) Putnam, S. A.; Cahill, D. G. *Langmuir* **2005**, *21*, 5317−5323.

(26) Dhont, J. K. G.; Wiegand, S.; Duhr, S.; Braun, D. *Langmuir* **2007**, *23*, 1674−1683.

(27) Stadelmaier, D.; Köhler, W. *Macromolecules* **2008**, *41*, 6205−6209.

(28) Würger, A. *Phys. Rev. Lett.* **2009**, *102*078302.

(29) Kita, R.; Wiegand, S.; Luettmer-Strathmann, J. *J. Chem. Phys.* **2004**, *121*, 3874.

(30) Wienken, C. J.; Baaske, P.; Rothbauer, U.; Braun, D.; Duhr, S. *Nat. Commun.* **2010**, *1*, 100.

(31) Lippok, S.; Seidel, S. A. I.; Duhr, S.; Uhland, K.; Holthoff, H.-P.; Jenne, D.; Braun, D. *Anal. Chem.* **2012**, *84*, 3523−3530.

(32) Seidel, S. A. I.; Dijkman, P. M.; Lea, W. A.; van den Bogaart, G.; Jerabek-Willemsen, M.; Lazic, A.; Joseph, J. S.; Srinivasan, P.; Baaske, P.; Simeonov, A.; Katritch, I.; Melo, F. A.; Ladbury, J. E.; Schreiber, G.; Watts, A.; Braun, D.; Duhr, S. *Methods* **2013**, *59*, 301−315.

(33) Deshmukh, S. A.; Sankaranarayanan, S. K. R. S.; Suthar, K.; Mancini, D. C. *J. Phys. Chem. B* **2012**, *116*, 2651−2663.

(34) Kita, R.; Wiegand, S. *Macromolecules* **2005**, *38*, 4554−4556.

(35) Scales, C. W.; Convertine, A. J.; McCormick, C. L. *Biomacromolecules* **2006**, *7*, 1389−1392.

(36) Cho, Y.; Zhang, Y.; Christensen, T.; Sagle, L. B.; Chilkoti, A.; Cremer, P. S. *J. Phys. Chem. B* **2008**, *112*, 13765−13771.

(37) Baaske, P.; Wienken, C. J.; Reineck, P.; Duhr, S.; Braun, D. *Angew. Chem., Int. Ed.* **2010**, *49*, 2238−2241.

(38) Mergny, J.-L.; Lacroix, L. *Oligonucleotides* **2003**, *13*, 515−537.

(39) Stocker, G.; Vandevyver, C.; Hilbrig, F.; Freitag, R. *Biotechnol. Prog.* **2006**, *22*, 1621−1629.

Understanding the similarity in thermophoresis between single- and double-stranded DNA or RNA

Maren Reichl, Mario Herzog, Ferdinand Greiss, Manuel Wolff, and Dieter Braun[*]

Systems Biophysics, Physics Department, Nanosystems Initiative Munich and Center for NanoScience,
Ludwig-Maximilians-Universität München, Amalienstraße 54, 80799 München, Germany

Thermophoresis is the movement of molecules in a temperature gradient. For aqueous solutions its microscopic basis is debated. Understanding thermophoresis for this case is, however, important since it proved very useful to detect the binding affinity of biomolecules and since thermophoresis could have played an important role in early molecular evolution. Here we discuss why the thermophoresis of single- and double-stranded oligonucleotides - DNA and RNA - is surprisingly similar. This finding is understood by comparing the spherical capacitor model for single-stranded species with the case of a rod-shaped model for double-stranded oligonucleotides. The approach describes thermophoresis of DNA and RNA with fitted effective charges consistent with electrophoresis measurements and explains the similarity between single- and double-stranded species. We could not confirm the sign change for the thermophoresis of single- versus double-stranded DNA in crowded solutions containing polyethylene glycol [Y. T. Maeda, T. Tlusty, and A. Libchaber, Proc. Natl. Acad. Sci. USA **109**, 17972 (2012)], but find a salt-independent offset while the Debye length dependence still satisfies the capacitor model. Overall, the analysis documents the continuous progress in the microscopic understanding of thermophoresis.

PACS number(s): 87.15.−v, 82.40.Ck, 66.10.−x, 83.80.Rs

I. INTRODUCTION

The theoretical understanding of thermophoresis is becoming increasingly important since biologists over the world are using thermophoresis to measure biomolecule affinities from the thermophoretic contrast between bound and unbound molecules [1–4]. Recently, a microscopic mechanism for the thermophoresis of charged molecules was experimentally confirmed for Debye lengths both larger and smaller than the molecule size [5]. The main contribution to charge-based thermophoresis could be rationalized by the transition from a spherical to a plate capacitor model of ionic shielding.

As an interesting detail in these experiments, double-stranded DNA did not behave much differently from its single-stranded counterparts, despite the naïve expectation of twice the molecule charge and the expected influence of the large persistence length of double-stranded oligonucleotides. The latter makes it hard to assume a spherically shaped molecule for Debye lengths shorter than the molecule size. Here, we will explain in more detail why such a spherical capacitor model, despite the nonspherical geometry, is still a good approximation. This is confirmed by measurements of single- and double-stranded oligonucleotides. In addition, we will revisit results for double- and single-stranded DNA under crowded conditions where we obtain conflicting results with previous reports.

Below, we will use the term "capacitor model" (see Fig. 1) for the model originally proposed by both Dhont and Braun [6,7], building on thermodynamic local equilibrium approaches previously elaborated on by Dhont [8,9], later extended [10] to include a temperature-dependent charge. In a similar adaptation of particle geometry, the effect of molecule geometry was studied for elongated virus particles [11] under the assumption of a constant surface charge density. The length

of the viruses is, however, always longer than the Debye length and therefore capping effects at the end can be neglected, in contrast to the geometry of short double-stranded DNA or RNA. Alternatively the authors proposed to approximate the geometry by a string of spheres [11].

The electrical, local equilibrium theoretical description that is used here to describe thermophoresis has been under scrutiny by opposing approaches, most notably by theories describing thermophoresis as similar to electrophoresis [12–14]. However, thermophoresis differs from electrophoresis in an important point. In electrophoresis, the shielded particle displays no overall charge and thus its enthalpy does not depend on the location along the electrical field. In thermophoresis, the electrical field energy stored with the particle does depend on its position and—if the Peclet number and temperature variations are small—a diffusion-based mechanism can be envisaged that brings about a drift of the particle towards its local Boltzmann distribution.

It is true that the microscopic, electrical force mechanisms for local equilibrium thermophoresis have yet to be revealed [15] to obtain a fully convincing picture of thermophoresis. It is well possible that short-range, non-electric mechanisms in thermophoresis lack the long-range field mechanisms to enforce a local equilibrium. We think that the confirmation of thermophoresis across the transition from a spherical to plate capacitor over a considerable range of molecule sizes without fitting parameters [5] is a strong case for the local equilibrium approach followed here. These experiments yet have to be explained by an effective slip flow approach to thermophoresis [13,14,16] with recent arguments supporting a local equilibrium approach for the limit of $R < \lambda_{DH}$ [16] and significant progress being made for thermophoresis in the nondilute regime [17]. Notably, the results were recently confirmed for hard particles [18].

Much discussed is the discrepancy between thermophoresis measurements on the size scaling. Single-particle tracking together in combination with fluorescence depletion used in this study allowed us to measure the size scaling of

---

[*]Author to whom correspondence should be addressed: dieter.braun@lmu.de
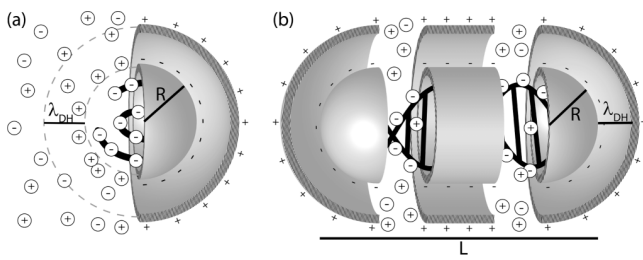
FIG. 1. Models of thermophoresis for single- and double-stranded oligonucleotides. (a) A charged molecule, here DNA or RNA, is screened by the counterions in solution. This can be modeled as a spherical capacitor with the molecule as the inner shell with radius R and the counterions at the outer sphere. (b) The spherical capacitor model is extended to a rod shape with spherical end caps for double-stranded DNA. The radius of the sphere and the cylinder is R; the overall length is L.

carboxyl-modified polystyrene beads with a diameter from 20 nm to 2 μm. The particles were cleaned by washing, and pH stabilized with buffers; their surface charge was determined from electrophoresis. Both the dependence on the Debye length and the size scaling matched the capacitor theory [7]. No fitting parameters were necessary since the effective charge was determined from electrophoresis. Measurements on the size scaling of similar beads over a shorter size range indicated a different size scaling $S_T \propto R$ [19,20]. However, the surface charge was not determined to compare the theory quantitatively and no dependence on the Debye length was measured. Most importantly, in both studies washing of the particles and a stabilization of pH was not documented. It is well possible that the significant Seebeck effect from the thermophoresis of dissociated water (H^+ or OH^-) or from stabilization agents that remained in the solution from the production of the beads leads to a Seebeck-dominated thermophoresis that scales with $S_T \propto R$. This hypothesis is supported by the fact that the Soret coefficients reported in [20] and reviewed in [21] were consistently larger than in [7], indicating a possible additional mechanism of particle movement. This is important to note since for equally charged particles, a dissipative flow theory of thermophoresis would actually predict a considerably smaller, not larger, Soret coefficient. On a similar line of argument, the now well confirmed Seebeck effect allows for an electrophoretic explanation of the experimentally observed particle attraction from pseudo–slip flows at the particle surface [22].

Here, we follow a direct analytical method with a full geometrical description, valid for Debye lengths both smaller and larger than the molecule size. To model an extended molecule, we insert a cylindrical capacitor into the spherical capacitor model [5,6] (see Fig. 1). All shielding capacitors are acting in parallel. Such a cylinder, capped at the ends with hemispheroids, was also used in modeling of electrophoresis [23]. The subsequent study will show in detail that the persistence length of DNA and RNA does not significantly affect the thermophoresis for a range of salt concentrations and lengths below 50 bases.

After the experimental and theoretical discussion of the rod capacitor model for double-stranded oligonucleotides, we will show that this model still holds to a good extent in an environment with a crowding agent. We model this with an additive contribution to the Soret coefficient, i.e., the strength of thermophoresis, originating in the depletion force. Maeda and Libchaber [24] reported a fundamental difference between single- and double-stranded DNA, claiming that molecular crowding enforces only double-stranded DNA motifs to accumulate in a heated spot. We repeated their experiments, but this time we used fluorescence labels covalently attached to the DNA for both the single- and double-stranded measurements. In [24], intercalating dyes were used for the double-stranded measurements, possibly leading to artifacts due to the different temperature-dependent fluorescence of the two labels. We could confirm the weaker accumulation for single-stranded molecules. But we find that the difference between single- and double-stranded molecules is rather an additive contribution. In contrast to [24], we do not find a robust sign change or a convergence towards zero effective Soret coefficients for larger salt concentrations. The capacitor model is still confirmed in these crowded environments.

II. RESULTS AND DISCUSSION

A. Experiments

The setup consisted of a modified fluorescent microscope with infrared heating as described previously [5,7]. The following sequences were used in the experiments, where the below described strand was labeled at the 5′ end with the fluorescent dye Hex (6-carboxy-2′,4,4′,5′,7,7′-hexachlorofluorescein, Biomers, Germany). The sequences were designed to have minimal secondary structure also in the single-stranded version to form a random coil.

DNA:

22-mer: 5′–Hex–ATT GAG ATA CAC ATT AGA ACT A–3′

50-mer: 5′–Hex–ATA ATC TGT AGT ACT GCA GAA AAC TTG TGG GTT ACT GTT TAC TAT GGG GT–3′

RNA:

22-mer: 5′–Hex–AUU GAG AUA CAC AUU AGA ACU A–3′

50-mer: 5′–Hex–AUA AUC UGU AGU ACU GCA GAA AAC UUG UGG GUU ACU GUU UAC UAU GGG GU–3′

Double-stranded probes contained an equal amount of complementary sequence and the complementary strand was unlabeled. DNA and RNA were used in a final concentration of 1 μM. The buffer for the first experiments in Fig. 2 contained 1 mM TRIS (2-amino-2-hydroxymethyl-propane-1,3-diol) with pH 7.8 at 25 °C and the Debye length was titrated with KCl. In all experiments, the monovalent TRIS buffer was accounted for when calculating the Debye length.

The measurements can be seen in Fig. 2. For the 50-mer we do not find any difference between single-stranded and double-stranded DNA, and also the 22-mer oligomers are surprisingly similar. Unexpectedly, the double-stranded polymers even show a lower Soret coefficient. Since the charge of a particle enters Eq. (3) quadratically, one could expect a factor of 4 difference between single-stranded and double-stranded DNA and RNA. However, their Soret coefficients are quite similar with a similar effective charge (see Table I). This can be explained by the Manning charge condensation theory also in the case of DNA [25]. Single- and double-stranded DNA
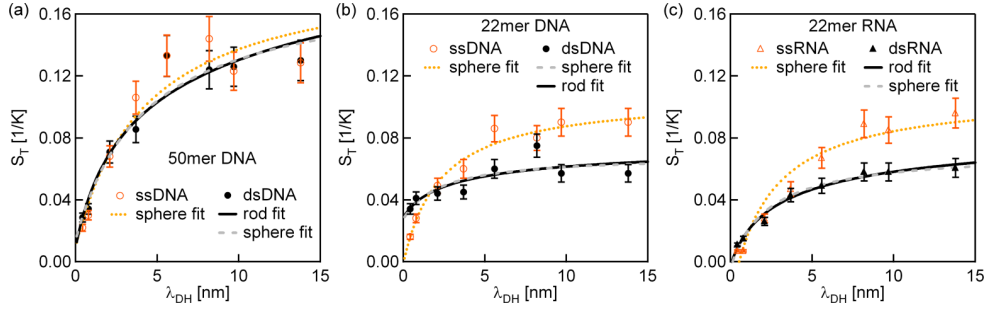
FIG. 2. (Color online) The thermophoresis of double-stranded DNA and RNA. The data can be fitted as a rod with radius $R = 1$ nm and a length of $L = 7.5$ and 17 nm for 22-mer and 50-mer, respectively. Single-stranded oligonucleotides can be viewed as spheres with a hydrodynamic radius of 2 and 3.7 nm for the 22-mer and the 50-mer, respectively. In each case the other model geometry can be similarly fitted to the thermophoresis measurements. The sphere and the rod fit and yield very similar effective charges Z_{eff} for the double-stranded measurement data (see Table I) The Debye length was titrated using KCl including the 1 mM TRIS buffer at pH 7.8. The measurements were conducted at 25 °C.

show for the same length about the same charge. Accordingly, the electrophoretic mobility of single- and double-stranded oligomers is very similar [26]. If the geometry does not add additional factors, thermophoresis, due to a similar effective charge, does not discriminate between single- and double-stranded RNA or DNA. In particular, the thermophoretic depletion does not differ by a factor of 4 due to the doubling of the charge and the Q_{eff}^2 factor in the thermophoresis models [5,6,7,10]. The fits shown in Fig. 2 are explained in the next section.

B. Theory

1. Nonspherical geometry

In previous studies short DNA was used as a model system to experimentally test the capacitor model of thermophoresis [5]. The persistence length of single-stranded DNA does depend on salt concentration with values ranging between 10 and 32 Å, i.e., a length ranging from two to seven bases [27]. So a spherical shape does not fully approximate the molecule shape, but the molecule might be better modeled by a rod, since their persistence length is about 170 base pairs [28]. Wang *et al.* [11] calculated the Soret coefficient for a long

cylinder with neglected end effects and for a known surface charge density. Here, we will adapt the spherical capacitor model to elongated rods. The molecule shape is modeled as a sphere, which is cut in halves, with an inserted cylinder of the same radius (see Fig. 1). Thus, also the end effects can be included in the model. For comparison we will calculate all three models: the sphere, the cylinder without end caps, and the combined structure, which we call a rod.

2. Calculation

The rod capacitor (capacitance C_{rod}) is composed of two capacitors in parallel: a spherical capacitor (C_{sphere}) and a cylindrical capacitor (C_{cylinder} with the length L reduced by $2R$, i.e., the length of the end caps). Thus we start with the capacitances in Eq. (1).

$$C_{\text{sphere}} = 4\pi\varepsilon R(R/\lambda_{\text{DH}} + 1),$$
$$C_{\text{cylinder}} = \frac{2\pi\varepsilon L}{\ln(\lambda_{\text{DH}}/R + 1)},$$
$$C_{\text{rod}} = C_{\text{sphere}} + C_{\text{cylinder}}, \tag{1}$$

with ε being the dielectric constant of water; $\lambda_{\text{DH}} = \sqrt{\frac{\varepsilon kT}{N_A e^2 \sum_i c_i z_i^2}}$ the Debye-Hückel screening length, or Debye length in short; k the Boltzmann constant; T the absolute temperature; N_A the Avogadro constant; e the elementary charge; c_i the concentration of the ion species i and z_i the charge number of the ion species i; R the radius of the sphere and of the cylinder; and L the overall length; see Fig. 1. The energy stored in a capacitor is $W = Q^2/(2C)$, with $Q = Z_{\text{eff}}e$ being the effective charge of the particle, and Z_{eff} the effective charge number in multiples of the elementary charge e. Using Eq. (1) we find the energies [Eq. (2)]:

$$W_{\text{sphere}} = \frac{Q^2}{8\pi\varepsilon R(R/\lambda_{\text{DH}} + 1)},$$
$$W_{\text{cylinder}} = \frac{Q^2\ln(\lambda_{\text{DH}}/R + 1)}{4\pi\varepsilon L}, \tag{2}$$
$$W_{\text{rod}} = \frac{Q^2}{4\pi\varepsilon[2\text{R}(R/\lambda_{\text{DH}} + 1) + (L-2\text{R})/\ln(\lambda_{\text{DH}}/R+1)]}.$$

TABLE I. Effective charges assumed for the fits in Figs. 2 and 4. We fitted Z_{eff} and assumed the radius to be $R = 2.0$ nm and $R = 3.7$ nm for 22-mer and 50-mers based on measurements of the diffusion coefficient in the absence of PEG. The temperature was assumed to be 25 °C, the relative permittivity of water $\varepsilon_r = 78$ and its temperature derivative $\partial\ln\varepsilon/\partial\ln T = -1.35$.

	Z_{eff} for Fig. 2 without PEG	Z_{eff} for Fig. 4 with 3% PEG	Z_{eff} for Fig. 4 with 6% PEG
50-mer ssDNA sphere	20.3 ± 1.3	6.2 ± 0.9	10.6 ± 1.4
50-mer dsDNA sphere	19.5 ± 1.0		
50-mer dsDNA rod	18.6 ± 1.0		
22-mer ssDNA sphere	11.6 ± 0.4	6.1 ± 0.4	4.2 ± 0.3
22-mer dsDNA sphere	7.1 ± 1.0		
22-mer dsDNA rod	6.9 ± 1.0	4.7 ± 0.4	3.4 ± 0.5
22-mer ssRNA sphere	12.9 ± 0.6		
22-mer dsRNA sphere	9.7 ± 0.3		
22-mer dsRNA rod	9.3 ± 0.3		

Thus, the Soret coefficient of the sphere $S_{T\,\text{sphere}}$, the cylinder $S_{T\,\text{cylinder}}$, and the rod $S_{T\,\text{rod}}$ can be calculated from

the temperature derivative of the electric shielding energy [5–7,10,11] [Eq. (3)]:

$$S_T = \frac{1}{kT}\frac{\partial W}{\partial T},$$

$$S_{T\,\text{sphere}} = \frac{Q^2}{kT^2 16\pi\varepsilon\lambda_{\text{DH}}(R/\lambda_{\text{DH}}+1)^2}\left[1 - \frac{\partial\ln\varepsilon}{\partial\ln T}\left(1 + \frac{2\lambda_{\text{DH}}}{R}\right)\right],$$

$$S_{T\,\text{cylinder}} = \frac{Q^2}{kT^2 4\pi\varepsilon L}\left[\frac{\lambda_{\text{DH}}(1 + \partial\ln\varepsilon/\partial\ln T)}{2\text{R}(\lambda_{\text{DH}}/R + 1)} - \frac{\partial\ln\varepsilon}{\partial\ln T}\ln(\lambda_{\text{DH}}/R + 1)\right],$$

$$S_{T\,\text{rod}} = \frac{Q^2}{kT^2 4\pi\varepsilon[2\text{R}(R/\lambda_{\text{DH}}+1) + (L-2\text{R})/\ln(\lambda_{\text{DH}}/R+1)]^2}\left\{\frac{R^2}{\lambda_{\text{DH}}} + \frac{(L-2\text{R})\lambda_{\text{DH}}/R}{2(\lambda_{\text{DH}}/R+1)\ln^2(\lambda_{\text{DH}}/R+1)}\right.$$

$$\left. + \frac{\partial\ln\varepsilon}{\partial\ln T}\left[\frac{(L-2\text{R})\lambda_{\text{DH}}/R}{2(\lambda_{\text{DH}}/R+1)\ln^2(\lambda_{\text{DH}}/R+1)} - \frac{R^2}{\lambda_{\text{DH}}} - 2\text{R} - \frac{L-2\text{R}}{\ln(\lambda_{\text{DH}}/R+1)}\right]\right\}. \quad (3)$$

In case the length of the rod is exactly the diameter of the sphere ($L = 2R$), i.e., no cylinder is inserted, the equation for the rod does yield the spherical equation. The three equations are calculated in Fig. 3(a) resembling a 22-mer. Single-stranded DNA with no secondary structure is a random coil roughly in the shape of a sphere since the persistence length is about two to seven bases [27]. The hydrodynamic radius of the sphere depends on the DNA length, i.e., 2 and 3.7 nm for a 22-mer and a 50-mer, respectively. However, the radius of the rod or the cylinder is that of the DNA strand: 1 nm and the length of double-stranded DNA is (number of base pairs)×0.34 nm, i.e., 7.5 and 17 nm for the 22-mer and the 50-mer, respectively.

3. Debye length larger than the molecule size

For the limit at small salt concentrations, when the Debye length is larger than the hydrodynamic radius, the geometry difference between a sphere or a rod should not affect the capacity energy and thus the Soret coefficient. In the case of an infinite Debye length, a particle can be considered a point charge, regardless of its shape. Formally, $S_{T\,\text{cylinder}}$ goes to infinity for low salt concentrations, but for the rod the end effects become much more important, since the surface of the outer sphere (i.e., of the end caps) grows as λ_{DH}^2, whereas the surface of the outer cylinder only grows with λ_{DH}. For this limit, we obtain

$$S_{T\,\text{sphere}} = \frac{-Q^2\partial\ln\varepsilon/\partial\ln T}{kT^2 8\pi\varepsilon R}. \quad (4)$$

Therefore the Soret coefficient becomes constant for very large λ_{DH}. For the rod the final value equal to a sphere with the same radius is approached only for Debye lengths far too long to be achievable for real electrolytes. Thus, the Soret coefficient of an elongated particle is considerably lower than the Soret coefficient of a sphere with same diameter and charge, and it is about as large as the Soret coefficient of a particle with the same surface.

4. Debye length smaller than the molecule size

For the limit of high salt concentrations, i.e., small Debye lengths, the capacitance changes with surface area similar to a plate capacitor, since the areas of the two plates hardly differ. The Soret coefficient of a plate capacitor is linear in Debye length. Here, the spherical part and the cylindrical parts are separated, because the shielding of both parts does not overlap for such small screening lengths. The area for a spherical and a rodlike molecule of the same radius will differ, and thus the slope of the Soret coefficient will differ. However, the capacitor part of the Soret coefficient will in both cases vanish for the limit of very high salt concentrations. The surface of the two capping half spheres at the end of the rod (together $4R^2\pi$) is exactly as large as the surface of the additional cylinder, if the cylinder was extended all the way to the end ($2\pi RL$ with $L = 2R$). Thus, for the limit of high salt concentration the Soret coefficient of the rod is equal to the Soret coefficient of a cylinder with neglected end effects [see Eq. (5)].

$$\lim_{\lambda_{\text{DH}}\to 0} S_{T\,\text{sphere}} = Q^2/(kT^2 16\pi\varepsilon R^2)(1 - \partial\ln\varepsilon/\partial\ln T)\lambda_{\text{DH}},$$

$$\lim_{\lambda_{\text{DH}}\to 0} S_{T\,\text{cylinder}} = Q^2/(kT^2 8\pi\varepsilon LR)(1 - \partial\ln\varepsilon/\partial\ln T)\lambda_{\text{DH}}$$

$$= 2R/L \lim_{\lambda_{\text{DH}}\to 0} S_{T\,\text{sphere}}, \quad (5)$$

$$\lim_{\lambda_{\text{DH}}\to 0} S_{T\,\text{rod}} = Q^2/(kT^2 8\pi\varepsilon LR)(1 - \partial\ln\varepsilon/\partial\ln T)\lambda_{\text{DH}}$$

$$= \lim_{\lambda_{\text{DH}}\to 0} S_{T\,\text{cylinder}}.$$

This agrees with the approximations by Wang *et al.* [11]. They calculated and compared the Soret coefficient of a particle with constant surface charge. In contrast, we calculate and compare the Soret coefficient for a particle with constant charge, since in our experiments we know the effective charge of the molecule, determined from a length-dependent charge per base [5,7]. This charge per base is approximately the same for single- and double-stranded DNA [26]. If a constant surface charge is maintained, then the charge Q scales with the aspect ratio $L/(2R)$. Since the Soret coefficient is

proportional to the square of the charge Q, our equation matches the one of Wang *et al.* [11] for the limit of high salt concentrations.

The sphere in Fig. 3(b) again models a 22-mer ssDNA. Additionally, rods of different aspect ratios but with the same surface areas are shown. The aspect ratios for the 22-mer and the 50-mer are 3.75 and 8.5, respectively. Only for dsDNA longer than about 50 bases, i.e., an aspect ratio $L/(2R) = 9$, we start to see deviations from the spherical curve. For comparison, the persistence length of dsDNA is about 170 bases [28]. Considering this, the theoretical Soret coefficients are similar for single- and double-stranded oligomers in the range of experimentally accessible Debye lengths. The effects of the elongated shape and the smaller radius approximately cancel each other.

5. Fitting

Since the theoretical curves for the spherical and the rod model are alike, measurements of double-stranded DNA can be fitted equally well with a spherical and a rodlike model (Figs. 2 and 3). As free fitting parameters we choose the number of effective elementary charges and a salt concentration–dependent molecule specific offset, which includes other contributions to the Soret effect such as the ideal gas contribution $1/T$, the nonionic contribution or the Seebeck effect [5], and a depletion contribution from molecular crowding, discussed in the second part of this paper. Both the spherical and the rod model yield very similar effective charge numbers as fitting parameter (Table I).

C. Measurements in the crowding agent polyethylene glycol (PEG)

1. Theory

We shortly recapitulate the theoretical influence of a crowding agent on thermophoresis through depletion forces. As will be seen, the difference between single- and double-stranded DNA is moderate. If the sample concentration is on the order of 1 wt %, or if a crowding agent, e.g., PEG (polyethylene glycol) is present in the solution, an additional excluded volume effect can be noticed in thermophoresis measurements. It can be approximated according to [19,29,30]. The change in Soret coefficient for the molecule of interest, here DNA, has been described by

$$\Delta S_T = -2\pi \left(S_T^{\text{PEG}} - 1/T \right) R_{\text{DNA}} R_{\text{PEG}}^2 c_{\text{PEG}}, \qquad (6)$$

with S_T^{PEG} the infinite dilution Soret coefficient of the crowding agent, e.g., PEG; R_{PEG} its hydrodynamic radius; R_{DNA} the hydrodynamic radius of the particle of interest, e.g., DNA; and c_{PEG} the concentration of the crowding agent.

The Soret coefficient of the molecule of interest, which has a low concentration, depends on the Soret coefficient and concentration of the added crowding agent. If the Soret coefficient of the crowding agent has the same sign as the one of the probed molecule, the crowding agent will accumulate on the cold side and displace the molecule of interest. Jiang *et al.* measured the Soret coefficient of beads
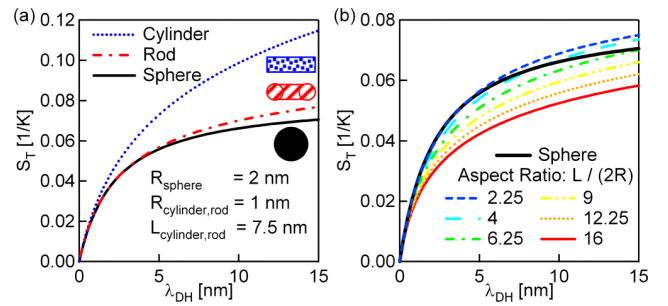

FIG. 3. (Color online) Calculation of the cylinder rod and sphere models for a 22-mer DNA. (a) The single strand is modeled as a sphere with radius $R = 2$ nm and the double strand as a cylinder with $R = 1$ nm and length $L = 7.5$ nm. Between rod and sphere not much difference is found. (b) In comparison to the sphere of (a), we plot rods with different aspect ratios $L/(2R)$ but with the same surface area as the sphere. The typical errors for the Soret coefficient are around 0.01 K^{-1} and given that the effective charge is known to be about 20% and modulates the Soret coefficient quadratically, the rod model and the spherical model cannot be distinguished experimentally for the plotted aspect ratios. A 22-mer and a 50-mer dsDNA have aspect ratios of 3.75 and 8.5, respectively. The Soret coefficients were calculated at temperature $T = 25\,°C$ with an effective charge of $Q = -10\ e$.

in a solution of the crowding agent PEG in the absence of salt [29].

2. Experiments

An apparently robust sign change in the thermophoresis between single- and double-stranded DNA was reported recently [24]. To reassess these results, we conducted salt-dependent experiments of 22-mer ssDNA and dsDNA and 50-mer ssDNA in 3 wt % and 6 wt % PEG poly(ethylene glycol) 10000 (Fluka, Sigma-Aldrich) as crowding agent. We used PEG at a molecular weight of 10000 Da, very similar to the conditions used before [24]. For the reported 5 vol% in solution we used 6 wt %, since pure PEG is a solid with a density of 1.2 g/cm^3. The buffer for the 22-mer contained $10\,\text{m}M$ TRIS pH 7.5 and 1 mM TRIS pH 7.8 for the 50-mer, corresponding to a maximal Debye length of 3.0 and 9.6 nm, respectively. The Debye length was reduced by adding NaCl.

In Fig. 4(a) both single- and double-stranded DNA of 22-mer length show accumulation at 25 °C, in 3 wt % and 6 wt % PEG. An accumulation is found when the Soret coefficient becomes negative, i.e., the molecules wander towards the hot side. Similar to the results in [24], the single-stranded DNA shows a lower accumulation, but the difference is rather a constant addition to the Soret coefficient, not a sign inversion as argued for in [24]. Besides this offset, the characteristic increase with Debye length according to the capacitor model is found. As expected from Eq. (6), we find a higher accumulation, i.e., lower Soret coefficients, for higher PEG concentrations. The reduction in the Soret coefficient caused by PEG is stronger for larger molecules, since the DNA radius enters Eq. (6) [Figs. 4(a) and 4(b)]. The difference is even larger, if we consider that without PEG the larger 50-mer DNA has a higher Soret coefficient than the smaller 22-mer
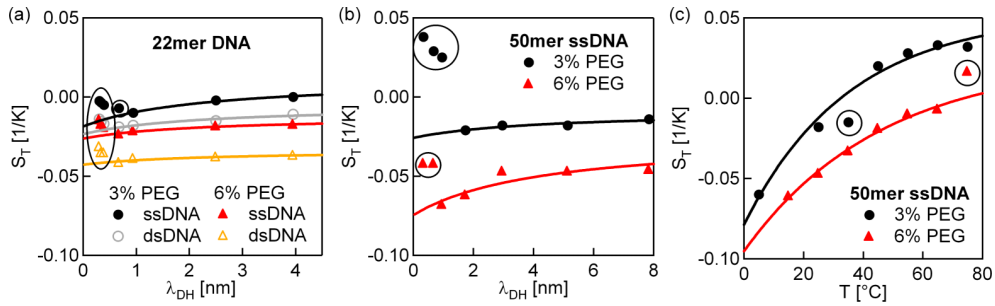
FIG. 4. (Color online) Thermophoresis of ssDNA and dsDNA with PEG in aqueous NaCl solutions. (a,b) Increased PEG concentration leads to more negative Soret coefficients. In contrast to the study of Maeda [24] we find negative Soret coefficients, i.e., accumulation also for ssDNA. We used covalently bound dyes for both dsDNA and ssDNA measurements, not intercalating dyes [24]. The spherical capacitor model was fitted to the data with large Debye lengths. Circled data points were excluded from the fits since at low Debye length we suspect deviations from sticking interactions to the measurement chamber or to PEG. (c) The sign change indicates no fundamental difference between ssDNA and dsDNA, but is merely the result of differential contributions to the Soret coefficient as is shown by measurements under varied base temperature. An empiric temperature dependence [31] was fitted to the data. The 50-mer was measured in $1\,\mathrm{m}M$ TRIS buffer at pH7.8, the 22-mer in $10\,\mathrm{m}M$ TRIS at pH7.5. TRIS was accounted for when titrating with NaCl. Measurements were conducted at 25 °C (a,b) and $10\,\mathrm{m}M$ NaCl (c).

(Fig. 2). Similar to [24], we do find a stronger accumulation for the 50-mer than for the 22-mer.

3. Discussion and Fitting

It was reported [24] that under crowding conditions, a thermophilic behavior of DNA was not found for single strands and only for double-stranded DNA, arguing that the flexible ssDNA could slip through the pores of PEG and show a distinct contrast to dsDNA sequences. We do not find a sign change, but rather a constant shift in the Soret coefficient between single- and double-stranded DNA. Both single- and double-stranded 22-mers of DNA show a thermophilic behavior in PEG. We were using the identical covalent labeling for ssDNA and dsDNA in our experiments, not relying on intercalating dyes for the dsDNA which can show length and temperature-dependent binding for the used short oligonucleotides. In addition, intercalating dyes show a different temperature dependence which needs to be subtracted to infer the Soret coefficient. Only at larger temperatures, both molecules have the known tendency to increase their Soret coefficient (see below), therefore showing the typical thermophobic behavior for charged molecules. As reported before [24], the depletion-based thermophilic effect is enhanced for increasing PEG concentration levels.

Similar to the finding in pure buffer, we find an increase of the Soret coefficient for decreasing salt concentrations [Figs. 4(a) and 4(b)], given the fact that the effective Soret coefficient introduced by [24] has an inverted sign characteristic and has a positive sign for thermophilic thermophoresis (Figs. 6 and 7 therein). This characteristic can fitted by a capacitor model (Table I). This can be understood since the PEG is uncharged and the Debye length should not be affected. Interestingly, the fitted effective charges decrease for increasing PEG concentration. It is known from both electrophoresis and thermophoresis of single-stranded DNA that the effective charge per base of the nucleotides decreases for larger molecules [5]. We could speculate that the addition of PEG could lead to a similar effect by increasing the interactions

of the single strands, therefore reducing their effective charge in the crowded environment. For exceedingly large high salt concentrations, the Soret coefficient increases, as indicated by circles, which can be an artifact from the increased tendency of DNA or RNA to stick to PEG or the capillary walls for increased salinity.

We do not expect the DNA-PEG interaction to depend on salt due to the lack of charges on the side of PEG. Therefore the fit to the capacitor model was performed without these outliers at small Debye lengths. The fit parameters are given in Table I, showing an about twofold reduction of the effective charge in the crowded environment. If we assume that the hydrodynamic radius does not depend significantly on the PEG and salt concentration, the fit yields about half of the effective charge which is found in aqueous solutions. This could mean that residual charge could enter the solution by the introduction of PEG and thus lead in reality to a reduced Debye length. Alternatively, a larger radius of the DNA would have to be assumed, which is, however, in contradiction with the crowding effect. The decrease of amplitude for the capacitor model likely requires the influence of PEG which requires additional contributions, more likely an added discussion of diffusiophoresis.

As a side note, one should not discriminate too strictly between positive and negative Soret coefficients. The sign is merely reporting which components of the Soret coefficients dominate. For example, when the base temperature of the experiment is varied in Fig. 4(c), we find a change in the sign for 50-mer ssDNA in PEG. But similar temperature dependences were measured before without PEG [5]. It is possible to fit the empiric temperature-dependence equation [31],

$$S_T = S_T^\infty \left[1 - \exp\frac{T^* - T}{T_0} \right], \qquad (7)$$

to the data. It yielded $S_T^\infty = 0.052 \pm 0.013$ and 0.024 ± 0.017; $T^* = 32.4 \pm 2.7$ and 73.8 ± 6; $T_0 = 35.4 \pm 9.8$

and 46.0 ± 15.2 for the 3% and 6% PEG solutions, respectively.

III. CONCLUSION

We have shown that single- and double-stranded DNA of the same length behave surprisingly similarly in a temperature gradient. We derived an analytical capacitor model for elongated rods with arbitrary Debye lengths. The spherical and rod-shaped capacitor model behave alike with respect to the Debye length, as shown both theoretically and in experiment. We reassessed the thermophoresis in the crowding agent PEG for single- and double-stranded DNA [24], but now with covalent markers. We cannot confirm a sign change between single- and double-stranded DNA, but find an additive shift in the Soret coefficient. Even for 3% and 6% PEG, we can fit the salt dependence of DNA thermophoresis with the capacitor model. With PEG, both single- and double-stranded DNA accumulate to comparable extents.
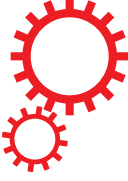
[1] X. Xiong, P. J. Coombs, S. R. Martin, J. Liu, H. Xiao, J. W. McCauley, K. Locher, P. A. Walker, P. J. Collins, Y. Kawaoka, J. J. Skehel, and S. J. Gamblin, Nature **497**, 392 (2013).

[2] S. Bhogaraju, L. Cajanek, C. Fort, T. Blisnick, K. Weber, M. Taschner, N. Mizuno, S. Lamla, P. Bastin, E. A. Nigg, and E. Lorentzen, Science **341**, 1009 (2013).

[3] V. Srinivasan, A. J. Pierik, and R. Lill, Science **343**, 1137 (2014).

[4] J. L. Parker and S. Newstead, Nature **507**, 68 (2014).

[5] M. R. Reichl, M. Herzog, A. Götz, and D. Braun, Phys. Rev. Lett. **112**, 198101 (2014).

[6] J. K. G. Dhont, S. Wiegand, S. Duhr, and D. Braun, Langmuir **23**, 1674 (2007).

[7] S. Duhr and D. Braun, Proc. Natl. Acad. Sci. USA **103**, 19678 (2006).

[8] J. K. G. Dhont, J. Chem. Phys. **120**, 1632 (2004).

[9] J. K. G. Dhont, J. Chem. Phys. **120**, 1642 (2004).

[10] J. K. G. Dhont and W. J. Briels, Eur. Phys. J. E **25**, 61 (2008).

[11] Z. Wang, H. Kriegs, J. Buitenhuis, J. K. G. Dhont, and S. Wiegand, Soft Matter **9**, 8697 (2013).

[12] E. Ruckenstein, J. Colloid Interface Sci. **83**, 77 (1981).

[13] R. Piazza and A. Guarino, Phys. Rev. Lett. **88**, 208302 (2002).

[14] A. Würger, Phys. Rev. Lett. **98**, 138301 (2007).

[15] R. D. Astumian, Proc. Natl. Acad. Sci. USA **104**, 3 (2007).

[16] Alois Würger, C. R. Mec. **341**, 438 (2013).

[17] S. Hartmann, G. Wittko, F. Schock, W. Groß, F. Lindner, W. Köhler, and K. I. Morozov, J. Chem. Phys. **141**, 134503 (2014).

[18] A. L. Sehnem, R. Aquino, A. F. C. Campos, F. A. Tourinho, J. Depeyrot, and A. M. Figueiredo Neto, Phys. Rev. E **89**, 032308 (2014).

[19] S.A. Putnam and D.G. Cahill, Langmuir **21**, 5317 (2005).

[20] M. Braibanti, D. Vigolo, and R. Piazza, Phys. Rev. Lett. **100**, 108303 (2008).

[21] R Piazza and A Parola, J. Phys.: Condens. Matter **20**, 153102 (2008).

[22] F. M. Weinert and D. Braun, Phys. Rev. Lett. **101**, 168301 (2008).

[23] S. A. Allison and S. Mazur, Biopolymers **46**, 359 (1998).

[24] Y. T. Maeda, T. Tlusty, and A. Libchaber, Proc. Natl. Acad. Sci. USA **109**, 17972 (2012).

[25] O. A. Hickey, T. N. Shendruk, J. L. Harden, and G. W. Slater, Phys. Rev. Lett. **109**, 098302 (2012).

[26] E. Stellwagen, Y. Lu, and N. C. Stellwagen, Biochemistry **42**, 11745 (2003).

[27] A. Y. L. Sim, J. Lipfert, D. Herschlag, and S. Doniach, Phys. Rev. E **86**, 021901 (2012).

[28] E. Stellwagen and N. C. Stellwagen, Electrophoresis **23**, 2794 (2002).

[29] H.-R. Jiang, H. Wada, N. Yoshinaga, and M. Sano, Phys. Rev. Lett. **102**, 208301 (2009).

[30] A. Würger, Rep. Prog. Phys. **73**, 126601 (2010).

[31] S. Iacopini, R. Rusconi, and R. Piazza, Eur. Phys. J. E **19**, 59 (2006).

SCIENTIFIC REPORTS

OPEN

Quantitative thermophoretic study of disease-related protein aggregates

Manuel Wolff[1], Judith J. Mittag[2], Therese W. Herling[3], Erwin De Genst[3], Christopher M. Dobson[3], Tuomas P. J. Knowles[3], Dieter Braun[1] & Alexander K. Buell[3,†]

Amyloid fibrils are a hallmark of a range of neurodegenerative disorders, including Alzheimer's and Parkinson's diseases. A detailed understanding of the physico-chemical properties of the different aggregated forms of proteins, and of their interactions with other compounds of diagnostic or therapeutic interest, is crucial for devising effective strategies against such diseases. Protein aggregates are situated at the boundary between soluble and insoluble structures, and are challenging to study because classical biophysical techniques, such as scattering, spectroscopic and calorimetric methods, are not well adapted for their study. Here we present a detailed characterization of the thermophoretic behavior of different forms of the protein α-synuclein, whose aggregation is associated with Parkinson's disease. Thermophoresis is the directed net diffusional flux of molecules and colloidal particles in a temperature gradient. Because of their low volume requirements and rapidity, analytical methods based on this effect have considerable potential for high throughput screening for drug discovery. In this paper we rationalize and describe in quantitative terms the thermophoretic behavior of monomeric, oligomeric and fibrillar forms of α-synuclein. Furthermore, we demonstrate that microscale thermophoresis (MST) is a valuable method for screening for ligands and binding partners of even such highly challenging samples as supramolecular protein aggregates.

Protein aggregation into highly ordered, insoluble amyloid fibrils and their oligomeric precursors is a hallmark of a range of disorders, many of them neurodegenerative in nature, such as Alzheimer's and Parkinson's diseases[1]. In the latter condition, intracellular amyloid deposits, known as Lewy bodies, of the intrinsically disordered protein α-synuclein form a major characteristic of the pathology[2]. To date, no cure for this disease exists, a consequence at least in part of the lack of fundamental understanding of the mechanism of aggregation and its associated toxicity, as well as the incomplete characterization of the interactions between aggregates of α-synuclein and other compounds, including small molecules and proteins.

Such interactions are important for both diagnostic (e.g. for positron emission tomography[3]) and therapeutic purposes (e.g. for targeted aggregation inhibitors[4]). In this context there is an urgent need for experimental techniques that can be used for high throughput screening to identify such compounds. Standard techniques, such as isothermal titration calorimetry (ITC)[5] or surface plasmon resonance (SPR)[6] can provide important information, but suffer from a number of limitations, including high levels of sample consumption (ITC), potential surface artifacts (SPR) and high sensitivity to solution conditions (both ITC and SPR).

Analytical methods based on thermophoresis have recently been introduced as alternatives to these established methods for the measurement of binding interactions of biomolecular compounds[7,8]. Thermophoresis, also known as the Soret effect[9], corresponds to the directed net diffusional flux of particles under the influence of a temperature gradient. If the temperature gradient is stationary, the molecular concentration eventually reaches a steady state through the simultaneous and opposite effects of thermal diffusion (with coefficient D_T) and standard (Fick) diffusion (with coefficient D). The phenomenon of thermophoresis was first described in the 19th

[1]Systems Biophysics, Physics Department, Nanosystems Initiative Munich and Center for NanoScience, Ludwig-Maximilians-Universität München, Amalienstr. 54, 80799 München, Germany. [2]Faculty of Physics and Center for Nanoscience (CeNS), Ludwig Maximilians University, Geschwister-Scholl-Platz 1, 80539 Munich, Germany. [3]Department of Chemistry, University of Cambridge, Lensfield Road, Cambridge CB2 1EW, UK. [†]Present address: Institute of Physical Biology, University of Düsseldorf, Universitätsstr. 1, 40225 Düsseldorf, Germany. Correspondence and requests for materials should be addressed to D.B. (email: dieter.braun@lmu.de) or A.K.B. (email: alexander.buell@uni-duesseldorf.de).
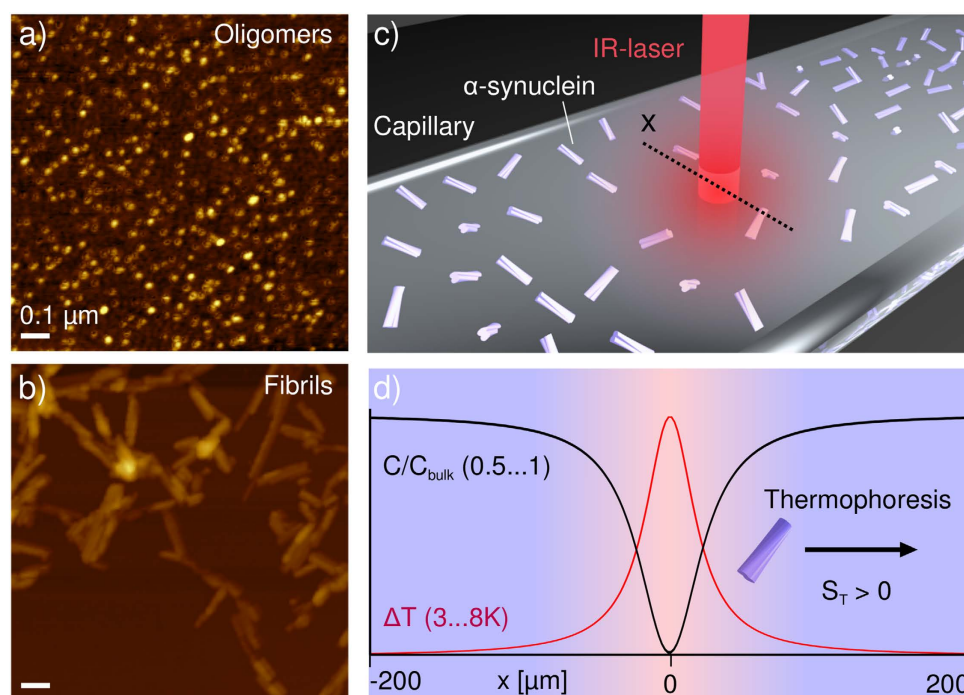
Figure 1. Quantitative thermophoresis of proteins. AFM images of oligomeric (**a**) and fibrillar (**b**) forms of the protein α-synuclein, associated with Parkinson's disease. The oligomers have an average diameter of 15 nm in solution, as determined by fluorescence correlation spectroscopy. (**c**) An initially homogeneous solution, or a suspension of a protein species, here illustrated with fibrillar aggregates, is subjected to localized heating by an IR-laser inside a borosilicate capillary, which leads to directed movement of molecules and complexes along the temperature gradient, until a steady state is established. (**d**) The radially averaged temperature profile (typically established within less than a second after turning on the laser), and the concentration profile (usually established within seconds to minutes) are illustrated schematically at steady state. A schematic fibril is displayed undergoing positive thermophoresis, i.e. migrating away from the heated spot.

century[9,10] and has recently seen a surge in attention, due to its many potential biophysical applications[11] and even possible role in the origins of life[12].

In a thermophoretic experiment, the concentration of thermally diffusing particles or molecules, c, can be described by a combination of local equilibrium and non-equilibrium effects, and follows an exponential distribution: $c(\vec{x})/c_0(\vec{x}_0) = \exp(-S_T(T(\vec{x}) - T_0(\vec{x}_0)))$[13], where $S_T = D_T/D$ is the Soret coefficient. Through the creation of well-defined temperature gradients and the subsequent measurement of concentration distributions at steady state, the intrinsic propensities of particles to exhibit thermophoresis can be determined. Temperature gradients can be created through Joule heating[14], the generation of a hot reservoir[15] or by absorption of infrared (IR) laser radiation (Fig. 1c)[16], and the concentration profiles of the species undergoing thermophoresis can be mapped via measurements of variations in refractive index[17], light scattering[18] or fluorescence intensity[16], provided that the species are suitably labeled or show intrinsic fluorescence[11].

The increasing recognition of the potential importance of thermophoresis for the characterization of biomolecular binding equilibria is paralleled by extensive fundamental research activity on the thermophoretic properties of polymeric and colloidal systems[16,19–21], as well as solvent mixtures[22]. Despite the current lack of an overarching theory of thermophoresis of different systems, interesting trends have been observed in a variety of systems. For nonionic polymers a saturation of the thermal diffusion coefficient after several Kuhn segments has been found in a large set of nonpolar solvents[23] as well as in water[20,24]. Nevertheless, no general tendency of increasing or decreasing Soret coefficient with size for uncharged polymers has been observed[20,25] and theoretical models are still under debate[26,27]. For charged polymers, substantial progress has been made in the understanding of ionic effects in recent years. Thermal gradients lead to the development of concentration gradients for the ionic species[28], which contribute to the movement of charged polymers by the build-up of electric fields[16,29] and diffusiophoresis[30]. Furthermore, thermal gradients also introduce contributions to the Soret coefficient which arise from the change in free energy of the Debye layer associated with the temperature change[31] and can be described by considering local equilibrium[13]. These models have been successfully tested for spherical particles by variation of ionic strength[16,32,33] and extended to elongated structures, such as viruses[34] and DNA[35]. The Soret coefficients of proteins and various other charged polymers have also been found to increase with temperature in a manner that is described by an empirical formula[17]. Although fundamental research into the origin of this temperature dependence is ongoing, the Soret effect has already been exploited for particle separation[15] and the detection of phase transitions[36].
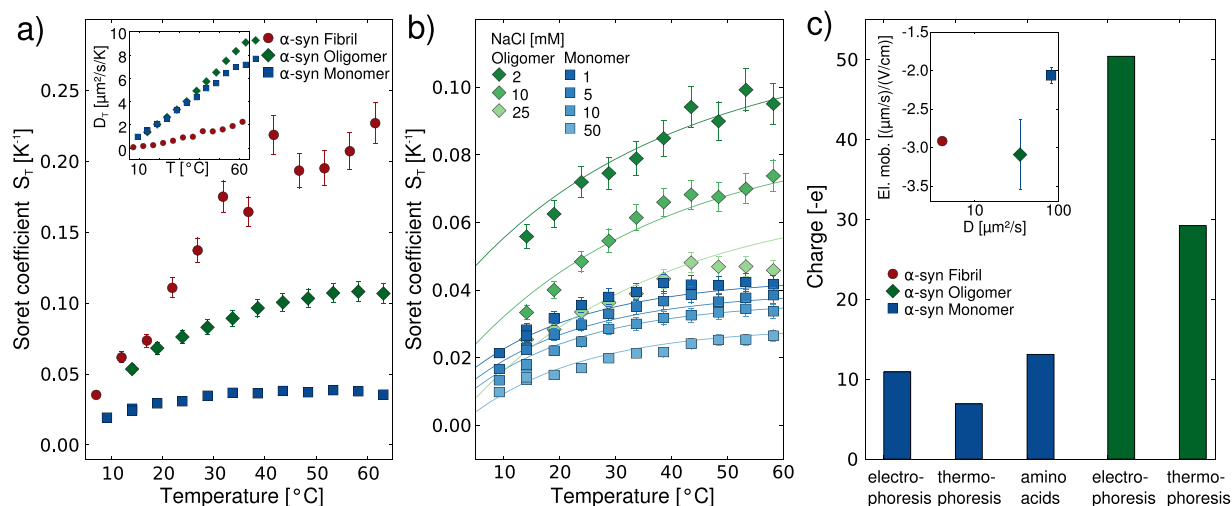
Figure 2. Thermophoretic characterization of three distinct α-synuclein species. (a) The Soret coefficients, S_T, of monomeric, oligomeric and fibrillar α-synuclein (in 1 mM Tris buffer at pH 7.4) as a function of temperature, showing their strong size-dependence. Inset: The thermal diffusion coefficient, $D_T = D S_T$, as a function of temperature. **(b)** Fit of the temperature dependence of S_T of α-synuclein monomers (blue) and oligomers (green) at different concentrations of added NaCl. The data are globally fitted to a model that includes the electrostatic effects relevant for thermophoresis and where the effective charges of the species and the Soret coefficient of the Tris ion are the only free parameters. **(c)** The charges determined from the fits in **(b)** compared with the charges determined from an analysis of the electrophoretic mobilities (supplementary section 6). For the monomer, the charge expected from the amino acid composition is also plotted. Inset: The free flow electrophoretic mobilities[43] of fluorescently labeled monomeric, oligomeric and fibrillar α-synuclein (in 5 mM Tris buffer pH 7.4) are plotted against their diffusion coefficients (from FCS measurements[42], and supplementary section 5).

The binding of a ligand to a biomolecule can in many cases induce a change in thermophoretic behavior that is sufficiently large to be detected, and hence a binding curve can be obtained through measurements of a dilution series of one of the binding partners. It has been shown, for example, that binding constants for protein-ligand interactions can be obtained rapidly in this way, even under the most challenging solution conditions and using only minute quantities of sample[8].

Despite the increasing attention being focused on such effects and the great potential of thermophoresis for high throughput screening, it is not yet possible to predict from first principles the value of the Soret coefficient of any protein under a given set of conditions, or even the sign and magnitude of a change in the Soret coefficient induced by the binding of a ligand. Indeed, very few studies have so far addressed the problem of quantitative measurements of the thermophoresis of proteins[17] or protein assemblies[37]. The aim of the studies described here is to advance our fundamental understanding of protein thermophoresis through the study of distinct forms of the protein α-synuclein. We have chosen this protein because of its relevance to Parkinson's disease, as well as its well-established ability to form different types of stable aggregates, such as oligomeric structures[38] and mature amyloid fibrils[39]. In addition, the monomeric protein is kinetically highly stable in bulk solution, and in the absence of catalytic surfaces it does not aggregate at a detectable rate even at high concentrations[40,41], facilitating its study by biophysical techniques. Therefore, α-synuclein represents an excellent system through which to study the influence of the size and nature of protein assemblies on their thermophoretic behavior. In particular, we have used a combination of fluorescence correlation spectroscopy (FCS)[42] and microfluidic free flow electrophoresis[43], along with measurements of the Soret coefficients of fluorescently labeled monomeric and aggregated α-synuclein to examine the importance of electrostatic effects in protein thermophoresis. We find that while the different aggregated species cannot be discriminated based on their electrophoretic mobilities, they exhibit very distinct thermophoretic mobilities. In addition, we show that the binding of a high affinity single domain antibody (nanobody) as well as of a natural small molecule, epigallocatechin gallate (EGCG[44,45]) to α-synuclein aggregates can be probed by exploiting changes in thermophoretic behavior upon binding. These results establish thermophoresis as a useful method for binding studies to a highly challenging class of target structures.

Results

Thermophoresis of protein structures is size-dependent. We have produced fluorescently labeled monomeric, oligomeric and fibrillar α-synuclein (see supplementary section 2 for detailed protocols) and characterized these different species by atomic force microscopy (AFM, Fig. 1) and FCS (supplementary section 5). For the aggregated forms of the protein, we used a minimally invasive labeling strategy, in which only a small fraction of the protein molecules within each aggregate is labeled. We then measured the Soret coefficients, S_T, of these three distinct and well-defined forms of α-synuclein at low ionic strength (1 mM Tris buffer) as a function of temperature (Fig. 2a), using a thermophoresis setup with laser heating and a camera[16] (see supplementary

section 4) to record the time evolution and steady-state distribution of the concentration of fluorescently labeled protein aggregates. In these experiments unlabeled protein molecules and aggregates are invisible. The absolute magnitude of S_T was found to increase with the size of the α-synuclein structure (Fig. 2a). A size dependence of the Soret coefficient has been observed previously[13,21,46], but the question of whether or not the thermal diffusion coefficient $D_T = DS_T$ also depends on size has been controversial, although most results point towards the size independence of D_T for simple colloid systems[24,46]. We find here that while monomeric and oligomeric forms of α-synuclein have very similar thermal diffusion coefficients, D_T is markedly smaller for the fibrillar form of the protein (Inset to Fig. 2a). In order to investigate the origin of the size dependence of S_T in more detail, therefore, we have performed experiments under a range of different solution conditions.

The thermophoresis of proteins is dominated by electrostatic effects. We first explored the effects of variations in ionic strength on the thermophoretic behavior of the various proteinacious species studied here, as significant effects have been observed previously for DNA[16]. The magnitude of the Soret coefficient decreases when the ionic strength is increased for monomeric and oligomeric α-synuclein species (Fig. 2b). The absolute change in S_T for a given variation in ionic strength is, however, observed to depend on the size and charge of the α-synuclein species, with a more pronounced dependence being observed for the oligomers. Similar experiments for fibrillar α-synuclein were not pursued because an increase in ionic strength can induce higher order assembly of fibrils, as reported previously[39], making an accurate determination of the absolute Soret coefficient difficult.

We have recently presented a theoretical description that for DNA quantitatively captures the various electrostatic effects important in thermophoresis, such as the capacitor effect and the Seebeck effect[16] and (see supplementary section 7). The most important parameters in this model are the size, charge and electrophoretic mobility of the macromolecule under investigation. We have here been able to determine all of these parameters independently for the three distinct types of α-synuclein species (inset to Fig. 2c) by using FCS[42] to measure the standard (Fick) diffusion coefficients (supplementary section 5); the latter can be used to determine the dimensions of the structures. Assuming spherical geometry[38], we obtain hydrodynamic diameters of 5.6 nm and 15 nm for the monomeric and oligomeric α-synuclein, respectively. In addition, the (sonicated) fibril length distributions were characterized in detail by AFM and we found an average length of ~200 nm and a diameter of ~8 nm. Furthermore, we used microfluidic free flow electrophoresis[43] and (supplementary section 6) to determine the electrophoretic mobility of each species (inset to Fig. 2c). We have fitted the data to a model that takes both the capacitor and Seebeck effects into account (supplementary section 7), allowing us to decompose the Soret coefficient into charge-dependent effects and non-ionic contributions. The fits yield an effective charge that appears to be responsible for the strong dependence of the thermophoresis on the ionic strength of the solution. We can also estimate the charges of the distinct α-synuclein species from their electrophoretic mobilities. To that end, the monomeric and oligomeric forms of α-synuclein were approximated as spheres and the fibrils as rods, enabling us to use the theoretical framework already developed for colloids[47], yielding charges of -10.9 e for the monomer, -50.4 e for the oligomer and a value in the range from -200 e to -300 e for the fibrils (supplementary section 6). The value for the monomer is in good agreement with that calculated from the amino acid composition at this pH (-9.1 e) in addition to the charges carried by the fluorescent label (-4 e). It is interesting to see that the oligomers, despite being composed of ca. 30 monomers on average[38], have a net charge only about 5 times higher than that of the monomer. This difference between expected and determined charge, which is even more pronounced for fibrillar α-synuclein, can be explained through a shift of the pK_a values of the ionizable residues in the aggregates with respect to the monomeric state, as well as the absorption and incorporation of counter ions into the oligomers and fibrils[48]. The values of the effective charges (see Fig. 2c for an overview) of the α-synuclein monomers and oligomers calculated from the thermophoretic data (-6.9 e and -29.2 e) are significantly smaller than those resulting from the fits to the electrophoretic mobilities (-10.9 e and -50.4 e). Due to the lack of experimental data on the ionic strength dependence of the S_T values of the fibrils, we cannot estimate the thermophoretic charge of the fibrils. Since studies that directly compare effective charges determined from electrophoretic and thermophoretic measurements are rare[30,33], the data shown here provide an important benchmark through which to improve the theoretical descriptions of both electrophoretic and thermophoretic phenomena of complex biomolecular structures such as protein molecules and supramolecular protein aggregates. Note that the Soret coefficient of the positively charged Tris ion was determined from a global fit to the ionic strength dependence of the thermophoresis of monomeric and oligomeric α-synuclein to be 0.0031/K, and the value obtained is at least comparable in magnitude to the one of the sodium ion with 0.00469/K[16,49].

We next tested whether or not the presence of an excess of unlabeled monomeric α-synuclein leads to a change in the thermophoresis of the fluorescently labeled monomeric, oligomeric and fibrillar α-synuclein (Fig. 3). We find that the thermophoresis of both labeled monomeric and oligomeric α-synuclein is decreased by the presence of an excess (70 μM) of unlabeled monomeric α-synuclein (Fig. 3a). Furthermore, we find that the Soret coefficient of fibrillar α-synuclein at 20 °C in the presence of 40 μM unlabeled monomeric α-synuclein shows also a decreased value compared to the sample without added monomeric protein (Fig. 3b). Under these conditions of low ionic strength and relatively low temperature, the rate of incorporation of monomeric protein into the amyloid fibrils is negligibly slow[39]. However, when we heat the samples for 20 min to 70 °C, and again determine the Soret coefficient (Fig. 3b), we find that S_T has significantly increased for the sample with the added monomer, whereas the increase is smaller for the sample without any added monomer. Analysis of the length distributions of the amyloid fibrils before and after the incubation at 70 °C illustrates that the fibrils have increased in length due to monomer incorporation (Fig. 3c). As the temperature is increased, the structural rearrangements and/or desolvation necessary for the incorporation reaction of the α-synuclein monomers into the fibrils are significantly accelerated[39,50].

These results suggest that the presence of unlabeled monomeric α-synuclein does indeed affect the thermophoresis of monomeric and aggregated α-synuclein. In order to elucidate the physical origin of this effect, we have
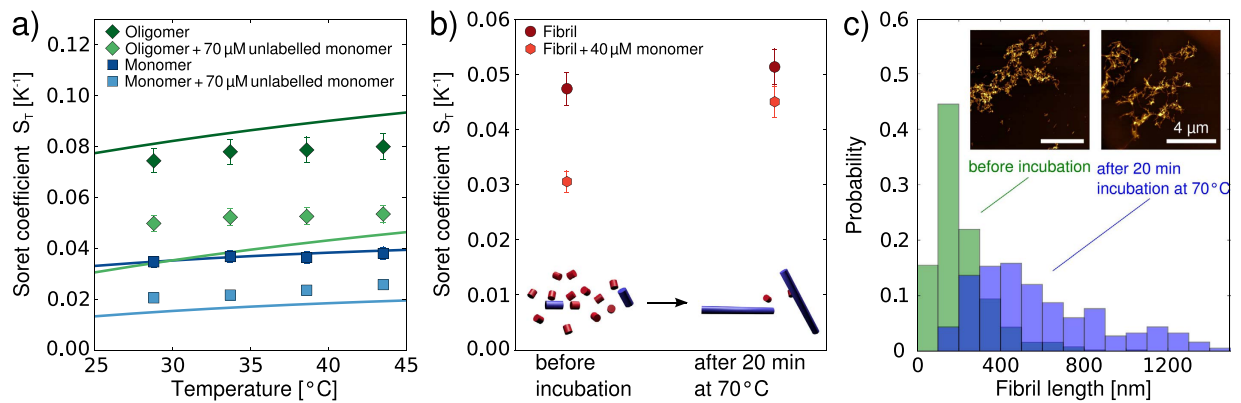
Figure 3. The effect of unlabeled (and hence invisible) monomeric α-synuclein on the thermophoresis of the distinct α-synuclein species. (**a**) Temperature dependence of S_T for labeled monomeric and oligomeric α-synuclein in the presence and absence of a high background concentration (70 μM) of unlabeled monomeric α-synuclein in 1 mM Tris buffer pH 7.4. The solid lines are predictions if the unlabeled monomer is treated as an ionic species within the theoretical thermophoretic model used here (see main text and supplementary section 7). (**b**) The Soret coefficient of fibrillar α-synuclein at 20 °C, in the presence and absence of 40 μM unlabeled monomeric α-synuclein, before and after a 20 min period of heating to 70 °C. (**c**) Length distributions of the α-synuclein fibrils with added unlabeled monomer before and after 20 min heating to 70 °C.

computed the predicted decrease in Soret coefficient due to the additional Seebeck and capacitor effects caused by the presence of the unlabeled monomer, treating the latter as an additional salt species with the Soret coefficient and charge as determined above for labeled monomer (mean value over the examined temperature range: $S_T^{mon} = 0.031/K$). The predictions are shown in Fig. 3a as solid lines and show that the decrease in Soret coefficient induced by the presence of the unlabeled monomer can be quantitatively described by treating the unlabeled α-synuclein monomer as a dissolved electrolyte. It is surprising that this simple approximation yields a relatively good description of the observed behavior, given the limited validity of Debye Hückel theory when treating highly charged macromolecules, such as the α-synuclein monomers, as counterions in the capacitor effect. Indeed, the Debye length at the ionic strength that can be formally attributed to the presence of the 70 μM unlabeled α-synuclein (ca. 5 nm) is much shorter than the average distance between the protein molecules at this concentration (ca. 30 nm). Nevertheless, based on the agreement between the experiments and the modeling, the decrease in Soret coefficient of the three α-synuclein species in the presence of an excess of unlabeled monomeric α-synuclein appears to be caused, at least in part, by the electrostatic effects exerted by the latter on the former. In the case of labeled α-synuclein monomer, the addition of unlabeled monomer is of course equivalent to an increase in the total concentration of the protein, and it has been reported previously that an increase in concentration of a charged species decreases the Soret coefficient[16]. Since the concentration of unlabeled monomer is far below the overlap concentration (~0.01 Mol/l), effects of the added species upon viscosity are expected to play a minor role here. Furthermore, even at higher viscosities, the steady state distributions of molecules in a temperature gradient are not necessarily affected, due to the dependence of both D and D_T on viscosity[23], which can lead to viscosity independent Soret coefficients S_T. Therefore the results of our particular experimental design where only part of the protein molecules are visible allow us to conclude that the effect of an increase in concentration on thermophoresis can be understood in the general framework of electrostatic interactions in the dilute regime.

Measurement of ligand binding constants to monomeric and aggregated α-synuclein. Having established the general principles governing the thermophoresis of protein aggregates, we proceeded to investigate the application of this technique for ligand screening and characterization of the binding of ligands to the aggregates. For this purpose, we investigated the effects of the binding of a single domain camelid antibody (nanobody), which has been shown to bind to the disordered C-terminal region of α-synuclein[5], on the thermophoresis of different α-synuclein species. We first determined the S_T values of monomeric and oligomeric α-synuclein in the presence of a saturating concentration of the nanobody (Fig. 4a) and found that in both cases the bound state displays a reduced thermophoretic effect. The nanobody is positively charged at neutral pH (+1.5 e), and therefore the net global charge of the protein-nanobody complex is lower than that of the protein alone. If the observed decreases in Soret coefficient are attributed solely to decreases in charge, it would correspond to a change in charge of +2.7 e for the monomer and +7.0 e for the oligomer (compare solid lines in Fig. 4a). Therefore, at least for the monomer, which is known to bind with a stoichiometry of 1:1 to the nanobody, the observed effect appears larger than expected purely on electrostatic grounds. One reason for this enhanced effect might be the change in overall size and hydrophobicity[51] associated with the binding of the nanobody. For the oligomers, the value of the reduced charge suggests a stoichiometry much larger than 1:1, which is consistent with the fact that the oligomers consist on average of 30 monomers. However, due to lack of detailed structural information for the oligomer, and hence the accessibility of the binding epitopes, it is difficult to estimate the stoichiometry. We were unable to perform similar experiments with fibrillar α-synuclein, as the charge reduction associated with the binding of
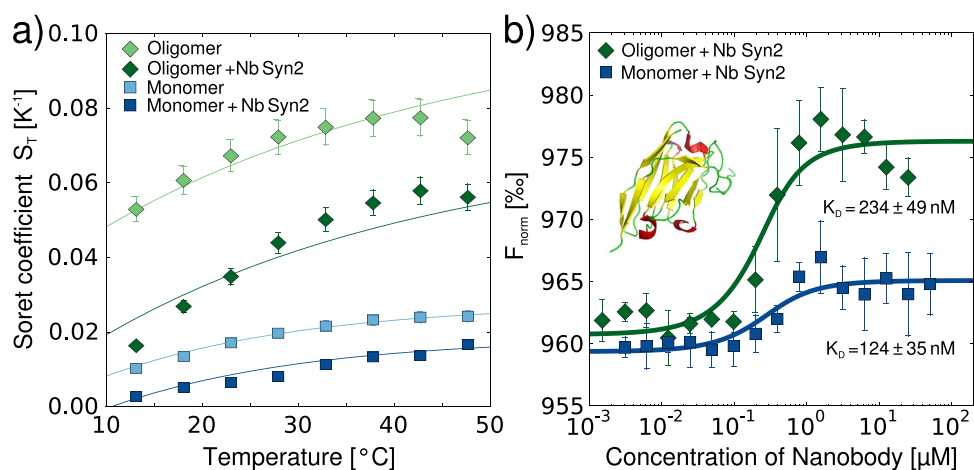
Figure 4. Measurements of the effects of the binding of an antibody on the different α-synuclein species.
(**a**) Temperature dependence of S_T for monomeric and oligomeric α-synuclein in the presence and absence of the single domain camelid antibody (nanobody) Nb Syn2 (structure of Nb Syn2 with coordinates taken from PDB 2X6M[53]). The solid lines are fits that allow the determination of the reduction in effective charge due to the binding of the nanobody. (**b**) Binding curves of Nb Syn2 to monomeric and oligomeric α-synuclein obtained with a thermophoresis setup that monitored the time course of the fluorescence intensity at the position of heating. Each data set combines the results from three independent experiments. The data for the monomer were shifted up by 40‰ for better clarity.

the nanobody led to almost instantaneous formation of macroscopic assemblies of fibrils, that rendered accurate determination of the Soret coefficient impossible.

Based on the observed change in Soret coefficient upon nanobody binding, however, we tested if the binding constant of the nanobody to both monomeric and oligomeric α-synuclein could be measured by using a simplified thermophoresis setup that monitors the time evolution of the total fluorescence intensity in the area of elevated temperature, rather than the full spatial distribution as in the setup used for the determination of the Soret coefficients (integrated vs. spatially resolved approach, see supplementary section 4). In Fig. 4b, we show the corresponding binding curves from the integrated measurements. We obtain binding affinities of the nanobody to monomeric α-synuclein that are in excellent agreement with a previously determined value, obtained from ITC measurements (124 ± 35 nM vs. 130 ± 23 nM[5]). The binding affinity to the oligomers (234 ± 49 nM) had not previously been reported, partly due to the challenge of obtaining sufficient quantities of pure oligomers, which we have been able to overcome by exploiting the low sample requirements of thermophoresis. Interestingly, the thermophoresis values of the oligomer-nanobody system in the fully bound state do not reach a stable plateau, but rather decrease linearly. This effect could be caused by the electrostatic influence of the excess free nanobody on the thermophoresis of the oligomer-nanobody complex. In general, electrostatic effects of free ligand molecules might in this way be able to distort binding curves of charged molecules determined by thermophoresis, if the affinity is sufficiently low such that high ligand concentrations need to be employed. However, in the present case, we do not expect a significant influence on the K_d value, due to the small net charge of the nanobody and the relatively high affinity.

We then investigated the binding of the small molecule epigallocatechin gallate (EGCG), one of the main constituents of green tea, to α-synuclein aggregates. This molecule has been reported to bind to various species on the aggregation pathway of α-synuclein and even to remodel mature amyloid fibrils[44]. We again first probed whether or not the binding to fibrillar and oligomeric α-synuclein manifests itself in a change in Soret coefficient. Despite the fact that EGCG is not charged, we measured a decrease in Soret coefficient upon its binding to both oligomeric and fibrillar α-synuclein (Fig. 5a). The global charge of the aggregates is not expected to change upon binding; indeed, the electrophoretic mobilities of the oligomers and fibrils of α-synuclein are very similar with and without bound EGCG (see inset of Fig. 5a). Therefore it is likely that changes in the overall protein-solvent interactions are responsible for the observed change in S_T. Indeed, it has been proposed that thermophoresis represents a way of probing interactions of particles and molecules with the solvent[32]. Such a proposition is rendered plausible by a significant, temperature-dependent non-electrostatic contribution to S_T (see supplementary section 7) that we were able to determine by subtracting the electrostatic contributions from the overall value of S_T.

Furthermore, as in the case of the nanobody, the binding constant of EGCG to oligomeric and fibrillar α-synuclein can be determined by using the rapid and straightforward integrated approach (Fig. 5b). In these experiments, we found that the ratio of labeled to unlabeled protein within the aggregates is an important experimental parameter, in particular in the case of a compound that is able to influence the fluorescence intensity of the label upon binding, such as EGCG. In addition, if the ratio of the labeled to the unlabeled protein is too high, the surface properties, and hence the binding behavior of α-synuclein aggregates can change significantly as compared to a completely unlabeled structure (supplementary section 4). Using an optimized ratio of labeled to unlabeled protein of ~0.02–0.03 for both aggregate species, we determined the binding constant of EGCG to α-synuclein amyloid fibrils and oligomers under these conditions to be $2.5 \pm 0.4\,\mu$M and $4.3 \pm 0.8\,\mu$M,
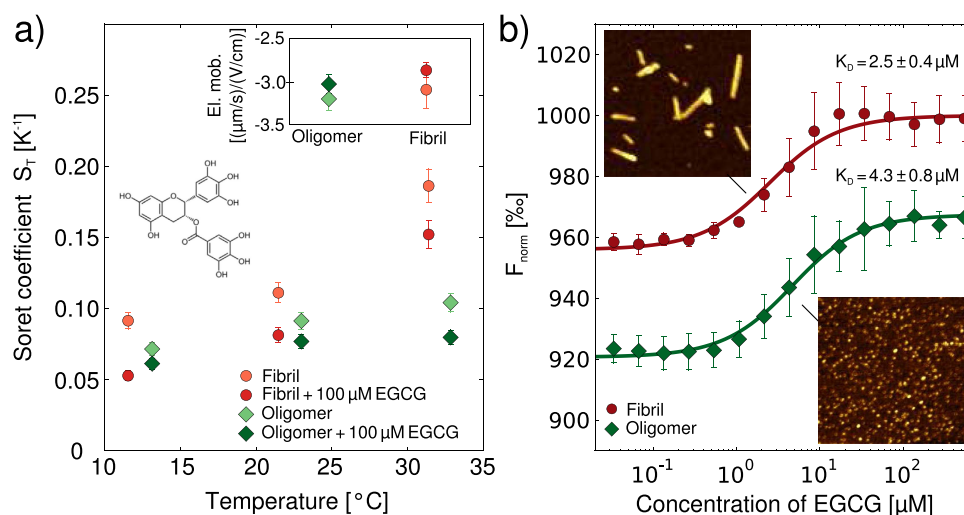
Figure 5. Measurement of binding of EGCG (structure shown in a) to α-synuclein aggregates. (**a**) Measurements of the Soret coefficients of oligomeric and fibrillar α-synuclein in the presence and absence of 100 μM EGCG. In contrast to thermophoresis, the electrophoretic mobilities remain virtually unchanged in the presence of EGCG (see inset). (**b**) Binding constants for the interactions of EGCG with oligomeric and fibrillar α-synuclein were measured using the integrated thermophoresis approach. Each data set is an average of three independent experiments. The insets show AFM images (image sizes are 1 μm $\times$ 1 μm) taken after incubation of oligomers and fibrils for 12 h with 100 μM EGCG. No morphological changes could be detected (compare with Fig. 1a,b).

respectively. The affinity for the fibrils is approximately one order of magnitude lower than the value reported previously under conditions of higher ionic strength[44], whereas the affinity of EGCG for oligomers has not previously been measured. It has, however, been reported that EGCG can induce structural changes in amyloid fibrils and other protein aggregates[44], and such a substantial structural rearrangement can be expected to affect the thermophoretic behavior, complicating the determination of binding constants. In order to test whether or not such effects occurred during our binding studies, we incubated oligomeric and fibrillar α-synuclein for 12 h in the presence of 100 μM EGCG followed by AFM imaging, to allow for sufficient time for even slow remodeling processes to take place. The resulting images are shown as insets in Fig. 5b and reveal no noticeable change in morphology compared to freshly prepared oligomers and fibrils (compare with Fig. 1c,d), suggesting that under the conditions employed here, no significant remodeling of fibrils and oligomers is induced by EGCG.

Discussion

We describe in this paper the results of a comprehensive experimental approach that has allowed substantial progress to be made towards a quantitative understanding of the thermophoresis of monomeric and aggregated forms of proteins. The approach consists of a combination of precise control of sample preparation (solution conditions, labeling position and density), independent and quantitative measurements of size, electrophoretic mobility and thermophoretic mobility, as well as theoretical modeling. With this strategy, we have shown that electrostatic effects, in particular electrophoresis in the field created by the temperature-induced ion gradient ('Seebeck effect'), as well as the temperature dependence of the ion cloud extension and its associated electrostatic energy ('capacitor effect') (supplementary section 7 and for details of the modeling process)[16], are important factors in the thermophoresis of proteins and protein aggregates. These conclusions are consistent with those reported previously for nucleic acids[16,32], and therefore suggest that there may be universal principles that govern the thermophoresis of charged macromolecules. Such a general understanding of the well-established physico-chemical phenomenon of thermophoresis represents an important step in the further development of this technique as an experimental strategy for characterizing biomolecular interactions.

We were able to combine the advances made using custom built research tools, which allow for the characterization of a range of well-defined physical properties (diffusion coefficient, electrophoretic mobility and Soret coefficient), with the ease of use of a simplified thermophoresis setup that can be applied in a straightforward manner for the determination of binding constants. This dual strategy has allowed us to exploit the precise control of sample preparation for the detection and characterization of the binding of a range of ligands (small molecules and macromolecules) to different types of disease-related protein aggregates. Indeed, we were able to investigate structures ranging from soluble monomeric protein molecules to oligomeric structures and mature amyloid fibrils. Because of the importance of electrostatic effects in defining the magnitude of the observed thermophoretic effect, these results show that thermophoresis is very well suited for the study of binding events that lead to a change in charge.

Even in cases where there is no change in global charge, however, we found that thermophoresis allowed for detection of binding events, due to the additional dependence on parameters such as size and interaction with the solvent. Indeed, we observed that protein aggregates that are very different in size and structure, but which display a very similar electrophoretic mobility, such as oligomeric and fibrillar α-synuclein, show a marked difference

in thermophoretic mobility. Furthermore, the binding of a ligand that does not lead to a change in global charge and electrophoretic mobility, such as of the compound EGCG, to oligomeric and fibrillar α-synuclein leads to a detectable change in thermophoretic behavior. It has recently been shown in this regard that the binding of EGCG to α-synuclein oligomers changes their surface properties significantly, and renders them less disruptive to lipid membranes[45]. The thermophoretic response to changes in surface hydrophobicity reflects the physical complexity of systems with non-uniform temperature that leads to a potentially greater discriminatory power compared to other separation techniques based only on size or electrophoretic mobility.

Conclusions

The results of this study have contributed significantly to the rationalization of the size and charge-dependence of protein thermophoresis, and therefore have significantly advanced our fundamental understanding of this phenomenon and enabled a general strategy to be outlined that would deepen this understanding further in the future. This strategy consists of specifically designed sample preparation and labeling strategies, combined with state-of-the-art thermophoretic, electrophoretic and size measurements of the structures under study and theoretical analysis and modeling of the physico-chemical factors that determine thermophoresis. We have been able to show that species such as oligomeric and fibrillar protein aggregates show very similar electrophoretic, but very distinct thermophoretic behavior.

Equally importantly, we have also established the possibility of using thermophoresis for the screening and characterization of ligand binding to disease-related protein aggregates. Despite the fact that microscale thermophoresis is in the process of becoming a well-established experimental technique for protein-ligand binding affinity measurements, it has not previously been reported for the study of ligand binding to supramolecular aggregates, such as amyloid fibrils. Due to their polymeric nature these types of samples are substantially more challenging to handle than most soluble monomeric proteins and we present here a comprehensive protocol for the use of microscale thermophoresis for amyloid-ligand binding assays. The possibility of characterizing novel types of ligands that bind to protein aggregates, both small and large molecules, at high throughput and using minute sample quantities is a highly valuable addition to the experimental toolbox available for the development of diagnostic and therapeutic strategies against protein misfolding diseases. In particular, we would like to emphasize that oligomeric structures, which have been highlighted as the most toxic species on the aggregation pathway[52], often occur only at low concentration and with short lifetimes and hence experimental methods that are rapid and require only small amounts of sample are vital for their study.

Materials and Methods

Detailed protocols for sample preparation and for the measurements of diffusion coefficients, electrophoretic mobilities, Soret coefficients and binding curves can be found in the supplementary materials.

References

1. Knowles, T. P. J., Vendruscolo, M. & Dobson, C. M. The amyloid state and its association with protein misfolding diseases. *Nat Rev Mol Cell Biol* **15,** 384–396 (2014).
2. Spillantini, M. G. *et al.* Alpha-synuclein in lewy bodies. *Nature* **388,** 839–840 (1997).
3. Klunk, W. E., Debnath, M. L. & Pettegrew, J. W. Development of small molecule probes for the beta-amyloid protein of Alzheimer's disease. *Neurobiol Aging* **15,** 691–698 (1994).
4. Mirecka, E. A. *et al.* Sequestration of a β-hairpin for control of α-synuclein aggregation. *Angew Chem Int Ed Engl* **53,** 4227–4230 (2014).
5. Guilliams, T. *et al.* Nanobodies raised against monomeric α-synuclein distinguish between fibrils at different maturation stages. *J Mol Biol* **425,** 2397–2411 (2013).
6. Ge, J.-F., Qiao, J.-P., Qi, C.-C., Wang, C.-W. & Zhou, J.-N. The binding of resveratrol to monomer and fibril amyloid beta. *Neurochem Int* **61,** 1192–1201 (2012).
7. Jerabek-Willemsen, M., Wienken, C. J., Braun, D., Baaske, P. & Duhr, S. Molecular interaction studies using microscale thermophoresis. *Assay Drug Dev Technol* **9,** 342–353 (2011).
8. Seidel, S. A. I. *et al.* Microscale thermophoresis quantifies biomolecular interactions under previously challenging conditions. *Methods* **59,** 301–315 (2013).
9. Soret, C. *Archives des Sciences Physiques et Naturelles de Genève* **II,** 48–61 (1879).
10. Ludwig, C. *Sitzungber Bayer Akad Wiss Wien - Math-Naturwiss Kl* **20,** 539 (1856).
11. Seidel, S. A. I. *et al.* Label-free microscale thermophoresis discriminates sites and affinity of protein-ligand binding. *Angew Chem Int Ed Engl* **51,** 10656–10659 (2012).
12. Braun, D. & Libchaber, A. Thermal force approach to molecular evolution. *Phys. Biol.* **1,** 1–8 (2004).
13. Duhr, S. & Braun, D. Thermophoretic depletion follows Boltzmann distribution. *Phys Rev Lett* **96,** 168301 (2006).
14. de Mello, A. J., Habgood, M., Lancaster, N. L., Welton, T. & Wootton, R. C. R. Precise temperature control in microfluidic devices using joule heating of ionic liquids. *Lab Chip* **4,** 417–419 (2004).
15. Vigolo, D., Rusconi, R., Stone, H. A. & Piazza, R. Thermophoresis: microfluidics characterization and separation. *Soft Matter* **6,** 3489–3493 (2010).
16. Reichl, M., Herzog, M., Götz, A. & Braun, D. Why charged molecules move across a temperature gradient: the role of electric fields. *Phys Rev Lett* **112,** 198101 (2014).
17. Iacopini, S. & Piazza, R. Thermophoresis in protein solutions. *Europhys. Lett.* **63(2),** 247–253 (2003).
18. Wiegand, S., Ning, H. & Kriegs, H. Thermal diffusion forced Rayleigh scattering setup optimized for aqueous mixtures. *J Phys Chem B* **111,** 14169–14174 (2007).
19. Würger, A. Transport in charged colloids driven by thermoelectricity. *Phys Rev Lett* **101,** 108302 (2008).
20. Wang, Z., Afanasenkau, D., Dong, M., Huang, D. & Wiegand, S. Molar mass and temperature dependence of the thermodiffusion of polyethylene oxide in water/ethanol mixtures. *The Journal of Chemical Physics* **141(6),** 064904 (2014).
21. Braibanti, M., Vigolo, D. & Piazza, R. Does thermophoretic mobility depend on particle size? *Phys Rev Lett* **100,** 108303 (2008).
22. Hartmann, S. *et al.* Thermophobicity of liquids: Heats of transport in mixtures as pure component properties. *Phys. Rev. Lett.* **109,** 065901 (2012).
23. Stadelmaier, D. & Köhler, W. Thermal diffusion of dilute polymer solutions: The role of chain flexibility and the effective segment size. *Macromolecules* **42(22),** 9147–9152 (2009).

24. Chan, J., Popov, J. J., Kolisnek-Kehl, S. & Leaist, D. G. Soret coefficients for aqueous polyethylene glycol solutions and some tests of the segmental model of polymer thermal diffusion. *J. Sol. Chem.* **32(3),** 197–214 (2003).

25. Kishikawa, Y. *et al.* Temperature dependence of thermal diffusion for aqueous solutions of monosaccharides, oligosaccharides, and polysaccharides. *Phys. Chem. Chem. Phys.* **14,** 10147–10153 (2012).

26. Würger, A. Molecular-weight dependent thermal diffusion in dilute polymer solutions. *Physical Review Letters* **102,** 078302 (2009).

27. Morozov, K. I. & Köhler, W. Thermophoresis of polymers: nondraining vs draining coil. *Langmuir* **30,** 6571–6576 (2014).

28. Römer, F., Wang, Z., Wiegand, S. & Bresme, F. Alkali halide solutions under thermal gradients: Soret coefficients and heat transfer mechanisms. *J Phys Chem B* **117,** 8209–8222 (2013).

29. Vigolo, D., Buzzaccaro, S. & Piazza, R. Thermophoresis and thermoelectricity in surfactant solutions. *Langmuir: the ACS journal of surfaces and colloids* **26,** 7792–7801 (2010).

30. Eslahian, K. A., Majee, A., Maskos, M. & Würger, A. Specific salt effects on thermophoresis of charged colloids. *Soft Matter* **10,** 1931 (2014).

31. Dhont, J. K. G., Wiegand, S., Duhr, S. & Braun, D. Thermodiffusion of charged colloids: single-particle diffusion. *Langmuir* **23,** 1674–1683 (2007).

32. Duhr, S. & Braun, D. Why molecules move along a temperature gradient. *Proc Natl Acad Sci USA* **103,** 19678–19682 (2006).

33. Ning, H., Dhont, J. K. G. & Wiegand, S. Thermal-diffusive behavior of a dilute solution of charged colloids. *Langmuir* **24,** 2426–2432 (2008).

34. Wang, Z., Kriegs, H., Buitenhuis, J., Dhont, J. K. G. & Wiegand, S. Thermophoresis of charged colloidal rods. *Soft Matter* **9,** 8697–8704 (2013).

35. Reichl, M., Herzog, M., Greiss, F., Wolff, M. & Braun, D. Understanding the similarity in thermophoresis between single- and double-stranded DNA or RNA. *Phys. Rev. E* **91,** 062709 (2015).

36. Wolff, M., Braun, D. & Nash, M. A. Detection of thermoresponsive polymer phase transition in dilute low-volume format by microscale thermophoretic depletion. *Anal Chem* **86,** 6797–6803 (2014).

37. Blanco, P., Kriegs, H., Lettinga, M. P., Holmqvist, P. & Wiegand, S. Thermal diffusion of a stiff rod-like mutant Y21M fd-virus. *Biomacromolecules* **12,** 1602–1609 (2011).

38. Lorenzen, N. *et al.* The role of stable α-synuclein oligomers in the molecular events underlying amyloid formation. *J Am Chem Soc* **136,** 3859–3868 (2014).

39. Buell, A. K. *et al.* Solution conditions determine the relative importance of nucleation and growth processes in α-synuclein aggregation. *Proc Natl Acad Sci USA* **111(21),** 7671–7676 (2014).

40. Campioni, S. *et al.* The presence of an air-water interface affects formation and elongation of alpha-synuclein fibrils. *J Am Chem Soc* **136(7),** 2866–2875 (2014).

41. Galvagnion, C. *et al.* Lipid vesicles trigger α-synuclein aggregation by stimulating primary nucleation. *Nat Chem Biol* **11,** 229–234 (2015).

42. Mittag, J. J., Milani, S., Walsh, D. M., Rädler, J. O. & McManus, J. J. Simultaneous measurement of a range of particle sizes during Aβ1-42 fibrillogenesis quantified using fluorescence correlation spectroscopy. *Biochem Biophys Res Commun* **448,** 195–199 (2014).

43. Herling, T. W. *et al.* Integration and characterization of solid wall electrodes in microfluidic devices fabricated in a single photolithography step. *Applied physics letters* **102,** 184102 (2013).

44. Bieschke, J. *et al.* EGCG remodels mature alpha-synuclein and amyloid-beta fibrils and reduces cellular toxicity. *Proc Natl Acad Sci USA* **107,** 7710–7715 (2010).

45. Lorenzen, N. *et al.* How epigallocatechin gallate can inhibit α-synuclein oligomer toxicity *in vitro.* *J Biol Chem* **289,** 21299–21310 (2014).

46. Vigolo, D., Brambilla, G. & Piazza, R. Thermophoresis of microemulsion droplets: size dependence of the Soret effect. *Phys Rev E Stat Nonlin Soft Matter Phys* **75,** 040401 (2007).

47. Hunter, R. J. *Zeta Potential in Colloid Science: Principles and Applications* (Academic Press, 1981).

48. Manning, G. S. Limiting laws and counterion condensation in polyelectrolyte solutions. V. Further development of the chemical model. *Biophys Chem* **9,** 65–70 (1978).

49. Takeyama, N. & Nakashima, K. Proportionality of intrinsic heat of transport to standard entropy of hydration for aqueous ions. *Journal of Solution Chemistry* **17(4),** 305–325 (1988).

50. Buell, A. K. *et al.* Detailed analysis of the energy barriers for amyloid fibril growth. *Angew Chem Int Ed Engl* **51,** 5247–5251 (2012).

51. Maeda, K., Shinyashiki, N., Yagihara, S., Wiegand, S. & Kita, R. Ludwig-Soret effect of aqueous solutions of ethylene glycol oligomers, crown ethers, and glycerol: Temperature, molecular weight, and hydrogen bond effect. *J. Chem. Phys.* **143,** 124504 (2015).

52. Kayed, R. *et al.* Common structure of soluble amyloid oligomers implies common mechanism of pathogenesis. *Science* **300,** 486–489 (2003).

53. Genst, E. J. D. *et al.* Structure and properties of a complex of α-synuclein and a single-domain camelid antibody. *J Mol Biol* **402,** 326–343 (2010).

Acknowledgements

Author Contributions

A.K.B., M.W. and D.B. conceived and designed the study. A.K.B., M.W., J.J.M. and T.W.H. performed the experiments and analysed the data. E.D.G. contributed reagents. A.K.B., M.W., D.B., T.P.J.K. and C.M.D. wrote the manuscript. The authors declare no conflicts of interest.

Additional Information

Supplementary information accompanies this paper at http://www.nature.com/srep

Competing financial interests: The authors declare no competing financial interests.

How to cite this article: Wolff, M. *et al.* Quantitative thermophoretic study of disease-related protein aggregates. *Sci. Rep.* **6,** 22829; doi: 10.1038/srep22829 (2016).

Supplementary information: Quantitative thermophoretic study of disease-related protein aggregates

Manuel Wolff[1], Judith J. Mittag[2], Therese W. Herling[3], Erwin De Genst[3], Christopher M. Dobson[3], Tuomas P.J. Knowles[3], Dieter Braun[1,*] and Alexander K. Buell[3,4,*]

[1]Systems Biophysics, Physics Department, Nanosystems Initiative Munich and Center for NanoScience, Ludwig-Maximilians-Universität München, Amalienstr. 54, 80799 München, Germany
[2]Faculty of Physics and Center for Nanoscience (CeNS), Ludwig Maximilians University, Geschwister-Scholl-Platz 1, 80539 Munich, Germany
[3]Department of Chemistry, University of Cambridge, Lensfield Road, Cambridge CB2 1EW, UK
[4]Present address: Institute of Physical Biology, University of Düsseldorf, Universitätsstr.1, 40225 Düsseldorf, Germany

*authors to whom correspondence should be addressed: dieter.braun@lmu.de, alexander.buell@uni-duesseldorf.de

Content

1 Chemicals and reagents

Thioflavin-T (ThT), Epigallocatechin gallate (EGCG), NaCl, Na_2HPO_4, NaH_2PO_4, PBS tablets and Tris-HCl were purchased from Sigma Aldrich. BCECF, Alexa Fluor® 568 C_5 maleimide and Alexa Fluor® 647 C_2 maleimide were purchased from Life Technologies Ltd (Paisley, UK).

2 Preparation of protein samples and protein labeling

2.1 Monomeric unlabeled and labeled α-synuclein

Wild type α-synuclein (α-syn) was recombinantly expressed and purified as reported previously [1]. After the last step of the purification protocol, the protein solution (in 20 mM phosphate buffer) was divided into aliquots of 500-1000 μl at concentrations between 200 and 300 μM, flash frozen with liquid nitrogen and stored at -80 °C. When the monomeric protein was required in a different buffer, it was dialysed for 24 h against a thousandfold larger volume of the required buffer. For the fluorescent labeling, we used the N122C variant [2], in order to be able to attach the fluorescent label. This variant was expressed and purified similarly to the wild type protein, except that the lysis buffer and all subsequent buffers contained 1 mM EDTA and 1 mM DTT. For the labeling, ca. 0.2 μmol of N122C variant α-syn in 500 μl buffer was injected into a Superdex 200 Increase 10/300 GL gel filtration column (GE Healthcare, Little Chalfont, UK) that had been incubated with labeling buffer (Tris or phosphate buffer at ~pH 7, 5-20 mM). The fluorescent dyes (maleimide derivatives) were dissolved at 10 mg/ml in DMSO or DMF and 100 μl of this stock solution were added to the combined protein fractions immediately after elution. The protein was left to react with the label for 1 h at room temperature and afterwards for 12 h at 4 °C. Then the solution was concentrated to 500 μl

1

using Amicon centrifugal concentrators with 3 kDa MW cut-off (Millipore, Watford, UK) and injected into a Superdex 200 Increase 10/300 GL gel filtration column that had been incubated with the buffer the protein was required in, i.e. 20 mM PB buffer pH 6.5 or 5 mM Tris buffer pH 7.4. The most concentrated fractions of the labeled protein were combined and divided into aliquots of 25 μl. The aliquots were flash frozen in liquid nitrogen and stored at -80 °C until use. Labeling efficiency was evaluated with mass spectrometry (Figure 1 a) and the protein concentration was determined using amino acid analysis (both services provided by PNAC facility, Department of Biochemistry, University of Cambridge). We also kept some of the fractions of free dye label for control experiments (see below). The single chain camelid antibody NbSyn2 was expressed and purified as described in [3].

2.2 Preparation of labeled α-synuclein oligomers

The preparation of stable α-synuclein oligomers is similar to the protocol described in detail in [4]. In short, monomeric α-synuclein is dialysed for 1-3 days against pure water. The solution is then freeze-dried and the lyophilized protein is stored at -80 °C until use. For oligomer formation, the dry protein is dissolved in phosphate buffer saline (PBS) at concentrations between 600 and 800 μM and incubated at 37 °C for several hours (10-20 h) under quiescent conditions. In most cases, the protein solution had not visibly aggregated/gelled despite the high protein concentration after this incubation period. It has been shown that quiescent α-synuclein solutions in the absence of pre-formed seeds [5] and of other aggregation stimulating conditions, such as lipid bilayers [6] aggregate only very slowly, due to the fact that the fibril nucleation is a heterogeneous process that requires catalytic interfaces, such as the air-water interface [7]. 500 μl of the protein solution are then injected into a Superdex 200 Increase 10/300 GL gel filtration column, which had been incubated with 5 mM Tris buffer. The protein is eluted at 0.5 ml/min and the oligomers elute as a small peak of ca. 0.75 ml volume after ca. 20 min, followed by a largely dominant monomer peak (Figure 1 b).

In order to produce fluorescently labeled oligomers, we reasoned that it would be best to minimize the labeling density; the lowest possible label density corresponds to one dye molecule per oligomer. Using various light scattering techniques, we have in previous work determined these stable α-synuclein oligomers to consist of ∼30 monomers on average [4]. Therefore, we used ratios of unlabeled to labeled protein of 30 or higher. Figure 1 b shows an example of a chromatogram illustrating the relative populations of oligomers and monomers and giving an idea about the labeling density.
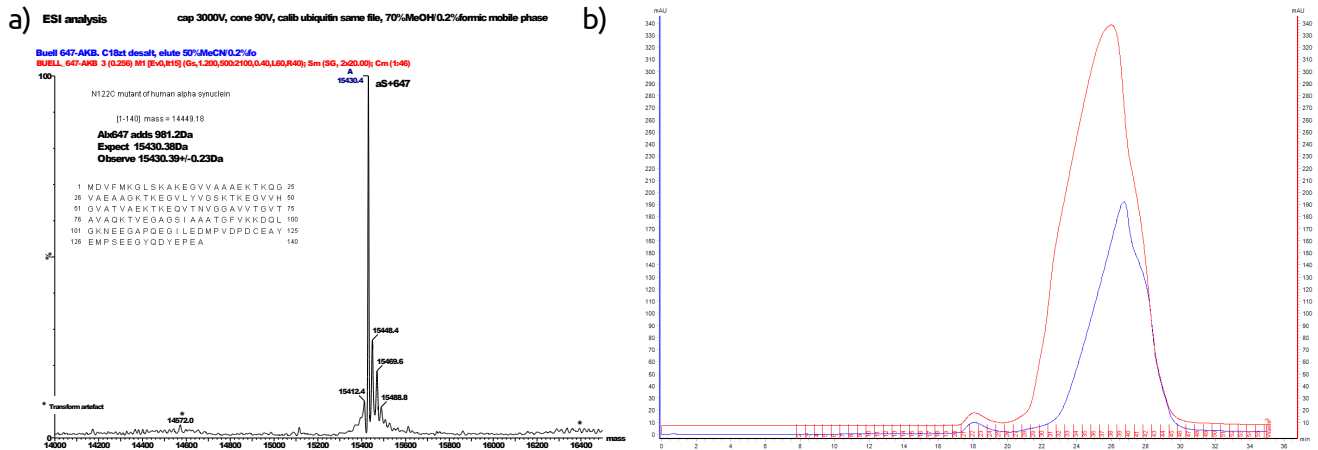

Figure 1: a) Mass spectrum of α-synuclein N122C labeled with Alexa Fluor® 647, showing the essentially quantitative labeling. b) Example of a size exclusion chromatogram of a mixture of labeled (with Alexa Fluor® 647) and unlabeled α-synuclein, treated according to the protocol described above. The small peak to the left of the large monomer peak corresponds to the oligomers (red: absorption at 647 nm; blue absorption at 280 nm). Fractions 22 and 23 were combined and used as the oligomeric species. It can be seen that the labeled and unlabeled monomers have slightly different retention times. Also, the relative absorptions at 280 and 647 nm are comparable for the monomer and oligomer peaks, suggesting that the labeled monomer is incorporated statistically into the oligomers and that therefore the labeling density of the oligomers corresponds to the initial proportion of labeled monomer.

Our attempts to label the oligomers proved insightful regarding their mechanism of formation. Adding the labeled protein at different points in the oligomer formation protocol led to very different incorporation efficiencies. When the labeled protein was added after the freeze-dried unlabeled protein had been dissolved in PBS, virtually no labeled oligomers were obtained. Furthermore, the duration of the incubation had very little effect on the labeling yield.

However, the best incorporation efficiency (equal to the ratio of added labeled protein) was achieved when labeled and unlabeled protein were mixed before the dialysis against water. These findings strongly suggest that these stable α-synuclein oligomers form during the process of dialysis and/or lyophilisation and are therefore possibly not directly connected with the molecular pathway that leads to the formation of amyloid fibrils; we have drawn similar conclusions in the past based on kinetic experiments with these oligomers [4].

After gel filtration, the most concentrated oligomer fractions were combined (typically ∼500 µl) and concentrated to about ten times the eluted concentration, using Amicon centrifugal concentrators with 3 kDa MW cut-off (see above). For the measurements of the Soret coefficients, we required the oligomers in 1 mM Tris buffer. In those cases we diluted the concentrated oligomers 1:4 into water and re-concentrated them to the desired final concentration. Once the oligomers were purified and concentrated, they were stable and could be used for several days, as confirmed by fluorescence correlation spectroscopy (see below).

2.3 Preparation of labeled α-synuclein fibrils

Fibrils with varying labeling densities were prepared by seeding a mixture of labeled and unlabeled protein with small percentages (5% or less) of unlabeled fibrils prepared at pH 6.5 and sonicated to create short seeds as described in [5]. For the accurate measurements of S_T, the seeds were incubated with the monomeric fractions (either directly as eluted or concentrated) from the oligomer purification experiments, yielding the same range of labeling densities as for the oligomers ($\leq$ 1:30). Under the conditions of low ionic strength (5 mM Tris buffer, pH 7.4) under which the oligomers were purified, the growth of the seed fibrils is relatively slow, due to electrostatic repulsion between the monomer and the fibril end [8]. Therefore we incubated the seeded protein solution at elevated temperature (50 °C) for 2-3 days under heavy stirring with a magnetic stirrer. We verified by fluorescence correlation spectroscopy (FCS, see below) that the monomer content of these fibril samples was below 20%. Under those conditions of very low ionic strength, that have to our knowledge not been studied in detail before, α-synuclein appears to have a relatively high concentration of free monomer at equilibrium, presumably because the free energy of aggregation has an unfavorable electrostatic component [9] that contributes more strongly at lower ionic strength. The yield can be improved by adding NaCl (10 mM) to the seeded protein solution, which can be tolerated as the subsequent dilution of the fibril sample for the thermophoretic measurement will sufficiently dilute the NaCl. Due to the slow dissociation of monomer from the fibril ends, such a diluted fibril suspension will not immediately re-equilibrate to a high free monomer concentration. For the measurements of the Soret coefficients and for FCS measurements, the fibrils were diluted 30-60 fold (to achieve suitable signal intensity and particle counts) into 1 mM Tris buffer pH 7.4 and sonicated for 5 min with a Sonopuls 2070 sonicator with a MS 72 tip (Bandelin electronic, Berlin, Germany) at minimal power and 30% pulses.

Our overall strategy of the production of labeled fibrils was based on our previous extensive studies of α-synuclein fibril formation and growth [5]. We avoided the production of labeled fibrils at higher values of the ionic strength, as we had previously found that the higher order assembly ('flocculation') of fibrils induced at higher ionic strength values is only partly reversible upon dilution into lower ionc strength buffer, even after sonication. In all cases, we produced labeled fibrils by seeded growth reactions, as we have previously shown that in seeded growth, the kinetics of aggregation is independent of the ratio of labeled to unlabeled monomer [2]. Therefore, it is reasonable to assume that the labeled monomer will be incorporated statistically into the growing fibrils, and that therefore the labeling densities correspond to the initial proportions of labeled to unlabeled monomer.

For the measurements of small molecule binding using the commercially available Monolith instrument (Nanotemper, Munich, Germany), the absolute concentration of the amyloid fibrils is an important parameter, and hence we prepared the fibrils from mixtures of unlabeled and labeled protein solutions at known concentrations. 5% seed fibrils were incubated with a total of 50 µM of monomeric protein with varying proportions of labeled and unlabeled α-synuclein molecules in 20 mM phosphate buffer pH 6.5. The samples were incubated at 37 °C overnight, then they were diluted 1:2 into H_2O, sonicated for 3 s and incubated at room temperature overnight. Then the samples were flash frozen in liquid nitrogen and stored at -80 °C until used. No differences in morphology were observed by AFM between fibrils prepared with different proportions of labeled protein.

3 Atomic force microscopy (AFM)

AFM images of purified oligomers and sonicated fibrils were taken using a Nanowizard II atomic force microscope (JPK, Berlin, Germany) using tapping mode in air. The samples were diluted to ∼1 µM total protein concentration in water and 10 µl were deposited on freshly cleaved mica (Agar Scientific, Stansted, UK) and left to dry. The length distributions were extracted with in-house written Python code, where the ends of the fibrils were manually selected and the program then draws a line onto the fibril, in order to avoid double-counting of fibrils.

4 Thermophoresis experiments

We pursued a dual strategy in this work in order to both improve our fundamental understanding of the physical origins of protein thermophoresis and to demonstrate its usefulness in screening strategies for ligands of disease-related protein aggregates. We performed measurements of the Soret coefficients of different types of aggregates under different conditions in order to test the applicability to proteins of the theoretical description of biomolecular thermophoresis that we have presented in the past for the simpler case of nucleic acids [10, 11]. These experiments were performed using a home-built setup, based on an inverted fluorescence microscope [11], that records the full spatial distribution of fluorescence intensity, and hence concentration of α-synuclein species, as a function of time. Having optimized our experimental protocols (labeling density, solution conditions etc.), we then performed detailed binding experiments with monomeric, oligomeric and fibrillar α-synuclein and small molecule and protein ligands using a commercially available instrument, that measures the total fluorescence intensity in the region of interest as a function of time.

For the measurements of Soret coefficients, the concentration of labeled α-synuclein was between 0.1 and 1 µM. Correspondingly, the total protein concentration (by mass) was 30-50 fold higher in the case of the oligomers and fibrils, as these species were produced from mixtures of unlabeled protein doped with 2-3% fluorescently labeled monomer. For the measurements of the binding constants of the antibody NbSyn2 and the small molecule EGCG to oligomeric and fibrillar aggregates, the total protein concentrations by mass were between 0.2 and 0.5 µM with the concentration of labeled protein accordingly 30-50 times lower. For accurate measurements of binding constants, it is important to keep the concentration of one binding partner constant at a value at or below the expected K_D. The resulting low concentrations of labeled α-synuclein were compatible with the sensitivity of the instrument (see below).

4.1 Measurements of Soret coefficients of monomeric and aggregated α-synuclein

Measurements were performed with an upright fluorescence microscope (Zeiss Vario Scope.A1) using an air objective (Zeiss EC-Plan NeoFluar, 40x, NA=0.9), a CCD camera (Andor Luca DL-658M-TIL) and heating from an infrared laser (Fibotec, $\lambda = 1480$ nm absorbed in water) [11], coupled into the optical path right above the objective. To keep convection artifacts below experimental error, measurements were performed in borosilicate capillaries with an inner rectangular cross section of 50 x 500 µm^2 (VitroCom Vitrotubes #5005-050). The thin sample, low numerical aperture and moderate concentration depletion ($<50\%$) ensured that temperature and concentration profiles were equally averaged along the optical axis. For a sketch of the setup, see Figure 2.

The chamber base temperature was controlled by a PID loop using Peltier elements (Telemeter Electronic GmbH, PC-128-10-05) and a heat bath. The chamber height of 50 µm and the moderate temperature rise of less than 9 K above base temperature kept thermal convection small. The measurement was automated and the LED, IR, motorized stage, temperature, and camera trigger were controlled with LabVIEW. The response of the concentration of labeled protein in space and time was recorded at 2.5 Hz by fluorescence imaging. Ten seconds of the equilibrated sample were imaged, followed by different time periods of thermophoretic depletion (depending on the nature of the sample) under optical heating and different time periods to monitor the back-diffusion after switching off the laser.

The profile of the intermittent local optical heating was measured using the temperature dependent fluorescence of the dye BCECF (acid form, Invitrogen B-1151) at a concentration of 50 µM in 10 mM Tris, pH 7.8 (Figure 3a and b). First the peak temperature ΔT for the applied laser power was determined in two dimensions by the assumption of Lorentzian temperature profile $T(r) = T_0 + \Delta T \frac{w^2}{(r^2 + w^2)}$. Second the temperature dependence of ΔT as a function of base temperature was assumed as predicted by COMSOL simulations and confirmed by measurements (supplementary section 8). The Soret coefficient was deduced by evaluating the radial concentration profile at steady state in correspondence to the image after temperature jump according to $S_T \Delta T(T, r) = -\log\left(\frac{c(r)}{c_0}\right)$ (Figure 3c and d). The error bars for individual Soret coefficients are based on the uncertainties of the temperature jump ΔT (see also supplementary section 8).

4.2 Measurements of ligand binding affinities of monomeric, oligomeric and fibrillar α-synuclein

The measurements of the ligand binding constants were performed with a Monolith NT.115 instrument (Nanotemper, Munich, Germany). We obtained the best experimental results (complete absence of sample absorption onto the inner walls of the glass capillaries) using the hydrophobically coated glass capillaries provided by Nanotemper.

The binding experiments between monomeric/oligomeric α-synuclein and the nanobody NbSyn2 were performed as follows. A dilution series was prepared in PBS buffer of the Nb (from 202 µM-6.2 nM, 10 µl at each concentration). The labeled monomers (in PB pH 6.5) were diluted to a concentration of 0.4 µM into H$_2$O, and then 10 µl of the diluted protein solution were added to the 10 µl aliquots of the NbSyn2 dilution series, yielding a final monomer concentration
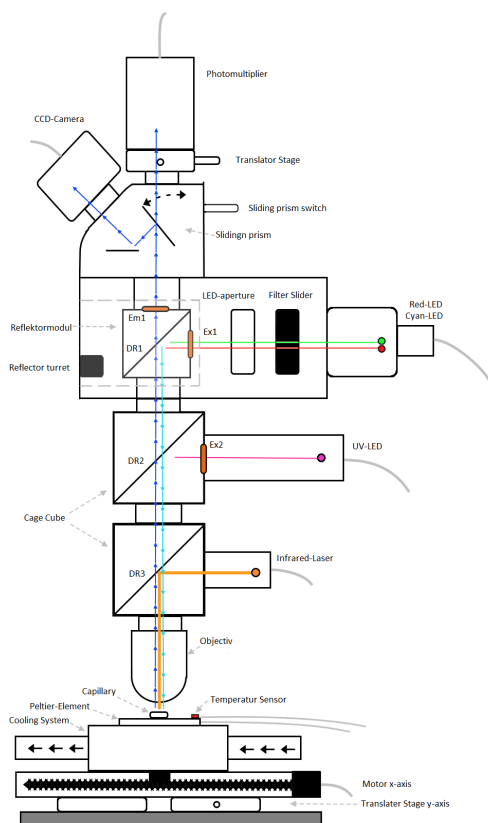
Figure 2: Schematic illustration [12] of the thermophoresis setup for quantitative measurements of the Soret coefficients of protein aggregates. The setup is based on a fluorescence microscope. The heating is carried out with an infrared laser that is coupled into the light path. Detection can be performed either with a CCD camera or with a PMT.

of 0.2 μM. The glass capillaries were filled through capillary action and thermophoretic measurements were performed (25 °C, 15% red LED intensity, 20 and 40% IR laser intensity, 30 s laser on). The labeled oligomers were diluted in 5 mM Tris buffer pH 7.4 to a concentration of approximately 1 μM, as estimated from the size chromatogram during the isolation and purification of the oligomers. Then 10 μl of the oligomer solution were added to the 10 μl of the NbSyn 2 dilution series and the capillaries were filled and thermophoresis measurements performed analogously to the monomer case, except that the LED intensity was 60%. Representative data for nanobody binding to monomeric and oligomeric α-synuclein are shown in Figure 4. In the case of the oligomers, the thermophoretic amplitude was measured before steady state was reached (ca. 5 s after the heating laser was switched on), due to the fact that the data became noisier at later times. This is presumably due to the higher order assembly of the oligomers, that experience a decrease in charge due to the nanobody binding. In the case of the monomer, the thermophoretic amplitude was measured at steady state, 30 s after the heating laser was switched on.

For the experiments with EGCG, we first prepared stock solutions of 50 mg/ml (109.08 mM) in dimethylsulfoxide (DMSO) and then diluted it 50-fold into water to reach a concentration of 2.18 mM with 2% residual DMSO. We then prepared a dilution series into water with 2% DMSO (10 μl per sample) and added 10 μl of the monomer (1.5 μM total monomer, 2% labeled, 98% unlabeled monomer), oligomer or fibril (1.5 μM total protein, 2% labeling density) samples. Then we performed thermophoresis experiments at 25 °C and 20 as well as 40% of the IR laser power.

During our experiments that probed EGCG binding to oligomeric and fibrillar α-synuclein, we noticed that the apparent binding constant changed during the first hour after sample preparation; the binding was observed to become tighter (Figure 5). While we are not certain about the origin of this change in apparent affinity, it is unlikely to be caused by a pronounced change in aggregate structure (see AFM images in Figure 5 of main manuscript), but could indicate multi-step binding with rapid kinetics of initial and slower kinetics of later stages. An alternative explanation could also be a chemical modification of the fluorescent label by the bound ligand. The experiments shown in the main manuscript were performed after 1 h incubation of the samples.

For all the measurements of binding constants, we combined data from three independent experiments.

We also performed binding and stability time course experiments with fibrils prepared with different percentages of
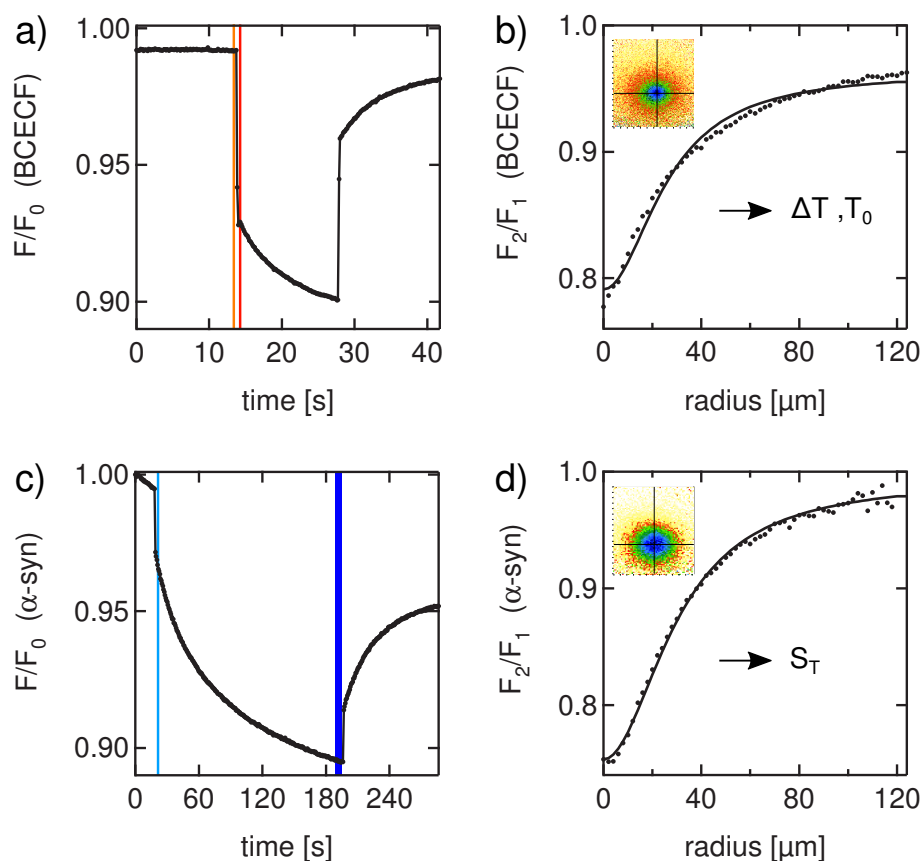
Figure 3: Data evaluation for the quantitative measurements of the Soret coefficient. The temperature gradient which was induced by the IR-laser was determined by BCECF fluorescence. a) The mean fluorescence on the CCD camera drops when the temperature gradient is established within 300 ms. Afterwards thermophoresis takes place. When the IR-laser is turned off the mean fluorescence recovers due to back diffusion. Dividing the picture after the temperature jump (red bar) by the one beforehand (orange bar) gives the radial fluorescence profile as indicated in b). The radial fluorescence profile is approximated by a Lorentzian function and the temperature gradient is then determined with the help of a calibration curve. c) For the α-synuclein species, here illustrated with monomer, the mean fluorescence is monitored over a longer period of time to reach a steady state. The change of concentration due to thermophoresis is obtained by division of the mean picture at the steady state (dark blue bar) by the one after temperature jump (light blue bar). d) The radial concentration profile together with the temperature profile gives the respective Soret coefficient. Here the measurement of α-synuclein monomer at 1 mM Tris pH 7.4 is shown. The base temperature is set to 25 °C in the presented examples.

incorporated labeled protein. Figure 6 a) shows a comparison of experiments with fibrils with 2% and 50% labeling density. It can be seen that the apparent affinity and the time-dependent behavior depend on the labeling density. The overall result of these studies was that the labeling density should be minimized. Obviously, it is always desirable to minimize the impact that any label might have on the process under study, but if the label concentration is decreased too much, then the signal is too weak at the low (μM) total protein concentrations that needed to be used in order to probe the binding affinity accurately. We found that 2% of labeled protein in the fibrils gave consistently the best results.

We also performed oligomer binding experiments with Thioflavin-T instead of EGCG (Figure 6 b), starting with a 2.33 mM ThT solution in H_2O with 2% DMSO. A weak interaction could be detected, that displays no time dependence. Furthermore, we found that also monomeric α-synuclein interacts with EGCG (Figure 6 c), whereas the free dye label shows no change in thermophoresis upon incubation with an EGCG concentration series, confirming that the binding curves presented in this work are not artifacts from ligand-label interactions.
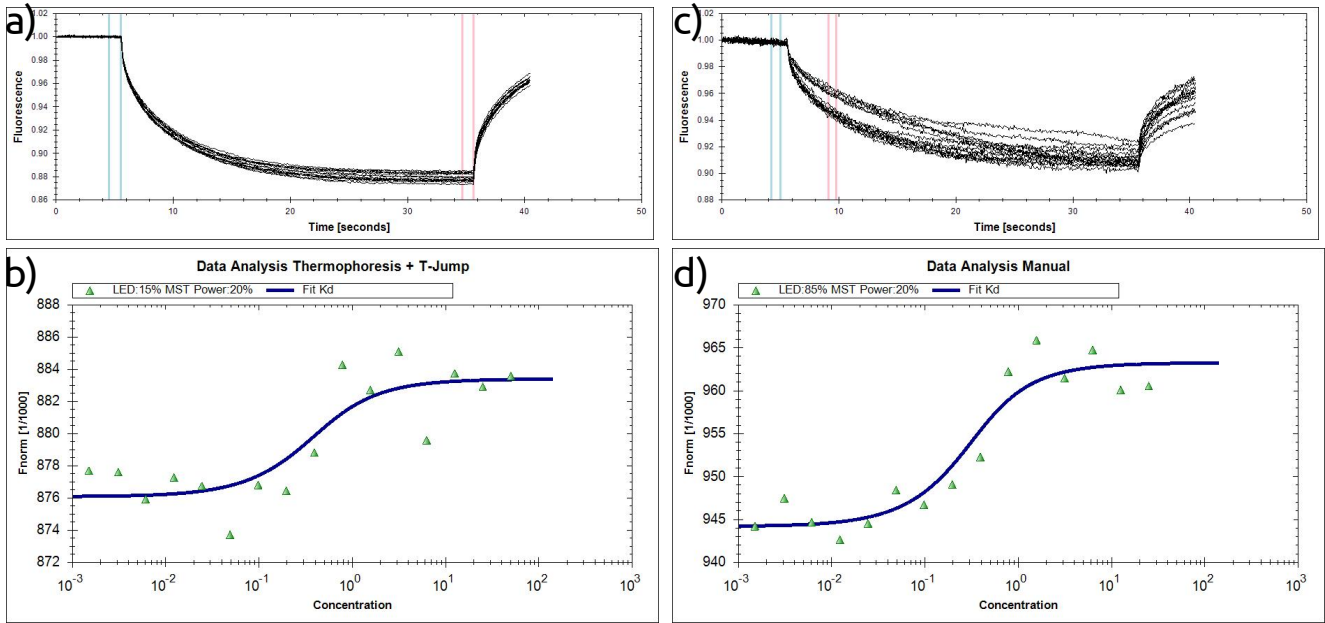
Figure 4: Microscale thermophoresis (MST) binding data of monomeric and oligomeric α-synuclein with the nanobody NbSyn2. a) Raw MST curves for monomeric α-synuclein. b) Binding curve for monomeric α-synuclein. c) Raw MST curves for oligomeric α-synuclein. d) Binding curve for oligomeric α-synuclein.
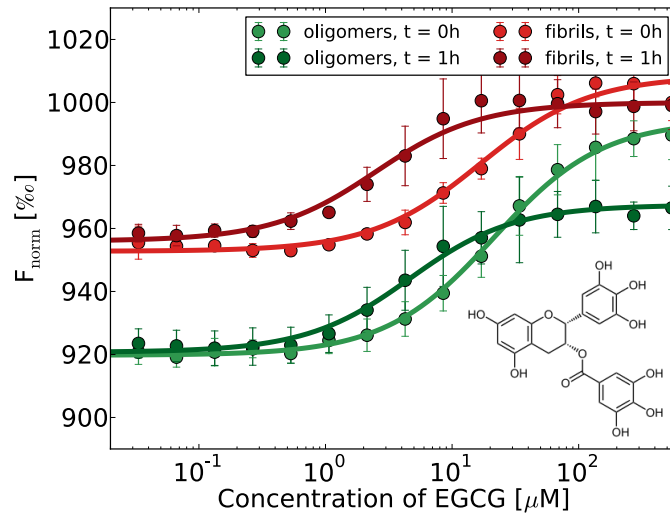

Figure 5: Change in apparent binding affinity of EGCG to oligomeric and fibrillar α-synuclein. For both species, the binding appears to become tighter over the course of an hour, changing from 16.5±1.6 µM and 21.2±2 µM, for fibrils and oligomers, respectively, to 2.5±0.4 µM and 4.3±0.8 µM.

5 Fluorescence correlation spectroscopy (FCS) of monomeric and aggregated α-synuclein

FCS measurements were performed on a Axiovert 200 microscope equipped with a ConfoCor2 unit (Carl Zeiss Jena, Germany), a 543 nm and 633 nm helium-neon laser and an apochromatic 40x water-immersion objective with a NA of 1.2 (Carl Zeiss). Fluorescence emission was separated from laser light using a bandpass filter (560-615 nm) for excitation with 543nm and a long pass filter (650 nm) for excitation with 633 nm. Calibration was performed with Alexa546 or Alexa633, respectively, to determine the dimensions of the observation volume. Samples were filled in NUNC 8-Well-Plates (Thermo Scientific). All measurements were performed at room temperature (22 °C, air conditioned). For analysis the ConfoCor2 software was used.
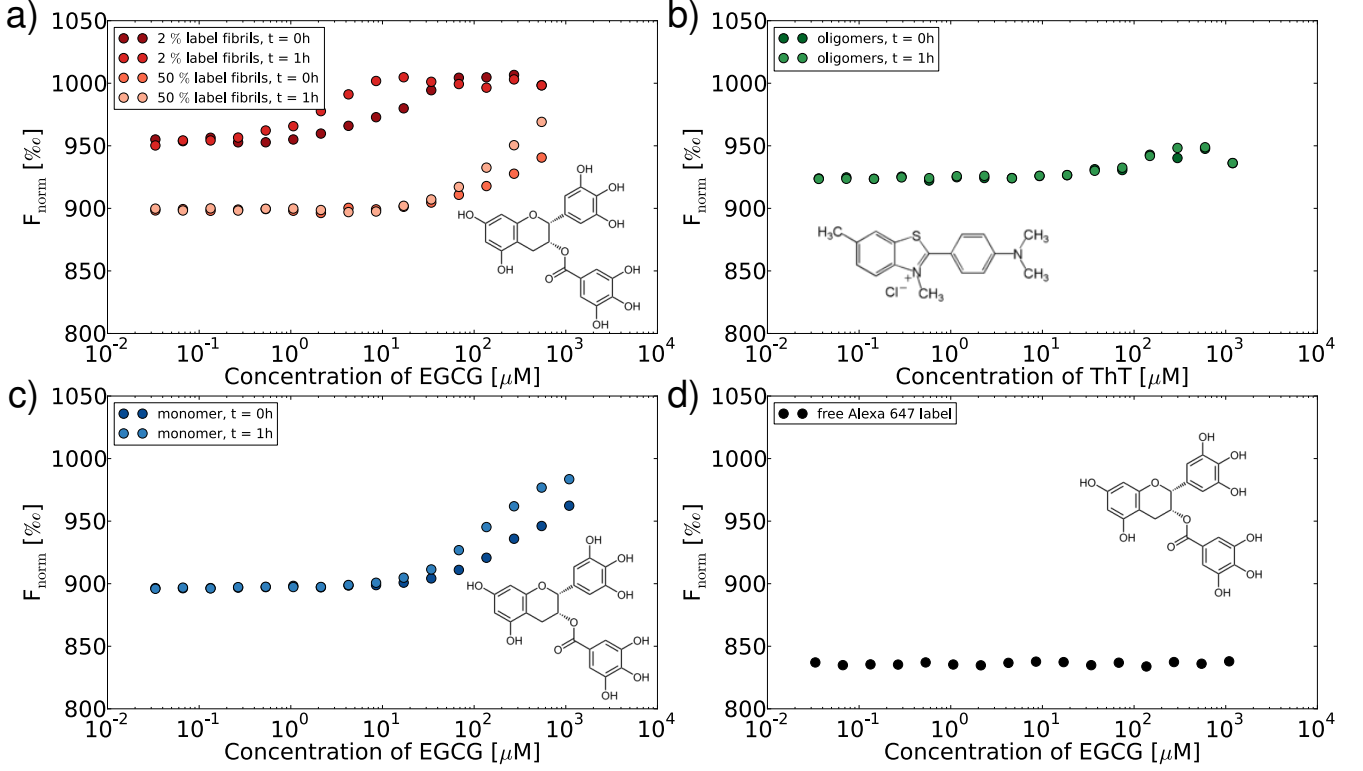
Figure 6: a) α-synuclein amyloid fibrils with either 2% or with 50% of the constituent monomers labeled with Alexa 647 are incubated with increasing concentrations of EGCG. Thermophoresis measurements were performed immediately after sample preparation and again after 1 h incubation period. It is apparent from this data that the labeling density is an important experimental parameter, and that it should be minimized as much as possible. b) α-synuclein oligomers show a weak interaction with Thioflavin-T, that does not change over time. c) Monomeric α-synuclein shows a weak interaction with EGCG, which also displays some time dependence. d) Free Alexa Fluor® 647 malimide does not display any interactions with EGCG.

5.1 Data analysis

We follow here the procedures outlines in [13]. The normalized correlation function $G(\tau)$ is defined as:

$$\frac{\langle F(t)F(t+\tau)\rangle}{\langle F(t)\rangle^2} \tag{1}$$

where angular brackets denote the average over time, F(t) the fluorescence signal at time t and F(t+τ) the fluorescence signal at a later time t+τ. An ideal three dimensional Gaussian shape is assumed for the confocal volume. The structure parameter ω describes the ratio of the half axis z_0 to the radius of the laser beam w_0. By fitting a model to the experimental data, physically relevant information can be extracted from the correlation curve. The autocorrelation curve for a single component freely diffusing in a 3D Gaussian element can be described by:

$$G(\tau) = \frac{1}{N}\left(\frac{1}{1+\frac{\tau}{\tau_D}}\right)\left(\frac{1}{1+\frac{\tau}{\omega^2\tau_D}}\right)^{\frac{1}{2}} + 1 \tag{2}$$

where N is the number of particles inside the confocal volume, τ_D is the translational diffusion time of the species, τ is the correlation time and ω the structure parameter. For samples containing two components of different size a two component fit is used:

$$G(\tau) = \frac{1}{N}\left[(1-y)\left(\frac{1}{1+\frac{\tau}{\tau_{D1}}}\right)\left(\frac{1}{1+\frac{\tau}{\omega^2\tau_{D1}}}\right)^{\frac{1}{2}} + y\left(\frac{1}{1+\frac{\tau}{\tau_{D2}}}\right)\left(\frac{1}{1+\frac{\tau}{\omega^2\tau_{D2}}}\right)^{\frac{1}{2}}\right] + 1 \tag{3}$$

where τ_{D1} and τ_{D2} are the diffusion times of the two components and y is the fraction of the second component. To take optical dark states of the dye into account, a function that describes the triplet can be integrated into the fitting equation:

$$G_{\text{Triplet}}(\tau) = \left(1 + \frac{T}{1 - T}\exp\left(-\frac{\tau}{\tau_T}\right)\right) \tag{4}$$

τ_T is the triplet state relaxation time and T the fraction of fluorophores in the dark state. The total correlation curve then becomes a product of the triplet function and the model G (τ):

$$G_{\text{total}}(\tau) = G_{\text{Triplet}}(\tau)G(\tau) \tag{5}$$

The translational diffusion time describes the average dwell time of a molecule with diffusion constant D in the confocal volume:

$$\tau_D = \frac{w_0{}^2}{4D} \tag{6}$$

The hydrodynamic radius R_h of a spherical molecule can be determined with the Stokes-Einstein-equation:

$$R_h = \frac{k_B T}{6\pi\eta D} \tag{7}$$

where k_B, is the Boltzman constant, T is the temperature in [K] and η the viscosity of the surrounding medium.

5.2   Results

We have determined the sizes of fluorescently labeled monomeric, oligomeric and fibrillar α-synuclein using FCS. Figure 7 shows the normalized correlation functions that clearly illustrate the difference in diffusion behavior between the different species.
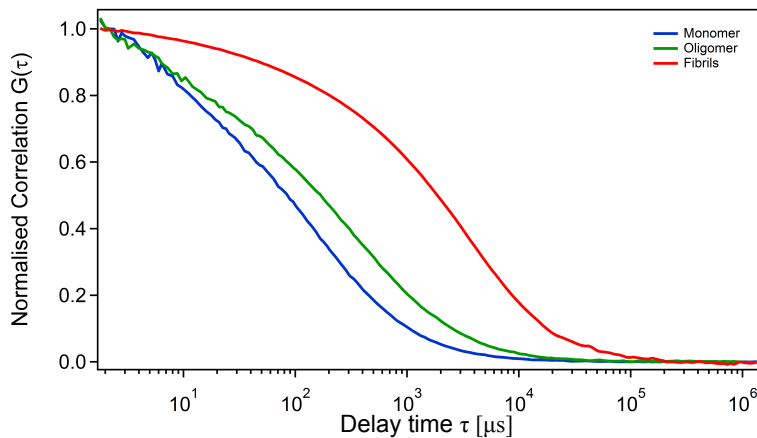

Figure 7: Normalized correlation curves of monomeric (blue), oligomeric (green) and fibrillar (red) α-synuclein. FCS measurements enable accurate determination of the diffusion coefficient and hence the (effective) hydrodynamic radii of the different species, using the Stokes-Einstein equation (Equation 7). The shift to the right towards longer diffusion times is an indicator for an increase in size.

The experiment shown in Figure 7 yields values of the diffusion coefficient of $8.2\pm0.34\cdot10^{-11}$ $\frac{m^2}{s}$ (monomer), $3.5\pm0.34\cdot10^{-11}$ $\frac{m^2}{s}$ (oligomer) and $4.1\pm0.4\cdot10^{-12}\frac{m^2}{s}$ (fibrils). In the case of the monomers and oligomers, the Stokes-Einstein equation (Eq. 7) can be directly applied in order to determine the hydrodynamic radii, as these species can be approximated as spheres. As averages from several independent experiments, we obtain $R_M = 2.8\pm0.1$ nm for the hydrodynamic radius of the monomer and $R_O = 7.5\pm0.7$ nm for the hydrodynamic radii of the oligomers. The average diffusion coefficient measured for the sonicated fibrils is 4.1 ± 0.4 $\cdot10^{-12}$ $\frac{m^2}{s}$. In all cases when fibrillar samples were measured by FCS, the quality of a two-component fit was considerably better, where the second component was fixed to have the size of the monomer. The monomer component of the fibril samples varied between 15 and 23%, which also introduces an error into the values of the Soret coefficients measured for the fibrils. In order to calculate the diffusion coefficient

and subsequently the dimensions of the fibrils, we make use of the AFM images that we have taken of these fibrils (see Figure 3 of main manuscript). These images in principle already provide us with the necessary information about the dimensions of the fibrils, but we will nevertheless check whether the results of the FCS measurements that are performed under the same conditions as the thermophoresis and electrophoresis experiments, are consistent with the AFM images. According to the detailed analysis of the AFM images, the sonicated fibrils have an average length of 171 nm and a thickness of approximately 8 nm. With these dimensions, we can calculate the rotational diffusion coefficient, according to:

$$D_r = \frac{k_B T}{\gamma_r} \tag{8}$$

where γ_r is the rotational friction coefficient, given according to Broersma [14] by:

$$\gamma_r = \frac{\pi \eta L^3}{3(\log{(2L/D)} - c_r)} \tag{9}$$

where L is the length of the rod, D is its diameter and c_r is a numerical factor that corrects for end effects:

$$c_r = 1.57 - 7 \left(\frac{1}{\log{(2L/D)}} - 0.28 \right)^2 \tag{10}$$

The rotational diffusion coefficient has units of radians^2/s. We obtain a value of ~ 1725 rad^2/s. The diffusion time of a fibril through the confocal volume of the FCS instrument is approximately 5 ms, a value directly obtainable from the FCS measurements. During this time, the fibril will rotate on average about 168°. This is probably not enough to assume complete orientational averaging, but some degree of averaging can be assumed. We can therefore expect the difference between the measured apparent diffusion coefficient of the fibrils and the calculated diffusion coefficient of a rod with 171 nm length and 8 nm thickness to be not too large. In order to calculate the translational diffusion coefficient of a rod, we use the results by de la Torre [15]:

$$D_t = \frac{k_B T(\log{(L/D)} + c_t)}{3\pi \eta L} \tag{11}$$

where c_t is again a numerical correction factor for end effects:

$$c_t = \frac{c_{t,\perp} + c_{t,\parallel}}{2} \tag{12}$$

with

$$c_{t,\perp} = 0.5 + 4.2 \left(\frac{1}{\log{(2L/D)}} - 0.39 \right)^2 \tag{13}$$

and

$$c_{t,\parallel} = -0.58 + 7.4 \left(\frac{1}{\log{(2L/D)}} - 0.34 \right)^2 \tag{14}$$

We obtain $c_t = 0.0122$ and $D_t = 8.1 \cdot 10^{-12}$ $\frac{m^2}{s}$. This value is in acceptable agreement with the value determined from FCS ($4.1 \pm 0.4 \cdot 10^{-12}$ $\frac{m^2}{s}$, see above). The difference in these values is likely to stem from the polydispersity of the fibrillar sample. The FCS measurements are likely to be biased towards the shorter fibrils, due to faster diffusion and less likely absorption on the walls etc., whereas the AFM measurements might be biased towards the longer fibrils, due to preferential absorption on the AFM substrate.

We have also performed FCS measurements of α-synuclein fibrils before and after incubation with additional unlabeled monomeric protein at 70 °C, as in the experiment shown in Figure 3 of the main manuscript. The correlation data of this experiment is shown in Figure 8, and the growth of the fibrils is clearly apparent from this data.

Finally, we also used FCS in order to probe the temporal stability of the purified oligomers. We measured a sample of oligomers continuously for more than 60 h at RT (Figure 9) and found only a very slight trend towards increasing sizes. This result confirms that the oligomers are thermodynamically highly stable and display negligible kinetics of dissociation on the time scale of days. Therefore purified samples of oligomers were stored during up to several days (at RT or 4 °C) and used for thermophoresis experiment throughout this period.
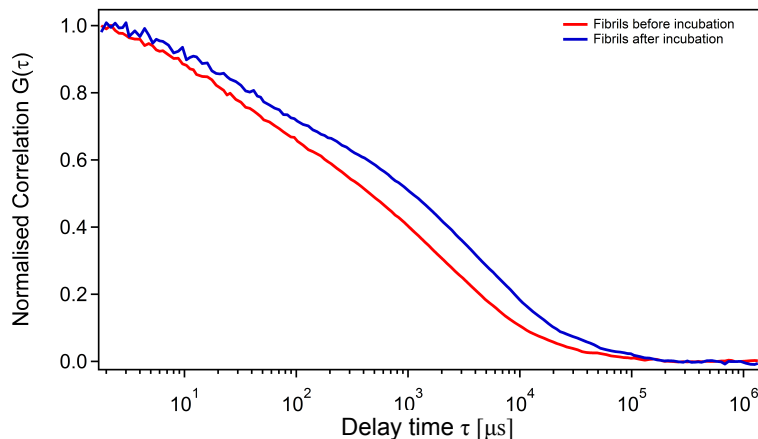
Figure 8: Normalized correlation curves from FCS experiments of α-synuclein amyloid fibrils before and after a 20 min incubation period with 70 μM added unlabeled monomeric protein at 70 °C. The shift to the right towards longer diffusion times is an indicator for an increase in size. This shift corresponds to a change in diffusion coefficient from $3.8\pm0.2\cdot10^{-12}\ \frac{m^2}{s}$ to $2.4\pm0.2\cdot10^{-12}\ \frac{m^2}{s}$.
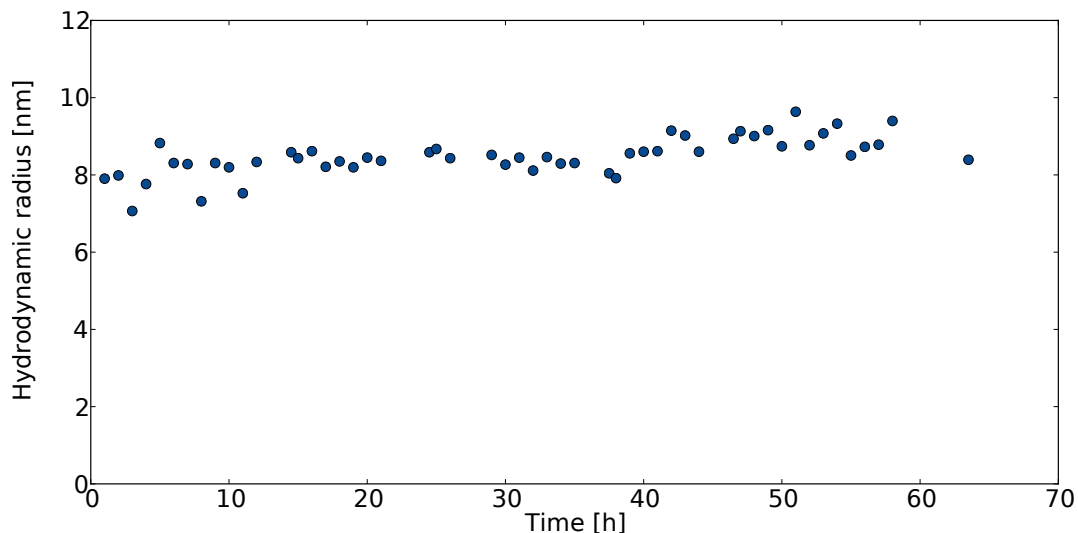

Figure 9: Time course of FCS size measurements of labeled α-synuclein oligomers over more than 60 h, confirming the high structural stability of these types of aggregates.

6 Free flow electrophoresis measurements of monomeric and aggregated α-synuclein

As will be discussed in detail in the next section, the net charge and electrophoretic mobility are important parameters for the quantitative description of thermophoresis. The thermophoresis of the salt ions in solution creates a macroscopic electric field at steady state that leads to electrophoresis of the macromolecule under study, such as the monomeric or aggregated α-synuclein in the present case. Furthermore, the potential energy stored in the double layer depends on both the charge and the temperature and hence yields another temperature-dependent contribution to the Soret coefficient. Therefore, independent estimates of the effective charges of the different α-synuclein species are important for the quantitative analysis and understanding of the thermophoretic behavior.

We used a variant of microfluidic free flow electrophoresis that was recently developed in our laboratory [16] in order to measure the electrophoretic mobilities of monomeric, oligomeric and fibrillar α-synuclein in 5 mM Tris buffer at pH 7.4 (Figure 10).

The measured electrophoretic mobilities are -2.06±0.11 $\frac{μm/s}{V/cm}$ (labeled monomers), -3.09±0.46 $\frac{μm/s}{V/cm}$ (oligomers) and
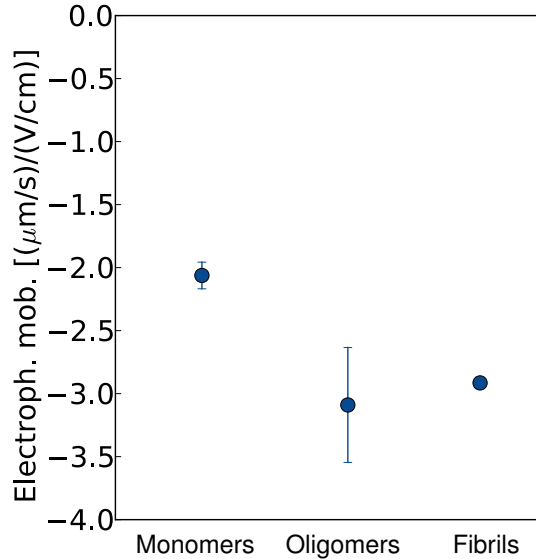
Figure 10: Electrophoretic mobilities, measured via microfluidic free-flow electrophoresis [16]. The mobilities were measured in 5 mM Tris buffer, pH 7.4. Error bars come from two independent repeats with independent sample preparations.

-2.91±0.02 $\frac{\mu m/s}{V/cm}$ (fibrils). The values for both monomeric and fibrillar α-synuclein are well-defined and display a trend of increasing mobility with increasing size. However, the variation in the values measured for the oligomers is much larger, potentially reflecting a degree of polydispersity of the oligomer preparations [4]. In particular, oligomeric and fibrillar α-synuclein display an essentially identical electrophoretic mobility. In the light of the very different sizes and structures of oligomers and fibrils, this is a very interesting finding which highlights the power of thermophoresis to discriminate more easily between different types of particles, compared to electrophoresis. For our quantitative modeling of the thermophoresis data, we require the surface charge density or the absolute charge of the protein monomers and aggregates, in addition to the electrophoretic mobilities. A comprehensive theoretical framework for relating mobilities to surface potentials for colloid-like systems of all sizes has been first presented by Henry [17]. In particular for particles that can be approximated as spheres, such as monomeric and oligomeric α-synuclein, this is well-established.

6.1 From electrophoretic mobility to effective charge for monomeric and oligomeric α-synuclein

The ζ-potential is the potential difference between the (neutral) bulk solution and the surface of a charged particle, including tightly absorbed counter ions [18], and is therefore a measure for the charge density of the particle surface. The electrophoretic mobility and the ζ-potential are related through Henry's formula [17]:

$$\mu_e = \frac{2\epsilon_0\epsilon_r\zeta f(\kappa R)}{3\eta} \tag{15}$$

where ζ is the ζ-potential, η the viscosity and $f(\kappa R)$ is Henry's function with the argument κR, the product of inverse Debye length κ and particle radius R. Henry's function varies from $1.0 \leq f(\kappa R) \leq 1.5$. For $\kappa R \ll 1$, $f(\kappa R) =1.0$ (Hückel limit) and for $\kappa R \gg 1$, $f(\kappa R) = 1.5$ (Smoluchowski limit). Ohshima has presented a formula for $f(\kappa R)$ that is valid for all values of κR and accurate to within 1% [19]:

$$f(\kappa R) = 1 + 0.5\frac{1}{(1 + \frac{2.5}{\kappa R(1+2e^{-\kappa R})})^3} \tag{16}$$

However, the applicability of Henry's expression for the particle mobility depends on the absolute value of the charge and mobility, due to the fact that Henry's treatment neglects relaxation effects of the counterion atmosphere [18]. We can define a reduced mobility:

$$\mu_{\text{red}} = \frac{3\eta e}{2\epsilon_0\epsilon_r k_B T}\mu_e \tag{17}$$

12

Depending on the relative values of μ_{red} and κR, either Henry's simplified treatment or a more sophisticated one has to be applied. We obtain $\mu_{\text{red,M}} = -1.74$ and $\mu_{\text{red,O}} = -2.62$. From the FCS measurements (see above), we know that the radius of the monomeric protein, R_m, is ca. 2.8 nm and the radius of the oligomers, R_o, is ca. 7.5 nm. The free flow electrophoresis experiments were carried out in 5 mM Tris buffer pH 7.4, where the Debye length $\lambda = 1/\kappa$ = 4.7 nm. Hence $\kappa R = 0.6$ for monomeric α-synuclein and 1.6 for oligomeric α-synuclein. It turns out that Henry's simplified treatment for the calculation of the ζ-potential is applicable for the monomer (with f(κR)=1.02), but for the oligomer, we need to use Hunter's inversion [18] of Booth's formula [20]:

$$\zeta_r = \frac{\mu_{\text{red}}}{f(\kappa R)} - \left[\frac{C_3(\mu_{\text{red}}/f(\kappa R))^3 + C_4(\mu_{\text{red}}/f(\kappa R))^4}{f(\kappa R) + 3C_3(\mu_{\text{red}}/f(\kappa R))^2 + 4C_4(\mu_{\text{red}}/f(\kappa R))^3} \right] \tag{18}$$

where ζ_r is the reduced ζ-potential:

$$\zeta_r = \frac{\zeta e}{k_B T} \tag{19}$$

and where C_3 and C_4 are numerical coefficients that depend on the product κR and the limiting molar conductance of the counter- and coions. Hunter [18] gives the expressions for these coefficients that we are not reproducing here. The limiting conductances of the Tris$^+$ ion and the Cl$^-$ ion are $2.97 \cdot 10^{-3} \Omega^{-1} \text{m}^2 \text{mol}^{-1}$ [21] and $7.64 \cdot 10^{-3} \Omega^{-1} \text{m}^2 \text{mol}^{-1}$ [22].

We are now in a position to calculate the ζ-potentials for monomeric (44.0 mV) and oligomeric (40.3 mV) α-synuclein. In order to calculate the charges from these values of the ζ-potentials, we follow the methodology outlined by Ohshima [23]. We define the dimensionless surface charge density Σ:

$$\Sigma = \frac{e\sigma}{\epsilon_0 \epsilon_r \kappa k_B T} \tag{20}$$

where σ is the surface charge density. Ohshima derives the following expression relating reduced ζ-potential and reduced surface charge density:

$$\Sigma = 2\sinh(\zeta_r/2) \left[1 + \frac{2}{\kappa R \cosh^2\left(\frac{\zeta_r}{4}\right)} + \frac{8\log\left(\cosh\left(\frac{\zeta_r}{4}\right)\right)}{(\kappa R)^2 \sinh^2\left(\frac{\zeta_r}{2}\right)} \right]^{\frac{1}{2}} \tag{21}$$

The absolute charge Q can be computed from the surface charge density σ as $Q = 4\pi R^2 \sigma$. Using these expressions, we obtain values for the absolute charge of Q_M = -10.9 e for the monomeric protein and Q_O = -50.4 e for the oligomers. The value of the monomer is in good agreement with theoretical predictions, based on the combined charge of the individual amino acids at this pH value (-9.1 e) and the charge of the Alexa 647 label (-4 e). For the oligomers, on the other hand, the effective charge corresponds to only ~5 times the charge of a monomer, while each oligomer consists on average of ~30 monomers. This strong difference can be explained through processes such as counter ion incorporation into the oligomer structure, as well as Manning condensation of counterions [24] onto the surface of the oligomer. Indeed, without such charge compensation mechanisms, the electrostatic contribution to the formation of an oligomer would render such a structure highly energetically unfavorable.

6.2 Free flow electrophoresis of rod-like particles

The determination of effective charges from electrophoretic mobilities of rod-like particles represents an additional difficulty, due to the anisotropic nature of the rod and the possibility of alignment in the electric field. In addition, if the electrophoretic mobility is measured in free (shear) flow, alignment could also occur in the flow direction. We start by evaluating whether or not alignment effects have to be taken into account in our setup. Dhont and Briels [25] have given a comprehensive treatment of the behavior of Brownian rods in shear flow. A rotational Péclet number can be defined that quantifies the relative importance of shear forces and random Brownian rotational motion:

$$\text{Pe}_r = \frac{\dot{\gamma}}{D_r} \tag{22}$$

where $\dot{\gamma} = \frac{du_x}{dy}$ is the shear rate, u_x is the flow velocity and y is a direction perpendicular to the flow. The microfluidic channel is 2200 μm wide and 25 μm high. It is therefore clear that in the horizontal direction, the shear rate will be negligibly small in the center of the channel, while it might be considerable in the vertical direction. Therefore we limit our treatment to this direction. The flow rate is 500 μl per hour, corresponding to an average flow velocity of $2.5 \cdot 10^{-3} \frac{m}{s}$. We take the flow rate to be approximately constant throughout the wide dimension of the channel and approximate the parabolic flow profile across the narrow dimension by a linear one, and therefore the maximum flow velocity is twice the average flow velocity. Hence we obtain a shear rate of $4 \cdot 10^2 \text{s}^{-1}$. The rotational diffusion coefficient

has been determined above to be 1700 $\frac{\text{rad}^2}{s}$, and hence we obtain Pe$_r$≈0.24. This is smaller than the threshold for the beginning of orientation, Pe$_r$∼1 [26]. Therefore, shear alignment is negligible in our setup for short amyloid fibrils.

Next, we investigate whether the α-synuclein fibrils can be aligned by the electric field applied during the electrophoretic measurements. Alignment in an electric field can occur by means of a permanent or an induced electric dipole. We can apply phenomenological, as well as theoretical arguments. Phenomenologically, the electrophoretic mobility is expected to increase with the applied voltage in the case of significant alignment, as the degree of alignment should increase with the field strength and aligned rods have a lower friction factor - this argument has been given in favor of alignment in the case of tobacco mosaic viruses [27]. However, as can be seen in Figure 11, the electrophoretic velocity increases linearly with the electric field, and therefore an increase in mobility is not detected. This observation hints towards no significant alignment effects.

Next, we treat the question of whether alignment by the field plays a role or not theoretically. The first question is whether the fibrils possess a permanent dipole moment. Measurements of permanent dipole moments of rod-like protein aggregates are rare. It has been reported that β-lactoglobulin amyloid fibrils with an average length of ca. 4 µm have a permanent dipole moment of $3.1 \cdot 10^{-19}$Cm. This value, which agrees remarkably well with the value calculated for a chain-like assembly of monomers, has been obtained from electric field-induced birefringence at pH 2.0, where the protein carries a significant net charge of ∼+20 e. On the other hand, it has been reported that the tobacco mosaic virus, a rod-like structure of ∼300 nm in length and 18 nm in diameter, possesses a permanent dipole moment of only $8.3 \cdot 10^{-26}$Cm [28] at pH 7.5, where the virus coat protein carries a net charge of -3.4 e. It therefore seems likely that the α-synuclein fibrils possess a permanent dipole moment, but it is difficult to estimate its magnitude, especially as no detailed structural information is available for the fibrils.

Furthermore, fibrillar protein structures display a polarizability due to the mobile counterions that are associated with the charged rod, leading to an induced dipole moment. An expression for this induced dipole moment has been given by Fixman [29, 30]:

$$\mu_{\text{ind}} = \frac{4\pi\epsilon_0\epsilon_r LK z_1 E_0}{\gamma^2(z_1 - z_2)} \left(1 - \frac{\tanh\left(\gamma L/2\right)}{\gamma L/2}\right) \tag{23}$$

where z$_1$ and z$_2$ are the counter- and co-ion valencies and γ is a characteristic length scale:

$$\gamma^2 = \frac{4\pi c_1 K b}{\phi} \tag{24}$$

where c$_1$ is the bulk concentration of counter ions, K is a numerical factor, given by:

$$K = \frac{1}{2\log\left(2L/D\right) - 14/3} \tag{25}$$

The fraction of bound counter ions ϕ depends on the mean spacing between charges on the rod-like macromolecule, b, and the Bjerrum length, $\lambda_B = \frac{e^2}{4\pi\epsilon\epsilon_0 k_B T}$, according to:

$$\phi = 1 - \frac{b}{\lambda_B} \tag{26}$$

With a fibril diameter of 8 nm, a fibril density of 1.35 g/cm^3, a molecular mass and charge of the α-synuclein monomer of 14.46 kDa and -9 e, respectively, we obtain a mean spacing of the charges of 0.4 Å. The Bjerrum length in water at room temperature is ∼0.7 nm and hence $\phi \approx 0.945$. Using those values, we obtain an induced dipole moment of ∼$1.1 \cdot 10^{-27}$ Cm. This value is negligible compared to the potential permanent dipole moments mentioned above. We can now compute the orientational order parameter Φ ($\Phi \in [0,1]$) for various values of μ_0, the permanent dipole moment. The orientational order parameter can be calculated as [31]:

$$\Phi = 1 - 3\frac{\coth\left(\beta\right) - 1/\beta}{\beta} \tag{27}$$

with β defined as $\beta = \frac{\mu_0 E}{k_B T}$. If we take the range of values for μ_0 from the ones reported above: 10^{-25} Cm$< \mu_0 < 10^{-20}$ Cm, we obtain values of Φ that vary between 0.0008 and 0.9997, and hence between negligible and complete alignment. Therefore it is impossible to say from theoretical arguments alone, without a more precise estimate of the fibrils' permanent dipole moment, whether or not alignment with the field direction occurs. We will therefore analyze the electrophoresis data assuming complete and no alignment and compare the results. Expressions relating the electrophoretic mobilities of aligned and randomly oriented rods have been given by Ohshima [32]:

$$\mu_{\parallel} = \frac{\epsilon_0 \epsilon_r}{\eta} \zeta \tag{28}$$

and

$$\mu_{\text{rand}} = \frac{\epsilon_0 \epsilon_r}{3\eta} \zeta (1 + 2f(\kappa R)) \tag{29}$$

where f(κR) is Henry's function for a cylinder, that varies between 0.5 and 1. Therefore

$$\frac{\mu_{\parallel}}{\mu_{\text{rand}}} = \frac{3}{1 + 2f(\kappa R)} \tag{30}$$

varies between 1.5 and 1.0. Henry's function for a cylinder is given by [32]:

$$f(\kappa R) = 0.5 + 0.5 \frac{1}{(1 + \frac{2.55}{\kappa R(1 + e^{-\kappa R})})^2} \tag{31}$$

which yields f(κR) = 0.55 in the case of fibrils of a radius of R = 4 nm in 5 mM Tris buffer. With this value of f(κR), we can calculate the ζ-potential for the cases of complete alignment (42.2 mV) and random orientation (60.2 mV). Hunter [18] gives the relationship between the total charge of a cylinder and the ζ-potential:

$$\zeta = \frac{2Q_F K_0(\kappa R)}{4\pi\epsilon_0\epsilon_r \kappa R(2R + L)K_1(\kappa R)} \tag{32}$$

where $K_0(\kappa R)$ and $K_1(\kappa R)$ are the modified Bessel functions of the second kind ($K_0(\kappa R)/K_1(\kappa R) \approx 0.85$ under these conditions [18]). Using this relationship, we can calculate average total charges of the fibrils of -205 e (aligned case) and -292 e (random orientation). Both of these values are in good agreement with a rough estimate of the total charge based on the fraction of condensed counter ions calculated above. A fraction of bound counterions of 0.945 leaves the fibrils with a net charge of -238 e. This analysis is therefore consistent with both aligned and randomly oriented fibrils and we conclude that the fibrils possess a net charge of between 200-300 e.

6.3 Electrophoresis under different solution conditions

In order to check this analysis for its robustness and consistency, we have also performed similar electrophoresis experiments in 10 mM Tris buffer instead of 5 mM Tris. We obtain electrophoretic mobilities of -1.20 $\frac{\mu m/s}{V/cm}$ and -1.95 $\frac{\mu m/s}{V/cm}$ for monomeric and oligomeric α-synuclein under these conditions. This translates into charges of -7.2 e and -37.3 e. This apparent decrease in charge compared to the conditions of lower ionic strength might have its origin in more pronounced counter-ion binding, but could also stem from the fact that the measurement become more difficult and inaccurate at higher ionic strengths. The contribution of the fluorescent sample to the overall current, and hence the measured deflection of the sample beam, decreases with increasing solution ionic strength.

Furthermore, we have also performed experiments in 5 mM Tris buffer in the presence of 100 μM EGCG, and we found that the measured values for the mobilities are almost indistinguishable in the presence and absence of EGCG for all α-synuclein species.

7 Modeling electrostatic effects in protein thermophoresis

One of the aims of this study is to be able to quantitatively understand and model the effects of changes in solution conditions on the thermophoresis of proteins. We have recently presented an analysis of nucleic acid thermophoresis that highlighted the importance of electrostatic effects [11]. We apply this model to the thermophoresis of proteins and protein aggregates in the present study.

In our model the Soret coefficient of a biopolymer consists of three main contributions. For charged biomacromolecules, the capacitor effect $\left(S_T^{CM}\right)$ and Seebeck effect $\left(S_T^{EL}\right)$ play an important role.

$$S_T = S_T^{CM} + S_T^{EL} + S_T^{NI} \tag{33}$$

The nonionic contribution $\left(S_T^{NI}\right)$ cannot, at present, be modeled and is likely to involve surface properties of the molecule undergoing thermophoresis, such as its hydophobicity. We shown in the present study that changes in such properties lead to changes in thermophoretic behavior (e.g. the binding of the neutral molecule EGCG to α-synuclein oligomers and fibrils).
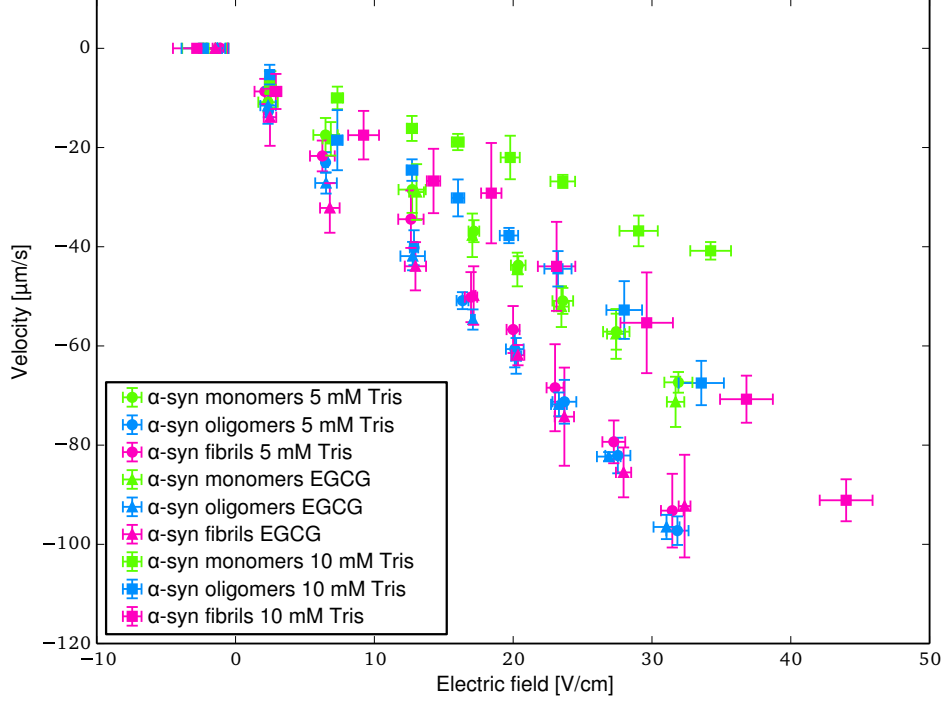
Figure 11: Plot of electrophoretic velocities vs. electric field. Shown is data for monomeric, oligomeric and fibrillar α-synuclein, in 5 and 10 mM Tris buffer, pH 7.4, as well as in 5 mM Tris buffer in the presence of 100 μM EGCG.

7.1 Capacitor effect

One important contribution to S_T of charged macromolecules is given by the capacitor effect S_T^{CM}. It results from the change in free energy of the molecule's ion cloud upon temperature variation and is dependent on the properties of the Debye layer [11, 33]. The crucial parameters are the Debye length λ_D, as well as the polymer's charge Q and radius R. In addition the density ρ, permittivity $\epsilon = \epsilon_0 \epsilon_r$ and temperature T of the solvent water affect the magnitude of S_T^{CM}. Therefore the Soret coefficient of a charged biopolymer at any given temperature is a function of the ionic strength. For spherical particles or molecules, as monomers and oligomers the capacitor model yields a contribution to S_T of:

$$S_T^{CM} = \frac{(Qe)^2}{16\pi k_B T^2 \epsilon \lambda_D \left(1 + R/\lambda_D\right)^2} \left(1 - \frac{\partial \log[\rho(T)]}{\partial \log[T]} - \frac{\partial \log[\epsilon(T)]}{\partial \log[T]} \left(1 - \frac{2\lambda_D}{R}\right)\right) \tag{34}$$

For rodlike structures, such as amyloid fibrils, the capacitance can be expressed as a superposition of a spherical and a cylindrical capacitor [34].

7.2 Seebeck effect

The salt ions in solution have themselves different Soret coefficients and are therefore affected differently by thermophoresis. As a consequence, a macroscopic electric field builds up if a thermal gradient is applied to a salt solution [11, 35, 36]. The charged macromolecules under study will undergo electrophoresis in the electric field thus created. This dependence, which in analogy to solid state thermoelectric phenomena has been dubbed the Seebeck effect, can be expressed as:

$$S_T^{EL} = -\frac{k_B T \mu}{eD} \frac{\sum_i z_i c_i S_{Ti}}{\sum_i z_i^2 c_i} \tag{35}$$

The mobility is related to the zeta potential via Eq. 15 and $\zeta = \frac{Qe}{4\pi\varepsilon r(1+r/\lambda)}$. For the Soret coefficients of single ions in water, S_{Ti}, literature values according to the reduction rule were applied ([37] and see also Reichl et al. [11])

$$S_T^{Cl^-} = 7.18 \cdot 10^{-4}/K \tag{36}$$

16

$$S_T^{Na^+} = 4.69 \cdot 10^{-3}/K \tag{37}$$

7.3 Nonionic contribution

The non-ionic contribution to the Soret coefficient of biomacromolecules is likely to be linked to surface properties of the molecule, such as hydrophobicity and hydrogen bonding capacity with water [10]. At present, no general framework exists that is able to describe these effects quantitatively. Therefore we restrict our theoretical description to the ideal gas contribution and an empirical temperature dependent part according to Piazza [38].

$$S_T^{NI} = \frac{1}{T} + S_T^{\infty}(1 - e^{-(T-T_0)/T^*}) \tag{38}$$

Here S_T^{∞} denotes the empirical Soret coefficient at infinite temperature, T_0 the temperature where the Soret coefficient changes sign and T^* is a measure for the broadness of the range where S_T increases with temperature.

7.4 Determination of 'thermophoretic charge' and nonionic contribution

On the basis of the model for the electrostatic contributions to the Soret coefficient of the protein molecules and aggregates outlined above, the 'thermophoretic charges', Q_T, and nonionic contributions, S_T^{NI}, are determined from the ionic strength series for the monomeric and oligomeric α-synuclein species (Figure 2 of the main manuscript). Taking into account the temperature dependent physical parameters of water (viscosity, permittivity, density), as well as salt concentration, concentration and size of the protein species an optimization of χ^2 for the measured data yields the parameters listed below for monomers and oligomers. Unfortunately it was not possible to perform measurements of the Soret coefficient as a function of the ionic strength for the α-synuclein amyloid fibrils due to higher order assembly of the fibrils at higher ionic strengths [5] and sticking interactions with the capillary walls.

For Soret coefficient of the Tris ion, individual parametric sweeps were performed on the salt series of monomeric and oligomeric α-synuclein. For the two α-synuclein species the best fits yields $S_T(Tris)^{Mon}$=0.0024/K and $S_T(Tris)^{Oligo}$=0.0038/K. Consequently the Soret coefficient was set to the median of both measurements $\overline{S_T(Tris)}$=0.0031/K. This value is reasonable since it is quantitatively comparable to the one of sodium with 0.00469/K [11, 37].

The best fit of the model to the data yields the following effective thermophoretic charges and nonionic contributions for monomeric and oligomeric α-synuclein:

	Q_T	$S_T^{\infty}[1/K]$	$T_0[K]$	$T^*[K]$
Monomer	-6.9 e	0.0126	292.4	20.7
Oligomer	-29.2 e	0.0161	320.6	33.4

Nonionic Contribution: Interestingly S_T^{NI} is higher for the monomers in the observed temperature range, but increases more strongly for the oligomers over base temperature (Figure 12). Whether hydrophobic effects play a role here is not clear. It is also under discussion whether the strong temperature dependence of the empirical nonionic contribution is connected to additional electrostatic effects not currently included. The thermophoresis of salt ions changes over temperature [39] and can result in further diffusiophoretic or electrophoretic influence on S_T of the macromolecule [36].

Thermophoretic charge Q: Overall the obtained charges on the basis of thermophoresis measurements are significantly smaller than the charges determined from electrophoretic measurements: Q_T^{Mon} =-6.9 e, Q_T^{Oligo} =-29.2 e from thermophoresis vs. Q_E^{Mon} =-10.9 e, Q_E^{Oligo} =-50.4 e from electrophoresis. This difference might originate in an incomplete description of the electrostatic effects involved in thermophoresis and does indeed provide an important comparison that will be helpful for further theoretical studies of protein electrophoresis and thermophoresis.

Influence of unlabeled monomers (Fig 3a of main manuscript): The Soret coefficient of the additional unlabeled monomer was set according to the expected contribution for labeled monomers in 1mM Tris: $S_T^{unl.mon} = \overline{S_T^{NI-mon.} + S_T^{CM-mon.}} = 0.031/K$. Note that this Soret coefficient corresponds to the median value over the observed temperature range in Figure 3a of main manuscript. The monomers were then incorporated as additional salt species in the Seebeck effect and taken into account for the the Debye length (Capacitor Model). The observed decrease in the Soret coefficient of the labeled monomers and oligomers in the presence of unlabeled monomers coincides with similar findings on DNA [34] in the dilute regime.

Influence of the nanobody Syn2 (Fig 4a of main manuscript): In the case of nanobodies present, the best fit to the data yields the following charges:
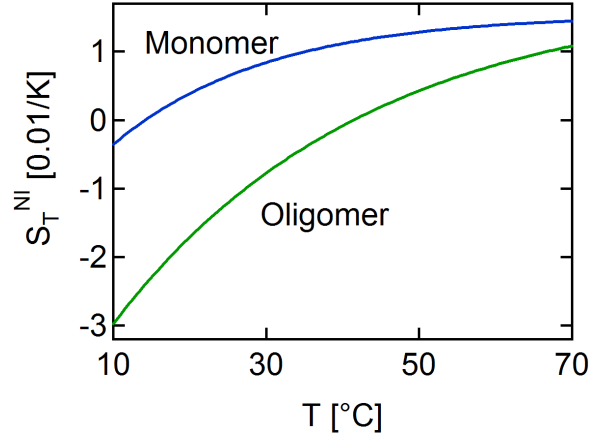
Figure 12: The non-ionic contribution to the Soret coefficient, S_T^{NI}, for monomeric and oligomer α-synuclein as a function of temperature.

	Monomer	Oligomer
No nanobody	-4.5 e	-27.6 e
Nanobody	-1.8 e	-20.6 e

The reason for the differences in charge listed here in the absence of nanobody and the charge determined for the monomers and oligomers stated above is likely to be due to the modified solution conditions (presence of phosphate ions in the nanobody solution and respectively also added to the control) and the associated altered Seebeck effect. For monomers, we obtain a $\Delta Q = +2.7$ e, which is in reasonable agreement with the expected binding of one nanobody ($+1.5$ e). In the case of the oligomers, the observed value of $\Delta Q = +7$ e is consistent with the attachment of more than one molecule of nanobody. It is difficult to estimate the expected stoichiometry of binding of nanobody to the oligomers, due to lack of detailed structural information of the oligomer and hence of the accessibilities of the epitopes.

8 ComSol simulations of the thermophoresis setup

The Soret coefficient determined from the experimentally measured concentration depletion value depends linearly on the magnitude of the induced temperature jump ΔT. In order to obtain insight into the experimental uncertainty of the induced temperature gradient, we performed a finite element simulation and compared the results with the measured values for ΔT. The decrease of ΔT with increasing base temperature T for simulation is in good agreement with the measurements. Furthermore the effect of errors in capillary thickness ($\pm 10\%$) could be tested in the simulations and the resulting error for ΔT deduced.

The simulation was performed in COMSOL Multiphysics (COMSOL Inc., USA) whereby the physics of infrared-absorption and heat transfer were incorporated (Figure 13 a). In our simulation we assumed radial symmetry and incorporated the capillary with dimensions of 50 µm x 500 µm. The capillary is coupled to a silicon wafer of 350 µm thickness with high thermal conductivity. For borosilicate, silicon and water standard material properties were used. Only temperature dependent absorption of water in the IR at the wavelength was additionally incorporated into the model [40]. As heating source a Gaussian laser profile was assumed with a beam waist of 30 µm.

As boundary conditions the bottom of the silicon was set to a base temperature and the top of the capillary thermally insulated since heat conduction of the air above is very low. Individual simulation runs were performed for base temperatures in the range of T=5-65 °C. ΔT was extracted by line averaging in the water region over capillary height and subtracting temperatures at the inner and the outer boundary. It can be observed that ΔT decreases with increasing base temperature (Figure 13 b). The main reason is found in the decreasing infrared-absorption coefficient of water with increasing temperature. The result of the numerical evaluation is in good agreement with our measurements of ΔT which was obtained using the temperature sensitive fluorescence of the dye (2',7'-Bis-(2-Carboxyethyl)-5-(and-6)-Carboxyfluorescein) (BCECF). Additionally we probed the effect of variations in capillary thickness ($\pm 10\%$, as stated by the manufacturer). The resulting shift in ΔT is of the order of $\pm 6.3\%$ and was assumed as statistical error for our experiments.
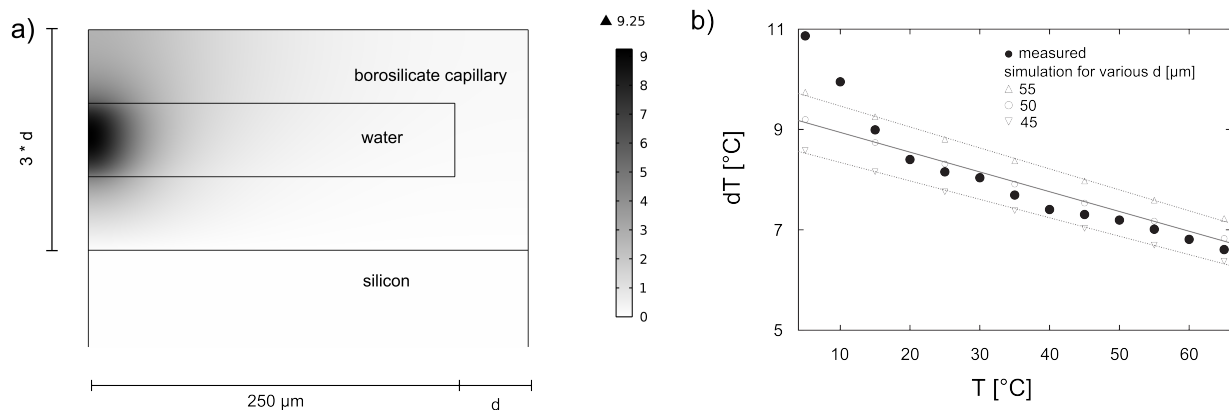
Figure 13: a) Finite Element Simulation for a capillary filled with water which is heated by an infrared (IR)-laser. In this example the temperature at the bottom of the silicon wafer was set to T = 25 °C and the resulting shift by line averaging is $\Delta T \sim 8$ °C. b) Since the IR absorbance of water is decreasing with increasing temperature [40], the extracted values for ΔT decrease with increasing base temperature T. Experimental results are in good agreement with our simulation results. The numerical evaluation was also performed for varying capillary thickness d of 45, 50 and 55 µm (variation stated by the supplier). A variation of capillary thickness by 10% entails a variation of ΔT of $\pm 6.3\%$ around the mean temperature. This value is used as statistical error of our experiments.

References

[1] Hoyer, W. *et al.* Dependence of α-synuclein aggregate morphology on solution conditions. *J Mol Biol* **322**, 383–393 (2002).

[2] Pinotsi, D. *et al.* Direct observation of heterogeneous amyloid fibril growth kinetics via two-color super-resolution microscopy. *Nano Lett* **14**, 339–345 (2014).

[3] Guilliams, T. *et al.* Nanobodies raised against monomeric α-synuclein distinguish between fibrils at different maturation stages. *J Mol Biol* **425**, 2397–2411 (2013).

[4] Lorenzen, N. *et al.* The role of stable α-synuclein oligomers in the molecular events underlying amyloid formation. *J Am Chem Soc* **136**, 3859–3868 (2014).

[5] Buell, A. K. *et al.* Solution conditions determine the relative importance of nucleation and growth processes in α-synuclein aggregation. *Proc Natl Acad Sci U S A* **111(21)**, 7671–7676 (2014).

[6] Galvagnion, C. *et al.* Lipid vesicles trigger α-synuclein aggregation by stimulating primary nucleation. *Nat Chem Biol* **11**, 229–234 (2015).

[7] Campioni, S. *et al.* The presence of an air-water interface affects formation and elongation of alpha-synuclein fibrils. *J Am Chem Soc* **136(7)**, 2866–2875 (2014).

[8] Buell, A. K. *et al.* Electrostatic effects in filamentous protein aggregation. *Biophys J* **104**, 1116–1126 (2013).

[9] Shammas, S. L. *et al.* Perturbation of the stability of amyloid fibrils through alteration of electrostatic interactions. *Biophys J* **100**, 2783–2791 (2011).

[10] Duhr, S. & Braun, D. Why molecules move along a temperature gradient. *Proc Natl Acad Sci U S A* **103**, 19678–19682 (2006).

[11] Reichl, M., Herzog, M., Götz, A. & Braun, D. Why charged molecules move across a temperature gradient: the role of electric fields. *Phys Rev Lett* **112**, 198101 (2014).

[12] Keil, L. A setup for RNA melting curves and label free thermophoresis: Bachelor thesis (2011).

[13] Mittag, J. J., Milani, S., Walsh, D. M., Rädler, J. O. & McManus, J. J. Simultaneous measurement of a range of particle sizes during Aβ1-42 fibrillogenesis quantified using fluorescence correlation spectroscopy. *Biochem Biophys Res Commun* **448**, 195–199 (2014).

[14] Broersma, S. Rotational diffusion constant of a cylindrical particle. *J. Chem. Phys.* **32**, 1626–1631 (1960).

[15] de la Torre, J. G. G. & Bloomfield, V. A. Hydrodynamic properties of complex, rigid, biological macromolecules: theory and applications. *Q Rev Biophys* **14**, 81–139 (1981).

[16] Herling, T. W. *et al.* Integration and characterization of solid wall electrodes in microfluidic devices fabricated in a single photolithography step. *Applied physics letters* **102**, 184102 (2013).

[17] Henry, D. C. The cataphoresis of suspended particles. Part I. The equation of cataphoresis. *Proc R Soc Lond A* **133**, 106–129 (1931).

[18] Hunter, R. J. *Zeta Potential in Colloid Science: Principles and Applications* (Academic Press, 1981).

[19] Ohshima, H. J. A simple expression for Henry's function for the retardation effect in electrophoresis of spherical colloidal particles. *J. Colloid Interf. Sc.* **168**, 269–271 (1994).

[20] Booth, F. The cataphoresis of spherical, solid non-conducting particles in a symmetrical electrolyte. *Proc R Soc Lond A* **203**, 514–533 (1950).

[21] Klein, S. D. & Bates, R. G. Conductance of tris(hydroxymethyl)-aminomethane hydrochloride (TrisHCl) in water at 25 and 37°C. *J Sol Chem* **9(4)**, 289–292 (1980).

[22] Quist, A. S. & Marshall, W. L. Assignment of limiting equivalent conductances for single ions to 400°C. *J. Phys. Chem.* **69(9)**, 2984–2987 (1965).

[23] Ohshima, H., Healy, T. W. & White, L. R. Accurate analytic expressions for the surface charge density/surface potential relationship and double-layer potential distribution for a spherical colloidal particle. *J. Colloid Interf. Sc.* **90(1)**, 17–26 (1982).

[24] Manning, G. S. Limiting laws and counterion condensation in polyelectrolyte solutions. V. Further development of the chemical model. *Biophys Chem* **9**, 65–70 (1978).

[25] Dhont, J. K. G. & Briels, W. J. *Rod-like Brownian Particles in Shear Flow* (WILEY-VCH Verlag Berlin GmbH, 2004).

[26] Tannous, C. Orientation control of rodlike objects by flow. *arXiv:0905.0091v3* (2009).

[27] Grossman, P. D. & Soane, D. S. Orientation effects on the electrophoretic mobility of rod-shaped molecules in free solution. *Anal Chem* **62**, 1592–1596 (1990).

[28] Newman, J. & Swinney, H. L. Length and dipole moment of tmv by laser signal-averaging transient electric birefringence. *Biopolymers* **15**, 301–315 (1976).

[29] Fixman, M. Charged macromolecules in external fields. 2. preliminary remarks on the cylinder. *Macromolecules* **13**, 711–716 (1980).

[30] Rogers, S. S. *et al.* Electric birefringence study of an amyloid fibril system: the short end of the length distribution. *Eur Phys J E Soft Matter* **18**, 207–217 (2005).

[31] O'Konski, C. T., Yoshioka, K. & Orttung, W. H. Electric properties of macromolecules. IV. Determination of electric and optical parameters from saturation of electric birefringence in solutions. *J. Phys. Chem.* **63(10)**, 1558–1565 (1959).

[32] Ohshima, H. Henry's function for electrophoresis of a cylindrical colloidal particle. *J. Colloid Interf. Sc.* **180**, 299–301 (1996).

[33] Dhont, J. K. G., Wiegand, S., Duhr, S. & Braun, D. Thermodiffusion of charged colloids: single-particle diffusion. *Langmuir* **23**, 1674–1683 (2007).

[34] Reichl, M., Herzog, M., Greiss, F., Wolff, M. & Braun, D. Understanding the similarity in thermophoresis between single- and double-stranded DNA or RNA. *Phys. Rev. E* **91**, 062709 (2015).

[35] Guthrie Jr., G., Wilson, J. N. & Schomaker, V. Theory of the thermal diffusion of electrolytes in a Clusius column. *J. Chem. Phys.* **17**, 310 (1949).

[36] Eslahian, K. A., Majee, A., Maskos, M. & Würger, A. Specific salt effects on thermophoresis of charged colloids. *Soft Matter* **10**, 1931 (2014).

[37] Takeyama, N. & Nakashima, K. Proportionality of intrinsic heat of transport to standard entropy of hydration for aqueous ions. *J. Sol. Chem.* **17(4)**, 305–325 (1988).

[38] Iacopini, S., Rusconi, R. & Piazza, R. The "macromolecular tourist": universal temperature dependence of thermal diffusion in aqueous colloidal suspensions. *Eur Phys J E Soft Matter* **19**, 59–67 (2006).

[39] Römer, F., Wang, Z., Wiegand, S. & Bresme, F. Alkali halide solutions under thermal gradients: Soret coefficients and heat transfer mechanisms. *J Phys Chem B* **117**, 8209–8222 (2013).

[40] Goldstein, R. & Penner, S. The near-infrared absorption of liquid water at temperatures between 27 and 209°C. *Journal of Quantitative Spectroscopy and Radiative Transfer* **4(3)**, 441–451 (1964).